# Solid-State NMR Investigations of Materials with Magnetoplumbite and Perovskite Structures

**Thesis Submitted to AcSIR for the Award of the Degree of**

**DOCTOR OF PHILOSOPHY**
**In Chemical Sciences**

**By**
**Ms. Bindhu Baby**
**Registration Number: 10CC11J26014**

**Under the Guidance of**

**Dr. T.G. Ajithkumar**
**and**
**Dr. P.A.Joy**

**CSIR-National Chemical Laboratory,**
**Pune - 411008, India.**

**March 2015**

राष्ट्रीय रासायनिक प्रयोगशाला
(वैज्ञानिक तथा औद्योगिक अनुसंधान परिषद)
डॉ. होमी भाभा रोड, पुणे - 411 008. भारत
NATIONAL CHEMICAL LABORATORY
(Council of Scientific & Industrial Research)
Dr. Homi Bhabha Road, Pune - 411008. India

# CERTIFICATE BY RESEARCH GUIDE

This is to certify that the work presented in the thesis entitled "**Solid-State NMR Investigations of Materials with Magnetoplumbite and Perovskite Structures**" by **Ms. Bindhu Baby**, submitted for the degree of **Doctor of Philosophy in Chemical sciences** was carried out under our supervision at the Physical and Materials Chemistry Division, CSIR-National Chemical Laboratory, Pune - 411008, India. All the materials from other sources have been duly acknowledged in the thesis.

Date:

Place: Pune

Dr. T. G. Ajithkumar
(Research Guide)

Dr. P.A.Joy
(Research Co-Guide)

Communications Channels ☎ +91 20 25902000 +91 20 25893300 +91 20 25893400 Fax +91 20 25902601 (Director) +91 20 25902660 (Admin.) +91 20 25902639 (Business Development) URL : www.ncl-india.org

## DECLARATION BY RESEARCH SCHOLAR

I hereby declare that the work incorporated in this thesis entitled "**Solid-State NMR Investigations of Materials with Magnetoplumbite and Perovskite Structures**" submitted by me for the degree of Doctor of Philosophy to the AcSIR is the record of the work I have carried out at the Physical and Materials Chemistry Division, CSIR-National Chemical Laboratory, Pune – 411008 under the joint supervision of Dr. T. G. Ajithkumar and Dr. P. A. Joy is original and has not formed the basis of award of any degree or diploma. All the materials from other sources have been duly acknowledged in the thesis.

Date:

Bindhu Baby
Physical and Materials Chemistry Division
CSIR-National Chemical Laboratory
Pune-411008

*Dedicated to*

*my Family....*

# Acknowledgements

*I am very glad in this occasion to thank one and all, who have helped me in completing my research work through their constant support in the form of their prayers, and assistance at the hour of need.*

*First and foremost I would like to thank* ***God****, the almighty for all the glorious things he has done in both small and great things in my life.*

*I would like to express my sincere gratitude to my research guide* ***Dr. T. G. Ajithkumar****, who gave me an incredible opportunity to pursue my career as a Ph.D. student. My sincere thanks to him for his timely helps and supports both scientifically and personally during my research period. It is my privilege to thank my research co-guide* ***Dr. P. A. Joy*** *who provided me a fascinating outlook towards the research. I really admire the way he teaches complicated things in very simple and easy manner. I am deeply indebted to him for his immense help, the extreme care he has taken in the analysis of the data presented in the thesis.*

*I am grateful to* ***Dr. P. R. Rajamohanan*** *and* ***Dr. Anilkumar*** *who allowed me to do the collaboration work without any difficulty in their respective departments. I also thank* ***Dr. Sourav Pal****, Director, NCL, for allowing me to work in this prestigious laboratory.*

*I acknowledge UGC for giving me the research fellowship.*

*I have enjoyed enormous support from the members of the Central NMR Facility during my research period. It is my great pleasure to thank Dr. S. Ganapathy, Dr. Sapna Ravindranath, Sathe Sir, Phalgune madam, Suryavamshi sir, Mane sir, Umesh and Sachin.*

*I would like to acknowledge Dr. P. K. Madhu (TIFR Bombay), who has always helped with my stays at TIFR, Dr. K. K. Dey (Sagar University, Madhya Pradesh), Dr. T. S. Mahesh (IISER Pune) and Dr. K. V. Ramanathan (IISc, Bangalore) for providing me with the facilities in their laboratories. The National Facility for High-Field NMR, TIFR, Bombay, NMR Facility at CBMR, Lucknow, NMR Research Center, IISER Pune, NMR Research Center, IISc, Bangalore are*

*gratefully acknowledged. I am also grateful to CSIR-NCL, Pune for providing the high field NMR facility, Bruker AV-700, on which I had done all the* $^{139}La$ *experiments without which the work could not have been completed.*

*I am certainly obliged to all my labmates who provided a peaceful atmosphere in the lab to work with satisfaction. Eldho, Renny, Jima, Aany, Hari, Yamuna, Anu, Anjali, Amol, Deepak, Sreekant, Snehal, Mayur, Anjali, Athira, Sreedevi and Sanoop from NMR and Vijay, Sreeja, Khaja, Mangesh, Pankaj, Lenin, Jaya, Govind, Ram, Manjunath, Ananth, Mohan and Arun from Joy sir's lab and all the project students are gratefully acknowledged.*

*I have enjoyed the care and affection from the friends in NCL which is an endless list and among those I especially thank leena chechi, Jaya chechi, Roshna chechi, Biyas and my little friend Aamish. It was totally fun in our room with you Vinisha, Deepa, Nisha, Neha and Swati. I thank all of you for making my stay at NCL memorable.*

*I want to thank all the friends from my childhood to my post graduation and particularly I thank Sajesh for doing the SHG measurements. Special thanks goes to my best friends Priya Mary Abraham, Hilda Davis and Remya Ramachandran who have motivated me towards a research career and was always there with me with their constant prayers and support.*

*I cannot finish without saying how grateful I am to my parents, siblings and near relatives. I dedicate the thesis to them. I have got a full hearted support from my great Velupparambil and Padapurackal family. I take pride of being a member of that family. I simply adore the way they love and understand me. I am forever indebted to my parents, sisters and brother. Daddy, I love you so much that I still cannot believe, you are not there with us. You are always there in our prayers. Finally I express my thanks to Bibin chettan for his love, patience, trust and support.*

*Bindhu Baby*

# Contents

# List of Tables

# List of Figures

# List of abbreviations and symbols commonly used

CT – Central transition

DAS – Dynamic angle spinning

DOR – Double rotation

MAS – Magic angle spinning

NMR – Nuclear magnetic resonance

MQMAS – Multiple quantum magic angle spinning

QA – Quadrupolar anisotropy

SSNMR – Solid-state nuclear magnetic resonance

XRD – X-ray diffraction

RF – Radio frequency

1Q – Single quantum

3Q – 3 quantum

3QMAS – 3 quantum magic angle spinning

$C_q$ – Quadrupole coupling constant

$\nu_q$ – Quadrupole frequency

$\delta_{iso}$ – Isotropic chemical shift

$\Delta_{CS}$ – Chemical shift distribution

$\eta$ – Asymmetry parameter

$\chi^2$ – Goodness of fit indicator

$R_{F^2}$ – R-structure factor

$R_{wp}$ – R-weighted pattern

# Abstract

The fundamental relationships between structure and properties of materials and how their properties can be changed and tuned by the various chemical, thermal, mechanical or other treatments is very crucial for the development of new materials with unusual combination of properties. Structural characterization is an important part of the development of materials and techniques such as XRD, EXAFS, IR, UV, Raman, solid-state NMR (SSNMR), etc, are used for determining the structure of materials. Among these, solid-state NMR is the best tool to probe the local symmetry and the coordination environments, since particular nuclei are probed which extends over several coordination spheres.

Strontium ferrite is an important magnetic material with the magnetoplumbite crystal structure. In La-Co substituted strontium ferrite, $Sr_{1-x}La_xFe_{12-x}Co_xO_{19}$, an improvement in the magnetic properties was observed at x $\approx$ 0.3. Mössbauer spectroscopic studies have shown that Co ions occupy the 2a and $4f_2$ crystallographic sites in the magnetoplumbite structure. It is not clear why the best performance is observed at $x$ close to $\approx$ 0.3.

Perovskite type materials of the general formula $ABO_3$ exhibit interesting properties which are used for different applications and the properties are closely related to their crystal structure. The properties of the perovskite materials can be tuned by proper substitution at the A-site or B-site. For example, A-site substitution in the rare earth manganites $RMnO_3$ gives rise to ferromagnetic properties, colossal magnetoresistance and charge ordering near their Curie Temperatures. The improvement in the properties of the materials is associated with the local structural changes.

The properties of the oxides with the magnetoplumbite and perovskite structures can be changed upon substitution arising from the local structural distortions. To understand the local structural changes on substitution, suitably substituted compositions of $SrAl_{12}O_{19}$ which is the non-magnetic equivalent of $SrFe_{12}O_{19}$ with the magnetoplumbite structure and $LaAlO_3$ which is the non-magnetic equivalent of $LaMnO_3$ with the perovskite structure are studied with solid-state NMR.

Strontium aluminate was simultaneously substituted with $La^{3+}$ and $Zn^{2+}$ at the $Sr^{2+}$ and $Al^{3+}$ sites, respectively. $LaAlO_3$ was substituted with $Y^{3+}$ at the $La^{3+}$ site and $Co^{3+}$ and $Ga^{3+}$ at the $Al^{3+}$ site.

Solid-state NMR studies on the La-Zn substituted strontium aluminate samples, $Sr_{1-x}La_xAl_{12-x}Zn_xO_{19}$, showed the occupancy of the Zn ions in the 2a (octahedral) and $4f_2$ (octahedral) Al sites in the hexagonal magnetoplumbite crystal structure as reported for La-Co substituted strontium ferrite from Mössbauer spectroscopic studies. Large changes in the quadrupolar coupling constant of the 2a and 4e sites are observed between $x = 0.2$ and 0.3, corresponding to the compositional region in $Sr_{1-x}La_xFe_{12-x}Co_xO_{19}$, showing higher performance, indicating the role of distortion of local coordination environments in controlling the performance parameters. Additional information is obtained on the stabilization of the penta coordinated 2b Al site along with a corresponding decrease in the occupancy of Al in the distorted tetrahedral 4e Al site as the degree of substitution is increased.

Studies on the $^{27}Al$ magic angle spinning (MAS) and static SSNMR of $LaAlO_3$, along with Rietveld analysis of the powder XRD pattern, indicated that centre of inversion is absent in rhombohedral $LaAlO_3$ and the correct space group of the material is R3c instead of $R\bar{3}c$, as concluded from the recent resonant Raman spectroscopic studies.

$^{139}La$ and $^{27}Al$ solid-state NMR studies on Y substituted $La_{1-x}Y_xAlO_3$ showed a change in the NMR parameters at $x = 0.13$. Rietveld refinement of the XRD patterns on different samples showed that there is a structural change above $x = 0.13$, where the structure changes from R3c to a mixed phase of R3c and orthorhombic Amm2, since the structure of $LaAlO_3$ is rhombohedral and that of $YAlO_3$ is orthorhombic. The structural changes are associated with the replacement of $1/8^{th}$ of the A site ions in the perovskite structure.

Studies on Al-site substitution in $LaAlO_3$, when $Al^{3+}$ is substituted by $Co^{3+}$ which has a size comparable to $Al^{3+}$ and by $Ga^{3+}$ which has relatively larger size indicated that the rhombohedral structure is unaffected on substitution. However,

the space group of Ga substituted samples changed from R3c to R$\bar{3}$c above $x = 0.375$ in $LaAl_{1-x}Ga_xO_3$. $^{139}La$ and $^{27}Al$ SSNMR studies showed large changes in the NMR parameters for the $Ga^{3+}$ substituted samples indicating local structural distortions. On the other hand, since the sizes of $Co^{3+}$ and $Al^{3+}$ are comparable, only small distortions in the Al octahedra, arising from the electronic environment differences, are expected. Correspondingly, only minor changes in the NMR parameters are observed for the $Co^{3+}$ substituted samples.

# Chapter 1

# Introduction

## 1.1 Materials science

From the very beginning of the history of mankind, materials have been playing a pivotal role for the growth, prosperity, security and quality of life of humans. The early civilizations are designated by the level of their materials development such as stone age, iron age, copper age, etc. The earliest humans, at first, were aware of only the naturally occurring materials. However, with time, they have discovered techniques for producing materials that have superior properties than that of the natural ones. Later, it was discovered that the properties of a material could be altered by various methods like, heat treatment and by the addition of other substances. Now scientists have understood the relationships between the structural elements of the material and their properties. This knowledge has helped them in fabricating thousands of materials including the metals, plastics, glasses and fibers which meet the needs of the society [1]. It is now impossible for us to imagine a life without the use of materials which are being used in the area of transportation, housing, clothing, recreation, food production, telecommunication, health, and energy consumptions. There are different types of solid substances that serve the above mentioned applications [2]. They include metals, polymers, ceramics, semiconductors and composites. Based on the properties, materials are classified as electrical, magnetic, dielectric, optical, etc [3].

Most of the materials which we use for our day-to-day applications are complex oxide materials, which are compounds derived from metals and oxygen. Metal oxides are unique materials on account of their richness in terms of physical, chemical and structural properties [4]. Complex oxide systems are the most common class of materials found on the earth, for example, the most abundant minerals on the earth are oxides. They are of interest in many commercial technologies from displays in the electronics to the integrated circuits and communication to sensors and actuators. They represent a broad range of functionalities such as high temperature superconductivity, colossal magnetoresistance, ferromagnetic, ferroelectric and multiferroic properties [5]. These oxides exist in a wide range of chemical compositions and crystal structures obtained through varying synthesis

paths [6,7]. Some of the important classes of complex oxide materials are:

- Spinels with the general formula $AB_2O_4$ where A (divalent) and B(trivalent) are two different metal ions of comparable ionic sizes, such as the transition metal ions. Examples are $MgFe_2O_4$, $ZnAl_2O_4$, $MnCo_2O_2$.

- Perovskites with the general formula $ABO_3$ where A and B are metal ions where A is a larger ion such as the divalent alkaline earth ions or the trivalent rare earth ions and B is a smaller ion such as the transition metal ions which can have different oxidation states such as $Mn^{3+}$, $Mn^{4+}$, $Ti^{4+}$, $Mg^{2+}$, etc. Examples are $LaMnO_3$, $BiFeO_3$, $SrTiO_3$, $LiNbO_3$.

- Magnetoplumbites with the general formula $AB_{12}O_{19}$, where A is a large divalent ion such as $Sr^{2+}$ and B is a trivalent ion such as $Al^{3+}$, $Ga^{3+}$, $Fe^{3+}$, etc. Examples are $SrAl_{12}O_{19}$, $BaFe_{12}O_{19}$.

- Ruddlesden-Popper phases are derived from the perovskites with the general formula $A_{n+1}B_nO_{3n+1}$ or $AO(ABO_3)_n$. Examples are $Sr_2TiO_4$, $Ca_2MnO_4$ and $SrLaAlO_4$.

- Pyrocholores with the general formula $A_2B_2O_7$ where A is a larger ion and B is a smaller ion. Examples are $Y_2Ti_2O_7$, $La_2Zr_2O_7$, $Dy_2Ti_2O_7$.

Functional materials are a class of materials which possess physical properties and functions of their own, serving specific application needs [8]. They cover a broad range of materials like ferroelectrics such as $BaTiO_3$, magnetic field sensors like $La_{1-x}Ca_xMnO_3$, surface acoustic wave sensor $LiNbO_3$, semiconductor light detectors CdS and CdTe, high temperature piezoelectric $Ta_2O_5$ and high temperature superconductors such as $YBa_2Cu_3O_7$, high-k dielectrics such as $HfO_2/HfSiO_x$, $Al_2O_3$, $TiO_2$ and $LaAlO_3$, etc [9]. The properties of the functional materials depend on a number of parameters like temperature, pressure, electric field, magnetic field, etc.

Magnetic materials are one of the important class of functional materials. Magnetic materials are used everywhere in modern high technology society since their

use ranges from applications in permanent magnets in electric motors to the very high density storage of information on the hard disk drives used in computers [10]. There have been lot of studies on the magnetic materials such as shape memory alloys, magnetocaloric and magnetostrictive materials, magnetic nanomaterials, multiferroics and high energy materials. Most of the ceramic magnets are made up of ferrites, which are crystalline minerals composed of iron oxides combined with some other metals. There are continuous magnetization and demagnetization processes taking place in these ferrites by the passage of electric current, which give rise to the information flow when we do some calculations, chat with someone, or do some simple processes [11]. The hexaferrites with the magnetoplumbite structure occupy a major share of the consumer magnet market and these materials are being used for the colourful fridge magnets as well as in numerous motors, actuators and sensors [12]. Another important class of materials having potential technological applications is the colossal magnetoresistive materials (CMR) which are generally the perovskite structured manganites with the general formula $La_{1-x}D_xMnO_3$, where D is a divalent alkaline earth ion such as Ca, Sr or Ba [13,14].

Materials science is the study of the correlation between the structure, properties and applications of different materials. Control of the properties of materials is an important factor in material science and engineering since the materials are used in various applications, and for this a basic understanding of the structure of a given material is essential [15]. It is very important to understand the fundamental principles that make these materials functional by which we can create multifunctional materials based on same physical principles. The broad field of materials science and engineering studies the various aspects [16] such as:

- The structure and composition of a material, including the type of atoms and their arrangement in the crystal structure.

- The synthesis and processing by which the particular arrangement of atoms is achieved.

- The properties of the material resulting from atoms and their arrangement that make the material interesting or useful.

- The performance of the material, that is the measurement of its usefulness in actual conditions, taking account of economic and social costs and benefits.

The design and the synthesis of new materials as well as tailoring the properties of the existing materials by manipulating their structure is the driving force for the expansion of the field of materials science that leads to new technologies and applications. Therefore, it becomes meaningless unless the structures and the properties of materials are investigated before using them for any application [17]. A number of experimental techniques exist for investigating the structure of materials. On the large scale, materials are characterized by measurements of their bulk properties including density, surface area, chemical composition and physical properties. At the next level, magnified images are used to study the morphology, structure and shape of various features through the microscopy. In the medium range of atomic ordering, structures can be probed by spectroscopic techniques such as X-ray diffraction (XRD), extended X-ray absorption fine structure (EXAFS), X-ray absorption near edge structure (XANES), infrared (IR), UV-Visible, Raman, etc, or by various multinuclear nuclear magnetic resonance (NMR) techniques. Among the various techniques, NMR is the best tool to probe the local symmetry and the local coordination environments, since one can probe the nuclei which extends over several coordination spheres.

## 1.2 Importance of NMR studies on materials

Materials exists in various states of structural disorder and heterogeneity. Unlike the diffraction techniques which require the presence of long range order, NMR is a versatile technique which can probe atomic environments of most disordered systems like glasses to the most ordered systems like single crystals. NMR technique depends on the nuclear spins and since the nuclear spins are affected by a variety of structure-dependent interactions, the technique is able to provide detailed

insight into the atomic scale environment within a solid. Thus, it provides element specific insights into structure, disorder and dynamics of the materials [18]. NMR is, thus, able to monitor the changes occurring in atomic environment when materials change from one state of structural disorder or heterogeneity to another and has proved to be a powerful technique for studying transition from glasses to melts, nucleation of polycrystals from glasses and the formation and growth of crystalline phases from colloids or gels. NMR is also an ideal method for studying the intermediate phases formed when minerals react or transform to other phases by heating or mechanical grinding, which often lack the long-range order necessary for conventional diffraction studies. For example, dynamic effects in the double perovskite $Na_3AlF_6$ have been studied by the multinuclear NMR studies of the material by probing $^{23}$Na, $^{27}$Al, and $^{19}$F [19]. $^{27}$Al NMR studies have been used to get detailed coordination environment of the spinels like magnesium aluminate, zinc aluminate and gamma-alumina [20–22]. NMR has been successfully used to characterize the ferroelectric, piezoelectric and the related materials [23]. The evolution of crystalline phase in the titania gels has been studied using $^{47,49}$Ti NMR [24]. $^{91}$Zr NMR has been used to directly probe the metal centers in layered zirconium phosphates [25]. The metal-insulator phase transitions in colossal magnetoresistive manganites have been studied by $^{55}$Mn NMR [26–29]. In strontium ferrite, with the magnetoplumbite structure, $^{57}$Fe NMR has been carried out to locate the different substitutional sites in the structure [30–32].

However, while using the technique, it is important to establish a relationship between the experimental NMR spectrum and the recurring structural motifs, to determine the structural characteristics of materials [33]. This is done by a fingerprinting procedure, where the characteristics of unknown compound are deduced by comparison with the extensive database of NMR spectra established for materials of known composition and structure. The parameter most readily determined from an NMR spectrum is the position of the resonance peak, and although this may not be true isotropic shift, empirical relationships have been developed for a limited range of similar compounds between resonance position and character-

istic feature of a structural unit. Thus, NMR technique can differentiate local coordination environments. For example, peaks in the NMR spectra for different coordination environments for the same nuclei appear at different chemical shifts. In some cases, recording spectra at a particular field may not give the proper information, and therefore, measurements need to be made at more than one magnetic field and should use specialized techniques to improve the resolution of spectral lineshapes so that accurate spectral parameters can be extracted.

A typical NMR investigation combines several types of 1D, 2D and sometimes even 3D experiments. The accumulated information provides often a detailed picture of the molecular structure. Variations in the NMR parameters such as chemical shift can give information on the coordination environment and local structural distortions.

## 1.3 Basic principles of NMR

NMR spectroscopy is one of the scientific fields where one can analyze the interaction of electromagnetic waves, particularly the radio frequency waves, with the matter in the frequency range between 10 kHz and 1000 MHz. The spectrometers operating at ultra high fields are equipped with superconducting magnets. In NMR, we characterize a nuclei using the properties of electric charge or the electric charge distribution inside the nucleus and the nuclear spin. NMR involves detailed manipulation of the spins. The detailed description on the principles of NMR are given in the excellent books by Abragam [35], Slichter [36] and Malcolm H. Levitt [37].

### 1.3.1 Nuclear spin and the splitting of energy levels in a magnetic field

Quantum mechanically, subatomic particles (protons, electrons, neutrons) have a characteristic spin ($I$) and it is an intrinsic property of the particle. The spin of a nucleus is given by the sum of the proton and neutron spin quantum numbers. A

nucleus with an odd mass number has a half integer spin [e.g. $^{1}$H, $^{13}$C ($I = 1/2$)]. If the number of protons and number of neutrons are both odd, then the nucleus has an integer spin [e.g. $^{2}$H, $^{14}$N ($I = 1$)]. A nucleus with both even number of protons and neutrons have a spin zero [e.g. $^{12}$C, $^{16}$O, $^{32}$S]. For a nucleus to be NMR active, it should have a non-zero spin value.

The nuclear magnetic dipole moment of a nuclei is given by,

$$\mu = \gamma I \tag{1.1}$$

where $\gamma$ is the gyromagnetic ratio of the nucleus, which is a constant for a given nucleus. Generally, the external field is considered to be applied along the $z$-axis of the Cartesian coordinate system and is called the lab frame. Thus the $z$-component of the spin angular momentum is

$$I_z = m\hbar \tag{1.2}$$

where $m$ is the magnetic quantum number, and takes the values $-I, -I{+}1 \ldots 0 \ldots {+}I$. Thus, a nucleus of spin $I$ will have $2I + 1$ possible orientations. So, a nucleus with spin = 1/2 will have 2 possible orientations. In the absence of an external magnetic field, these orientations are of equal energy. If a magnetic field is applied, then the energy levels split. Each level is given a magnetic quantum number, $m_s$, which is shown in figure 1.1

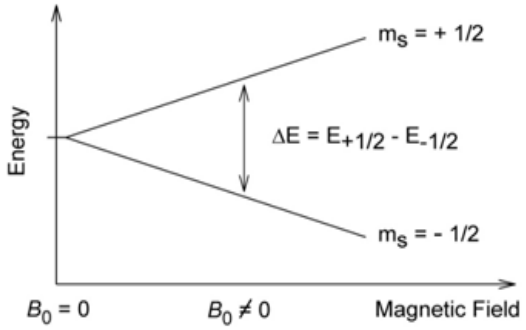


*Figure 1.1: Splitting of the nuclear energy levels in the presence of an applied magnetic field.*

When a nucleus is in a magnetic field, the initial populations of the energy levels are determined by thermodynamics, as described by the Boltzmann distribution. The lower energy level will contain slightly more number of nuclei than in the higher level. It is possible to excite the nuclei at the lower energy level into the higher level with electromagnetic radiation. The frequency of radiation needed is determined by the difference in energy between the energy levels, which is given as

$$\Delta E = \frac{\gamma h B}{2\pi} \tag{1.3}$$

where $h$ is the Planck's constant, $\gamma$ is the gyromagnetic ratio and B is the magnetic field.

### 1.3.2 The absorption of radiation by a nucleus in a magnetic field

A nucleus is spinning on its own axis. In the presence of a magnetic field, this axis of rotation will precess around the magnetic field, called Larmor precession. The frequency of precession, Larmor frequency ($\omega$), is directly proportional to the strength of the applied field. Since the nucleus has a charge, the precession will generate an oscillating electric field of the same frequency. When the frequency of the oscillating electric field component of the incoming radiation just matches with the frequency of the electric field generated by the precessing nucleus, the two fields can couple, and the energy can be transferred to the nucleus, thus causing a spin change. This condition is called resonance.

### 1.3.3 Fourier transform (FT) NMR

In the earlier days of NMR, experiments were carried out by varying the frequency of radiation at a constant magnetic field (frequency sweep) and by measuring the absorption of radiation by a different nuclei (Continuous Wave spectroscopy). A far better resolution and sensitivity in NMR was achieved by the introduction of pulsed Fourier transform techniques (FT-NMR) which employs a powerful but

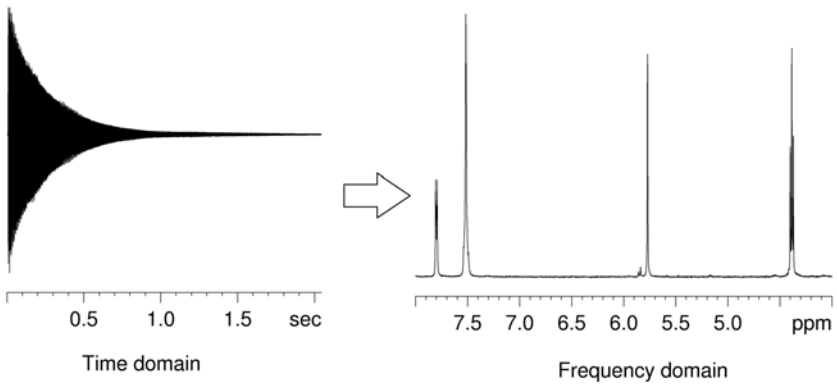


*Figure 1.2: Fourier transformation of a time domain signal to the frequency domain spectrum.*

short burst of energy called pulse that excites all nuclei simultaneously. Whenever the pulse is discontinued, all these nuclei will re-emit the radio frequency (RF) radiation at their respective resonance frequencies, creating an interference pattern resulting in the RF emission versus time, known as Free Induction Decay (FID) or time-domain signal. A frequency domain spectrum is then obtained by the Fourier transformation of the FID signal, as shown in figure 1.2. The Fourier transformation is mathematically expressed as

$$S(\omega) = \int_0^\infty S(t) \exp(-i\omega t) dt \tag{1.4}$$

where S($\omega$) is the spectrum in the frequency domain and S(t) is the spectrum in the time domain.

Solution-state NMR is the most widely used characterization technique in small molecule chemistry. The compounds containing C, H, F, Si, P, etc, are being extensively studied using solution-state NMR. This requires the material of interest to be dissolved in a suitable solvent but in some cases, dissolving solid materials in a solvent may be impossible or may destroy the integrity of the material. The anal-

ysis of solids by NMR is a more challenging problem. Many important materials do not contain spin-1/2 nuclei traditionally investigated by NMR spectroscopy and the ordered arrangement of the solids give rise to very broad spectrum compared to the solution-state NMR. However, with the development of the high-resolution techniques in solid-state NMR, it is now possible to characterize different ranges of materials.

## 1.4 Solid-state NMR

Solid-state NMR (SSNMR) spectroscopy is a powerful technique capable of providing information about the structure of materials and about the dynamics of the processes occurring within those materials. It is a non-destructive probe for the study of local structural environment in materials. Using this technique, we can get information regarding molecular structure, inter-nuclear distance, nature of interaction, molecular dynamics, molecular degrees of freedom, etc, of solid materials.

A nucleus having an electric charge and magnetic moment interacts with the electric and the magnetic fields generated by the electrons and other nuclei of molecules or external magnetic field. Thus, the total Hamiltonian for the NMR interaction includes Zeeman interaction ($H_Z$), J-coupling interaction ($H_J$), chemical shift ($H_{CS}$), dipolar interaction ($H_D$) and for the nuclei with $I > 1/2$, the quadrupolar interaction ($H_Q$). Thus, the total Hamiltonian is written as

$$H = H_z + H_J + H_{CS} + H_D + H_Q \tag{1.5}$$

The through- space, J-coupling interactions are too small in solids and is the most important interaction in solution-state NMR. In solution-state NMR, the rapid molecular motion serves to average out all these interactions and the NMR spectrum exhibits only isotropic chemical shifts and yields high resolution spectra. On the other hand, in solids, the random molecular motions are restricted since the atoms are close-packed within the structure and the NMR resonances broaden. Therefore, the spectra of solids is less resolved due to the anisotropy in dipolar,

quadrupolar and chemical shift interactions. All NMR interactions are anisotropic and their three-dimensional nature can be described by second-rank tensors, which are 3×3 matrices.

### 1.4.1 Zeeman interaction

Zeeman interaction is the interaction of a nucleus with the magnetic moment $\mu$ and external magnetic field $B_0$ and is characterized by the Zeeman Hamiltonian,

$$H_z = -\mu B_0 \tag{1.6}$$

Since the external field is along the $z$-axis, Zeeman Hamiltonian becomes

$$H_z = -\gamma \hbar B_0 I_z = \hbar \omega_0 I_z \tag{1.7}$$

where $\omega_0$ is the Larmor frequency or the resonance frequency of an isolated nucleus in a magnetic field. This is the largest interaction in NMR.

### 1.4.2 Chemical shift

Chemical shift is the most important parameter in NMR spectroscopy arising due to the electronic environment around a nuclei and it has turned NMR from simply an interesting physical observation of the nuclear magnetic moment into a widely useful analytical technique. When an atom is placed in a magnetic field, its electrons circulate about the direction of the applied magnetic field which produces a small magnetic field at the nucleus opposing the externally applied field. Hence, the magnetic field experienced by a particular nucleus is modified as,

$$B_{local} = B_0 - B_0\sigma = B_0(1 - \sigma) \tag{1.8}$$

where $B_0$ is the applied magnetic field, $B_{local}$ is the local magnetic field and $\sigma$ is called the shielding constant arising due to the circulating electrons. The three dimensional nature of the electron density in a material means that chemical shielding is represented by a second rank tensor $\sigma$ and the corresponding Hamiltonian is

$$H_{CS} = \gamma\hbar I.\sigma.B_0 \tag{1.9}$$

The chemical shielding tensor in the principal axis system (PAS) is diagonal with its principal components $\sigma_{XX}$, $\sigma_{YY}$ and $\sigma_{ZZ}$ and is given as

$$\sigma^{PAS} = \begin{pmatrix} \sigma_{XX} & 0 & 0 \\ 0 & \sigma_{YY} & 0 \\ 0 & 0 & \sigma_{ZZ} \end{pmatrix} \tag{1.10}$$

In a crystalline powder sample, all orientations of the PAS system of the shielding tensor are present and $\sigma^{PAS}$ when transformed to laboratory frame becomes

$$\sigma^{LAB} = \begin{pmatrix} \sigma_{xx} & \sigma_{xy} & \sigma_{xz} \\ \sigma_{yx} & \sigma_{yy} & \sigma_{yz} \\ \sigma_{zx} & \sigma_{zy} & \sigma_{zz} \end{pmatrix} \tag{1.11}$$

The two frames are related by rotation of the axes using matrices with the Euler angles defining the rotation to give

$$\sigma^{LAB} = R(\alpha\beta\gamma)\sigma^{PAS}R^{-1}(\alpha\beta\gamma) \tag{1.12}$$

However, commonly, the chemical shift tensor($\delta$) is used instead of the chemical shielding tensor ($\sigma$) and

$$\delta^{PAS} = -\sigma^{PAS} \tag{1.13}$$

The chemical shift tensor is characterized by three parameters which are isotropic chemical shift ($\delta_{iso}$), chemical shift anisotropy ($\delta_{aniso}$) and asymmetry parameter ($\eta$), which are defined as

$$\delta_{iso} = \frac{1}{3}(\delta_{XX} + \delta_{YY} + \delta_{ZZ}) \tag{1.14}$$

$$\delta_{aniso} = \delta_{ZZ} - \delta_{iso} \tag{1.15}$$

$$\eta = \frac{\delta_{YY} - \delta_{XX}}{\delta_{ZZ} - \delta_{iso}} \tag{1.16}$$

The isotropic part of the chemical shift, $\delta_{iso}$, is usually reported. The chemical shift is normalized by taking the difference between the resonance frequency of the standard reference sample ($\nu_{ref}$) and the sample frequency ($\nu_{sample}$). It is then normalized by the reference frequency and is then quoted in parts per million.

$$\delta_{sample} = \frac{\nu_{sample} - \nu_{ref}}{\nu_{ref}}(\times 10^6) \tag{1.17}$$

The normalization means that measurements at different magnetic fields can be directly compared. Different nuclear environments induce different chemical shifts. For example, Al in oxides is usually coordinated by 4, 5, or 6 oxygen atoms resulting in tetra, penta or hexa coordinations which appear at different chemical shift ranges which are 0–10 ppm for hexa, ≈20–50 ppm for penta and 60–80 ppm for tetra coordination, respectively.

### 1.4.3 Dipolar coupling

Every magnetic nucleus in a sample produces its own magnetic field. The interaction between the magnetic field produced by one nucleus and its neighboring nuclei is called dipolar coupling. The strength of this interaction depends on the internuclear distance, $r$, and the angle between the magnetic field and the line joining the two nuclei, $\theta$. It is known that the dipolar coupling, $D$, is directly proportional to $(3\cos^2\theta - 1)/r^3$. In a solution, this interaction is averaged to its isotropic value, zero, by molecular tumbling. However, the case is different in solids. The tumbling motions are not occurring in solids since they are closely packed. The resonance frequency of each nucleus depends on the total magnetic field, which it experiences, and therefore, the dipolar coupling results in a wide resonance peak.

The dipolar interaction arises from the coupling between two magnetic dipoles. The classical interaction energy between two magnetic dipoles $\vec{\mu_1}$ and $\vec{\mu_2}$ separated by a distance $r$, is given by

$$E_D = \frac{\mu_0}{4\pi}[\frac{\vec{\mu_1}.\vec{\mu_2}}{r^3} - \frac{3(\vec{\mu_1}.\vec{r})(\vec{\mu_2}.\vec{r})}{r^5}] \tag{1.18}$$

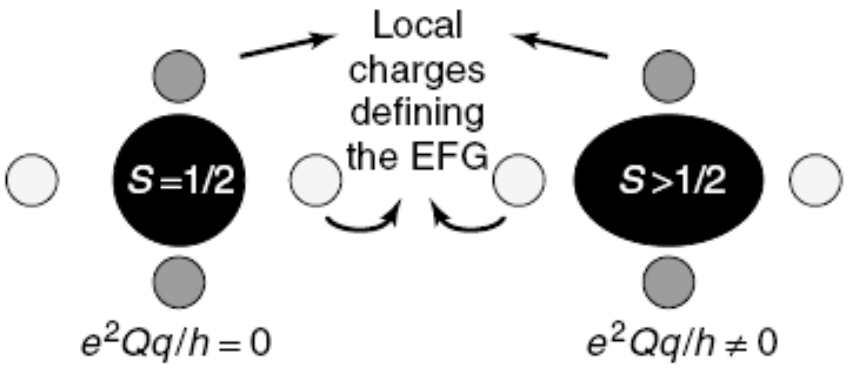


*Figure 1.3: Origin of the electrostatic quadrupole interaction in spins with $I > 1/2$.*

where $\vec{\mu_1}$=$\gamma_1\hbar\vec{I_1}$ and $\vec{\mu_2}$=$\gamma_2\hbar\vec{I_2}$. Thus, the dipolar Hamiltonian can be written as

$$H_D = \frac{\mu_0\gamma_1\gamma_2\hbar^2}{4\pi r^3}[\vec{I_1}.\vec{I_2} - \frac{3(\vec{I_1}.\vec{r})(\vec{I_2}.\vec{r})}{r^2}] \tag{1.19}$$

where in the cartesian coordinates

$$\vec{I_1}.\vec{r} = I_{1x}x + I_{1y}y + I_{1z}z \tag{1.20}$$

### 1.4.4 Quadrupole interaction

A spin 1/2 nucleus has spherical symmetry and the charge distribution is, therefore, symmetrical. However, a nucleus with spin $I > 1/2$ has non-spherical symmetry and hence, there is a distribution of nuclear charge. Nucleus with spin, $I > 1/2$ has its own quadrupole moment, indicating non-zero nuclear charge distribution, which is not spherically symmetric. The quadrupole moment interacts strongly with any electric field gradient (EFG), created by the surrounding electron cloud at the site of the nucleus, apart from the external or internal magnetic fields. It is termed as quadrupolar interaction and is schematically shown in figure 1.3. The strength of this interaction depends upon the magnitude of the nuclear quadrupole moment and the strength of electric field gradient.

The interaction energy of the nuclear charge distribution, $\rho$, with the electric potential V(r) is given by

$$E = \int \rho(r).V(r)d^3r \tag{1.21}$$

In the volume surrounding the nucleus, V(r) can be expanded as a Taylor series as

$$V(r) = V(0) + \sum_{i=x,y,z} i\frac{\partial V}{\partial i} \mid_{r=0} + \frac{1}{2!}\sum_{ij} ij\frac{\partial^2 V}{\partial i \partial j} \mid_{r=0} + ... \tag{1.22}$$

where,

$$V_{i,j} = \frac{\partial^2 V}{\partial i \partial j} \mid_{r=0} \tag{1.23}$$

$V_{ij}$ is the electric field gradient at the nuclear position. It is a symmetric traceless tensor and is diagonal in the PAS system given as

$$V^{PAS} = \begin{pmatrix} V_{XX} & 0 & 0 \\ 0 & V_{YY} & 0 \\ 0 & 0 & V_{ZZ} \end{pmatrix} \tag{1.24}$$

The PAS is generally defined such that the largest component of the EFG is oriented along the $z$-axis and smallest component along the $x$-axis so that $V_{XX} \leq V_{YY} \leq V_{ZZ}$. Because the tensor is symmetric, traceless and diagonal in PAS, it can be described fully by two components; the magnitude of the EFG tensor, eq and the quadrupolar asymmetry parameter $\eta$.

$$V_{ZZ} = eq \tag{1.25}$$

$$\eta = \frac{V_{XX} - V_{YY}}{V_{ZZ}} \tag{1.26}$$

where $0 \leq \eta \leq 1$. If $\eta = 0$, the EFG tensor is axially symmetric.

Using the Wigner-Eckart theorem and after some manipulations of the spin, the quadrupolar Hamiltonian in the PAS of this interaction is,

$$H_Q = \frac{\chi_Q h}{4I(2I-1)}[3\widehat{I}_z^2 - \widehat{I}^2 + \eta(\widehat{I}_x^2 - \widehat{I}_y^2)] = \frac{\chi_Q h}{4I(2I-1)}[3\widehat{I}_z^2 - \widehat{I}^2 + \frac{\eta}{2}(\widehat{I_+ I_-})] \tag{1.27}$$

where $\chi_Q$ is the quadrupole coupling constant and is defined as

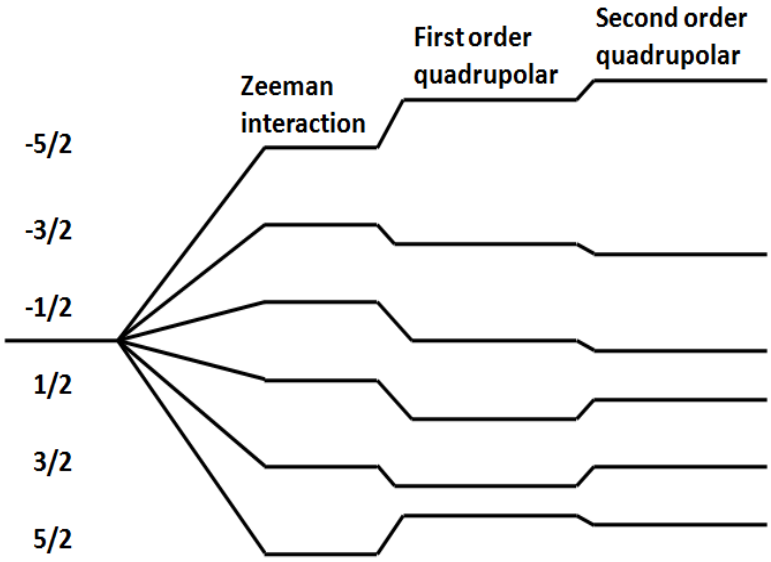


*Figure 1.4: The effect of quadrupolar interaction on energy levels of I = 5/2 nucleus.*

$$\chi_Q = \frac{e^2qQ}{h} \tag{1.28}$$

The magnitude of the quadrupolar Hamiltonian, $H_Q$, is larger than all other anisotropic NMR interactions. Therefore, during the analysis of a quadrupolar spectra, following the standard perturbation theory, the first two terms in the expansion of $H_Q$, the first order $H_Q^1$ and the second order $H_Q^2$ are considered.

For a half integer quadrupolar nuclei, the first order interactions affect the non-central transitions (i.e $m_z \neq 1/2$) causing considerable shift from the Larmor frequencies, as shown in figure 1.4, such that these transitions become difficult to be observed with conventional pulse techniques. However, the symmetric central transition ($m_z = 1/2$) is not affected by the first order effect and is affected only by the second order effects. This give rise to characteristic lineshapes for the quadrupolar nuclei as given in figures 1.5 and 1.6.

The transition frequencies that will result for any symmetric m $\leftrightarrow$ m transition upon second order effects in the static case can be written as:

$$\nu_m = (-9C_q^2/64\nu_0 I^2(2I-1)^2(I(I+1)-3/4)(1-cos^2\theta) \times (9cos^2\theta - 1)) \tag{1.29}$$

Thus the above described NMR interactions broaden the solid-state NMR spectra

of the solid samples. Since we have studied $^{27}$Al and $^{139}$La which are quadrupolar nuclei with spin I = 5/2 and 7/2, respectively, the methods available to obtain high resolution spectra are discussed in the next section.

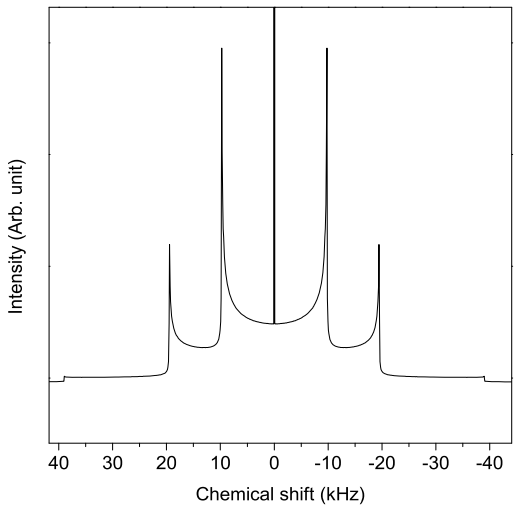


*Figure 1.5: A simulated $^{27}$Al NMR static spectrum of a system which has a $C_q$ of 150 kHz in a magnetic field of 7.04 T. A sharp central transition and the horns from the satellite transitions are clearly visible.*

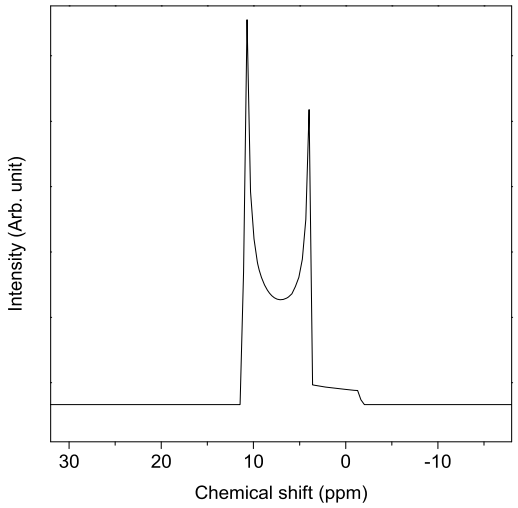


*Figure 1.6: A simulated $^{27}$Al static NMR spectrum of a system which has a $C_q$ = 4MHz. Only the central transition is seen. The satellite transitions are too broad to be seen.*

## 1.5 High resolution techniques for half-integer quadrupolar nuclei

### 1.5.1 Magic angle spinning (MAS)

Magic angle spinning is the single most widely used technique in solid-state NMR for improving the resolution by removing anisotropic interactions [38]. The prominent broadening mechanisms in solid-state spectra are chemical shift anisotropy, dipolar and quadrupolar interactions. In the solution-state, these interactions are averaged by rapid isotropic motions, whereas in the solid-state, there are no such motions and hence, the spectrum will be broadened. A mechanical rotation of the sample at the magic angle 54.74°, with respect to the static magnetic field, enhances the spectral resolution by averaging anisotropic spin interactions and thereby produces isotropic-like spectra with resolved chemical shifts.

MAS usually require high sample rotation speeds. To achieve significant improvements in resolution and sensitivity, the rate of the sample spinning must be fast in comparison to the anisotropy of the interaction being spun out (fast means around a factor of 3 or 4 greater than the anisotropy). Slower spinning produces a set of spinning side bands which are spaced by the rotation frequency along with the line at the isotropic chemical shift. The only characteristic feature of the isotropic chemical shift line is that it is the only line that does not change position with spinning rate, which is the only reliable way of identifying it. But it is important to note that this line is not necessarily the most intense line. Increasing the rotation frequency leads to a decrease in the number of side bands by keeping the peak position of central transition unchanged.

Although magic angle spinning averages out almost all the anisotropic interactions, there is only little magic to this choice of angle when it has to deal with the second order quadrupolar interactions present in the quadrupolar nuclei. The transition frequencies that will result for any symmetric m $\leftrightarrow$ m transition upon second order effects in the case of fast spinning half-integer quadrupolar nuclei can

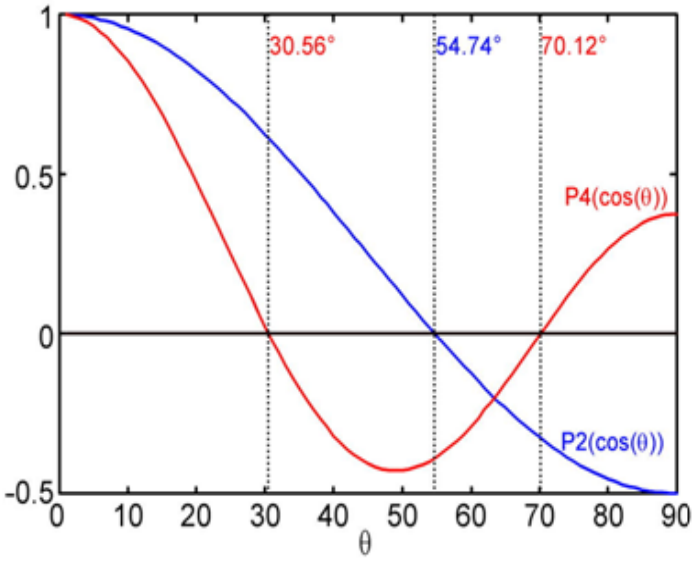


*Figure 1.7: Plot of the Legendre polynomials.*

be written as:

$$\nu_{m,-m} = C_0(I,m).\nu_0 + C_2(I,m).\nu_2(\alpha,\beta).(P_2(\cos\theta)) + C_4(I,m)\nu_4(\alpha,\beta).(P_4(\cos\theta)) \tag{1.30}$$

The equation shows the dependence of the transition frequency on the orientation dependent Legendre polynomials $\mathrm{P}_2(\cos\theta)$ and $\mathrm{P}_4(\cos\theta)$ with second and fourth rank terms, where,

$$P_2(\cos\theta) = 3\cos^2\theta - 1 \tag{1.31}$$

$$P_4(\cos\theta) = 35\cos^4\theta - 30\cos^2\theta + 3 \tag{1.32}$$

From the plot of the second rank and fourth rank Legendre polynomials $\mathrm{P}_2(\cos\theta)$ and $\mathrm{P}_4(\cos\theta)$, shown in figure 1.7, it is clear that there is no single angle at which both the $\mathrm{P}_2(\cos\theta)$ and $\mathrm{P}_4(\cos\theta)$ terms vanish. Thus, the spectrum corresponding to the central transition of the quadrupolar nuclei is still broader even under magic angle spinning due to the presence of second order quadrupolar anisotropic interactions. Therefore, several other techniques have been developed to get high resolution spectra of the half-integer quadrupolar nuclei by which the second order effects are also averaged which are discussed below.

### 1.5.2 Double rotation (DOR)

In the one-dimensional DOR technique, high-resolution NMR spectra of central transitions is achieved by spinning the sample simultaneously at two angles, one inclined at the magic angle (54.74°) with respect to the external magnetic field, and the other at either 30.56° or 70.12° to the first angle [39]. This involves one rotor spinning inside another. In order to achieve the spectra free from spinning side bands, it is necessary to spin each rotor at the rates of the order of the anisotropic line width. Unfortunately, this is rarely achievable, and in some cases, due to the low spinning rate, spinning side bands may obscure isotropic resonances. Nevertheless, the technique has been used with a great deal of success and is likely to find many further applications since NMR experiments are performed at higher fields.

### 1.5.3 Dynamic angle spinning (DAS)

DAS is a two-dimensional NMR experiment, which is used to improve the resolution of solid state NMR spectra from quadrupolar nuclei. In DAS, the sample is spun sequentially about two different angles (e.g. 37.38° and 79.19°) to the external magnetic field, for equal periods of time [40,41]. The experiment takes the advantage of the fact that the transition frequency depends on the sample spinning angle, $\theta$, to perform a type of refocusing or echo experiment. Evolution under the quadrupolar interaction during the first period of free precession is refocused during the second period by changing the transition frequency between the two periods, via a change in the sample spinning angle. There are many pairs of spinning angles, which allow the refocusing effect.

During the first evolution time, $t_1$, the sample is spun at an angle of $\theta_1$ degrees. The magnetization is stored along the $z$-axis and the angle of the spinning axis is changed to $\theta_2$. After the rotor is stabilized, the magnetization is brought to the $xy$ plane and the signal is acquired. The second order quadrupolar frequency of an individual crystallite of the powder sample depends on the angle of the spinning axis. During $t_1$, the quadrupole frequency is $\nu_1$, and $\nu_2$ during $t_2$. If $\nu_2$ is of

*Table 1.1: DAS complementary angles.*

| k | $\theta_1$ | $\theta_2$ |
|---|---|---|
| 5 | 0.0 | 63.43 |
| 1.87 | 30.56 | 70.12 |
| 1 | 37.38 | 79.19 |
| 0.3 | 39.23 | 90.0 |

opposite sign to that of $\nu_1$, the signal from the crystallite will be at its starting position again at some time during $t_2$. One can choose both angles in such a way that the signals from each individual crystallite will be at its starting position at the exactly same time. i.e., an echo will form and the effect of second order quadrupolar broadening is removed. The angles chosen should fulfil the following conditions

$$P_2 cos\theta_1 = -kP_2 cos\theta_2 \tag{1.33}$$

$$P_4 cos\theta_1 = -kP_4 cos\theta_2 \tag{1.34}$$

where $P_2$ and $P_4$ are the second and the fourth order Legendre polynomials and 'k' is the scaling factor given by $t_2/t_1$. There is a continuous set of solutions for $\theta_1$ and $\theta_2$, known as the DAS complementary angles, and each has a different scaling factor which are given in table 1.1. For these solutions, the second-order quadrupolar patterns at $\theta_1$ is exactly the scaled mirror image of the pattern at $\theta_2$ and an echo will form at $t_2 = kt_1$. For the experiment, the angle switching needs to be as fast as possible and reproducible. This technique is limited by the fact that the relaxation of the quadrupolar nuclei should be longer than the flipping time of the rotor axis. Moreover, DOR and DAS require dedicated NMR probes and their implementation is still possessing technical problems.

### 1.5.4 Multiple quantum magic angle spinning (MQMAS)

The multiple-quantum magic angle spinning (MQMAS) is a 2-dimensional NMR technique introduced by Frydman and Harwood in 1995 [42]. Here, narrow-

ing of the central transition is achieved by correlation of the phase evolutions of the symmetric multiple quantum (MQ) and single quantum (1Q) transitions under MAS [42,43]. MQMAS precludes most of the shortcomings of DOR and DAS. MQMAS affords a high-resolution central transition spectra of half-integer quadrupolar nuclei by using both spin and spatial manipulations of the broadening interactions. MAS perform the spatial averaging and remove the chemical shift anisotropy, the heteronuclear dipolar interactions and the second-rank elements of the first and second-order quadrupolar interactions. The RF pulses are used to manipulate the spin part and average out the fourth-rank elements of the second-order quadrupolar Hamiltonian.

MQMAS is a technique analogous to DAS. Here, instead of fixing the transition order m at 1/2 and using the $\theta$ as the degree of freedom, the spinning angle is fixed at $\theta$ which is the magic angle and the spins are allowed to evolve during the initial and final times, $t_1$ and $t_2$, respectively, under the effect of two transition orders $m_1$ and $m_2$. Then the conditions are chosen so as to fulfill the averaging

$$C_2^I(m_1)t_1 + C_2^I(m_2)t_2 = 0 \tag{1.35}$$

$$C_4^I(m_1)t_1 + C_4^I(m_2)t_2 = 0 \tag{1.36}$$

and then a pure isotropic signal will be detected at time

$$t_2 = \frac{C_4^I(m_1)}{C_4^I(m_2)} \tag{1.37}$$

which is then transformed into a high resolution spectrum.

Thus, in an MQMAS experiment, the averaging is done by changing the order of evolving coherences. The multiple quantum coherence of order 2m is first excited and allowed to evolve during $t_1$. The experiment is conducted under magic angle spinning which may be assumed to average the second rank terms throughout the experiment to zero. Thus, the only anisotropy in the evolution during $t_1$ arises from $P_4(\cos\theta)$. At the end of $t_1$ second RF pulses transfer the remaining multiple quantum coherences to single quantum coherence associated with +1/2 $\leftrightarrow$ -1/2 transition. The important point is that the evolution of multiple quantum

*Table 1.2: Values of the zero, second and fourth rank coefficients $C_i^I(m)$ in MQ NMR experiments.*

| I | m | $C_0$ | $C_2$ | $C_4$ |
|---|---|---|---|---|
| 3/2 | 1/2 | 3 | 24 | 54 |
| 3/2 | 3/2 | -9 | 0 | 42 |
| 5/2 | 1/2 | 8 | 64 | 144 |
| 5/2 | 3/2 | 6 | 120 | 228 |
| 5/2 | 5/2 | -50 | -40 | -300 |

coherences during $t_1$ is now 'undone' by the evolutions of single quantum coherence during $kt_1$ associated with the central transition's second order quadrupole broadening. The value of k is given by the ratio of the coefficient of the second order quadrupole coupling term in frequency of multiple quantum coherence and the central transition. The values of the coefficients are given in table 1.2.

At the end of $kt_1$, a normal FID is collected. In the MQMAS data, an echo analogous to the DAS is seen to shift in time with increasing $t_1$ values. Fourier transformation results in a two-dimensional frequency spectrum in which the F1 dimension exhibits an isotropic spectrum and the F2 dimension represents the anisotropic powder patterns associated with the central transition of different sites. The amplitude of the multiple quantum coherence generated depends upon the strength of the quadrupole coupling. Thus, after a 2D Fourier transformation, the resonances will show up as ridges lying along the quadrupolar anisotropy (QA) axis. The isotropic spectrum is obtained by the projection of the entire 2D spectrum on a line through the origin perpendicular to the QA-axis. Thus, in a 3QMAS experiment, for a spin 3/2 system, since we are correlating 3Q and 1Q anisotropies, the refocusing of the decay occurs along the slope $t_2 = (7/9)\ t_1$. The conventional 2D Fourier processing of the data gives rise to sharp parallel ridges tilted by a slope of 7/9. A shearing transformation of this data then produces a high resolution spectrum.

### 1.5.5 Satellite transition magic angle spinning (STMAS)

The STMAS experiment for the half integer quadrupolar nuclei is a 2D experiment introduced in 2000 by Gan to separate the anisotropic interactions from the isotropic interactions [44]. Single quantum transitions other than the central transitions are known as the satellite transitions and have received less attention because of the broadening from the first order quadrupolar effects. However for $I = 5/2$ spins, it has been found that the inner satellite transitions have smaller second order effects than the central transitions and hence satellite transition spectra yields better resolution, provided that the magic angle is precisely calibrated [45]. The STMAS experiment correlates the single quantum central transitions ($1/2 \leftrightarrow$ -$1/2$ ) to the satellite transitions ($1/2 \leftrightarrow 3/2$, $3/2 \leftrightarrow 5/2$, etc) of a half integer spin $I$. This generates coherence transfer echoes and isotropic NMR spectra in a way similar to the MQMAS experiment but with higher efficiencies.

## 1.6 Materials related to the present work

The thesis deals with the NMR study of local coordination environments and local structural distortions in two different aluminium containing oxides, $SrAl_{12}O_{19}$ with the magnetoplumbite and $LaAlO_3$ with the perovskite structure by probing $^{27}Al$ and $^{139}La$.

Aluminium is an abundant element in nature. $^{27}Al$ has a spin $I = 5/2$, and hence possesses a quadrupole moment arising from the non-spherical distribution of nuclear electric charge, which can interact with electric field gradients at the nucleus. The quadrupolar interactions cause broadening and distortion of the spectral peaks and also a displacement from isotropic chemical shift. Since these effects decrease with the square of the applied magnetic field strength, it is often advisable to acquire $^{27}Al$ spectra at the highest possible field. Magic angle spinning can also narrow the $^{27}Al$ resonances by a factor of about four; although the second order quadrupolar broadenings are not completely removed by this technique. Other methods, such as double rotation (DOR), dynamic angle spinning (DAS)

and multiple quantum (MQ) experiments can be applied for this purpose. Despite the limitations which are common to all quadrupolar nuclei, $^{27}$Al is a very favorable nucleus for NMR spectroscopy since it has a 100% natural abundance and often quite fast relaxation times which enable short delay times to be used allowing good quality spectra to be acquired in relatively short measurement times. These factors have made it one of the most thoroughly studied nuclei [34].

$^{139}$La is a spin $I = 7/2$ nucleus and has 99.9% natural abundance and good NMR sensitivity. But there are very few studies on $^{139}$La solid-state NMR because of its huge quadrupole broadening, which is greater by a factor of about 30 than for $^{27}$A1 in sites with the same structural distortion and in the same magnetic field [33].

### 1.6.1 Strontium aluminate ($SrAl_{12}O_{19}$)

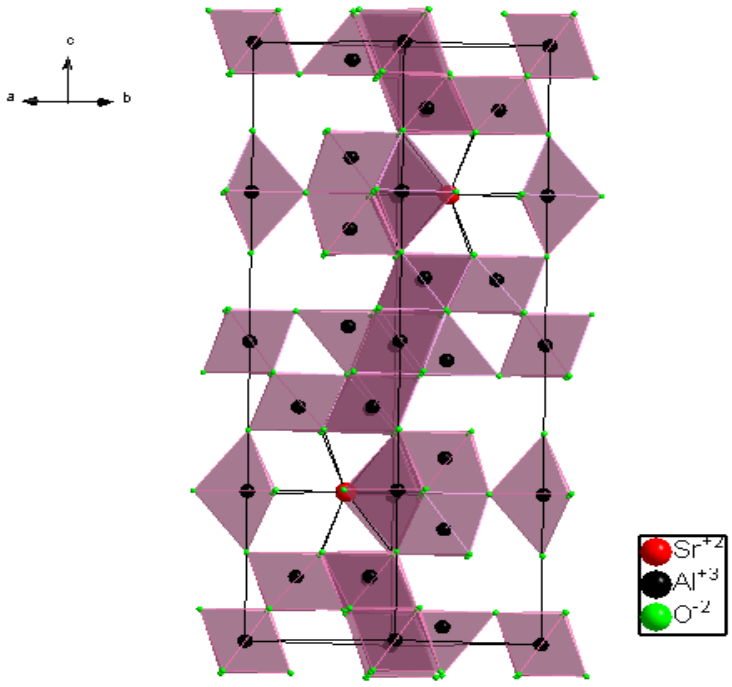


*Figure 1.8: Hexagonal unitcell of $SrAl_{12}O_{19}$.*

*Table 1.3: Different Al sites in $SrAl_{12}O_{19}$ with magnetoplumbite structure.*

| Site geometry | Wyckoff position | Site symmetry | Coordination |
|---|---|---|---|
| Regular octahedron (Al-VI-1) | 2a | $D_{3d}$ | 6 |
| Antiprism octahedron (Al-VI-2) | $4f_2$ | $C_{3v}$ | 6 |
| Distorted octahedron (Al-VI-3) | 12k | $C_s$ | 6 |
| [a]Trigonal bipyramid (Al-V) | 2b | $C_{3v}$ | 5 |
| [b]Distorted Tetrahedron (Al-IV-d) | 4e | $C_{3v}$ | 4 |
| Tetrahedron (Al-IV) | $4f_1$ | $C_{3v}$ | 4 |

[a]Only in the central atom model
[b]Only in the split atom model and this site is half occupied

Strontium aluminate is a ceramic material with the magnetoplumbite crystal structure and is used for various purposes in particular for the luminescent and laser host materials, high temperature catalyst hosts and as substrate materials for rare earth hexaferrite thin films [46–54]. The unit cell of $SrAl_{12}O_{19}$ contains 2 formula units. The hexagonal unit cell of $SrAl_{12}O_{19}$ is shown in figure 1.8. It consists of ten oxygen ions layers. Four of these layers contain 4 $O^{2-}$ ions each and are cubically packed. They form a spinel block. The fifth layer contains 3 $O^{2-}$ ions and the large $Sr^{2+}$ ion is located at the dodecahedral, 2d site. The next five layers are rotated over 180 degree with respect to the first five layers so that the layer containing the $Sr^{2+}$ ion acts as a mirror plane [55]. There are 24 $Al^{3+}$ ions in the structure which occupies the 5 inequivalent Al sites which are the 3 octahedral sites: hexa-1, the regular octahedral site with the site symmetry $D_{3d}$ which is

represented by the Wyckoff letter 2a, hexa-2, the antiprism octahedral site with the site symmetry $C_{3v}$ represented by the Wyckoff letter $4f_2$ and the hexa-3, or the distorted octahedral site which is having the least symmetry $C_s$ and denoted by the Wyckoff letter 12k. One penta coordinate site which is having the trigonal bipyramidal geometry, $C_{3v}$ site symmetry is represented by the Wyckoff letter 2b. The fifth inequivalent site is the tetrahedral site with the site symmetry $C_{3v}$ and the Wyckoff letter $4f_1$. The different cation sites in the magnetoplumbite structure are tabulated in table 1.3.

There is a controversy over the identity of the penta coordinate site as to whether the site is really a five-coordinated site or a distorted tetrahedral site, since the Al atoms can be located either in the mirror plane representing the trigonal bipyramidal structure or it can be slightly shifted either above or below the mirror plane so that the bond lengths are now stretched out such that the central atom now feels only four coordinations instead of a five. Thus, the crystal structure of magnetoplumbite-type oxides has been explained with the help of two different structural models which are the 'central atom model' and the 'split atom model' for the structure [56–58]. The Rietveld refinement studies on the structure has given slightly lower R-factor for for split atom model (R = 0.0331) compared to the central atom model (R = 0.0340) for $SrAl_{12}O_{19}$ [58]. However, incorporation of an anharmonic thermal vibration for the concerned Al atom gave identical R-values (R = 0.0331).

From the $^{27}$Al 5QMAS studies at a field of 7.05 T, the presence of the five-coordinated site in the material is proved, with a high shielding of 18 ppm [59]. The high shielding is ascribed to the distorted nature of the Al-V site. However, from a high field NMR study at 14.1 and 18.8 T, Du and Stebbins observed a site with very large quadrupole coupling constant which is assigned to the distorted tetrahedral site, and the authors could not observe the five coordinated Al [60]. Hence, it was argued that the split atom model is the correct structural model for $SrAl_{12}O_{19}$. Later, from both low-field and high-field SSNMR studies on the same sample, it has been shown that both the penta coordinated as well as the distorted

tetra coordinated Al sites are simultaneously present in strontium aluminate [61]. The present work is an attempt to get more insights into the different coordination environments of $SrAl_{12}O_{19}$ with detailed SSNMR studies at different magnetic fields in combination with the structural refinement studies.

### 1.6.2 Lanthanum aluminate ($LaAlO_3$)

Lanthanum aluminate, $LaAlO_3$, is an important ceramic material with many applications [7]. The properties which make the material very useful in dielectric resonators and as substrate for microwave devices include its high dielectric constant, high quality factor, excellent lattice matching and thermal expansion [62]. $LaAlO_3$ single crystal is used as a substrate to grow thin films of high-$T_c$ superconductors, colossal magnetoresistive oxides. Substituted lanthanum aluminates are potential candidates for cost effective solid electrolytes with enhanced oxygen ion conduction, catalytic activity, luminescence properties, etc [63–66]

The crystal structure of $LaAlO_3$ is rhombohedral perovskite. The perovskite structure of $LaAlO_3$ comprises of a framework structure, constructed from corner sharing $AlO_6$ octahedra with La cations placed at the twelve-coordinated interstices [67]. Each O of the octahedron is shared with another octahedron such that the Al-O-Al arrangement is linear. The octahedra are linked at their corners to form sheets and neighboring sheets are linked to form a 3-D structure. The rhombohedral perovskite structure of $LaAlO_3$ with the La ions occupying the dodecahedral lattice sites and the Al ions occupying the octahedral sites in the structure is shown in figure 1.9.

Even though the crystal structure of $LaAlO_3$ is rhombohedral, the lattice of points shown in 1.9 is hexagonal, that is, it possesses the symmetry elements characteristic of the hexagonal crystal system. The hexagonal cell is having axes a1 (H), a2 (H), and c (H). The same lattice points, however, may be referred to a primitive rhombohedral cell which has axes a1 (R), a2 (R), and a3 (R) [68]. For the conversion of indices (HK.L), corresponding to the hexagonal axes, to a plane whose indices ($hkl$), referred to rhombohedral axes, the following equations are

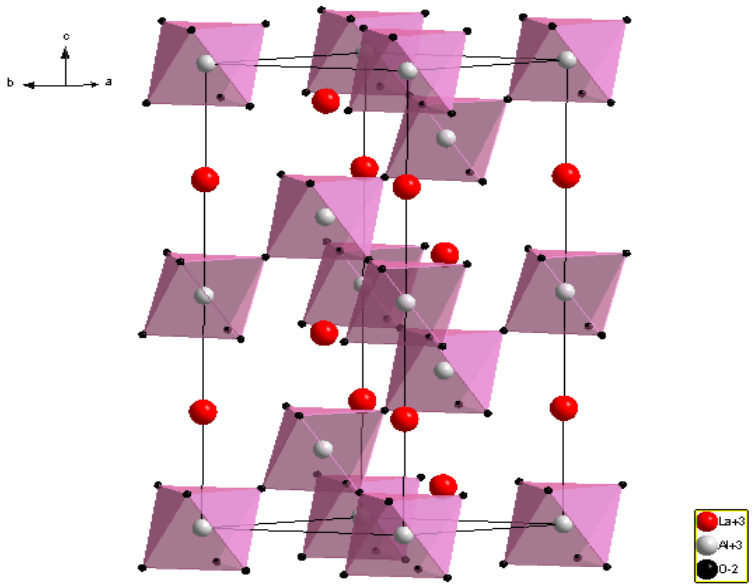


*Figure 1.9: Unitcell of $LaAlO_3$ in the hexagonal setting.*

used:

$$H = h - k, \tag{1.38}$$

$$K = k - l, \tag{1.39}$$

$$L = h + k + l \tag{1.40}$$

Thus it follows that

$$-H + K + L = 3k \tag{1.41}$$

When the pattern of a rhombohedral substance has been indexed, with reference to hexagonal axes, and if want to know the indices $(hkl)$ of the reflecting planes when referred to rhombohedral axes. The transformation equations are

$$h = \frac{1}{3}(2H + K + L), \tag{1.42}$$

$$k = \frac{1}{3}(-H + K + L) \tag{1.43}$$

$$l = \frac{1}{3}(-H - 2K + L) \tag{1.44}$$

The lattice parameters $a$ and $\alpha$ of the rhombohedral unit cell can be determined from the dimensions of the hexagonal cell using the following equations:

$$a_R = \frac{1}{3}\sqrt{3a_H^2 + c^2} \tag{1.45}$$

$$\sin\frac{\alpha}{2} = \frac{3}{2\sqrt{3+(c/a_H)^2}} \tag{1.46}$$

Lanthanum aluminate is known to crystallize with the rhombohedral R$\overline{3}$c space group. However, there is a controversy in the literature about the space group of the material from the first assignment itself. Geller and Bala, in 1956, first proposed the possible space group of rhombohedral $LaAlO_3$ at room temperature as R$\overline{3}$m [69]. Later, in 1964, from the electron paramagnetic resonance (EPR) measurements of crystals doped with $Fe^{3+}$, Muller *et al.* observed two octahedral Al sites rotated relative to each other along the [111] axis, but the NMR data showed that the axial deformation of each site is equal [70]. Based on these studies, it was proposed that the most probable space group is R$\overline{3}$c instead of R$\overline{3}$m [70,71]. At present, $LaAlO_3$ is believed to have the space group R$\overline{3}$c with only one octahedral Al site. However, in a recent study of $LaAlO_3$ using resonant Raman spectroscopy [72], a local breakdown of symmetry was observed at low temperatures and it is proposed that this is possible only if there are two Al coordination environments. Since the space group R$\overline{3}$c cannot account for the two different coordinations, R3c or R$\overline{3}$ are proposed as the possible space group of this material. The different space groups proposed for this system are due to the uncertainty in the local symmetry environments. The local coordination environment of $LaAlO_3$ has been studied in detail in the present work using $^{27}$Al and $^{139}$La NMR.

## 1.7 Scope of the present work

The thesis is aimed at understanding the local structural distortion in two different crystal structures among the technologically important materials; which are the magnetoplumbite and the perovskite structures. The best experimental technique available to probe local structural distortions is solid-state NMR, since the nucleus of an atom is probed which facilitates to explore the local structure which extends over several coordination spheres. Although the quadrupolar interaction can complicate the interpretation of the NMR spectrum, the quadrupolar coupling

constant is a very sensitive tool to probe the electric field gradient and hence the local structure and coordination environments. It also provides as the best method to identify the sites of substitution in materials with complex structures [33].

Among the different materials with the magnetoplumbite structure, strontium ferrite has gained a lot of attention in the magnetic industry. There are continuous attempts to improve the properties of strontium ferrite by proper substitutions. It has been reported that the magnetic properties of $SrFe_{12}O_{19}$ can be improved by simultaneous La-Co substitution, $Sr_{1-x}La_xFe_{12-x}Co_xO_{19}$, and is shown to improve the magnetic performance parameters [73–77]. Mössbauer spectroscopic, magnetic, Raman spectroscopic and $^{57}$Fe NMR studies have been carried out to identify the site(s) of substitution and most of the studies have shown that the substituted $Co^{2+}$ ions are occupied at some of the five different $Fe^{3+}$ sites in the magnetoplumbite structure and there is no agreement on the sites of substitution of Co ions in La-Co substituted strontium ferrite in the literature [30–32,78–82]. When the hexaferrites are substituted with other elements, a change in the crystal structure is not observed. But, the introduction of rare earth ions in the material improves the magnetic properties due to the modification of the magnetic interactions in the surroundings of the substituted rare-earth ion. The substituted hexaferrites have been studied mainly by Mössbauer spectroscopy, which have shown that the Co ions occupy the 2a and $4f_2$ Fe sites in the crystal structure. Strontium ferrites have also been studied by $^{57}$Fe NMR which also confirms the Co occupancy at the 2a and $4f_2$ Fe sites.

$SrAl_{12}O_{19}$ is an isostructural material to $SrFe_{12}O_{19}$, where the magnetic $Fe^{3+}$ has been replaced by the trivalent non-magnetic $Al^{3+}$ ions. In the present study, a detailed analysis of the local structure of $SrAl_{12}O_{19}$ and local structural variations in La-Zn substituted $Sr_{1-x}LA_xAl_{12-x}Zn_xO_{19}$ with the magnetoplumbite crystal structure have been carried out using $^{27}$A solid-state NMR studies.

The properties of the perovskite materials are known to be altered by suitable substitution at the A site or B site or simultaneously at the A and B-sites in the $ABO_3$ perovskite structure [7]. By the substitution at the A- and/or B-sites,

changes occur in the local environment which extends throughout the lattice. These changes are reflected in the bond distances and bond angles, which play a crucial role in governing the physical properties. Perovskite oxides such as $LaMnO_3$, $SrMnO_3$ and $CaMnO_3$ are antiferromagnetic materials, which changes to ferromagnetic upon A-site substitution as in $La_{1-x}Sr_xMnO_3$ and $La_{1-x}Ca_xMnO_3$ or B-site substitution as in $LaMn_{1-x}Co_xO_3$ and they show interesting properties such as colossal magnetoresistance, metal insulator-transition and charge ordering near the ferromagnetic Curie temperature [14]. Due to the structural similarity of lanthanum aluminate with the colossal-magnetoresistive material $LaMnO_3$, there is a comparative study reported with the help of Raman spectra of the material at room temperature [83]. In order to study the effects of substitution on the local structure in the perovskite oxides, we have selected lanthanum aluminate, $LaAlO_3$ with the perovskite crystal structure, for the SSNMR studies.

The perovskite oxide $LaAlO_3$, is known for the last 60 years. However, the space group (SG) of rhombohedral $LaAlO_3$ is a subject of controversy from the first assignment itself [69–72]. The different space groups proposed for this system are due to the uncertainty in the local symmetry environments. Therefore, solid-state NMR is used as the tool to probe the local symmetry and coordination environments of lanthanum aluminate. Both the $^{27}Al$ and $^{139}La$ NMR studies have been carried out to characterize the material. Structure refinement analysis using powder X-ray diffraction has also been carried out. The structural changes occurring in $LaAlO_3$ on substitution at the La-site, has been carried out by replacing the larger $La^{3+}$ ion by the smaller $Y^{3+}$ ion which have different electronic distribution and hence distort the local electronic environment. Similarly, the B-site ion $Al^{3+}$ is substituted by two different ions with different ionic sizes, one with a comparable size, $Co^{3+}$, and another with a larger size, $Ga^{3+}$. Detailed $^{27}Al$ and $^{139}La$ NMR studies have been carried to investigate the structural changes on substitution at the La and Al sites.

# Bibliography


[1] W. D. Callister *Materials Science and Engineering An Introduction: Seventh Edition* (John Wiley & Sons, New Jersey, 2007).

[2] H. R. Allcock, *Introduction to Materials Chemistry* (John Wiley & Sons, New Jersey, 2008).

[3] D. L. Chung, *Functional Materials, Vol. 2* (World Scientific, Singapore, 2010).

[4] J. Fierro, *Metal oxides: Chemistry and Applications* (CRC press, Bocarton, 2006).

[5] S. B. Ogale, T. V. Venketesan, and M. Blamire, *Functional Metal Oxides: New Science and Novel Applications* (Wiley, 2013).

[6] A. F. Wells, *Structural Inorganic Chemistry* (Clarendon Press, Oxford, 1984).

[7] F. S. Galasso, *Structure, Properties and Preparation of Perovskite-type Compounds* (Pergamon, Oxford, 1969).

[8] Z. L. Wang and Z. C. Kang *Functional and Smart Materials: Structural Evolution and Structure Analysis* (Plenum press, New York, 1998).

[9] B. Jaffe, W. R. Cook and H. Jaffe, *Piezoelectric Ceramics.* (Academic Press, London, 1971).

[10] E. T. Lacheisserie, D. Gignoux, M. Schlenker, *Magnetism: Materials and applications* (Springer, USA, 2003).

[11] N. C. Datta *Story of Chemistry* (Hydrebad Universities press, India, 2005).

[12] J. M. D. Coey, *Magnetism and Magnetic Materials* (Cambridge University Press, UK, 2010).

[13] C. N. R. Rao and B. Raveau, *Colossal Magnetoresistance, Charge Ordering and Related Properties of Manganese Oxides* (World Scientific, Singapore, 1998).

[14] Y. Tokura, *Colossal Magnetoresistive Oxides* (Gordon and Breach science publishers, Singapore, 2000).

[15] J. Mercier, G. Zambelli and W. Kurz, *Introduction to Materials Science* (Elsevier, Paris, 2002).

[16] M. C. Flemings, *Ann. Rev. Mater. Sci.* 1999, 29, 1-23.

[17] A. R. West, *Solid State Chemistry and its Applications* (John Wiley & Sons, Singapore, 2003).

[18] S. E. Ashbrook and S. Sneddon, *J. Am. Chem. Soc.* 2014, 136, 15440-15456.

[19] M. Kotecha, S. Chaudhuri, C. P. Grey and L. Frydman, *J. Am. Chem. Soc.* 2005, 127, 16701-16712.

[20] V. Sreeja, T. S. Smitha, D. Nand, T. G. Ajithkumar and P. A. Joy, *J. Phys. Chem. C.* 2008, 112, 14737-14744.

[21] N. Pellerin, C. D. Thiriet, V. R. Montouillout, M. Beauvy and D. Massiot, *J. Phys. Chem. B.* 2007, 111, 12707-12714.

[22] J. H. Kwak, J. Hu, D. Mei, C.-W. Yi, D. H. Kim, C. H. F. Peden, L. F. Allard and J. Szanyi, *Science* 2009, 325, 1670-1673.

[23] S. F. Dec, M. F. Davis, G. E. Maciel, C. E. Bronnimann, J. J. Fitzgerald and S. S. Han, *Inorg. Chem.* 1993, 32, 955-959.

[24] T. J. Bastow and H. J. Whitfield, *Chem. Mater.* 1999, 11, 3518-3520.

[25] Z. Yan, C. W. Kirby and Y. Huang, *J. Phys. Chem. C.* 2008, 112, 8575-8586.

[26] K. N. Mikhalev, Z. N. Volkova and A. P. Gerashchenko, *Phys. Metals Metallogr.* 115, 1139-1159.

[27] K. N. Mikhalev, I. A. Fogel, S. A. Lekomtsev, A. P. Gerashenko, V. V. Serikov and A. R. Kaul, *J. Magn. Magn. Mater.* 2003, 258, 268-270.

[28] C. Kapusta, P. C. Riedi, W. Kocemba, M. R. Ibarra and J. M. D. Coey, *J. Appl. Phys.* 2000, 87, 7121-7123.

[29] J. P. Renard and A. Anane, *Mater. Sci. Eng. B-Solid State Mater. Advanc.Tech.*, 1999, 63, 22-29.

[30] M. W. Pieper, A. Morel, and F. Kools, *J. Magn. Magn. Mater.* 2002, 242, 1408-1410.

[31] M. W. Pieper, F. Kools, and A. Morel, *Phys. Rev. B* 2002, 65, 184402.1-5.

[32] G. Wiesinger, M. Mller, R. Grssinger, M. Pieper, A. Morel, F. Kools, P. Tenaud, J. M. Le Breton, and J. Kreisel, *phys. status solidi (a)* 2002, 189, 499-508.

[33] K. J. D. Mackenzie and M. E. Smith, *Multinuclear Solid-State Nuclear Magnetic Resonance of Inorganic Materials* (Pergamon, Oxford, 2002).

[34] M. Smith, *Appl. Magn. Reson.* 1993, 4, 1-64.

[35] A. Abragam, *Principles of Nuclear Magnetism* (Oxford University Press, Oxford, 1961).

[36] C. P. Slichter, *Principles of Magnetic Resonance* (Springer- Verlag, Berlin, 1990).

[37] M. H. Levitt, *Spin Dynamics* (John Wiley & Sons, Chichester, 2008).

[38] M. Mehring, *High Resolution NMR Spectroscopy in Solids* (Springer-Verlag, Germany,1976).

[39] A. Samoson, E. Lippmaa and A. Pines, *Mol. Phys.* 1988, 65, 1013-1018.

[40] A. Llor and J. Virlet, *Chem. Phys. Lett.* 1988, 152, 248-253.

[41] K. T. Mueller, B. Q. Sun, G. C. Chingas, J. W. Zwanziger, T. Terao and A. Pines, *J. Magn. Reson.* 1990, 86, 470-487.

[42] A. Medek, J. S. Harwood, L. Frydman, *J. Am. Chem. Soc.* 1995, 117, 12779-12787.

[43] A. Medek and L. Frydman, *J. Braz. Chem. Soc.* 1999, 10, 263-277.

[44] Z. Gan, *J. Am. Chem. Soc.* 2000, 122, 3242-3243.

[45] Z. Gan, *J. Chem. Phys.* 2001, 114, 10845-10853.

[46] H. G. Kang, J. K. Park, C. H. Kim and S. C. Choi, *J. Cer. Soc. Japan* 2009, 117, 647-649.

[47] Y. Ikeda, K. Masada, H. Kurokawa, H. Motomura, M. Jinno and K. Tachibana, *J. Phys. D. Appl. Phys.* 2013, 46, 065305

[48] M. Fechner, F. Reichert, N. O. Hansen, K. Petermann and G. Huber, *Appl. Phys. B.* 2011, 102, 731-735.

[49] S. Chawla and A. Yadav, *Mater. Chem. Phys.* 2010, 122, 582-587.

[50] R. X. Zhong, J. H. Zhang, X. Zhang, S. Z. Lu and X. J. Wang, *Nanotech.* 2007, 18, 445707.1-5.

[51] Z. G. Nie, K. S. Lim, J. H. Zhang and X. J. Wang, *J. Lumin.* 2009, 129, 844-849.

[52] V. B. Mikhailik, *Mater. Lett.* 2009, 63, 803-805.

[53] J. M. P. J. Verstegen, J. L. Sommerdijk and A. Bril, *J. Lumin.* 1974, 9, 420-423.

[54] R. C. Pullar, *Prog. Mater. Sci.* 2012, 57, 1191-1334.

[55] R. Collongues, D. Gourier, A. Kahn-Harari, A. M. Lejus, J. Thery and D. Vivien, *Ann. Rev. Mater. Sci.* 1990, 20, 51-82.

[56] X. Obradors, X. Solans, A. Collomb, D. Samaras, J. Rodriguez, M. Pernet and M. Font-Altaba, *J. Solid State Chem.* 1988, 72, 218-224.

[57] A. Utsunomiya, K. Tanaka, H. Morikawa, F. Marumo and H. Kojima, *J. Solid State Chem* 1988, 75, 197-200.

[58] K. Kimura, M. Ohgaki, K. Tanaka, H. Morikawa and F. Marumo, *J. Solid State Chem.* 1990, 87, 186-194.

[59] S. R. Jansen, H. T. Hintzen, R. Metselaar, J. W. de Haan, L. J. M. van de Ven, A. P. M. Kentgens, and G. H. Nachtegaal, *J. Phys. Chem. B* 1998, 102, 5969-5976.

[60] L.S. Du and J. F. Stebbins, *J. Phys. Chem. B* 2004, 108, 3681-3685.

[61] K. Harindranath, K. A. Viswanath, C. V. Chandran, T. Bräuniger, P. K. Madhu, T. G. Ajithkumar, and P. A. Joy, *Solid State Commun.* 2010, 150, 262-266.

[62] S.-Y. Cho, I.-T. Kim and K. S. Hong, *J. Mater. Res* 1999, 14, 114-119.

[63] G. Malandrino, L. M. S. Perdicaro, G. Condorelli, I. L. Fragala, A. Cassinese and M. Barra, *J. Mater. Chem.* 2005, 15, 4718-4722.

[64] S. Jin, T. H. Tiefel, M. McCormack, R. A. Fastnacht, R. Ramesh and L. H. Chen, *Science* 1994, 264, 413-415.

[65] T. Tagawa and H. Imai, *J. Chem. Soc., Faraday Trans.* 1988, 84, 923-929.

[66] Z.-y. Mao, D.-j. Wang, Q.-f. Lu, W.-h. Yu and Z.-h. Yuan, *Chem. Commun.* 2009, 346-348.

[67] J. Zhao, N. L. Ross and R. J. Angel, *J. Phys.Condens. Matter* 2004, 16, 8763-8773.

[68] B. D. Cullity and S. R. Stock, *Elements of X-Ray Diffraction* (Prentice Hall, New Jersey, 2001).

[69] S. Geller and V. B. Bala, *Acta Crystallogr.* 1956, 9, 1019-1025.

[70] K. A. Mller, E. Brun, B. Derighetti, J. E. Drumheller and F. Waldner, *Phys. Lett.* 1964, 9, 223-224.

[71] B. Derighetti, J. E. Drumheller, F. Laves, K. A. Muller and F. Waldner, *Acta Crystallogr.* 1965, 18, 557.

[72] V. G. Sathe and A. Dubey, *J. Phys.: Condens. Matter* 2007, 19, 382201-382207.

[73] F. Kools, A. Morel, R. Grossinger, J. M. Le Breton, and P. Tenaud, *J. Magn. Magn. Mater.* 2002, 242, 1270-1276.

[74] K. Iida, Y. Minachi, K. Masuzawa, M. Kawakami, H. Nishio, and H. Taguchi, *J. Magn. Soc. Jpn.* 1999, 23, 1093-1096.

[75] J. C. Corral-Huacuz and G. Mendoza-Suarez, *J. Magn. Magn. Mater.* 2002, 242, 430-433.

[76] J. Bai, X. Liu, T. Xie, F. Wei, and Z. Yang, *Mater. Sci. Eng.: B* 2000, 68, 182-185.

[77] L. You, L. Qiao, J. Zheng, M. Jiang, L. Jiang, and J. Sheng, *J. Rare Earth* 2008, 26, 81-84.

[78] L. Lechevallier and J. M. Le Breton, *J. Magn. Magn. Mater.* 2005, 290, 1237-1239.

[79] A. Morel, J. M. Le Breton, J. Kreisel, G. Wiesinger, F. Kools, and P. Tenaud, *J. Magn. Magn. Mater.* 2002, 242, 1405-1407.

[80] L. Lechevallier, J. M. Le Breton, J. Teillet, A. Morel, F. Kools, and P. Tenaud, *Physica B.* 2003, 327, 135-139.

[81] L. Lechevallier, J. M. Le Breton, J. F. Wang, and I. R. Harris, *J. Phys.: Condens. Matter.* 2004, 16, 5359-5376.

[82] D. H. Choi, S. W. Lee, I.-B. Shim, and C. S. Kim, *J. Magn. Magn. Mater.* 2006, 304, e243-e245.

[83] M. V. Abrashev, A. P. Litvinchuk, M. N. Iliev, R. L. Meng, V. N. Popov, V. G. Ivanov, R. A. Chakalov and C. Thomsen, *Phys. Rev. B* 1999, 59, 4146-4153.

# Chapter 2

# Experimental Methods

## 2.1 Introduction

Different synthesis strategies are used and techniques such as solid state NMR and powder X-ray diffraction (XRD) have been employed to characterize the materials used in the present study. This chapter briefly describes the methods used for the synthesis of the different metal oxides studied in the present work and the techniques used for the characterization of the materials along with the details of the data analysis.

## 2.2 Synthesis methods

The most common methods for the synthesis of metal oxides are the ceramic or the solid state method, and the wet chemical methods such as co-precipitation, sol-gel, combustion, etc [1–4]. In the present study, only the co-precipitation and sol-gel methods are used for the synthesis of the different samples. Since the aim of the present study is structural characterization of some oxides using XRD and NMR, which requires highly pure samples, all the starting chemicals used for the synthesis are of high purity, greater than 99%. All the chemicals used in the present work are used as-received, without any further purification. Double distilled water is used for all the syntheses. A muffle furnace (30–1000 °, Kumar instruments, India) was used for the initial calcination of the samples and a programmable furnace with controlled heating and cooling arrangements was used for heating the samples in the temperature range 1000–1400 °C (Model HT1600, Nabertherm, Germany). All the samples were heated in high purity alumina crucibles.

### 2.2.1 Citrate-gel method

The citrate-gel method is a kind of sol-gel method for the synthesis of metal oxides using citric acid as a complexating agent and simple metal salts. The method is less time consuming and cost effective compared to the sol-gel method using metal alkoxides. For the synthesis of metal oxides using this method, the constituent metal salts are taken in the required stoichiometric ratio and dissolved

separately in a solvent (water). To the mixed metal solution, citric acid solution in water is added by keeping an appropriate ratio of total metal to citric acid. This mixed solution is then kept on a water bath for the evaporation of water. The solution becomes more and more viscous due to the continuous removal of the solvent during evaporation. After complete evaporation of the solvent, a gel is obtained which is then dried and calcined at a suitable temperature to obtain the corresponding metal oxides.

In the present work, different compositions in the La-Zn substituted strontium aluminate, $Sr_{1-x}La_xAl_{12-x}Zn_xO_{19}$, and Al-site substituted lanthanum aluminate, $LaAl_{1-x}M_xO_3$ (M = Co, Ga), were synthesized by the citrate-gel method following the procedures reported in the literature [5–7]. The corresponding metal nitrates, taken in the appropriate molar ratio, were dissolved separately in minimum amount of water and was then mixed together in a beaker. To this mixed metal nitrate solution, a mixture of citric acid and ethylene glycol was added. The molar ratio of 1:1 was maintained for citric acid to total metal cations and 1:4 ratio was maintained between citric acid and ethylene glycol. After complete dissolution, the solution was heated at 80 °C. After the complete evaporation of superfluous water, the resulting viscous mass was heated at 140 °C for 2 hours which produced a solid amorphous resin, which was transferred to a pre-heated oven at 250 °C for charring. The resulting powder was calcined in the temperature range 700–1000 °C for 2 hrs each with intermediate grindings. The calcined powders were finally heated in the temperature range 1200–1400 °C for 6 hours, so as to get the samples in single phase forms without any impurities. Details of the synthesis of the individual metal oxides are described in the respective chapters.

### 2.2.2 Co-precipitation method

The co-precipitation method is generally used to synthesize a precursor, such as mixed metal hydroxides, carbonates, etc, followed by the solid state reaction. As the name indicates, it is the precipitation of more than one species simultaneously. In this method, generally the precipitating agent, which is a solution of alkali such

as NaOH or $NH_4OH$, is added to a mixed metal salt solution to make a precipitate of mixed hydroxides. However, the reaction causes a continuous increase in the pH value of metal salt solution, affecting the precipitation conditions and products. To avoid this, the precipitation reaction can be carried out in a reverse manner, where the mixed metal salt solution is added to the alkali solution, where the pH value can be maintained in a particular range and this method is called the reverse co-precipitation method.

In the present work, the yttrium substituted lanthanum aluminate, $La_{1-x}Y_xAlO_3$, was prepared using a reverse co-precipitation method following the method reported in the literature [8]. A mixed water solution of lanthanum nitrate, yttrium nitrate and aluminium nitrate were taken in appropriate molar ratio (1-$x$:$x$:1) and was dropped into a dilute ammonia solution of pH $\sim$ 9. The precipitate formed was filtered and washed several times with distilled water and finally dried in an oven. The dried powder was then pre-calcined in the temperature range 700–1200 °C for two hours each and then finally calcined at 1400 °C for the complete phase formation.

## 2.3 Characterization methods

### 2.3.1 Powder X-ray diffraction

X-ray diffraction is one of the important characterization techniques used in materials science [9–11]. An X-ray diffraction pattern of a powder gives information on the crystalline phases present in solid materials under investigation. Each crystalline material has its own powder diffraction pattern. Hence, an X-ray diffraction pattern is a fingerprint of the crystalline materials.

X-rays are electromagnetic radiations having wavelength of approximately 1 Å. X-rays are produced when electrons of sufficient kinetic energy falls on a target made of a certain metal. In this process, electrons are ejected from the core shell around the nucleus and the resulting hole is filled by another electron of higher energy from the outer shells. These electrons give up their excess energies in

the form of X-rays. If the electron jumps from the L-shell, then it gives the $K_\alpha$ radiation, and $K_\beta$ radiation if the electron falls from the M-shell, etc. The K radiation is used for X-ray diffraction studies. The K radiation consists of $K_\alpha$ and $K_\beta$ lines. The $K_\beta$ line, which is far away from the $K_\alpha$ line can be removed using a suitable filter. However, the $K_\alpha$ line is a mixture of $K_{\alpha_1}$ and $K_{\alpha_2}$ radiations with the intensity ratio of 2:1, with comparable wavelength and hence difficult to separate. There are special techniques such as the use of a monochromator to remove the $K_{\alpha_2}$ radiation. If not removed, the different peaks in the X-ray diffraction pattern of a material will have both $K_{\alpha_1}$ and $K_{\alpha_2}$ components, often appearing as a doublet. The X-rays for the diffraction studies are usually generated in an evacuated and sealed tube by applying a high voltage (30-60 kV) between a cathode (usually tungsten) and a selected anode such as copper. X-rays leaves the tube through a window made of beryllium. There must be adequate cooling of the tube to remove the heat generated.

When a beam of X-rays are incident on parallel planes of a crystal at glancing angle '$\theta$', where the planes are separated by a distance 'd' as shown in figure 2.1, the diffracted beams will be in phase with each other, if the path difference is integral multiple of the wavelength, $\lambda$. Therefore, the condition for producing a maxima will be,

$$n\lambda = 2dsin\theta \tag{2.1}$$

where,

$\lambda$ is the wavelength of incident X-rays,

d is the spacing of diffracting planes ,

$\theta$ is the angle of diffraction and

n is the order of diffraction which is equal to 1, 2, 3 ... etc.

When this condition is satisfied, the diffracted beams are in phase and interfere constructively. This is called the Bragg's law [10].

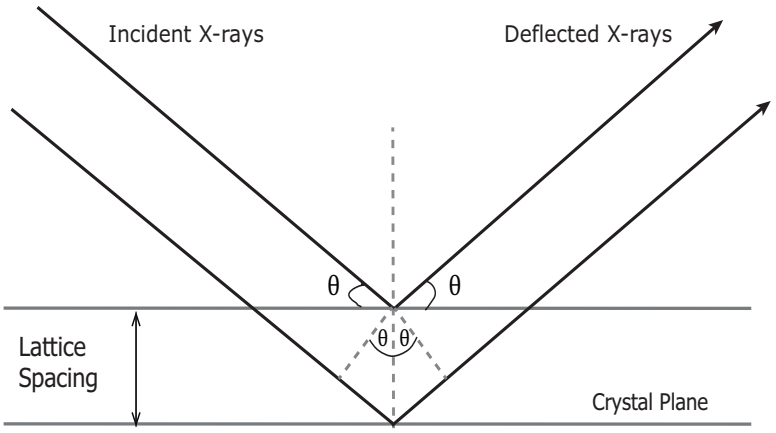


*Figure 2.1: Diffraction of X-Rays.*

An XRD pattern spans a range of $2\theta$ values, and the different peaks corresponding to reflections from different atomic planes in this $2\theta$ range will have different intensities. The angle of diffraction, $\theta$, is determined by the crystal lattice type and the lattice parameters whereas the intensity of a peak is mainly determined by the type of atoms in a solid, the position of the atom in a unit cell, etc, and everything put together is known as the structure factor, F [9].

The XRD analysis in the present work was carried out on a PANalytical X'pert pro powder X-ray diffractometer using Cu-$K_\alpha$ radiation, with Ni filter, and wavelength of 1.5418 Å. Since the $K_{\alpha_2}$ component was not removed, both the $K_{\alpha_1}$ and $K_{\alpha_2}$ components are present in all the recorded XRD patterns. The voltage applied to the X-ray tube was 40 kV. The sample was scanned in the $2\theta$ range 10–80 degrees. For general characterization of the materials, XRD patterns were recorded at a scanning rate of 2°/minute whereas for structural refinements, a very slow scan rate 0.36°/minute was used. The lattice parameters were calculated using a computer program 'Powder Cell for Windows' (PCW) version 2.4 [12], by least squares refinement of the experimental XRD patterns. The powder XRD patterns were simulated using the PCW software using the space group, lattice parameters and atomic positions, taken from the literature, as inputs. The experimental XRD patterns were compared with the simulated patterns to identify the phases. Further, structural analysis was carried out by Rietveld refinement of the XRD patterns, which is described in detail in the next section.

#### 2.3.1.1 Rietveld refinement method

Rietveld refinement of the powder XRD patterns to get structural information of crystalline materials was developed by Hugo Rietveld [13,14]. The X-ray diffraction from a powder sample results in a pattern characterized by reflections at certain Bragg angles. The intensity, width and position of these reflections can be used to determine many aspects of the crystal structure since an XRD pattern is the product of the symmetry, atomic positions and lattice spacings of the crystalline structure [15]. For the Rietveld refinement analysis, XRD patterns are recorded in a particular $2\theta$ range with small increments (typically 0.01 to 0.05°) called as steps.

The Rietveld method uses a least squares approach to obtain a best fit between entire experimental powder diffraction pattern and the entire calculated pattern, based on simultaneously refined models for crystal structure, diffraction effects, instrumental factors and other specimen characteristics. This is done by minimizing the residual $S_y$ given by the equation

$$S_y = \sum_i w_i (y_i - y_{ci})^2 \tag{2.2}$$

where $y_i$ is the observed intensity at the i'th step; $w_i$ is the statistical weight assigned to $y_i$ as $w_i = \frac{1}{y_i}$ and $y_{ci}$ is the calculated intensity at the i'th step.

The Rietveld method is able to deal reliably with strongly overlapping reflections since it creates a virtual separation of these overlapping peaks, thereby allowing accurate determination of the structure. A key feature of the Rietveld refinement is the feedback during the refinements between improving knowledge of the structure and improving allocation of observed intensity to partially overlapping individual Bragg reflections.

#### 2.3.1.2 Criteria of fit

Rietveld refinement process will adjust the refinable parameters until the residual is minimized. That is, until a best fit of the entire calculated pattern to the entire observed pattern is obtained. There are many residual factors (R-factors) which

indicate the goodness of fit. These are

$$\text{R-Structure factor, } R_{F^2} = \frac{\sum I_k^{1/2} - I_{ck}^{1/2}}{\sum I_k^{1/2}} \tag{2.3}$$

$$\text{R-Bragg factor, } R_B = \frac{I_k - I_{ck}}{\sum I_{ck}} \tag{2.4}$$

$$\text{R-pattern, } R_p = \sqrt{\frac{\sum (y_i - y_{ci})}{\sum y_i}} \tag{2.5}$$

$$\text{R-weighted pattern, } R_{wp} = \sqrt{\frac{\sum w_i (y_i - y_{ci})^2}{\sum w_i y_i^2}} \tag{2.6}$$

$$\text{R-expected, } R_e = \sqrt{\frac{M - m}{\sum w_i y_i^2}} \tag{2.7}$$

where, $I_k$ is the intensity of k'th Bragg reflection and $I_{ck}$ is the calculated intensity of k'th Bragg reflection, M is the number of steps in the pattern and m is the number of refinable parameters. Among these the $R_{wp}$ is the most meaningful R, because its numerator is the residual which is being minimized. Another useful goodness of fit indicator is the $\chi$-factor, which is given by,

$$\chi^2 = R_{wp}/R_e \tag{2.8}$$

#### 2.3.1.3 Data analysis

In the present study, the Rietveld refinement analysis of the powder diffraction data has been carried out using the software General Structure Analysis System (GSAS-EXPGUI) [16]. The raw XRD data as such was taken for the analysis, without any prior treatment such as data smoothing or $K_{\alpha_2}$ stripping. In the Rietveld method, no effort was made in advance to assign the observed intensity to a particular Bragg reflection or to resolve overlapped reflections. Therefore, a reasonably good starting model is needed. Also since the relationship between the adjustable parameters and the intensities are non-linear, the starting model should be close to the correct model, otherwise the non-linear least squares refinement will lead to a false minimum. Therefore, the known crystal structure parameters of the corresponding compounds were used for the refinement. The Rietveld refinement

was carried out following the reported procedure [15]. First of all, the scale factor and the background functions were refined till the intensity of the patterns are almost matched, followed by the refinement of the lattice parameters which almost fixed the positions of the peaks. Profile and the asymmetry parameters were then refined using the pseudo-Voigt function. Voigt function is a convolution of the Gaussian and Lorentzian functions, whereas the pseudo-Voigt function is a mixture of the Gaussian and Lorentzian components, defined by the fractions of the two components using a mixing parameter. Finally, the atomic coordinates were refined. The refinement was continued until a better fit of the experimental pattern is obtained. Multiple phases were refined simultaneously and comparative analysis of the separate over all scale factors for the phases offers the most reliable method for doing quantitative phase analysis.

### 2.3.2 Solid-state NMR techniques

#### 2.3.2.1 Spectrometer and probes

The present work is focused on the quadrupolar nuclei $^{27}$Al and $^{139}$La and therefore, a combination of low-field and high-field NMR measurements have been carried out for all the samples in order to determine the NMR parameters.

Low-field NMR experiments were done on a Bruker AV-300 (aluminium resonance frequency, $\nu_{Al}$ = 78.2 MHz) and a Bruker AV-500 ($\nu_{Al}$ = 130.2 MHz) spectrometers, operating at field strengths of 7.05 T and 11.7 T, respectively. For the experiments at 7.05 T, a 4 mm BL MAS probe which can attain a maximum magic angle spinning rate of 15 kHz was used. Experiments at high spinning rates, up to 34 kHz, were also carried out on the AV-300 spectrometer, using a 2.5 mm probe. For experiments on the AV-500 spectrometer, a 3.2 mm MAS probe was used and the sample was spun at the rate of 22 kHz.

The high-field experiments were carried out on a Bruker AV- 600 ($\nu_{Al}$ = 156.38 MHz) and a Bruker AV-700($\nu_{Al}$ = 178.42 MHz) operating at field strengths of 14.0 and 16.4 T, respectively. Data from AV-600 was collected using a 1.3 mm MAS probe at a spinning speed of 40 kHz. For experiments on AV- 700, a 2.5 mm MAS

probe, with a spinning speed of 34 kHz, was used. The experiments on AV- 700 were done on a 1.3 mm MAS probe at a spinning speed of 60 kHz.

The $^{27}$Al chemical shifts were referenced to the chemical shift of 1 M $AlNO_3$ solution. Similarly, for recording the $^{139}$La spectra, 1 M $LaNO_3$ was used as the reference. The NMR measurements were done at room temperature as well as low- and high temperatures.

#### 2.3.2.2 Magic angle spinning experiments

The present work deals with two half integer quadrupolar nuclei, which are Al ($I$ = 5/2), and La ($I$ = 7/2), in the same material, and therefore we must consider the coexistence of species with different selectivities for the irradiation pulse. To ensure a quasi-linear and thus quantitative excitation of the spin system, the RF pulse should be less than $\pi/(2(I + 1/2))$, which means $\pi/6$ for a 5/2 spin and $\pi/8$ for the 7/2 spin. If the quadrupolar frequency, $\nu_Q$ ($\nu_Q = 3C_q/2I[2I - 1]$) is much less than the $\nu_{RF}$, the excitation affects all the possible transitions and is called nonselective pulse. If the $\nu_Q$ is much greater than the $\nu_{RF}$, then the pulse becomes selective and excites only the central transition. Thus, for the quantitative evaluation of the site population we should take a MAS spectrum at a pulse width of less than or equal to $\pi/6$ for Al and $\pi/8$ for La. Therefore while doing the experiments, we have used $\pi/18$ pulses so that we get linear response for any kind of site.

An accurate determination of the pulse width for the $\pi/18$ pulse is essential to perform the NMR experiment. To obtain the exact $\pi/18$ pulse, one molar solution each of aluminium nitrate and lanthanum nitrate are prepared and static spectra of these solutions taken in the rotor at an optimum pulse width were recorded. Then, a series of spectra were acquired with adequate relaxation delays gradually increasing the pulse width. The intensity of the spectrum, when plotted as a function of pulse width gives a complete sinusoidal variation in the intensity. The null point defines the $\pi$ pulse and from this the $\pi/18$ pulse width was determined. The quantitative experiments were then done using this $\pi/18$ pulse.

#### 2.3.2.3 Multiple quantum magic angle spinning

In this work, the multiple quantum magic angle spinning (MQMAS) experiment has been carried out to obtain resolved spectra of the half-integer spin quadrupolar nuclei, Al. Basically, this experiment correlates the m $\leftrightarrow$ -m, multiple quantum transition to the single quantum 1/2 $\leftrightarrow$ -1/2 transition, which is the central transition. Enhancement in the resolution occurs due to the fact that the quadrupole frequencies for both the transitions are correlated. At specific times the anisotropic parts of the quadrupole interaction are refocused and an echo forms.

3QMAS NMR method is a widely used NMR technique, because triple quantum coherence is most readily excited and converted to single quantum coherences. Numerous schemes exist that are used to obtain 2D MQMAS spectra. For the 3QMAS NMR experiments, we have used the pulse sequence which includes a Z-filter pulse (selective, of low RF power) and has the advantage of having a symmetrical coherence transfer pathway. The pulse sequence and coherence diagram are given below, in figure 2.2, where d1 is the recycle delay, which is the delay between the two scans, d0 is the delay between excitation and conversion pulses and d4 is the Z-filter delay. The first pulse, p1, is used for the triple quantum excitation. The second pulse, p2, is used for the coherence transfer from triple quantum to zero quantum and the third pulse, p3, is the Z-filter pulse which is required to selectively excite the central transition line.

For setting up the 3QMAS experiment, all the pulse lengths p1, p2 and p3 should be optimized. A 1-dimensional slice of the MQMAS experiment is initially recorded using trial values for the pulse widths and the intensity is systematically monitored for different values of p1, p2 and p3. These optimized pulses are then used to carry out the 2-dimensional experiment. The set up of the experiment was first done with the help of yttrium aluminium garnet (YAG) having 2 different Al sites with known quadrupolar and chemical shift values. In the MQMAS spectra, the F1 dimension is the multiple quantum dimension and F2 is the single quantum dimension (see section 1.5.4, chapter 1). Conventional 2D Fourier processing of these data gave sharp parallel spectral ridges tilted by a slope which

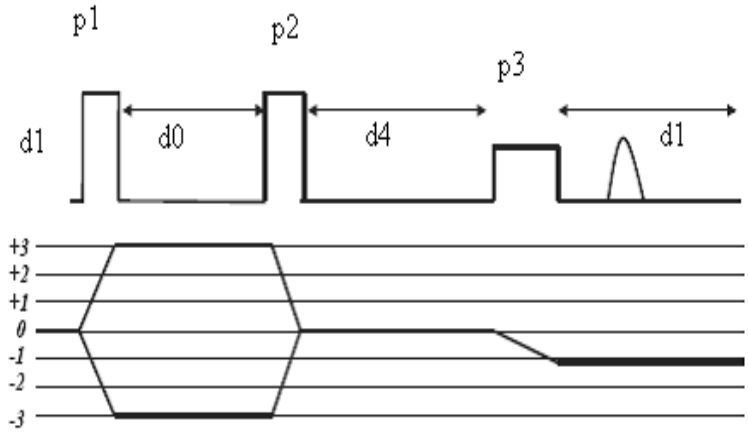


*Figure 2.2: Pulse sequence and coherence diagram of 3QMAS experiment.*

is the quadrupolar anisotropy (QA). Projection of such raw data does not yield a high resolution spectrum. Shearing transformation has to be done to obtain the isotropic high resolution spectra in the F1 dimension, whereby a point which has the frequency ($\nu_1$, $\nu_2$) will lie at a frequency ($\nu_1$-QA.$\nu_2$). For I= 5/2, QA = 19/12. In the present wok, the 2D spectra obtained from the experiment gave an idea of the different Al sites and an estimate of the isotropic shift and the quadrupolar parameters were deduced from the spectra which was then used for the quantitative estimation using the DMFIT program [17].

#### 2.3.2.4 Lineshape of the central transition of a half-integer quadrupolar nuclei

It is known that the lineshape of the half-integer quadrupolar nuclei changes with distribution in the various NMR parameters such as quadrupole frequency and the isotropic chemical shift, as shown in figure 2.3. The characteristic lineshape of a quadrupolar nuclei, where there is only quadrupolar interaction of the surrounding electric field gradients, is with two horns as shown in figure 2.3 and when there is a distribution of the quadrupolar frequencies in the spectrum, a trailing edge is developed towards the left of the spectrum and when there is both quadrupole and isotropic chemical shift distributions, the spectra broadens symmetrically producing a pure Gaussian lineshape. The different lineshapes arises because in the

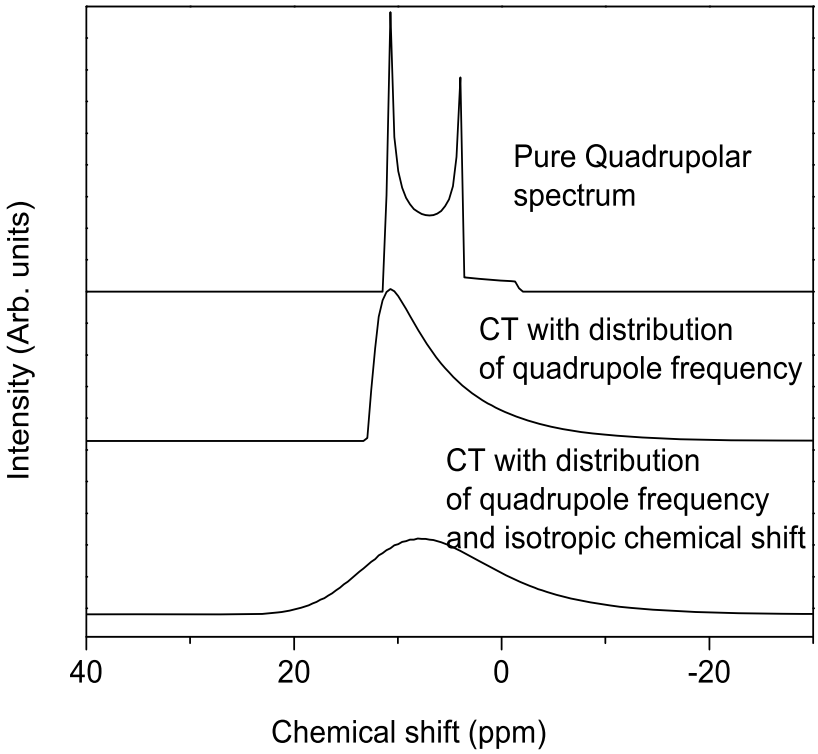


*Figure 2.3: Line shape of the central transition of a half-integer quadrupolar nucleus.*

case of quadrupolar nuclei, there is an electric field gradient present and so we have to address the distribution of these electric field gradient in the spectra. A Gaussian isotropic model (GIM) for the disordered solids have been proposed for use in Mössbauer spectra [19]. The GIM model has been incorporated in the computer simulation programme DMFIT [17]. The details of the fitting procedure are explained in the next session.

#### 2.3.2.5 Static wide line experiments

The static powder NMR patterns offer a way of characterizing different solid materials, since spectral features can be observed in the static pattern [18]. The simulation of the static pattern allows one, for the accurate determination of the NMR parameters. For a quadrupolar nuclei, this could either be an observation of just the central transition which would be applicable to those sites with the

larger quadrupolar interactions or sometimes it leads to the whole satellite transition manifold. If the singularities of the satellite transitions are observed, then an estimate of the $C_q$ can be made from the spectra. In the present work, for lanthanum aluminate which is having a low quadrupole coupling constant for the Al site, the static NMR experiments resulted in the observation of singularities allowing the estimation of $C_q$ from the spectrum and static NMR experiments at variable temperatures were also done.

#### 2.3.2.6 Deconvolution of NMR spectrum

Structural information contained in the experimental spectra are extracted by deconvoluting them into their components by estimating their chemical shift and quadrupolar parameters. Their relative abundance can be estimated by calculating the areas under each peak. This requires a deconvolution model, which accurately describes the experiment and the spin system at reasonable computational costs. This was carried out using the DMFIT program developed by Massiot et al. [17]. There also exists the general purpose NMR simulation programs such as SIMPSON that are versatile but it lacks the dedication for spectrum fitting. If the experimental spectrum contains spectral lines of multiple sites, that are not well resolved, the deconvolution model becomes more complex and the number of fit parameters increases. The integrated intensities of each line and the relative intensities of the different coordination environments are calculated from the simulated spectra. For glassy systems containing aluminum, which has a distribution of quadrupolar coupling constants, the Gaussian isotropic model (GIM) of the Czjeck distribution is the simplest and physically consistent model [20]. The Czjzek model in the DMFIT programme incorporates the Gaussian isotropic model, which takes into account a Gaussian distribution of isotropic chemical shift and a distribution of the electric field gradient which gives a mean isotropic shift ($\delta_{iso}$), a chemical shift distribution ($\Delta_{CS}$) and a mean quadrupolar product ($C_q^* = C_q(1+\eta^{2/3})^{1/2}$) for each site [21].

The lineshape fitting procedure is as follows: First, select the appropriate

model for fitting. The fitting is started with an approximate lineshape with guess parameters for isotropic shift, $\delta_{iso}$, the distribution of isotropic chemical shift, $\Delta_{CS}$, and the quadrupole coupling constant, $C_q$, in the model, followed by iteration of the different NMR parameters and amplitude to get a good match between the experimental and the simulated spectra. This procedure is repeated many times and is carried out on the spectra of all the samples until a very good match between the experimental and the simulated spectra is obtained. The individual lines can then be extracted from the spectra and then one can calculate the site intensities for the different sites.

#### 2.3.2.7 Intensity correction for Al MAS NMR

While quantifying an isotropic spectrum, it is assumed that the spectrum has been obtained at infinite spinning speeds even if the spectrum is recorded at finite spinning speeds and the quantification of population ratio of different sites implies the comparison of areas of the whole transition system. However, because of the difference in $C_q$ for the different sites in a material, it is not always possible to excite all the transition system with the excitation pulse $\nu_{RF}$. Hence, the spectrum will be distorted by the excitation function and this should be corrected. In the method described here, the proportion of the magnetization under a line is calculated which depends on the quadrupolar interaction, the field, and the spinning speed. The intensity of the isotropic line, as the fraction of the magnetization contained in this isotropic line, is defined as

$$I^{iso} = I^{iso}_{1/2} + \sum m \neq 1/2 I^{iso}_{m} \tag{2.9}$$

Here $I^{iso}_{m}$ depends on $\mid 1 - 2m \mid \nu_Q/\nu_r$ and $\eta_Q$, and $I^{iso}_{1/2}$ depends on $\nu_Q^2/\nu_r\nu_O$ and $\eta_Q$ where, $\nu_Q$ = quadrupolar frequency

$\nu_r$ = spinning frequency

$\eta_Q$ = asymmetry

$\nu_O$ = resonance frequency

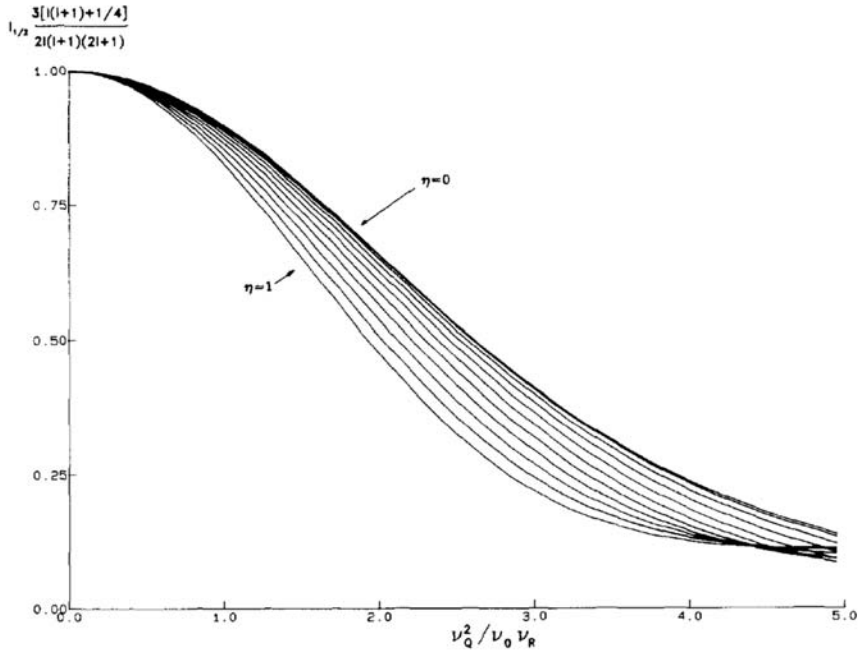


*Figure 2.4: $I_m^{iso}$ dependence for satellite transitions towards $\mid 1-2m \mid \nu_Q/\nu_r$, taken from reference [22].*

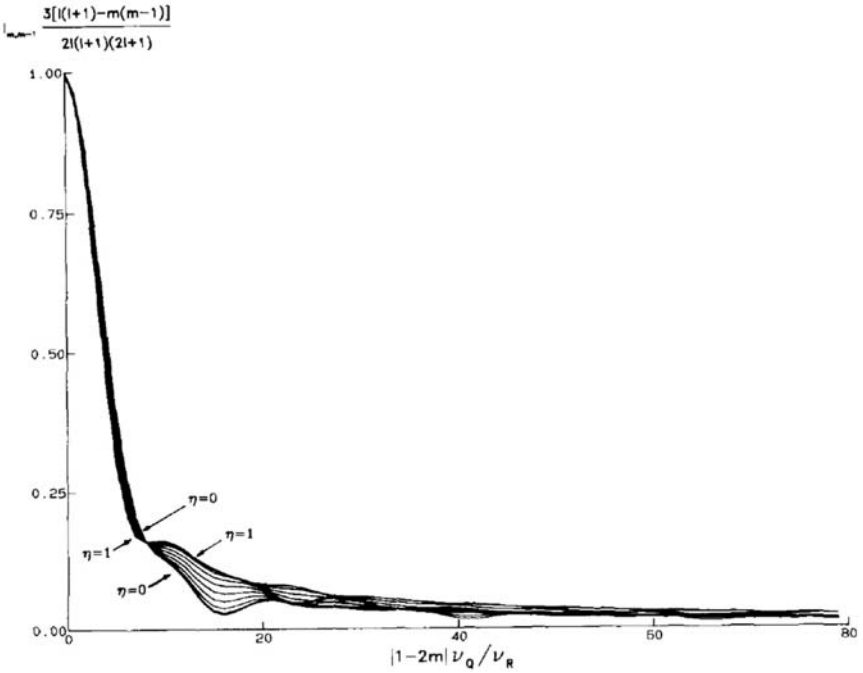


*Figure 2.5: $I_{1/2}^{iso}$ dependence for the central transition towards $\nu_Q^2/\nu_r\nu_O$, taken from reference [22].*

The intensities calculated for yttrium aluminium garnet by Massiot et al. [22] are shown in figures 2.4 and 2.5 for $\eta_Q$ varying from 0.0 to 1.0, in steps of 0.1. From figures 2.4 and 2.5, the amount of magnetization contained in the isotropic line can be obtained. Thus, by knowing the value of $\nu_Q$, $\nu_r$, $\nu_O$ and $\eta_Q$, the value of $\mid 1 - 2m \mid \nu_Q/\nu_r$ can be calculated, which allows us to read the value of $\mathrm{I}_m^{iso}$ on the figure corresponding to the $\eta_Q$ value of our interest. Similarly, by knowing the value of $\nu_Q^2/\nu_r\nu_O$, $\mathrm{I}_{1/2}^{iso}$ can be read from figure on the corresponding $\eta$ curve. Thus, the $\mathrm{I}^{iso}$ for the material can be calculated and the experimentally measured area is corrected by $1/\mathrm{I}^{iso}$.

We have compared the relative areas of the isotropic rotation line of the different sites, in strontium aluminate following the method in the quantitative $^{27}$Al NMR analysis of yttrium aluminium garnet [22]. This procedure was done for all the strontium aluminate samples which are having different Al sites.

# Bibliography


[1] J.M. Honig and C.N.R. Rao, *Preparation and Characterization of Materials* (Academic Press, San Diego, 1981).

[2] D. Segal, *Chemical synthesis of Advanced ceramic Materials* (Cambridge University Press, New York, 1991).

[3] C. N. R. Rao, *Chemical Approaches to the synthesis of Inorganic Materials* (Wiley Eastern Ltd., New Delhi, 1994).

[4] J. P. Jolivet; M. Henry and J. Livage, *Metal Oxide Chemistry and Synthesis: From Solution to Solid State* (John Wiley & Sons, Chichester, 2000).

[5] A. Matraszek, M. Miller, L. Singheiser, and K. Hilpert, *J. Am. Ceram. Soc.* 2003, 86, 1911-1917.

[6] Y. Xu, W. Peng, S. Wang, X. Xiang, and P. Lu, *Mater. Sci. Eng. B* 2005, 123, 139-142.

[7] K. Harindranath, K. A. Viswanath, C. V. Chandran, T. Bräuniger, P. K. Madhu, T. G. Ajithkumar, and P. A. Joy, *Solid State Commun.* 2010, 150, 262-266.

[8] W. Li, M. W. Zhuo and J. L. Shi, *Mater. Lett.* 2004, 58, 365-368.

[9] H. P. Klug and L. E. Alexander, *X-Ray Diffraction Procedures* (Wiley, New York, 1954).

[10] B. D. Cullity and S. R. Stock, *Elements of X-Ray Diffraction* (Prentice Hall, New Jersey, 2001).

[11] A. R. West, *Solid State Chemistry and its Applications* (John Wiley & Sons, Singapore, 2003).

[12] W. Kraus and G. Nolze, *PowderCell for Windows (PCW), version 2.4* (The software is freely available from http://www.ccp14.ac.uk.)

[13] H. M. Rietveld, *Acta Crystallogr.* 1967, 22, 151-152.

[14] H. M. Rietveld, *J. Appl. Crystallogr.* 1969, 2, 65-71.

[15] R. A. Young, *The Rietveld Method* (Oxford University Press, United States, 1995).

[16] B.Toby, *J. Appl. Crystallogr.* 2001, 34, 210-213.

[17] D. Massiot, F. Fayon, M. Capron, I. King, S. Le Calvé, B. Alonso, J.-O. Durand, B. Bujoli, Z. Gan and G. Hoatson, *Magn. Reson. Chem.* 2002, 40, 70-76.

[18] K. J. D. MacKenzie and M. E. Smith, *Multinuclear Solid-State Nuclear Magnetic Resonance of Inorganic Materials* (Pergamon, Oxford, 2002).

[19] G. Le Caer and R. A. Brand, *J. Phys. Condens. Matt.* 1998, 10, 10715-10774.

[20] G. Czjzek, J. Fink, F. Gatz, H. Schmidt, J. M. D. Coey, J. P. Rebouillat and A. Lionard, *Phys. Rev. B.* 1981, 23, 2513-2530.

[21] D. R. Neuville, L. Cormier, and D. Massiot, *Geochim. Cosmochim. Acta* 2004, 68, 5071-5079.

[22] D. Massiot, C. Bessada, J. P. Coutures, and F. Taulelle, *J. Magn. Reson.* 1990, 90, 231-242.

# Chapter 3

# Studies on Unsubstituted and La-Zn Substituted $SrAl_{12}O_{19}$

## 3.1 Introduction

The ferrimagnetic hexagonal ferrites with the magnetoplumbite structure and having the general formula $AFe_{12}O_{19}$ (A = Sr, Ba, Pb) continue to attract attention after their discovery in the early nineteen fifties [1]. Permanent magnets made from these ferrites are known to have sufficiently high coercive force; high thermal and electrical resistivity and they are chemically inert [2–4]. Due to their low cost combined with reasonable magnetic performance, they are preferred over the rare earth alloy based magnets for various applications [5,6]. At present, strontium ferrite, $SrFe_{12}O_{19}$, is mainly used for most applications and there have been numerous attempts to improve the magnetic properties of this class of ferrites for better performance. Considerable improvement in the magnetic performance parameters has been obtained when Sr is partially substituted by La along with simultaneous substitution of Fe by Co or Zn (known as La-Co or La-Zn substituted strontium ferrite) [7–11]. The most striking feature of La-Co substitution in strontium ferrite is the significant increase in the coercivity without any drop in the saturation magnetization as well as the remnant flux density for small amounts of substitution. In the substituted compositions, $Sr_{1-x}La_xFe_{12-x}Co_xO_{19}$, maximum coercivity is observed for $x \approx 0.2$-0.3 as shown in figure 3.1. The simultaneous introduction of trivalent rare earth and divalent transition metal ions, in strontium ferrite, improves the magnetic properties, without modifying the crystal structure, due to the comparable sizes of the substituted ions (ionic radii of $Sr^{2+}$ and $La^{3+}$ are 1.44 Å and 1.36 Å, respectively, for 12-fold coordination, and that of $Fe^{3+}$ and $Co^{2+}$ are 0.645 Å and 0.745 Å, respectively, for 6-fold coordination [12]). Mössbauer spectroscopic, magnetic, Raman spectroscopic and $^{57}Fe$ NMR studies have been carried out to identify the site(s) of substitution and most of the studies have shown that the substituted $Co^{2+}$ or $Zn^{2+}$ ions are occupied at some of the five different $Fe^{3+}$ sites in the magnetoplumbite structure as shown in table 3.1.

Mössbauer spectroscopic studies on La-Co substituted samples have shown that the substituted $Co^{2+}$ ions occupy the 2a and $4f_2$ octahedral Fe sites in the crystal structure [13–17]. This is in agreement with the results from Raman spec-

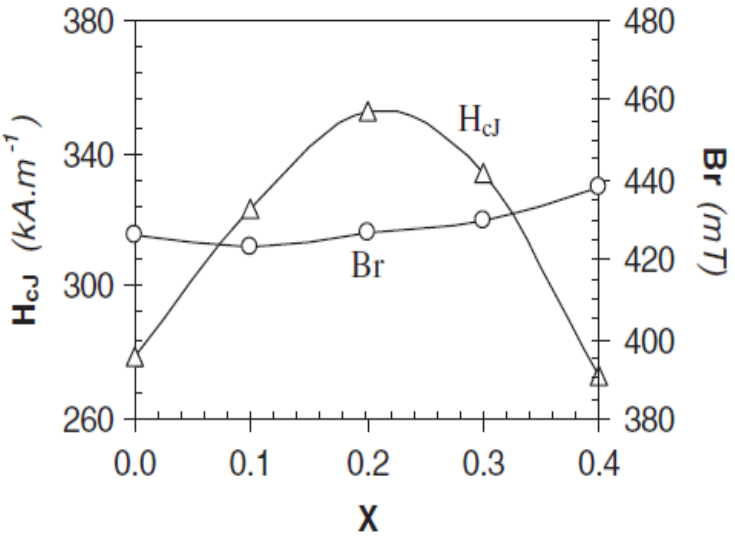


*Figure 3.1: Coercivity, $H_{cJ}$, and remnant flux density, $B_r$, as a function of $x$ for $Sr_{1-x}La_xFe_{12-x}Co_xO_{19}$ magnets, taken from reference [7].*

troscopic studies [15]. It has been pointed out that considerable changes occur in the hyperfine parameters for the 12k, $4f_2$, and 2b sites on substitution [16]. The change in the hyperfine parameter of the 12k site is attributed to the magnetic interactions due to the presence of Co on the neighboring 2a and $4f_2$ sites. On the other hand, the changes in the hyperfine parameters of the $4f_2$ and 2b sites are attributed to the increase in the electron density in the vicinity of these sites arising from the La substitution at the Sr site and a perturbation of the symmetry around the $4f_2$ and 2b sites. However, another Mössbauer spectroscopic study suggested that the Co ions occupy the 12k, $4f_2$, and 2b sites [18]. On the other hand, $^{57}$Fe NMR studies have shown that the Co ions occupy the $4f_1$ and $4f_2$ Fe sites [19]. Later, considering the crystal field arguments, it is suggested that Co ion is substituted at the $4f_2$ Fe sites [20]. In the case of La-Zn substituted compositions, Mössbauer spectroscopic studies have shown that the Zn ions preferentially occupy the tetrahedral $4f_1$ sites and induces a perturbation to the 2a octahedral site, as it is in the close vicinity to the $4f_1$ site [14,17]. In the case of La-Zn substituted strontium ferrite nanoparticles, Zn ions preferentially occupy $4f_1$ and 2b sites [21]. From the $^{57}$Fe Mössbauer spectroscopic study on Zn-Sn substituted

*Table 3.1: Different cation sites in the magnetoplumbite structure.*

| Site geometry | Wyckoff position | Site symmetry | Coordination | Occupancy (%) |
|---|---|---|---|---|
| Regular octahedron(VI-1) | 2a | $D_{3d}$ | 6 | 8.33 |
| Antiprism (VI-2) | $4f_2$ | $C_{3v}$ | 6 | 16.67 |
| Distorted octahedron (VI-3) | 12k | $C_s$ | 6 | 50 |
| [a]Trigonal bipyramid (V) | 2b | $C_{3v}$ | 5 | |
| or | | | | 8.33 |
| [b]Distorted tetrahedron(IV-d) | $4f_1$ | $C_{3v}$ | 4 | |
| Tetrahedron (IV) | $4f_1$ | $C_{3v}$ | 4 | 16.67 |

[a]Only in the central atom model
[b]Only in the split atom model

$SrFe_{12-x}(Sn_{0.5}Zn_{0.5})_xO_{19}$ thin films, it has been shown that Zn-Sn ions preferentially occupy the 2b and $4f_2$ sites [22]. Thus, there is no agreement on the sites of substitution of the Co or Zn ions in the La-Co or La-Zn substituted strontium ferrite, in the literature.

The exact sites of substitution and the local structural distortions can be probed using solid-state NMR (SSNMR) technique, where the nucleus of an atom is probed, facilitating the exploration of the local structure which extends over several coordination spheres. However, it is very difficult to apply high resolution SSNMR techniques to study the local structure and coordination behavior of highly magnetic M-type ferrites. The objective of this work is to gain insights into the local structural variation and sites of substitution by probing substituted strontium aluminate, $SrAl_{12}O_{19}$, which is isostructural to strontium ferrite, $SrFe_{12}O_{19}$ and non-magnetic.

In $SrAl_{12}O_{19}$, $^{27}Al$ solid-state NMR is used to locate the substitutional sites when $Al^{3+}$ is partially substituted by $Zn^{2+}$. We have selected Zn as the substituting element since the substituting element should be a metal from the transition

elements which is non-magnetic and should maintain the charge balance in the system. Thus, this study is aimed at the investigation of the site of substitution of Zn in strontium aluminate when $Sr^{2+}$ and $Al^{2+}$ are simultaneously substituted by $La^{3+}$ and $Zn^{2+}$. It is expected that the results can be extrapolated to explain the changes in the magnetic properties of strontium ferrite on similar modes of substitution, since it is very difficult to apply high-resolution solid-state NMR techniques to study the local structure and coordination behaviour of highly magnetic ferrite materials.

There are two closely related structural models reported for both strontium ferrite and strontium aluminate [28]. Both structures are identical, with the same space group $P6_3/mmc$, and similar tetrahedral as well as octahedral sites of occupancy. The only difference between the two models is that in the split atom model, the Al atoms occupy half of the distorted 4e sites instead of the trigonal bipyramidal 2b sites in the central atom model [28]. In $SrAl_{12}O_{19}$, the presence of penta coordinated Al site was shown from low-field (7.05 T) $^{27}$Al SSNMR studies by Kentgens and co-workers in 1998 [30]. On the other hand, from high-field (14.1 and 18.8 T) $^{27}$Al SSNMR studies by Du and Stebbins in 2003, the presence of distorted four-coordinated Al site was shown and it was argued that this is indeed the correct structure for this material [31]. However, recently, from both low-field and high-field SSNMR studies on the same sample, it has been shown that both the penta coordinated as well as the distorted tetra coordinated Al sites are simultaneously present in strontium aluminate [24]. Therefore, in order to understand the local structural changes on the simultaneous substitution of La and Co or Zn in hexagonal strontium ferrite, we have studied the analogous nonmagnetic compositions $Sr_{1-x}La_xAl_{12-x}Zn_xO_{19}$ ($x$ = 0, 0.1, 0.2, 0.3, 0.4) using $^{27}$Al solid-state NMR.

## 3.2 Synthesis

Different compositions in the La-Zn substituted $Sr_{1-x}La_xAl_{12-x}Zn_xO_{19}$ ($x$ = 0, 0.1, 0.2, 0.3, 0.4) were synthesized by the citric acid precursor method [23–25]. Ethy-

lene glycol (Ranbaxy), citric acid (Sd fine), aluminium nitrate (Sd fine), strontium carbonate (Aldrich), lanthanum nitrate (Aldrich) and zinc nitrate (Loba) were used as-received without any further purification. Aluminium nitrate was added to a mixture of citric acid and ethylene glycol. After complete dissolution, the solution was heated at 80 °C and stoichiometric quantities of strontium carbonate, lanthanum nitrate and zinc nitrate were added. The molar ratio of 1:1 was maintained for citric acid to total metal cations concentration and 1:4 ratio was maintained between citric acid and ethylene glycol. For example, for the synthesis of $x = 0.4$ composition, 9.09 g of citric acid were taken in ethylene glycol and dissolved, to this solution 14.49 g of aluminium nitrate was added. After the complete dissolution, the solution was heated at 80 °C and to this 0.29 g of strontium carbonate, 0.43 g of zinc nitrate and 0.40 g of zinc nitrate were added. After the complete evaporation of superfluous water, the resulting viscous mass was heated at 140 °C for 2 hours which produced a solid amorphous resin, which was transferred to a pre-heated oven at 250 °C for charring for 2 hrs. The resulting powder was calcined at 700, 800, 1000, and 1100 °C for 2 hrs each with intermediate grindings. The calcined powders were finally heated at 1200 °C for 6 hours, so as to get $Sr_{1-x}La_xAl_{12-x}Zn_xO_{19}$ in single phase forms without any impurities.

## 3.3 NMR methodology

Solid-state NMR experiments were carried out at room temperature on both low-field and high-field spectrometers. Low-field NMR experiments were done on a Bruker AV-300 (aluminium resonance frequency, $\nu_{Al} = 78.2$ MHz) and a Bruker AV-500 ($\nu_{Al} = 130.2$ MHz) spectrometers, operating at a field of 7.05 T and 11.7 T, respectively. For the experiments at 7.05 T, a 4 mm BL MAS probe, at the magic angle spinning rate of 13 kHz and with a short pulse duration 0.26 $\mu$s, was used. 2000 scans were collected with a recycle delay of 1 s. Experiments at a spinning rate of 33 kHz were also carried out on the AV-300 spectrometer, using a 2.5 mm probe with a pulse duration of 0.2 $\mu$s, acquiring 10,000 scans. For experiments on the AV-500 spectrometer, the sample was packed into a 3.2

mm rotor and spun at the rate of 22 kHz. The quantitative MAS spectrum was recorded by collecting 2000 scans with a pulse width of 0.4 $\mu$s and a recycle delay of 1 s. The 3-quantum magic angle spinning (3QMAS) experiment was carried out on a 2.5 mm probe using a standard Z-filter pulse sequence on the AV-300 spectrometer. The experiment was optimized at a spinning rate of 33 kHz with the excitation and conversion pulses as 2.8 and 0.8 $\mu$s, respectively with a radio frequency (RF) field of strength of 170 kHz. The selective 90° Z-filter pulse was set as 18 $\mu$s at an RF field strength of 8 kHz. A recycle delay of 6 s was used for the experiment.

The high field experiments were carried out on a Bruker AV- 600 ($\nu_{Al}$ = 156.38 MHz) and a Bruker AV-700 ($\nu_{Al}$ = 178.42 MHz) spectrometers operating at a field of 14.0 and 16.4 T, respectively. The quantitative MAS NMR data on AV-600 was collected using a 1.3 mm MAS probe with a spinning speed of 40 kHz. 16,000 scans were acquired using a short pulse of 0.4 $\mu$s and with a recycle delay of 3 s on AV-600. For experiments on AV- 700, a 2.5 mm MAS probe, with a spinning speed of 34 kHz, was used. The quantitative MAS NMR spectra were recorded using a pulse width of 1.8 $\mu$s and 10,000 scans were acquired with a recycle delay of 3 s. The 3QMAS experiment was carried out on the AV-700 spectrometer equipped with a 3.2 mm probe using a standard Z-filter pulse sequence. The experiment was optimized at a spinning rate of 20 kHz with the excitation and conversion pulses as 5.4 and 1.9 $\mu$s, respectively with a RF field strength of 119 kHz. The selective 90° Z-filter pulse was set as 35 $\mu$s at an RF field strength of 6 kHz. A recycle delay of 5 s was used for the experiment.

## 3.4 Studies on $SrAl_{12}O_{19}$

### 3.4.1 Characterization

The as-synthesized sample was initially characterized by powder X-ray diffraction to confirm the formation of single phase strontium aluminate. The experimental and simulated powder XRD patterns of strontium aluminate, simulated using the

PCW software [29], are shown in figure 3.2 for comparison. The XRD pattern is simulated using the crystallographic parameters of the central atom model reported in the literature [28]. The positions and intensities of the different peaks observed in the experimental XRD pattern are comparable with that in the simulated pattern. There are no additional peaks in the XRD pattern, indicating the absence of any impurities in the sample. The hexagonal lattice parameters are obtained as a = 5.5691 Å and c = 22.0184 Å, from least-squares refinement of the experimental pattern, using the space group $P6_3/mmc$. The calculated lattice parameters are in good agreement with that reported in the literature [28].

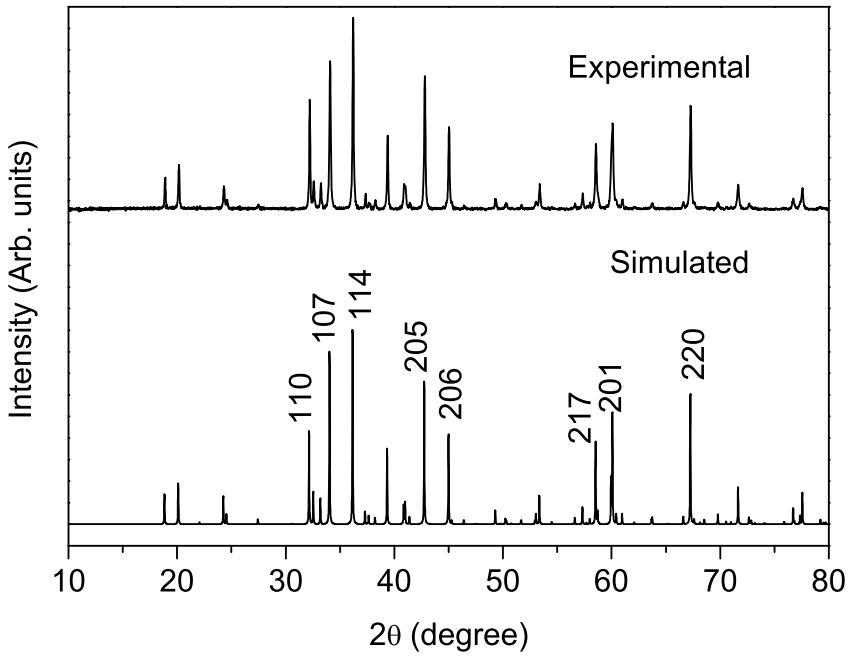


*Figure 3.2: Experimental and simulated XRD pattern of $SrAl_{12}O_{19}$ with the major peaks indexed.*

### 3.4.2 $^{27}$Al NMR

$^{27}$Al MAS NMR spectra of strontium aluminate recorded at different fields and at different spinning speeds, viz. on AV-300 (7.05 T) at 13 kHz and 33 kHz, on AV-500 (11.4 T) at 22 kHz, on AV-600 (14 T) at 40 kHz, and on AV-700 (16.4 T)

at 34 kHz, are shown in figure 3.3. The figure shows that the spectrum is highly broadened at low fields. The broad signals are overlapped at the spinning speed of 13 kHz at 7.05 T. As the spinning speed is increased to 33 kHz, the signals are partially separated out compared to the spectra recorded at 13 kHz. Moreover, the resolution is found to increase when recorded at higher field strengths, as seen in the spectra recorded at 14.0 and 16.4 T. Although the quadrupolar broadening decreases as the external field strength increases, it is seen that the resonances corresponding to the different Al sites in the material are not well resolved, except for the $AlO_4$ signal which is clearly separated from the signal corresponding to $AlO_6$, because of the large difference in the chemical shifts for the tetrahedral and octahedral coordination environments.

In the spectra recorded at high fields, a weak and broad component is observed close to the baseline, as shown in figure 3.4. This feature has been attributed to the distorted tetrahedral site in the magnetoplumbite lattice [31]. Because of the overlapping of the signals for the various sites and recorded at low fields, this peak is seen only in the spectra recorded at high fields of 14.0 and 16.4 T.

To test the existence of the five-coordinated $AlO_5$ coordination environment in $SrAl_{12}O_{19}$, a 3QMAS experiment was carried out at both 7.05 T and 16.4 T. The 3QMAS spectrum recorded at 7.05 T is shown in figure 3.5. Five distinct contours corresponding to the five different Al sites in the strontium aluminate structure are seen in the spectra. The contours corresponding to Al-VI-1 and Al-V are very small because of the low population of these sites (occupation at these sites is 8.33% against 16.7% at Al-IV as well as Al-VI-2 and 50% at Al-VI-3, see table 3.1). The 3QMAS spectra recorded at 16.4 T, however, does not show the contour corresponding to the Al-V site, as shown in figure 3.6, where the spectrum in the octahedral coordination region is shown for clarity. The three contours corresponding to the different octahedral sites are clearly observed in the spectra. The absence of the signal due to $AlO_5$ is because of the low quadrupolar excitation efficiency at higher fields, and that the Al-V signal is obscured among the signals from the octahedral sites.

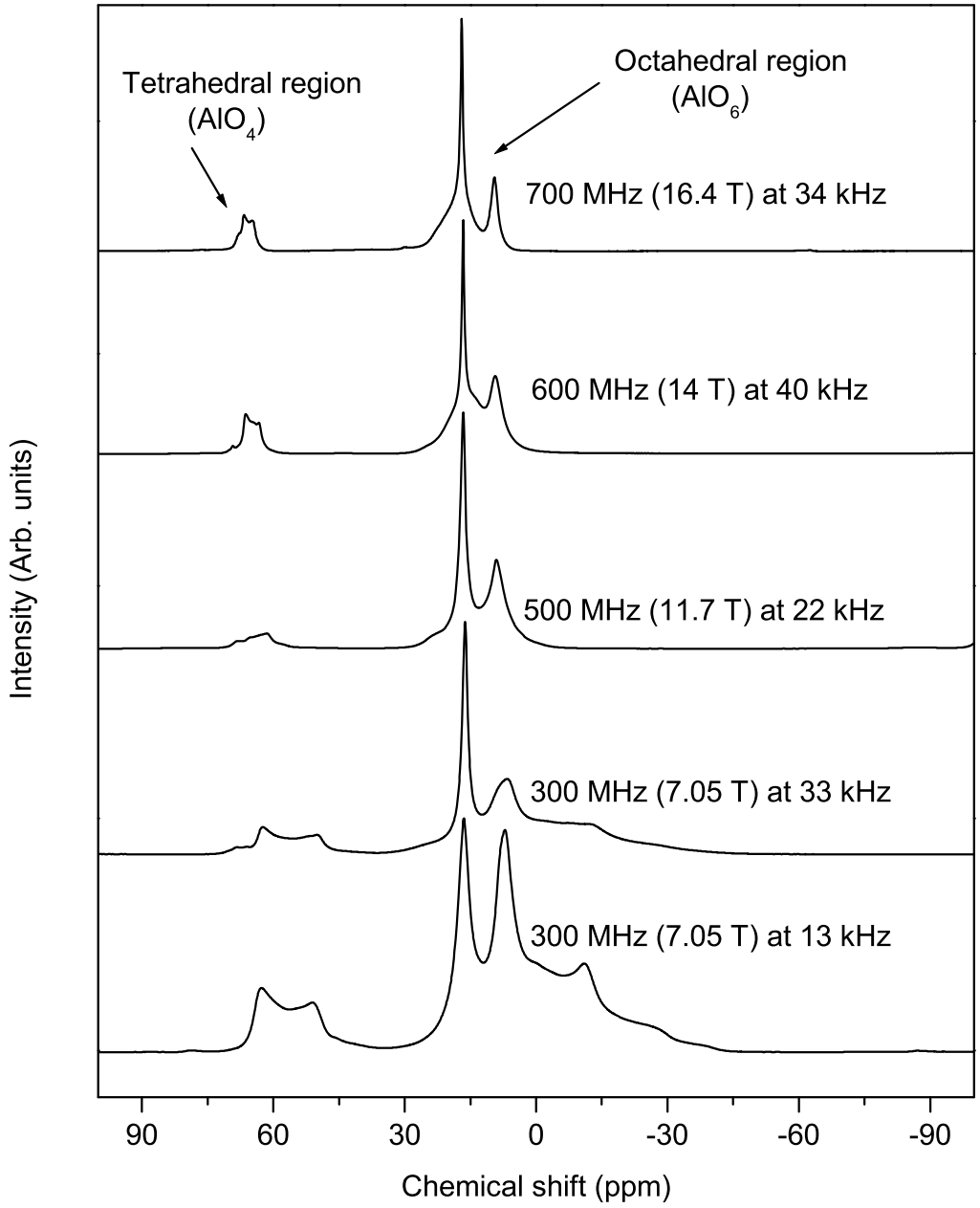


*Figure 3.3: $^{27}Al$ MAS NMR spectra of $SrAl_{12}O_{19}$ recorded at different field strengths and at different spinning speeds.*

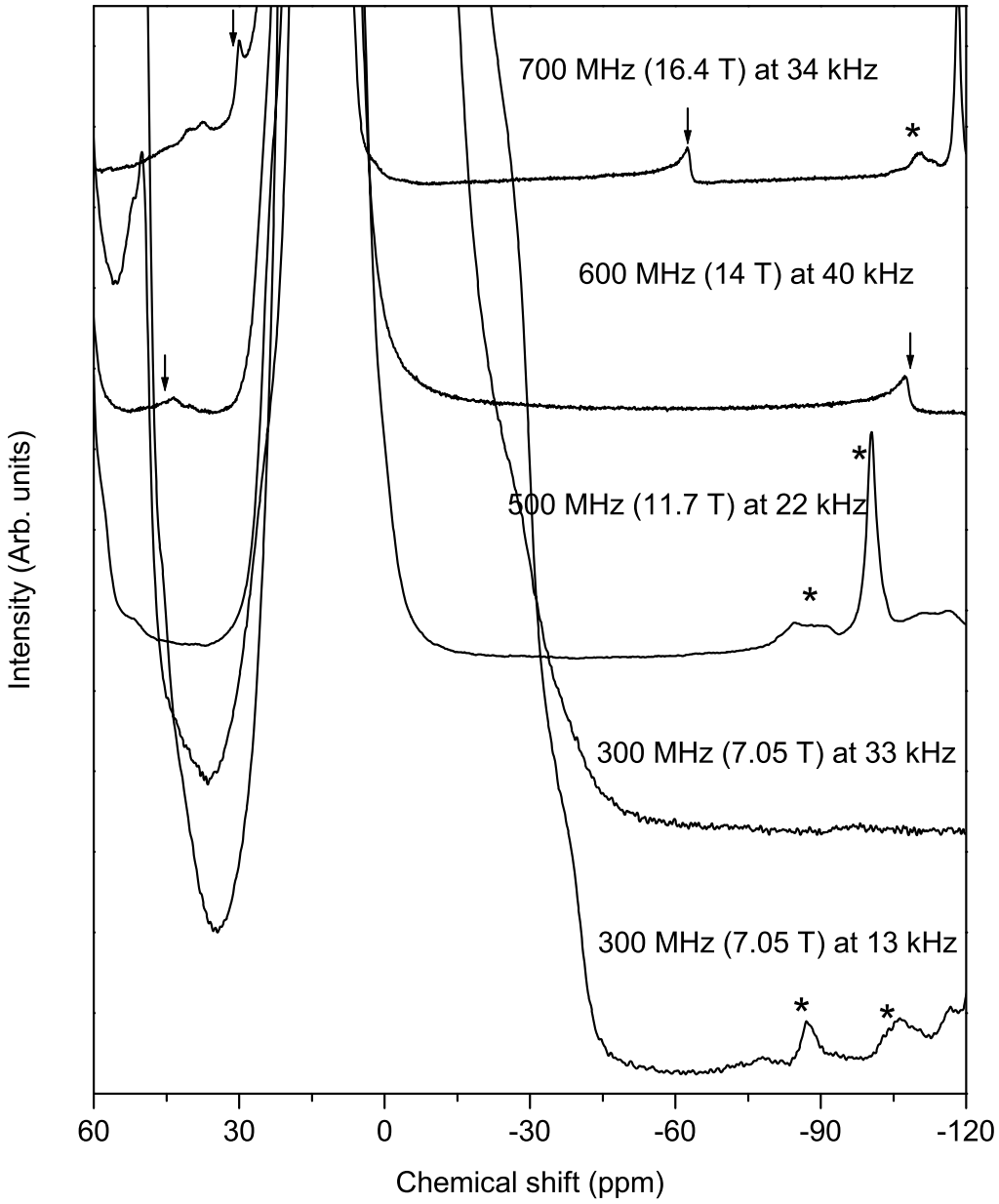


*Figure 3.4: Zoomed view of $^{27}Al$ MAS NMR spectra of $SrAl_{12}O_{19}$ recorded at different field strengths and at different spinning speeds (arrows indicate the peaks due to distorted tetrahedral coordination and stars represent the spinning sidebands).*

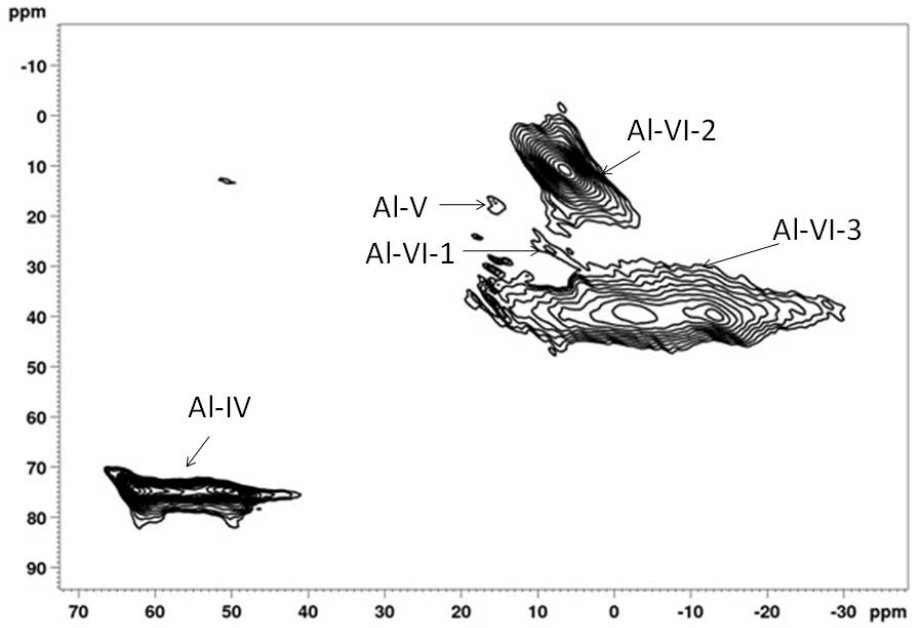


*Figure 3.5: 3QMAS spectra of $SrAl_{12}O_{19}$ recorded at 7.05 T.*

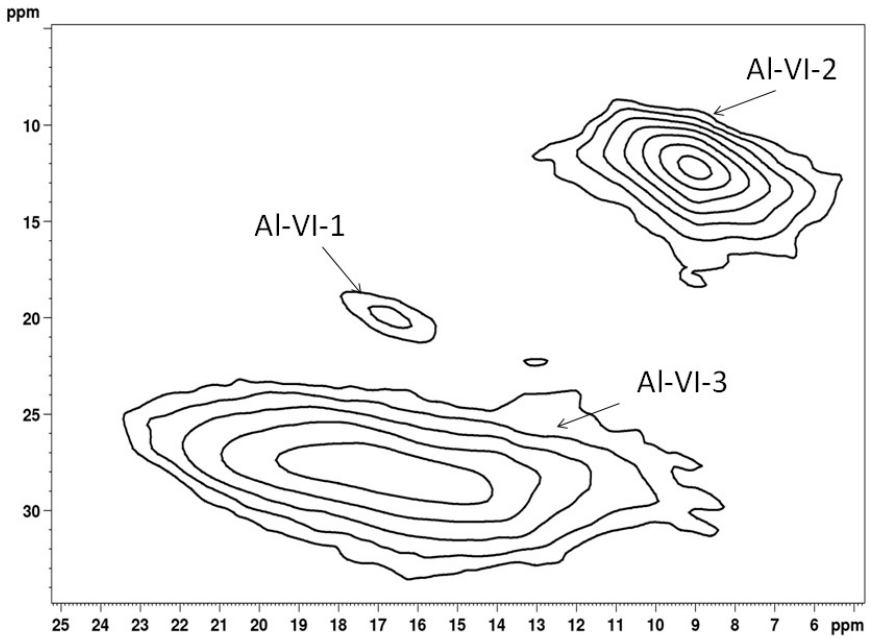


*Figure 3.6: 3QMAS spectra of $SrAl_{12}O_{19}$ recorded at 16.4 T. Spectra in the octahedral coordination region only is shown for clarity.*

An estimate of the quadrupolar parameters are obtained from the 3QMAS spectra and this was used for the calculation of site population of different Al sites. For the quantitative estimation of site populations of different Al coordination environments, the MAS spectra recorded at different field strengths, 7.05 T with spinning speed of 33 kHz and spectra recorded at the high fields, at 14.0 T with a spinning speed of 40 kHz and at 16.4 T with spinning speed of 34 kHz, are fitted and deconvoluted into individual components using the DMFIT program (see section 2.3.2.6, Chapter 2) [26]. The spectra with individual components, for the different field strengths, are shown in figures 3.7, 3.8 and 3.9.

The MAS spectra at 7.05 T could be fitted using only five components corresponding to the five different crystallographic sites in the structure (see table 3.1), as in the central atom model. The spectra could not be fitted with less than five components, indicating that the Al-V site is clearly present in the structure. It can be seen from figure 3.7 that the experimental and the simulated spectra match very well. The spectral parameters and the relative intensities for each site are given in table 3.2. The calculated intensities are corrected following the method reported in the literature [27], as explained in chapter 2 (section 2.3.2.7). The corrected values are also given in table 3.2. The calculated and the corrected intensities differ only by small amounts, indicating negligible contributions from the satellite transitions. The spectral parameters obtained are in close agreement with those reported by Jansen et al. [30].

The MAS spectra recorded at high fields 14.0 T and 16.4 T have a weak and broad component as shown in figure 3.4. This component is attributed to the distorted $AlO_4$ site, as suggested by Du and Stebbins [31], with a large quadrupole coupling constant. However, it is found that the $AlO_5$ component is essential to obtain a proper fit. Thus, the spectra recorded at high fields are fitted with six components: one $AlO_4$, three $AlO_6$, one $AlO_5$ and the distorted tetrahedral site, as reported by Harindranath et al. [24]. The spectral parameters and the relative intensities for each site are given in table 3.2.

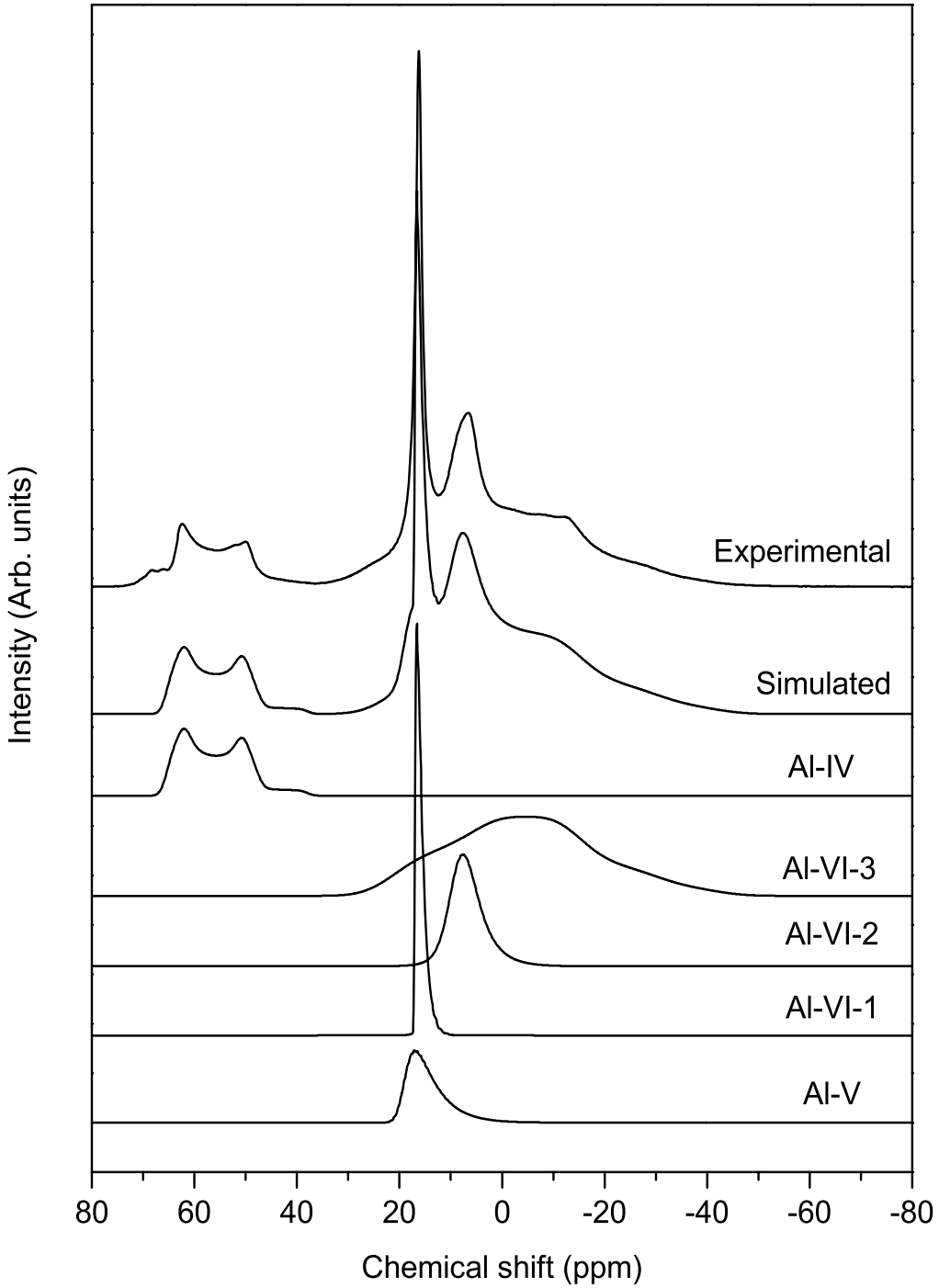


*Figure 3.7: Experimental and simulated $^{27}Al$ MAS NMR spectra of $SrAl_{12}O_{19}$ recorded at 7.05 T, along with the individual components.*

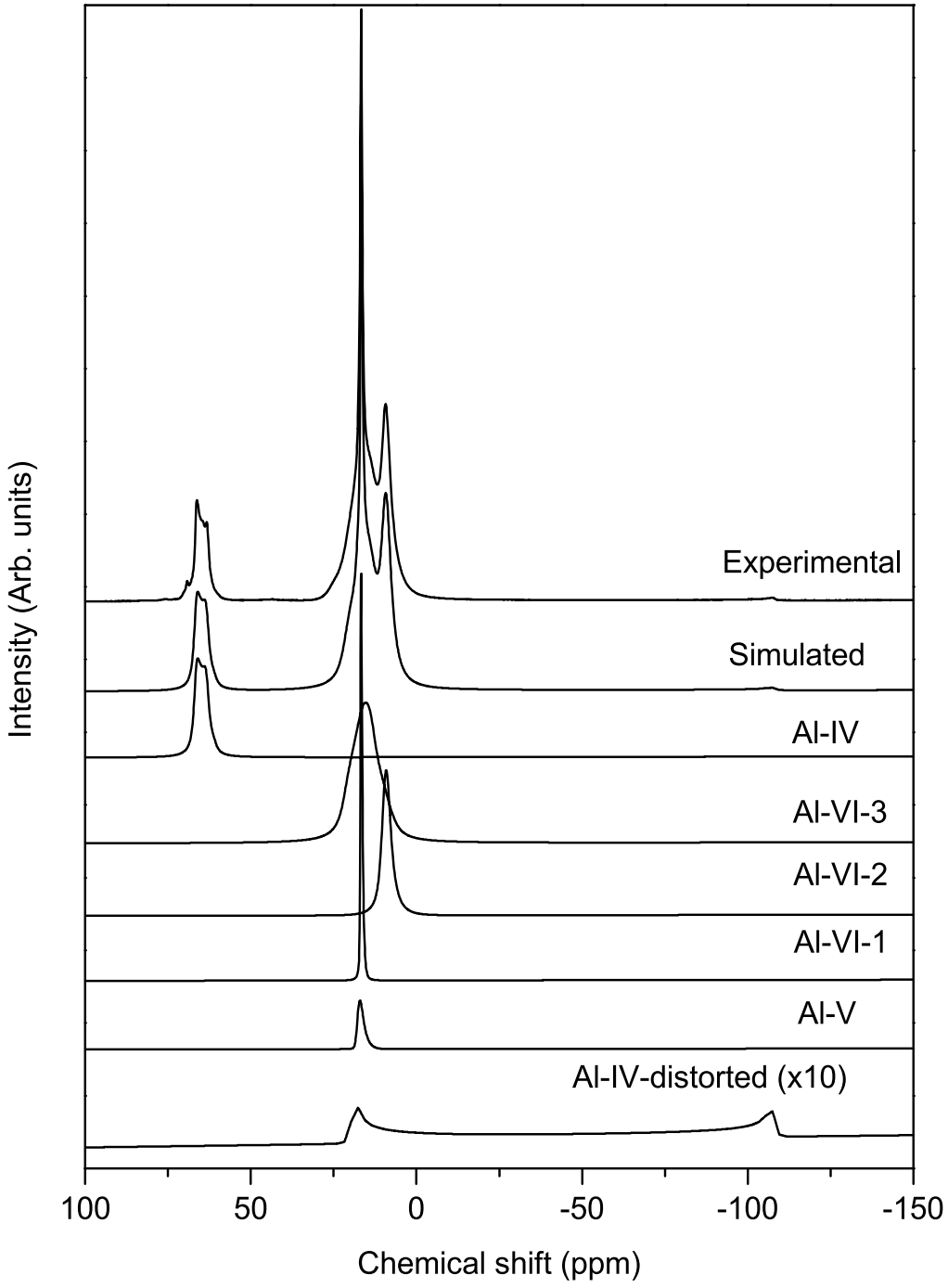


*Figure 3.8: Experimental and simulated $^{27}Al$ MAS NMR spectra of $SrAl_{12}O_{19}$ recorded at 14.0 T, along with the individual components.*

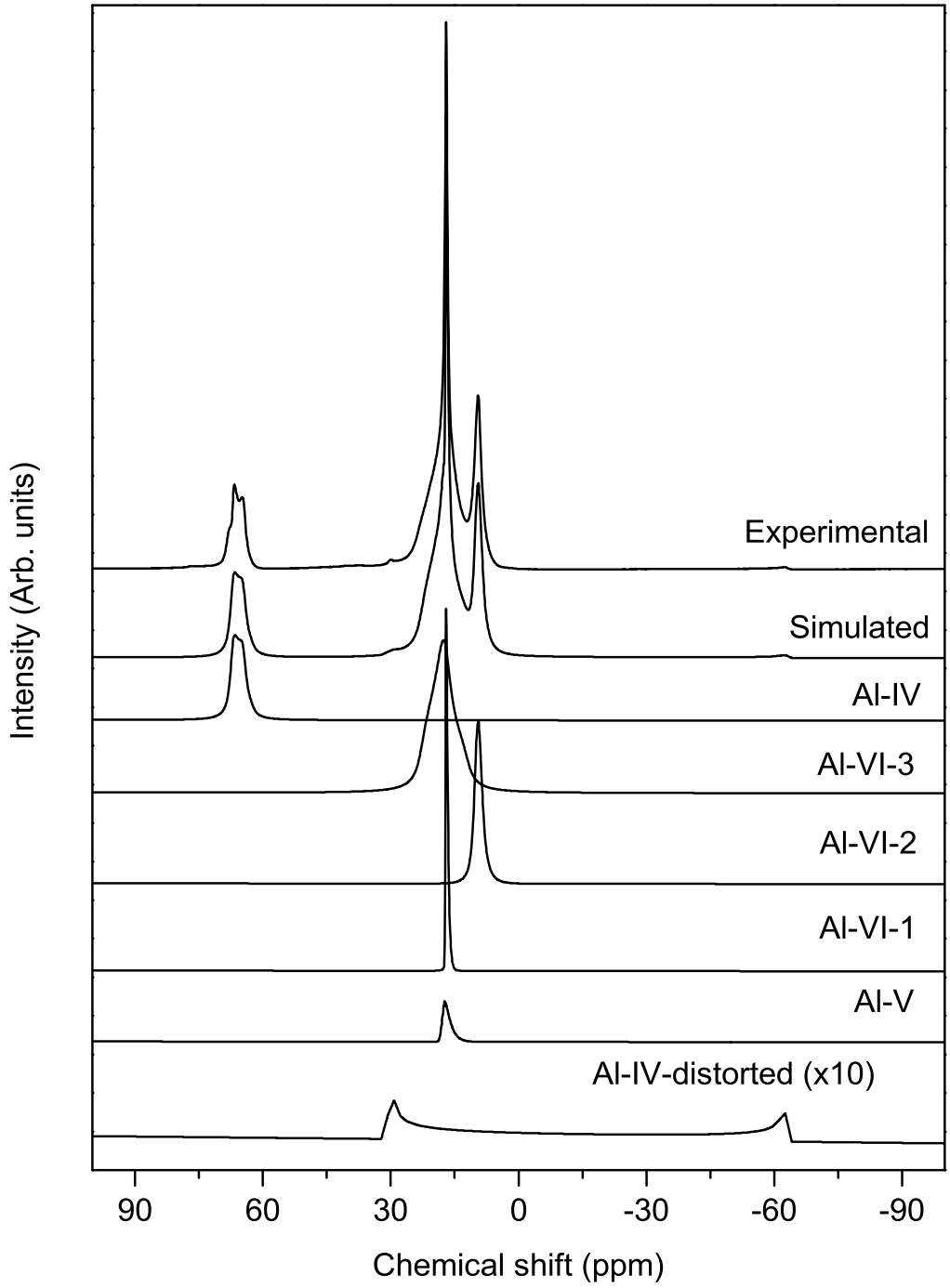


*Figure 3.9: Experimental and simulated $^{27}Al$ MAS NMR spectra of $SrAl_{12}O_{19}$ recorded at 16.4 T, along with the individual components.*

From the high-field NMR spectral studies, Du and Stebbins [31] argued that the penta coordinated site is actually a distorted tetrahedral coordinated Al site with the same site population but with a very large quadrupole coupling constant. However, according to the present simulation results of the high field spectrum, it is found that there are six Al sites present in strontium aluminate. 8.33% of aluminium ions is distributed among the the penta-coordinated and the distorted tetrahedral sites.

*Table 3.2: $^{27}Al$ MAS NMR parameters of $SrAl_{12}O_{19}$ obtained after deconvolution of the spectra recorded at different fields.*

| Field (T) | Al site | $\delta_{iso}$ (ppm) | $C_q$ (MHz) | $\eta$ | Observed occupancy (%) | Corrected occupancy (%) | Expected occupancy (%) |
|---|---|---|---|---|---|---|---|
| 7.05 | IV | 68.18 | 3.50 | 0.20 | 15.48 | 16.11 | 16.67 |
| | VI-1 | 17.04 | 2.02 | - | 9.27 | 8.80 | 8.33 |
| | VI-2 | 9.10 | 1.33 | - | 15.50 | 15.70 | 16.67 |
| | V1-3 | 22.95 | 4.99 | 0.68 | 48.98 | 49.70 | 50 |
| | V | 19.30 | 2.02 | - | 9.00 | 8.50 | 8.33 |
| 14.0 | IV | 67.65 | 3.41 | 0.12 | 16.54 | 16.57 | 16.67 |
| | VI-1 | 16.92 | 1.06 | - | 9.40 | 8.22 | 8.33 |
| | VI-2 | 9.55 | 1.49 | - | 17.45 | 15.88 | 16.67 |
| | V1-3 | 21.85 | 4.80 | 0.67 | 48.83 | 50.19 | 50 |
| | V | 17.81 | 2.03 | - | 3.80 | 3.67 | 8.33 |
| | IV-d | 56.58 | 20.68 | 0 | 3.99 | 5.47 | |
| 16.4 | IV | 68.00 | 3.56 | 0.10 | 16.25 | 16.38 | 16.67 |
| | VI-1 | 17.17 | 2.45 | - | 9.68 | 8.85 | 8.33 |
| | VI-2 | 9.70 | 1.25 | - | 16.96 | 15.37 | 16.67 |
| | V1-3 | 22.70 | 4.57 | 0.93 | 49.45 | 50.34 | 50 |
| | V | 17.17 | 1.31 | - | 3.74 | 3.69 | 8.33 |
| | IV-d | 57.80 | 20.67 | 0 | 3.92 | 5.37 | |

However, this is highly unlikely since only five different sites are possible according to the crystallographic data. It is not possible to have the same Al site as a penta-coordinated bipyramidal site and a distorted tetrahedral site with full site occupancy in the $P6_3/mmc$ space group in the central atom or the split atom model. Therefore, it is possible that the coordination environment of part of the Al in the structure is bipyramidal and the other part is distorted tetrahedral. The high-field NMR spectral results also indicate this possibility since the five coordinated and distorted tetrahedral sites are almost 50% each of the expected total occupancy of this site. It may be possible that both configurations (bipyramidal as well as distorted tetrahedral sites) co-exist in the structure. It is also possible that the central atom or the split atom models do not represent the correct structure of strontium aluminate or that the sample is a mixture of two different phases (one with the central atom model and the other with the split atom model) co-existing simultaneously. Another possible scenario is that the system undergoes a temperature induced dynamic disorder between distorted tetrahedral and bipyramidal sites and freezes in with some Al stuck in the distorted tetrahedral coordination and some in the bipyramidal coordination. In order to study the structural details, Rietveld refinement analysis of the XRD pattern is carried out, using different models. Similarly, XRD patterns are recorded at different temperatures, below room temperature, to look for any visible changes in the pattern due to the temperature induced dynamic disorder. The results are described in the next two sections.

### 3.4.3 Rietveld refinement studies

Since the presence of both the penta coordinated and the distorted tetra coordinated Al sites in strontium aluminate, from low-field and high-field $^{27}Al$ solid-state NMR studies, is confirmed unambiguously, and because of the controversy about the correct structural model, it is essential to have a re-look at the proposed structural models for strontium aluminate.

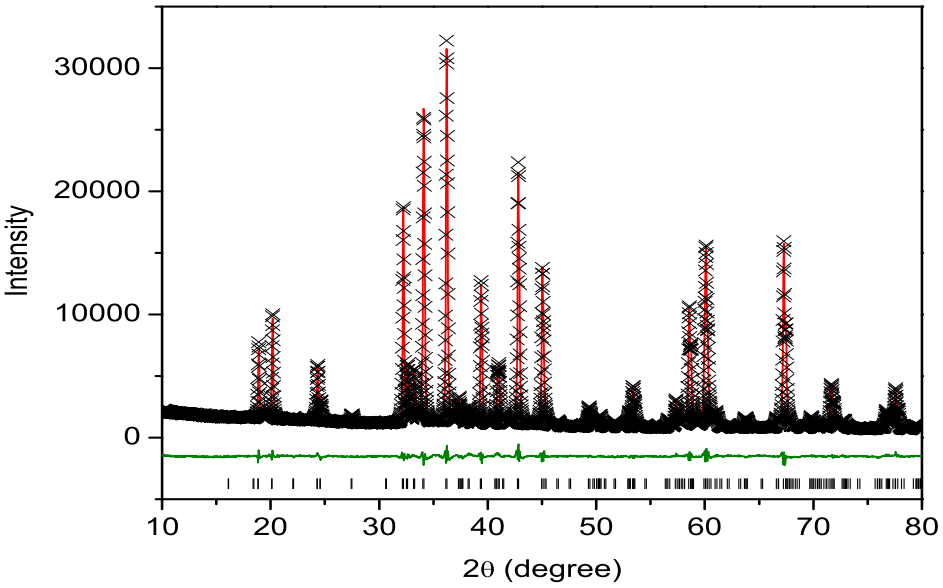


*Figure 3.10: Result of the Rietveld refinement of the XRD pattern of $SrAl_{12}O_{19}$ using the central atom model.*

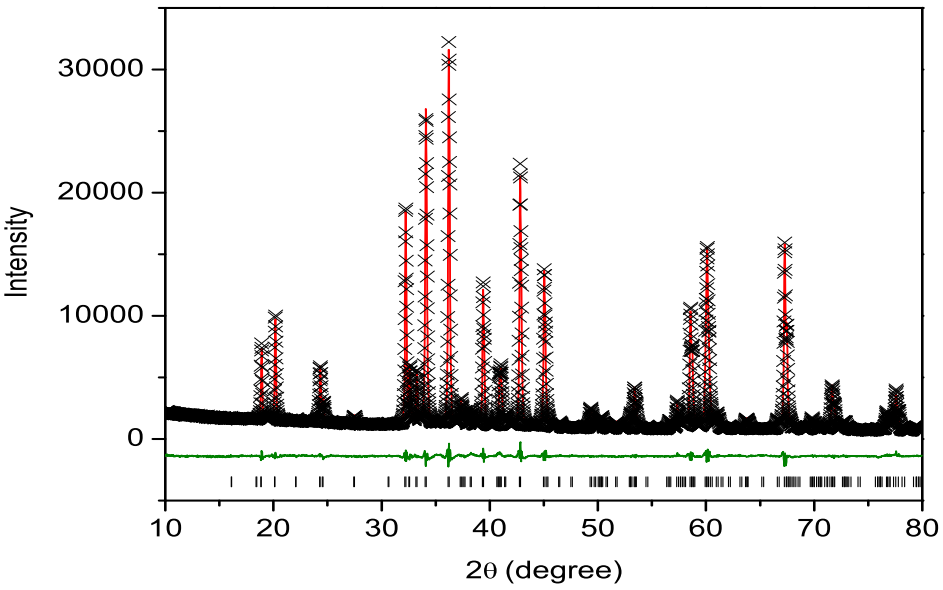


*Figure 3.11: Result of the Rietveld refinement of the XRD pattern of $SrAl_{12}O_{19}$ using the split atom model.*

Rietveld refinement analysis of the powder X-ray diffraction pattern of the synthesized strontium aluminate sample is carried out with the proposed different structure models of strontium aluminate using the same space group $P6_3/mmc$, as reported by Kimura et al. [28]. The authors concluded that the split atom model is the correct structure based on the slightly lower values of the R-factors (0.0331) for the split atom model compared to the central atom model (0.0340), obtained from the refinement. However, the authors found that comparable R-factors (0.0331) are obtained when anharmonic thermal vibration for the concerned Al-site (bipyramidal 2b as well as the distorted tetrahedral 4e) is incorporated in the refinement.

Rietveld refinement studies of the powder XRD data have been carried out using the software General Structure Analysis System (GSAS-EXPGUI). Initially, structural refinements are carried out with the central atom and split atom models, using the data taken from the literature [28] as inputs. Later on, a model with both the 2b (bipyramidal) and the 4e (distorted tetrahedral) sites simultaneously present in the structure with half the occupancies at the 2b and 4e sites is tried. Finally, refinement is carried out considering the presence of two different phases, one phase having the central atom model and the other with the split atom model. The results of the Rietveld refinement using the central atom model and split atom model for $SrAl_{12}O_{19}$ are shown in figures 3.10 and 3.11, respectively.

*Table 3.3: Results of the Rietveld refinement analysis of the XRD pattern of $SrAl_{12}O_{19}$ using different structural models.*

| Structure model | $\chi^2$ | $R_{wp}$ | $R_{F^2}$ | a (Å) | c (Å) |
|---|---|---|---|---|---|
| Central atom | 2.684 | 0.0375 | 0.0630 | 5.5639 | 21.999 |
| Split atom | 2.726 | 0.0378 | 0.0616 | 5.5648 | 22.0019 |
| Simultaneous occupancy at 2b and 4e sites | 2.847 | 0.0386 | 0.0656 | 5.5595 | 21.9802 |
| Two-phase mixture (central atom+split atom) | 2.292 | 0.0347 | 0.0515 | 5.5604 | 21.9864 |

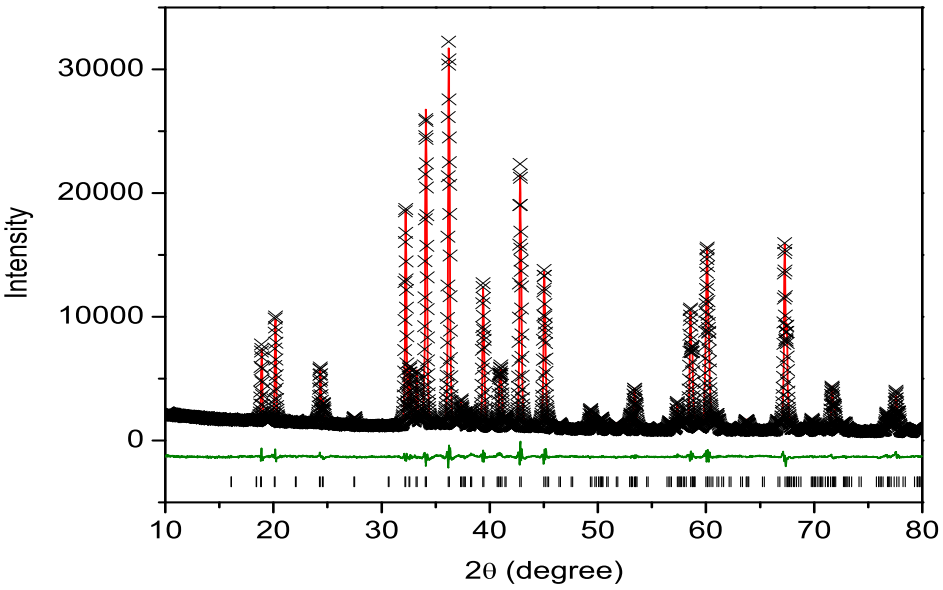


*Figure 3.12: Result of the Rietveld refinement of the XRD pattern of $SrAl_{12}O_{19}$ using a model with partial occupancies at the distorted tetrahedral and trigonal bipyramidal sites.*

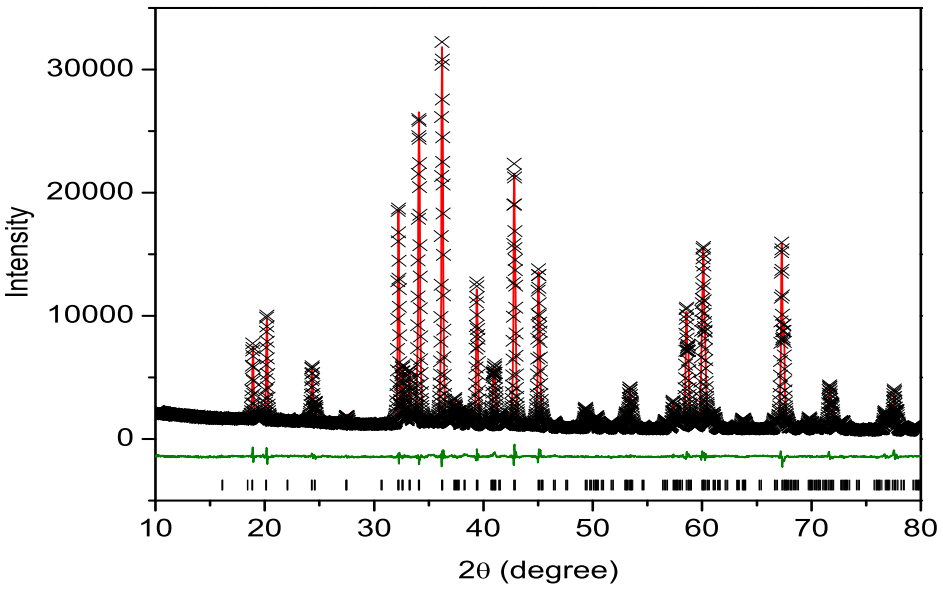


*Figure 3.13: Result of the Rietveld refinement of the XRD pattern of $SrAl_{12}O_{19}$ using a two-phase mixture consisting of the central atom and split atom models.*

The results of the Rietveld refinement are comparable using both the structural models, with only a minor difference in the residual factors (relatively lower $R_{wp}$ for the central atom model and lower $R_{F^2}$ for the split atom model) as shown in table 3.3. These results are comparable to that reported in the literature [28]. Results of the structural refinement with simultaneous partial occupancies at both the 2b (trigonal bipyramidal) and 4e (distorted tetrahedral) sites, and a two-phase mixture of central atom and split atom models are shown in figures 3.12 and 3.13, respectively. The $\chi^2$ and the R-factors for the simultaneous occupancies are relatively larger when compared to the results obtained for the individual models. On the other hand, from the table 3.3, it is clear that a model with two different phases simultaneously present gives much reduced values for $\chi^2$ and the R-factors. Hence, it may be assumed that the mixed phase model may be the correct structural model for strontium aluminate which can also account for the presence of distorted tetra coordinated (4e) and penta coordinated (2b) Al sites in the $^{27}$Al SSNMR spectrum.

### 3.4.4 Low temperature powder XRD studies

As discussed in the previous section, another possible reason for the observation of simultaneous occupancies of Al at the distorted tetrahedral (4e site) and the trigonal bipyramidal (2b sites) sites in $SrAl_{12}O_{19}$ is a temperature induced dynamic disorder, which would result in part of Al atoms to be located at the distorted tetrahedral and the rest in the trigonal bipyramidal sites. This is expected to be suppressed or the extent of occupancies at the two sites will be varied at low temperatures due to the availability of less thermal energy. In order to check this possibility of dynamics in the crystal structure, which may occur due to the interconversion of trigonal bipyramidal and distorted tetrahedral coordination environments, low-temperature powder XRD measurements have been carried out from room temperature (298 K) to 100 K. Since the intensities of the peaks in an XRD pattern is related to the position of the atoms in the crystal structure, a change in the intensities of some of the peaks are expected due to the suppres-

sion of the interconversion. The XRD patterns recorded at different temperatures are shown in figure 3.14 and the zoomed patterns are shown in figure 3.15 which indicate that there is no observable difference in the intensities of different peaks as the temperature is decreased or even at the lowest temperature, except for a small shift ($< 0.1°$) in the reflection positions, corresponding to lattice contraction, as the temperature is decreased. These results suggest that the model with simultaneous occupancies at the 4e and 2b sites to represent the crystal structure of $SrAl_{12}O_{19}$ is not the correct model.

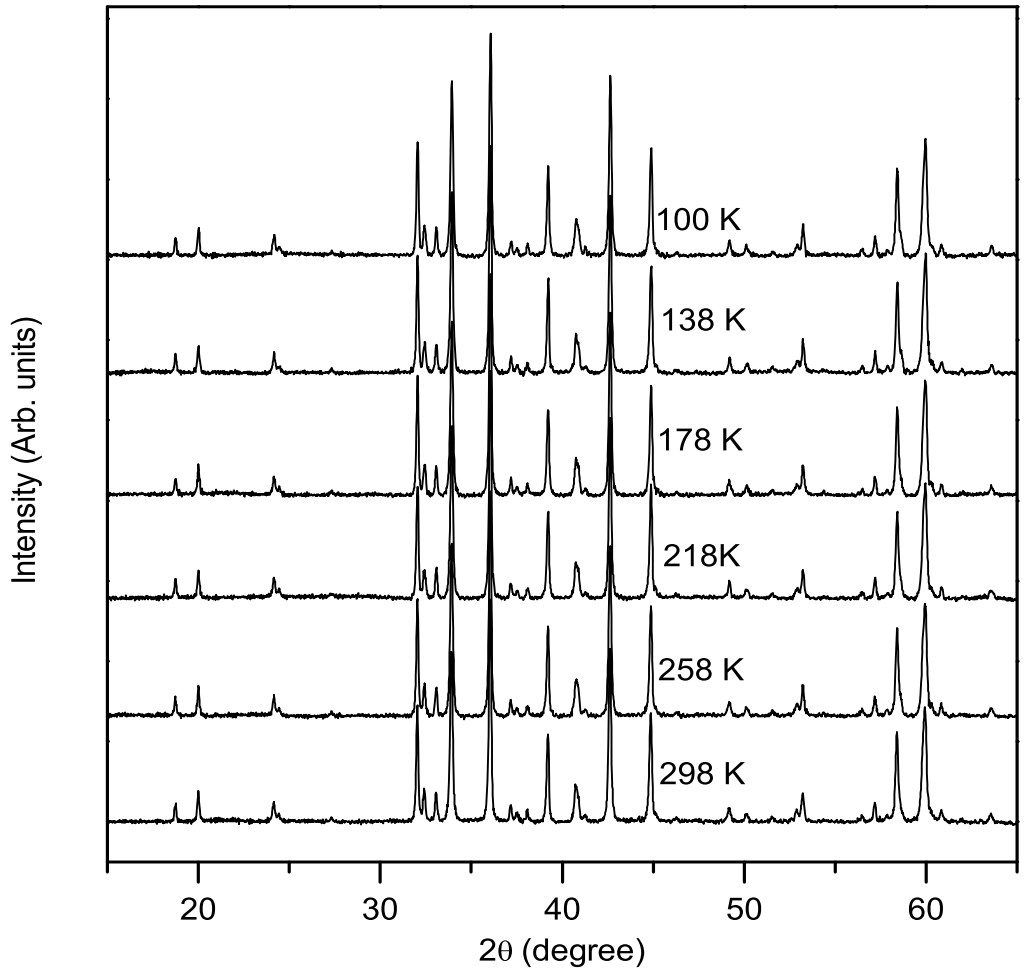


*Figure 3.14: Powder XRD patterns of $SrAl_{12}O_{19}$ recorded at low temperatures.*

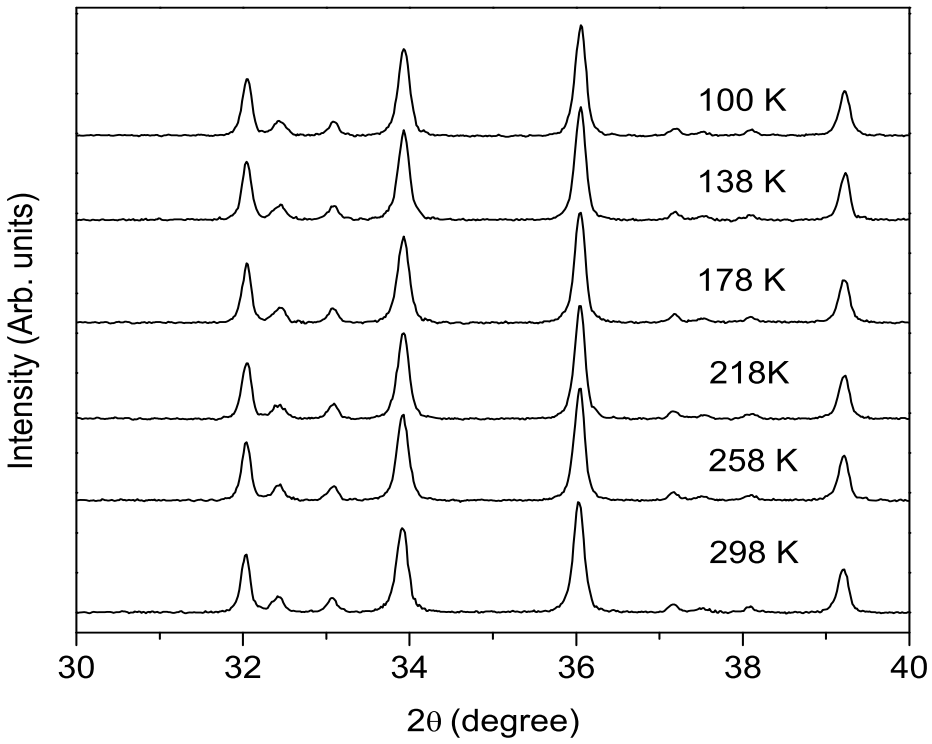


*Figure 3.15: Zoomed powder XRD patterns of $SrAl_{12}O_{19}$ recorded at low temperatures.*

### 3.4.5 Summary

Two different SSNMR studies have reported the occupancy of part of Al in $SrAl_{12}O_{19}$ at trigonal bipyramidal sites (from low-filed NMR studies) and at the distorted tetrahedral sites (from high-field NMR studies). However, NMR studies on the same sample at both low- and high fields indicated the presence of Al at both the distorted tetra coordinated and the penta coordinated Al sites. Rietveld refinement analysis of the XRD patterns of the strontium aluminate sample gave indication for a possible two-phase model. Based on the results from NMR and structural studies, it is concluded that a structural model where two phases co-exist simultaneously, one with the central atom model and another with the split atom model is the correct model for $SrAl_{12}O_{19}$ with the magnetoplumbite structure.

## 3.5 Studies on $Sr_{1-x}La_xAl_{12-x}Zn_xO_{19}$

### 3.5.1 Characterization

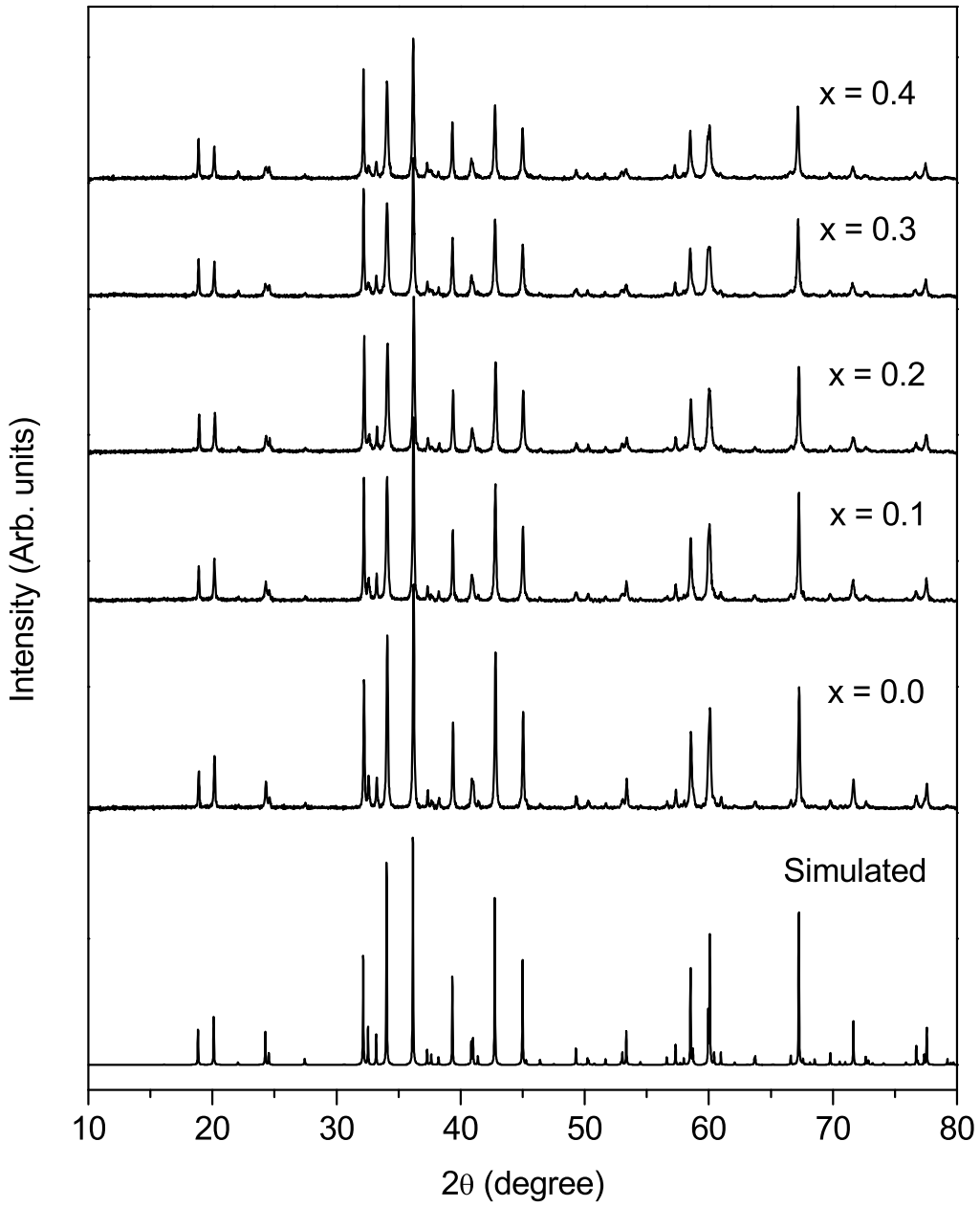


*Figure 3.16: Powder XRD patterns of $Sr_{1-x}La_xAl_{12-x}Zn_xO_{19}$. The simulated pattern of $SrAl_{12}O_{19}$ using the central atom model is shown for comparison.*

*Table 3.4: The hexagonal lattice parameters of $Sr_{1-x}La_xAl_{12-x}Zn_xO_{19}$ obtained from least squares fitting of the XRD patterns.*

| $x$ | a (Å) | c (Å) |
|---|---|---|
| 0.0 | 5.5691 | 22.0184 |
| 0.1 | 5.5707 | 22.0305 |
| 0.2 | 5.5741 | 22.0358 |
| 0.3 | 5.5751 | 22.0273 |
| 0.4 | 5.5763 | 22.0232 |

The samples were initially characterized using powder XRD studies to confirm the formation of the desired substituted materials in single phase form. The XRD patterns of the unsubstituted and the substituted strontium aluminate compositions are shown in figure 3.16. The simulated XRD pattern of strontium aluminate using the crystallographic parameters of the central atom model is also shown in the figure for comparison. Except for the changes in the relative intensities of some peaks, due to substitution of La for Sr and Zn for Al, there are no extra peaks observed in the XRD patterns of all the compositions, indicating phase purity. The hexagonal lattice parameters obtained from a least squares fitting of the experimental patterns are given in Table 3.4.

The hexagonal lattice parameter '$a$' increases continuously whereas the parameter '$c$' increases and reaches a maximum value for $x = 0.2$ and then decreases with increasing $x$. This is due to the larger ionic size of $Zn^{2+}$ (0.74 Å) compared to that of $Al^{3+}$ (0.535 Å) and the smaller size of $La^{3+}$ (1.36 Å) compared to that of $Sr^{2+}$ (1.44 Å). The compared ionic sizes are for six-fold coordination for $Al^{3+}$ and $Zn^{2+}$ and for twelve-fold coordination for $La^{3+}$ and $Sr^{2+}$ [12]. The difference in the ionic sizes of $Sr^{2+}$ and $La^{3+}$ is relatively smaller than the difference between the sizes for $Zn^{2+}$ and $Al^{3+}$, so that there is an effective increase in the lattice parameter $a$, with increasing $x$. Thus, the powder XRD studies confirm the formation of the La-Zn substituted strontium aluminate compositions.

### 3.5.2 $^{27}$Al NMR

From the studies on the unsubstituted $SrAl_{12}O_{19}$, it is clear that the distorted tetrahedral site can be seen only at high fields due to its high quadrupolar coupling constant. Therefore, all the studies on the substituted $SrAl_{12}O_{19}$ were carried out at 14.0 T and 16.4 T and the spectra are shown in figures 3.17 and 3.18, respectively. There is not much enhancement in the resolution of the spectra recorded at 16.4 T compared to the spectra recorded at 14.0 T. This is because the spectra at 16.4 T was recorded at the spinning speed of 34 kHz, while the spectra at 14.0 T was recorded at 40 kHz. From the spectra shown in figures 3.17 and 3.18, it can be seen that the $^{27}$Al resonances for the different coordination environments for all the samples are not well resolved except for the $AlO_4$ resonance around chemical shift ∼70 ppm, as observed for the unsubstituted strontium aluminate (see figure 3.3). It is very clear from the spectra that the Al coordination environments are affected as the degree of La-Zn substitution increases. Although there is no substantial change in the chemical shift of the individual spectral lines, the lineshape seems to be affected by the increase in the amount of substitution. Clear distortions of the peak originating from the tetrahedral coordination (∼70 ppm) and reduced intensity ratio of the peaks due to octahedral environments (∼10 ppm) are directly visible in the spectra of the substituted compositions recorded at both the fields.

The changes in the spectral characteristics could be due to various factors such as:

- The distortions are arising from the occupancy of Zn ions in the tetrahedral sites only which affect the nearby octahedral and penta coordinated sites,

- The substituted Zn ions occupy only the octahedral sites and the nearby tetrahedral sites experience only a distortion due to this,

- Simultaneous occupancy of the Zn ions in the tetrahedral and the octahedral sites.

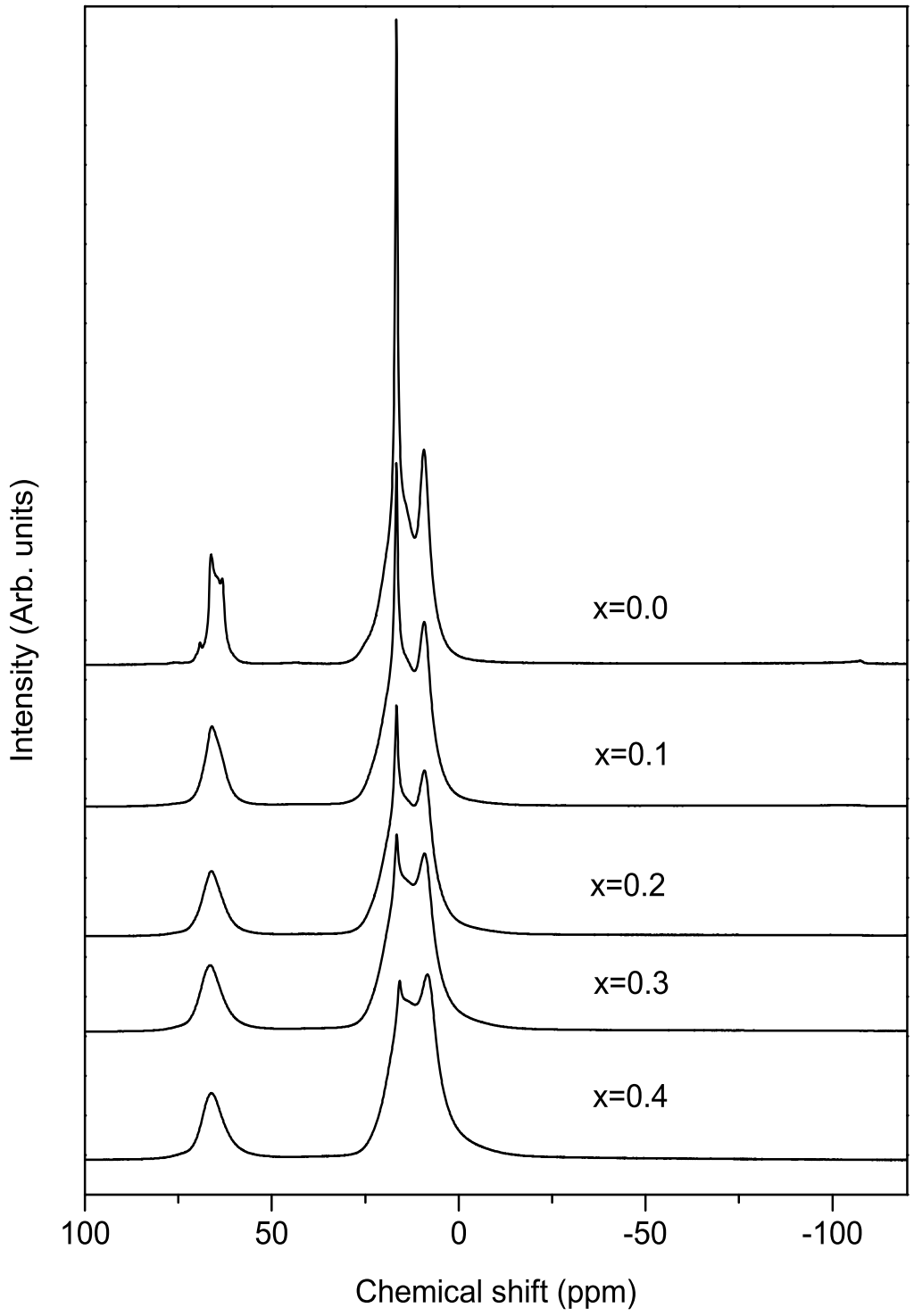


*Figure 3.17: $^{27}Al$ MAS NMR spectra of $Sr_{1-x}La_xAl_{12-x}Zn_xO_{19}$ recorded at 14.0 T.*

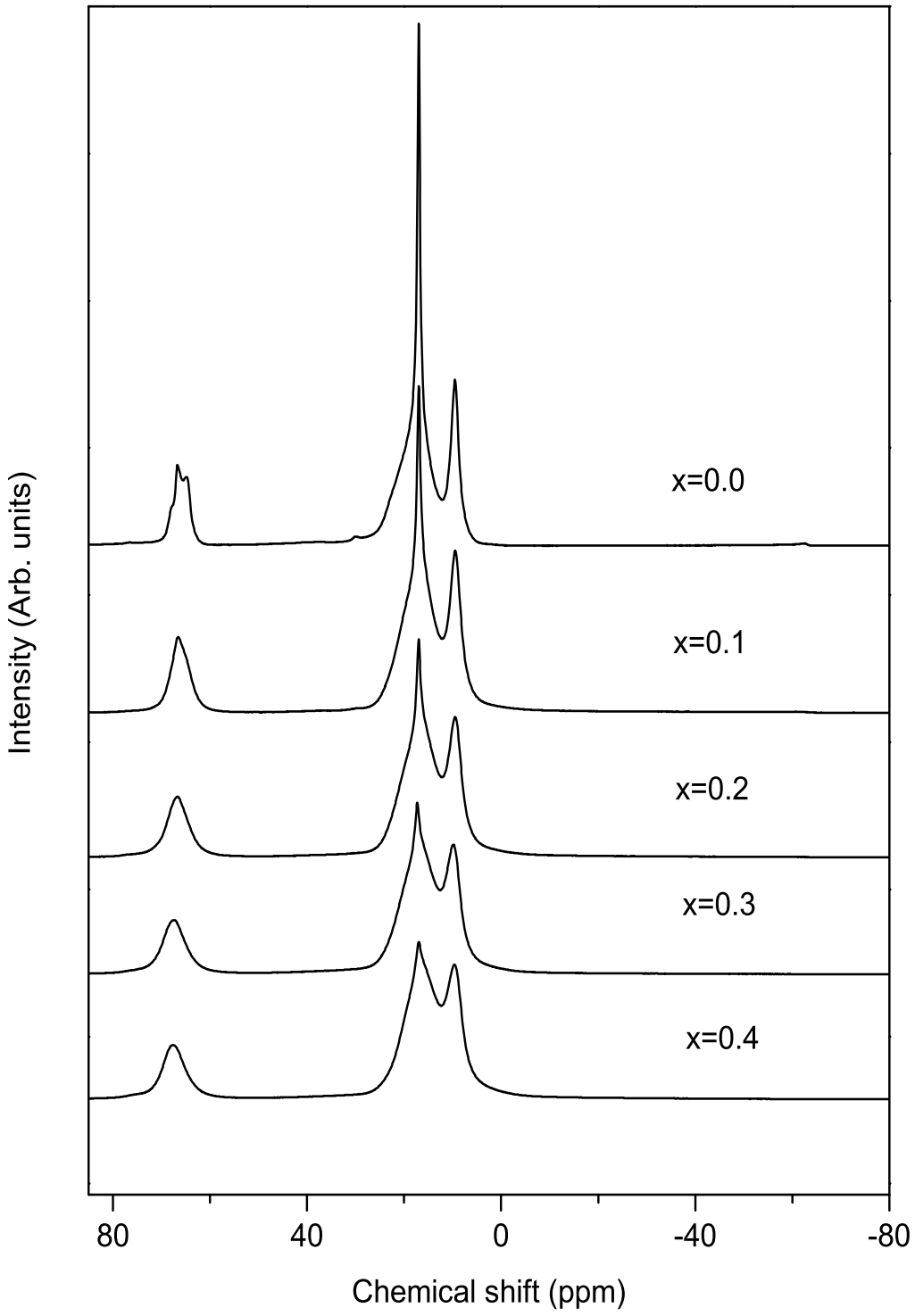


*Figure 3.18: $^{27}Al$ MAS NMR spectra of $Sr_{1-x}La_xAl_{12-x}Zn_xO_{19}$ recorded at 16.4 T.*

Mössbauer spectroscopic studies have shown that only the 2a and $4f_2$ octahedral Fe sites are occupied by Co in the case of La-Co substituted strontium ferrite [13–17]. Similarly, in the reported work on the Fe, La and Co NMR spectra of La-Co substituted strontium ferrite, it has been shown that a severe distortion of the tetrahedral symmetry can occur due to lattice distortions arising from the substitutions but do not play a major effect in determining the properties [20]. However, when the spectra of all the samples near the base line are enlarged and compared for the 14.0 T and 16.4 T spectra, as shown in figures 3.19 and 3.20, respectively, a remarkable effect of substitution on the spectra is the lowering of the intensity of the signal due to the distorted 4e tetrahedral site (shown by arrows), apart from the changes in the shapes and relative intensities of the peaks from tetrahedral and octahedral coordination environments.

Changes in the NMR lineshapes may arise from a change in the electric field gradient as well as the asymmetry parameters around the probe nucleus Al, when the surrounding nuclei are partially substituted by other elements such as Zn. Therefore, these visible spectral changes cannot give any quantitative information on the changes in the local symmetry environments. To obtain quantitative information about the site population of different coordination environments in the different samples, all the spectra were simulated and the individual lines were obtained by deconvolution of the simulated spectra, using the DMFIT program [26].

The experimental and simulated spectra recorded at 14.0 T and 16.4 T along with the components for $x = 0.4$ are shown in figures 3.21 and 3.22, respectively. The Al-IV, Al-VI-3 and Al-IV-d sites fitted very well to the central transition lineshape of a half-integer spin quadrupolar nucleus defined by a quadrupolar coupling constant $C_q$ and an asymmetry parameter $\eta$. To simulate the lineshapes for the Al-VI-1, Al-VI-2 and Al-V sites, the Czjzek model provided in the DMFIT program was used [26,32]. The NMR spectral parameters for all compositions for the spectra recorded at 14.0 T and 16.4 T are given in table 3.5 and table 3.6, respectively.

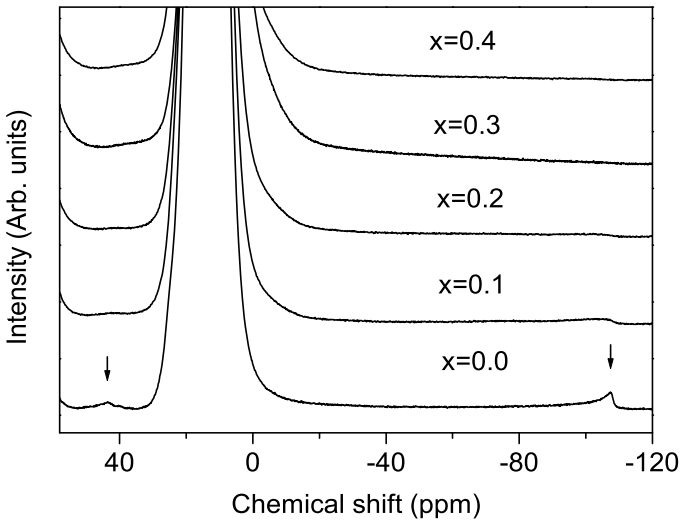


*Figure 3.19: Zoomed view of the $^{27}Al$ MAS NMR spectra of $Sr_{1-x}La_xAl_{12-x}Zn_xO_{19}$ recorded at 14.0 T showing the changes in the intensity of the signal from the distorted tetrahedral site.*

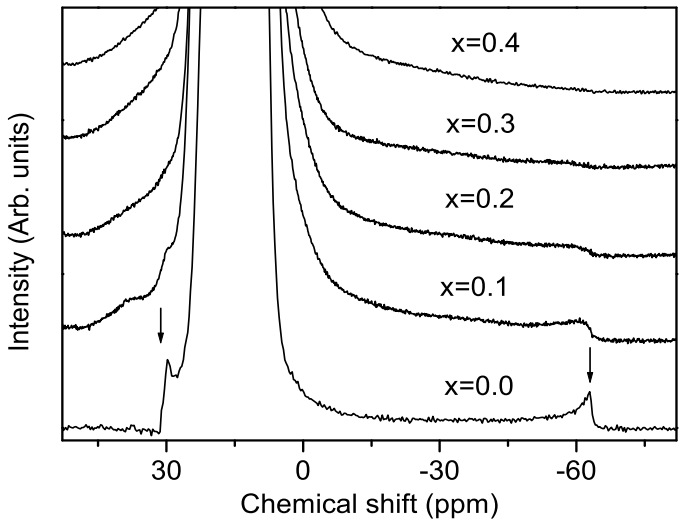


*Figure 3.20: Zoomed view of the $^{27}Al$ MAS NMR spectra of different compositions in $Sr_{1-x}La_xAl_{12-x}Zn_xO_{19}$ recorded at 16.4 T showing the changes in the intensity of the signal from the distorted tetrahedral site.*

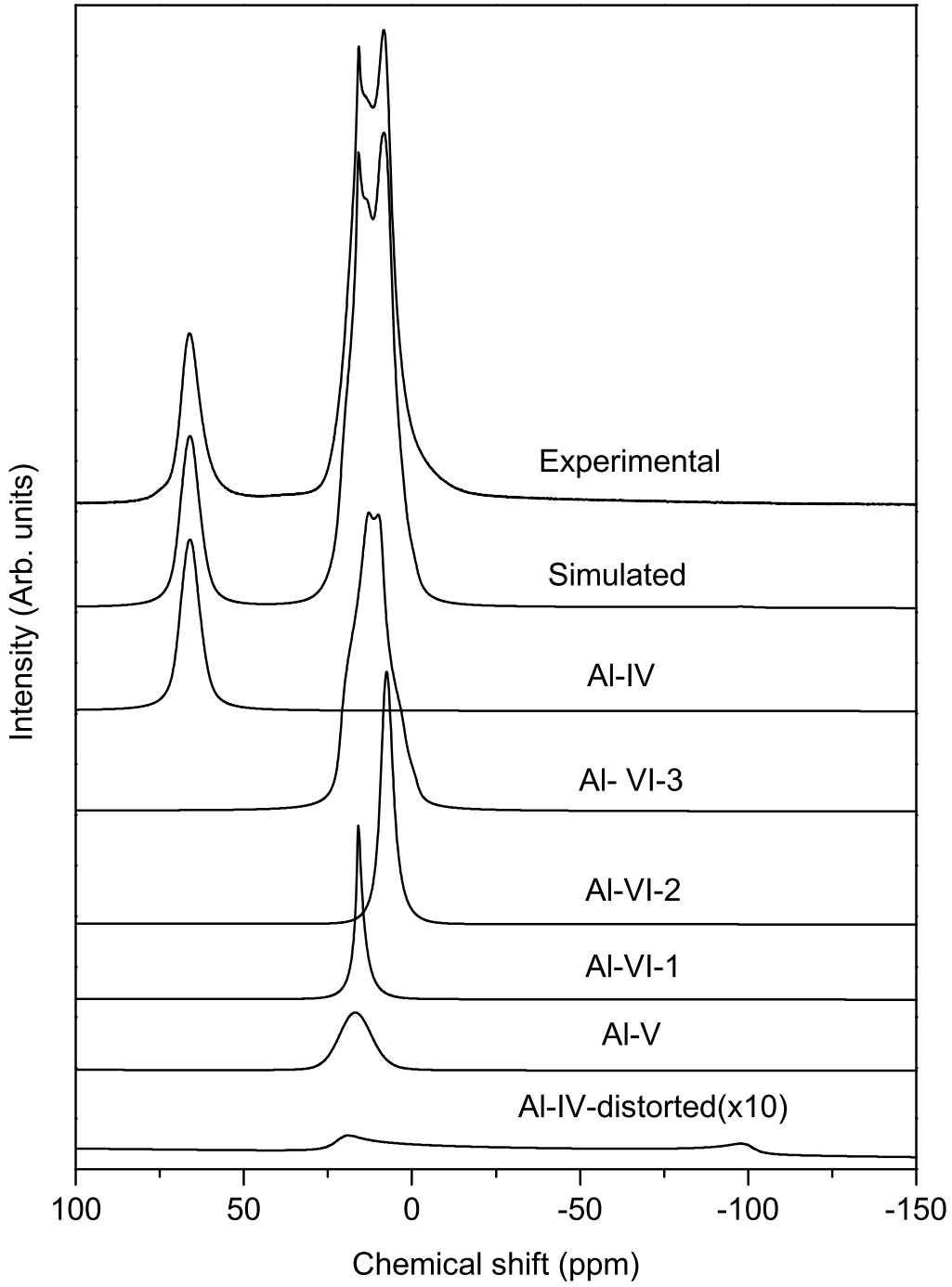


*Figure 3.21: Experimental and simulated $^{27}Al$ MAS NMR spectra along with the individual components of $Sr_{0.6}La_{0.4}Al_{11.6}Zn_{0.4}O_{19}$ recorded at 14.0 T.*

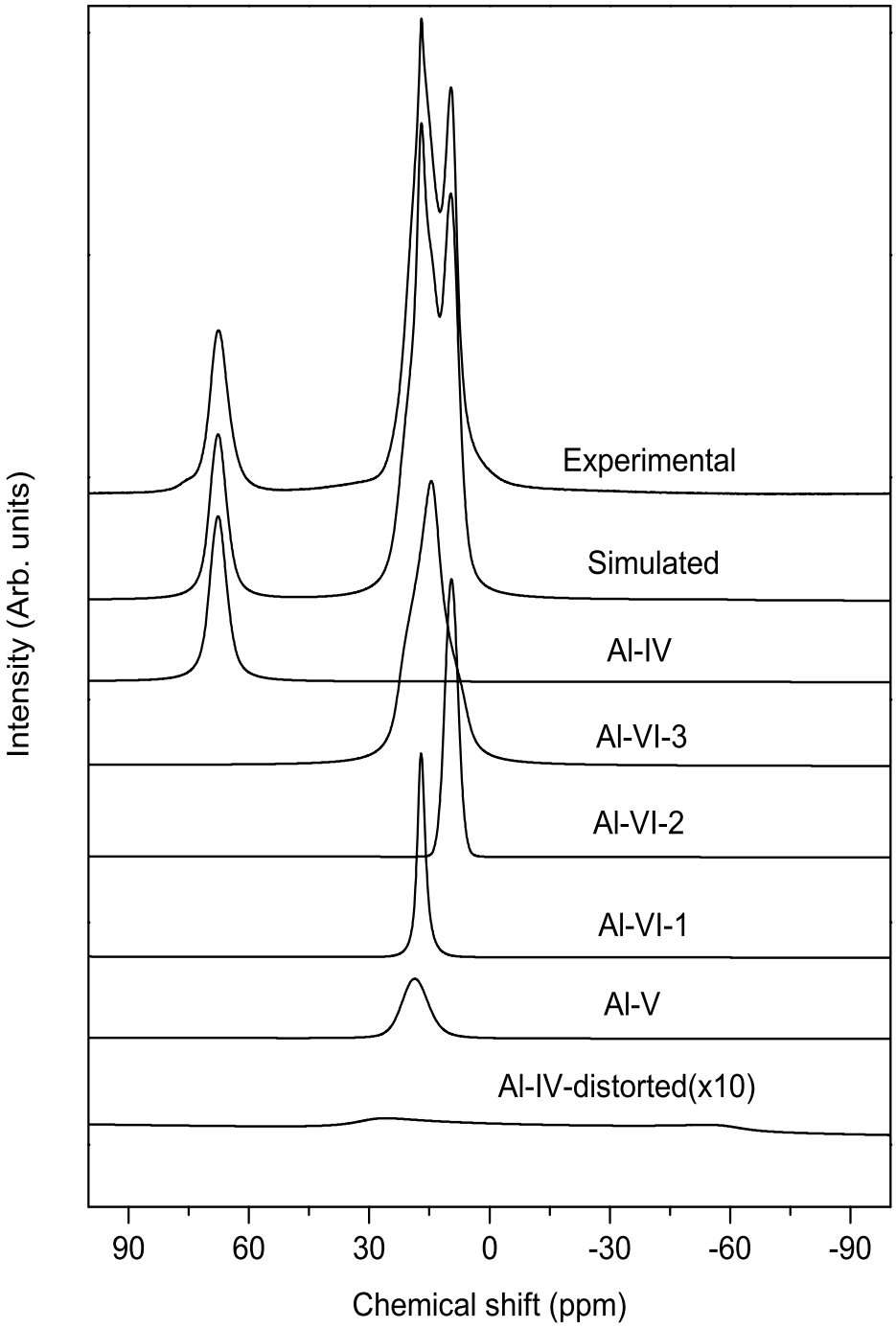


*Figure 3.22: Experimental and simulated $^{27}Al$ MAS NMR spectra along with the individual components of $Sr_{0.6}La_{0.4}Al_{11.6}Zn_{0.4}O_{19}$ recorded at 16.4 T.*

*Table 3.5: $^{27}Al$ MAS NMR parameters of $Sr_{1-x}La_xAl_{12-x}Zn_xO_{19}$ obtained from deconvolution of the spectra recorded at 14.0 T.*

| $\delta_{iso}$ (ppm) | | | | | | $\Delta_{CS}$ (ppm) | | | | | $C_q$ (MHz) | | | | | $\eta$ | | | | |
|---|---|---|---|---|---|---|---|---|---|---|---|---|---|---|---|---|---|---|---|---|
| Al site | x=0 | 0.1 | 0.2 | 0.3 | 0.4 | x=0 | 0.1 | 0.2 | 0.3 | 0.4 | x=0.0 | 0.1 | 0.2 | 0.3 | 0.4 | x=0 | 0.1 | 0.2 | 0.3 | 0.4 |
| IV | 67.65 | 68.82 | 69.25 | 69.85 | 69.69 | - | - | - | - | - | 3.41 | 3.53 | 3.53 | 3.59 | 3.71 | 0.12 | 0.55 | 0.60 | 0.60 | 0.60 |
| VI-1 | 16.9 | 16.86 | 16.83 | 16.92 | 16.1 | 0.3 | 0.38 | 0.70 | 0.40 | 0.30 | 1.06 | 1.04 | 1.08 | 1.48 | 1.54 | - | - | - | - | - |
| VI-2 | 9.55 | 9.56 | 9.30 | 9.27 | 7.89 | 1.85 | 2.95 | 3.35 | 2.40 | 2.40 | 1.49 | 1.37 | 1.34 | 1.47 | 1.46 | - | - | - | - | - |
| V1-3 | 21.85 | 23.67 | 23.10 | 23.10 | 21.50 | - | - | - | - | - | 4.80 | 5.50 | 5.62 | 5.74 | 5.92 | 0.67 | 0.84 | 0.79 | 0.79 | 0.64 |
| V | 17.81 | 18.99 | 18.61 | 18.60 | 17.80 | 1.20 | 2.73 | 6.00 | 7.04 | 9.50 | 2.03 | 1.96 | 1.96 | 1.97 | 1.87 | - | - | - | - | - |
| IV-d | 56.58 | 56.20 | 57.70 | 57.50 | 56.80 | - | - | - | - | - | 20.68 | 20.60 | 20.50 | 20.11 | 20.21 | 0 | 0 | 0 | 0 | 0 |

Al-V, Al-VI-1 and Al-VI-2 were fitted using the Czjzek model [32], where $\delta_{iso}$ is the mean isotropic chemical shift with the chemical shift distribution $\Delta_{CS}$, and $C_q$ is the mean quadrupolar product given by $C_q^* = C_q(1+\eta^{2/3})^{1/2}$.

*Table 3.6: $^{27}Al$ MAS NMR parameters of $Sr_{1-x}La_xAl_{12-x}Zn_xO_{19}$ obtained from deconvolution of the spectra recorded at 16.4 T.*

| $\delta_{iso}$ (ppm) | | | | | | $\Delta_{CS}$ (ppm) | | | | | $C_q$ (MHz) | | | | | $\eta$ | | | | |
|---|---|---|---|---|---|---|---|---|---|---|---|---|---|---|---|---|---|---|---|---|
| Al site | x=0 | 0.1 | 0.2 | 0.3 | 0.4 | x=0 | 0.1 | 0.2 | 0.3 | 0.4 | x=0 | 0.1 | 0.2 | 0.3 | 0.4 | x=0 | 0.1 | 0.2 | 0.3 | 0.4 |
| IV | 68.00 | 68.54 | 69.55 | 70.28 | 70.23 | - | - | - | - | - | 3.56 | 3.51 | 3.62 | 3.49 | 3.59 | 0.10 | 0.52 | 0.80 | 0.90 | 0.61 |
| VI-1 | 17.17 | 17.20 | 17.20 | 17.58 | 17.28 | 0.20 | 0.57 | 0.83 | 1.20 | 1.30 | 1.31 | 1.31 | 1.31 | 1.31 | 1.31 | - | - | - | - | - |
| VI-2 | 9.70 | 9.61 | 9.52 | 9.90 | 9.67 | 1.30 | 2.20 | 2.90 | 3.10 | 3.45 | 1.25 | 1.21 | 1.03 | 0.98 | 0.92 | - | - | - | - | - |
| V1-3 | 22.70 | 22.30 | 22.50 | 22.70 | 22.60 | - | - | - | - | - | 4.59 | 4.88 | 5.21 | 5.41 | 5.76 | 0.93 | 0.93 | 0.93 | 0.93 | 0.93 |
| V | 18.00 | 18.20 | 18.30 | 19.90 | 19.55 | 1.00 | 5.50 | 6.00 | 6.50 | 6.00 | 2.03 | 1.96 | 1.96 | 1.97 | 1.87 | - | - | - | - | - |
| IV-d | 57.80 | 56.50 | 56.50 | 56.00 | 56.00 | - | - | - | - | - | 20.67 | 20.46 | 20.40 | 20.31 | 20.23 | 0 | 0 | 0 | 0 | 0 |

Al-V, Al-VI-1 and Al-VI-2 were fitted using the Czjzek model [32], where $\delta_{iso}$ is the mean isotropic chemical shift with the chemical shift distribution $\Delta_{CS}$, and $C_q$ is the mean quadrupolar product given by $C_q^* = C_q(1+\eta^{2/3})^{1/2}$.

In the case of the spectra recorded at 14.0 T, for the Al-VI-3 (distorted octahedron, 12k site, $C_s$ symmetry) peak, a change in the lineshape is observed, and the $C_q$ has increased from 4.8 MHz for $x = 0$ to 5.9 MHz for $x = 0.4$, while the $\eta$ value remains almost the same ($\sim$0.6). For the Al-VI-2 peak (antiprism, $4f_2$ site, $C_{3v}$ symmetry), $C_q$ remains almost the same and therefore there is not much difference in the lineshape with increasing $x$. For the Al-VI-1 site (regular octahedron, 2a site, $D_{3d}$ symmetry), $C_q$ has increased from 1.06 to 1.54 MHz, which causes a broadening of the peak. For the Al-IV site, there is an increase in $C_q$ as well as $\eta$, where $C_q$ changes from 3.41 to 3.71 MHz and $\eta$ changes from 0.12 to 0.6 which causes a change in the lineshape. For the Al-V site, which is fitting to the Czjzek model [32], the change in the lineshape is due to the increase in the chemical shift distribution $\Delta_{CS}$ from 1.2 to 9.5 ppm. For this peak, change in the $C_q$ is from 2.03 to 1.87 MHz which is not responsible for the change in the lineshape. The intensity of the distorted Al-IV peak has decreased considerably, which is likely to be due to the decrease in the site population. The $C_q$ value has decreased from 20.68 to 20.21 MHz which did not cause a significant change in the lineshape.

Similar results are obtained from the deconvolution of the spectra recorded at 16.4 T as given in table 3.6. For the Al-VI-3 peak, a change in the lineshape is observed along with an increase in the value of $C_q$ from 4.59 MHz for $x = 0$ to 5.76 MHz for $x = 0.4$ and the value of $\eta$ remains the same as 0.93. However, there are some minor changes in the parameters compared to the 14.0 T spectral parameters which may be arising from the difference in the field strengths and spinning speeds.

The site occupancies are obtained after deconvolution of the simulated spectrum and the values are corrected according to the procedure given by Massiot et al. as described in section 2.3.2.6. [26]. The occupancies are also corrected for the degree of substitution. The corrected intensities for the different Al sites from the spectra recorded at 14 and 16.4 T are given in table 3.7.

*Table 3.7: The occupancies at various sites for $Sr_{1-x}La_xAl_{12-x}Zn_xO_{19}$ calculated from the NMR spectra.*

| Field (T) | Al site | Wyckoff position | [a]Expected occupancy (%) | Calculated occupancy (%) $x$=0 | 0.1 | 0.2 | 0.3 | 0.4 | [b]Maximum change of occupancy (%) |
|---|---|---|---|---|---|---|---|---|---|
| | IV | $4f_1$ | 16.67 | 16.47 | 16.39 | 16.04 | 15.91 | 16.21 | -3.4 |
| | VI-1 | 2a | 8.33 | 8.46 | 7.90 | 7.43 | 7.20 | 6.84 | -19.1 |
| | VI-2 | $4f_2$ | 16.67 | 16.13 | 15.45 | 15.04 | 14.80 | 14.23 | -11.8 |
| 14 | VI-3 | 12k | 50 | 49.85 | 49.86 | 50.61 | 50.29 | 50.06 | +1.5 |
| | V | 2b | 8.33/0 | 3.66 | 5.47 | 6.3 | 7.35 | 7.64 | +108.7 |
| | IV-d | 4e | 0/8.33 | 5.43 | 3.55 | 2.78 | 1.95 | 1.69 | -68.9 |
| | V + IV-d | 2b+4e | 8.33 | 9.09 | 9.02 | 9.21 | 9.30 | 9.30 | +2.6 |
| | IV | $4f_1$ | 16.67 | 16.38 | 16.06 | 15.91 | 15.90 | 15.84 | -3.3 |
| | VI-1 | 2a | 8.33 | 8.85 | 8.38 | 8.41 | 8.30 | 8.24 | -6.9 |
| | VI-2 | $4f_2$ | 16.67 | 15.37 | 15.30 | 15.0 | 14.22 | 14.66 | -7.5 |
| 16.4 | VI-3 | 12k | 50 | 50.34 | 51.02 | 50.87 | 52.21 | 51.88 | +3.7 |
| | V | 2b | 8.33/0 | 3.69 | 6.48 | 7.2 | 7.42 | 7.62 | +106.5 |
| | IV-d | 4e | 0/8.33 | 5.37 | 2.76 | 2.61 | 1.95 | 1.76 | -67.21 |
| | V + IV-d | 2b+4e | 8.33 | 9.06 | 9.24 | 9.31 | 9.37 | 9.38 | +3.4 |

[a]For the unsubstituted composition ($x = 0$)

[b]With respect to the calculated value for $x = 0$

The expected occupancy is the theoretically predicted occupancy for the different sites for the unsubstituted composition ($x = 0$). The maximum percentage changes in all the site occupancies are estimated with respect to the calculated values for $x = 0$ at the corresponding sites. From table 3.7, it is seen that some differences are observed between the expected and calculated site occupancies at the different sites for $x = 0$. For example, a difference of 3.4% (16.47 against 16.67) is observed between the calculated and expected site occupancy for the $4f_1$ site. Hence, the maximum change of 3.4% for the $4f_1$ site and below for other sites (1.5% for 12k and 2.6% for 2b+4e sites) is considered as the error in the fitting procedure. Since the percentage change in the site occupancy at the 2a and $4f_2$ sites is much larger than the 3.4% error limit considered, and also the Al occupancies in these two sites decrease monotonically as the amount of substituted Zn is increased, it is clear that the Zn ions occupy the 2a and $4f_2$ Al sites. This result is in accordance with the Mössbauer and Fe NMR studies on La-Co substituted strontium ferrite [13–17]. However, an important observation is that in addition to the changes in the occupancy at the 2a and $4f_2$ sites, the Al occupancy at the penta-coordinated site has increased with a corresponding decrease in the occupancy at the distorted tetrahedral site, with increasing degree of substitution. Moreover, the sum of the occupancies at the distorted tetrahedral and penta coordinated sites remain almost the same (maximum error of 2.6%), showing clearly that Zn ions are not occupied in the trigonal bipyramidal (2b) or the distorted tetrahedral (4e) sites. Similar results are obtained from the spectra recorded at 16.4 T also. From table 3.7, a maximum change of 3.3% is observed between the calculated and expected site occupancy for the $4f_1$ site and 3.7% for the VI-3 site. Thus, considering the error limit as 3.7%, large changes in the occupancies are observed at the 2a and $4f_2$ sites. Similarly, the occupancy at the bipyramidal site increases at the expense of the occupancy at the distorted tetrahedral sites.

A graph showing the variation of the quadrupolar coupling constant, $C_q$, with $x$ for the spectra recorded at 14.0 T is shown in figure 3.23. $C_q$ is a measure of the symmetry environment of the corresponding sites for a particular coordination. A

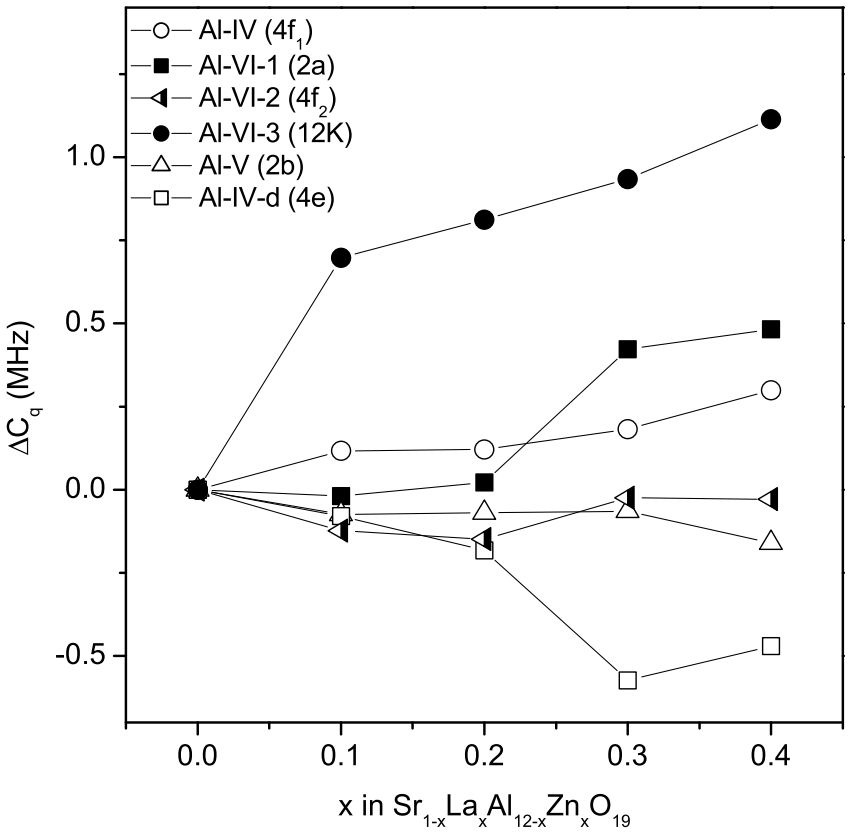


*Figure 3.23: Variation of the $C_q$ ($\Delta C_q$ = $C_q(x)$ - $C_q(x=0)$) for different sites as a function of $x$ in $Sr_{1-x}La_xAl_{12-x}Zn_xO_{19}$, from the spectra recorded at 14.0 T.*

large increase in the value of $C_q$ is observed for the 12k site for $x = 0.1$ and $\Delta C_q$ linearly increases further with increasing $x$. Since the Al occupancy at the 12k is not changed after substitution by Zn, the large increase in the value of $C_q$ is likely to be due to the increasing distortions caused by the Zn ions occupying the neighboring 2a and $4f_2$ sites, similar to that observed from Mössbauer spectroscopic studies on La-Co substituted strontium ferrite [9]. Similarly, $C_q$ has not changed much for the tetrahedral ($4f_1$) as well as the distorted tetrahedral (4e) sites. On the other hand, a positive jump in the value of $C_q$ is observed for the 2a and $4f_2$ sites between $x = 0.2$ and 0.3, the two sites showing changes in the Al site occupancies. The increased values of $C_q$ correspond to increased distortion of these sites. There is a corresponding negative jump in the value of $C_q$ for the 4e site also indicating

decreasing distortion. This implies stabilization of the penta-coordinated 2b sites from the distorted tetrahedral sites. The variation of $C_q$ for different sites shows that there is a considerable change in the parameter for $x > 0.2$. This means that the distortion to the particular coordination environment is minimum up to the level of substitution of $x = 0.2$ and major distortions take place above this level of substitution. The results also show that out of 2a and $4f_2$ sites, which are the sites of substitution of Al by Zn, the undistorted octahedral site 2a is not much distorted compared to the $4f_2$ site, up to $x = 0.2$, as evidenced from the changes in the quadrupolar coupling constant parameter. Above $x = 0.2$, the 2a site is considerably distorted compared to the $4f_2$ site.

### 3.5.3 Summary

The present $^{27}$Al solid-state NMR studies on La-Zn substituted hexagonal strontium aluminate, $Sr_{1-x}La_xAl_{12-x}Zn_xO_{19}$, show that the sites of substitution of Zn are the same as that reported for La-Co substituted hexagonal strontium ferrite from Mössbauer spectroscopic studies. Also, from the present NMR studies, evidence for larger distortions to the octahedral coordination environments is observed for $x > 0.2$, the composition corresponding to the maximum magnetic performance parameters in the case of La-Co and La-Zn substituted hexagonal strontium ferrite. Evidence is also obtained for the stabilization of the penta-coordinated sites over the distorted tetrahedral sites on substitution, which could be an additional reason behind the increased magnetic performance of the substituted ferrites.

## 3.6 Conclusions

$^{27}$Al solid-state NMR studies on the same sample of $SrAl_{12}O_{19}$, at both low- and high fields, indicated the presence of Al at both the distorted tetra coordinated and the penta coordinated Al sites. Rietveld refinement analysis of the XRD patterns of the strontium aluminate sample gave indication for a possible two-phase

model and based on the results, it is concluded that a structural model, where two phases co-exist simultaneously, one with the central atom model and another with the split atom model, is the best possible structure. The NMR studies on La-Zn substituted hexagonal strontium aluminate, $Sr_{1-x}La_xAl_{12-x}Zn_xO_{19}$, again confirmed the presence of distorted tetrahedral and penta coordinated Al sites in the structure. The sites of substitution of Zn ions in strontium aluminate are the same 2a and $4f_2$ octahedral sites as that reported for La-Co substituted hexagonal strontium ferrite from Mössbauer spectroscopic studies. However in addition to this, evidence is obtained for the stabilization of the penta-coordinated sites over the distorted tetrahedral sites on substitution, which could be the actual cause behind the increased magnetic performance of the isostructural substituted ferrites.

# Bibliography


[1] R. Collongues, D. Gourier, A. Kahn-Harari, A. M. Lejus, J. Thery and D. Vivien, *Ann. Rev. Mater. Sci.* 1990, 20, 51-82.

[2] Z. Jin, W. Tang, J. Zhang, H. Lin and Y. Du, *J. Magn. Magn. Mater.* 1998 182, 231-237.

[3] X. Li, G. Lu, and S. Li, *J. Mater. Sci. Lett.* 1996, 15, 397-399.

[4] B. Kaur, M. Bhat, F. Licci, R. Kumar, S. D. Kulkarni, P. A. Joy, K. K. Bamzai, and P. N. Kotru, *J. Magn. Magn. Mater.* 2006, 305, 392-402.

[5] J. M. D. Coey, *Magnetism and Magnetic Materials* (Cambridge University Press, UK, 2010).

[6] E.T. Lacheisserie, D. Gignoux, M.Schlenker, *Magnetism: Materials and Applications* (Springer, USA, 2003).

[7] F. Kools, A. Morel, R. Grossinger, J. M. Le Breton, and P. Tenaud, *J. Magn. Magn. Mater.* 2002, 242, 1270-1276.

[8] K. Iida, Y. Minachi, K. Masuzawa, M. Kawakami, H. Nishio, and H. Taguchi, *J. Magn. Soc. Jpn.* 1999, 23, 1093-1096.

[9] J. C. Corral-Huacuz and G. Mendoza-Suarez, *J. Magn. Magn. Mater.* 2002, 242, 430-433.

[10] J. Bai, X. Liu, T. Xie, F. Wei, and Z. Yang, *Mater. Sci. Eng.: B* 2000, 68, 182-185.

[11] L. You, L. Qiao, J. Zheng, M. Jiang, L. Jiang, and J. Sheng, *J. Rare Earth* 2008, 26, 81-84.

[12] R. D. Shannon, *Acta Cryst. A* 1976, 32, 751-767.

[13] L. Lechevallier and J. M. Le Breton, *J. Magn. Magn. Mater.* 2005, 290, 1237-1239.

[14] G. Wiesinger, M. Mller, R. Grssinger, M. Pieper, A. Morel, F. Kools, P. Tenaud, J. M. Le Breton, and J. Kreisel, *phys. status solidi (a)* 2002, 189, 499-508.

[15] A. Morel, J. M. Le Breton, J. Kreisel, G. Wiesinger, F. Kools, and P. Tenaud, *J. Magn. Magn. Mater.* 2002, 242, 1405-1407.

[16] L. Lechevallier, J. M. Le Breton, J. Teillet, A. Morel, F. Kools, and P. Tenaud, *Physica B.* 2003, 327, 135-139.

[17] L. Lechevallier, J. M. Le Breton, J. F. Wang, and I. R. Harris, *J. Phys.: Condens. Matter.* 2004, 16, 5359-5376.

[18] D. H. Choi, S. W. Lee, I.-B. Shim, and C. S. Kim, *J. Magn. Magn. Mater.* 2006, 304, e243-e245.

[19] M. W. Pieper, A. Morel, and F. Kools, *J. Magn. Magn. Mater.* 2002, 242, 1408-1410.

[20] M. W. Pieper, F. Kools, and A. Morel, *Phys. Rev. B* 2002, 65, 184402.1-5.

[21] S. W. Lee, S. Y. An, I.-B. Shim, and C. S. Kim, *J. Magn. Magn. Mater.* 2005, 290, 231-233.

[22] A. Ghasemi and V. Sepelak, *J. Magn. Magn. Mater.* 2011, 323, 1727-1733.

[23] B. Baby, K. K. Dey, T. G. Ajithkumar and P. A. Joy, *J. Am. Ceram. Soc.* 2014, 97, 2990-2995.

[24] K. Harindranath, K. A. Viswanath, C. V. Chandran, T. Bräuniger, P. K. Madhu, T. G. Ajithkumar, and P. A. Joy, *Solid State Commun.* 2010, 150, 262-266.

[25] Y. Xu, W. Peng, S. Wang, X. Xiang, and P. Lu, *Mater. Sci. Eng. B* 2005, 123, 139-142.

[26] D. Massiot, F. Fayon, M. Capron, I. King, S. Le Calvé, B. Alonso, J.-O. Durand, B. Bujoli, Z. Gan and G. Hoatson, *Magn. Reson. Chem.* 2002, 40, 70-76.

[27] D. Massiot, C. Bessada, J. P. Coutures, and F. Taulelle, *J. Magn. Reson.* 1990, 90, 231-242.

[28] K. Kimura, M. Ohgaki, K. Tanaka, H. Morikawa and F. Marumo, *J. Solid State Chem.* 1990, 87, 186-194.

[29] Powder Cell for Windows. The software is freely available from http://www.ccp14.ac.uk.

[30] S. R. Jansen, H. T. Hintzen, R. Metselaar, J. W. de Haan, L. J. M. van de Ven, A. P. M. Kentgens, and G. H. Nachtegaal, *J. Phys. Chem. B* 1998, 102, 5969-5976.

[31] L.S. Du and J. F. Stebbins, *J. Phys. Chem. B* 2004, 108, 3681-3685.

[32] G. Czjzek, J. Fink, F. Gätz, H. Schmidt, J. M. D. Coey, J. P. Rebouillat and A. Lionard, *Phys. Rev. B* 1981, 23, 2513-2530.

# Chapter 4

# Studies on $LaAlO_3$

## 4.1 Introduction

$LaAlO_3$, is an important ceramic material with many applications [1–5]. As discussed in chapter 1 (section 1.6.2), the crystal structure of $LaAlO_3$ is rhombohedral perovskite with distorted $AlO_6$ octahedra and $LaO_{12}$ dodecahedra [6]. However, there has been an uncertainty about the correct space group of $LaAlO_3$ as $R\overline{3}m$ or $R\overline{3}c$ [7–9]. The different space groups proposed for this system are due to the uncertainty in the local symmetry environments. It is very difficult to derive information on the correct space group from X-ray diffraction technique, as the patterns are almost identical for the proposed space groups, and the only difference being the minor variation of the intensity of the peaks arising from the similar reflection conditions for the two space groups discussed above. At present, $LaAlO_3$ is believed to have a space group $R\overline{3}c$ with only one octahedral Al site. However, in a recent study on $LaAlO_3$, using resonant Raman spectroscopy [10], a weak Raman band around 120 $cm^{-1}$ was observed below 240 K for the 488 nm excitation wavelength and this band became stronger as the temperature was lowered. This is attributed to the breakdown of local symmetry at low temperatures and it is proposed that this is possible only if there are two Al coordination environments. The space group $R\overline{3}c$ cannot account for the two different coordinations, and therefore R3c or $R\overline{3}$ is proposed as the possible space group of this material.

The crystal structure is known to play a very crucial role in determining the physical properties of perovskite type oxides [11]. Any minor changes in the structure is likely to affect the physical properties considerably. In many cases, minor structural variations or marginal breakdown of the local symmetry cannot be detected by diffraction experiments. However, solid-state NMR can be used to probe the local symmetry and the local coordination environments since it is possible to probe the nuclei which extends over several coordination spheres [12]. Previous SSNMR studies on $LaAlO_3$ indicated a very low quadrupolar coupling constant ($C_q$) of 150 kHz [8,13–16]. In general, the quadrupolar coupling constant gives an indication of the distortion of the coordination polyhedra. The unusually low value of $C_q$ observed for Al in $LaAlO_3$, compared to the high values ($> 600$ kHz)

reported for octahedrally coordinated Al in other materials such as different forms of alumina, aluminosilicates and calcium aluminates, and $AlO_6$ in structures such as magnetoplumbites, spinels, garnets and the layered perovskites, [12,17–23] has been attributed to the near-cubic local symmetry [15].

The main objective of the work reported in this chapter is a detailed study of the coordination environment of Al in $LaAlO_3$ using $^{27}Al$ solid-state NMR (SSNMR). Static and magic angle spinning (MAS) NMR studies have been carried out below and above room temperature to get detailed information and the results are compared with the structural information obtained from Rietveld analysis of the powder XRD patterns, so as to get information on the possible space group. Second harmonic generation experiment has been carried out to investigate if the material possesses a center of inversion.

## 4.2 Synthesis

Lanthanum aluminate was prepared using a reverse co-precipitation method as reported previously [24]. A mixed water solution of 3.90 g of lanthanum nitrate (Aldrich) and 3.38 g of aluminium nitrate (sd fine chemicals) taken in the 1:1 molar ratio was dropped into a dilute ammonia solution of pH $\sim$ 9. The precipitate formed was filtered and washed several times with distilled water and finally dried in an oven. The dried powder was then precalcined at 700 °C for two hours and then calcined at 1400 °C for 6 hours for the complete phase formation.

## 4.3 NMR methodology

High-resolution $^{27}Al$ solid-state magic angle spinning (MAS) NMR at room temperature and high temperatures and static variable temperature NMR experiments were carried out on a Bruker AV-300 ($\nu_{Al}$ = 78.2 MHz) spectrometer equipped with a 7.05 T magnet using 4 mm probe head. $^{27}Al$ solid-state MAS NMR experiments were carried out at the magic angle spinning speed of 10 kHz and with a short pulse duration 3 $\mu$s. 200 scans were collected with a recycle delay of 20 s.

The 3-quantum magic angle spinning (3QMAS) experiment was carried out using a standard Z-filter pulse sequence on the AV-300 spectrometer. The experiment was optimized at a spinning rate of 10 kHz with the excitation and conversion pulses as 5.8 and 2.2 $\mu$s, respectively with a RF field strength of 90 kHz. . The selective 90° Z-filter pulse was set as 25 $\mu$s at an RF field strength of 4 kHz. A recycle delay of 10 s was used for the experiment. The high temperature MAS experiments were carried out at a spinning speed of 8 kHz. The variable temperature static $^{27}$Al NMR experiments were done with a short pulse of 0.35 s and a total of 1,000 scans were collected with a recycle delay of 1 s between the scans.

$^{139}$La MAS NMR experiments were carried out on a Bruker AV-300 spectrometer equipped with a 4 mm probe and on Bruker AV-700 spectrometer equipped with a 16.4 T magnet using 1.3 mm probe head. The samples were spun at 12.5 and 60 kHz on AV-300 and AV-700 spectrometers, respectively. The quantitative MAS NMR spectra were recorded using a pulse width of 0.4 s and 10,000 scans were acquired with a recycle delay of 1 s on AV-300. Similarly, the spectra were recorded using a pulse width of 1 $\mu$s and 8,000 scans were acquired with a recycle delay of 0.25 s on AV-700.

## 4.4 XRD studies

The synthesized lanthanum aluminate powder was first characterized using powder X-ray diffraction studies. The experimental and simulated XRD pattern of lanthanum aluminate, simulated using the PCW software [26], are shown in figure 4.1. The XRD pattern is simulated with the hexagonal lattice parameters $a$ = 5.3647 Å and $c$ = 13.1114 Å reported for the material in the literature and using the space group R$\overline{3}$c [25]. The positions and intensities of the different peaks observed in the experimental XRD pattern are comparable with that in the simulated pattern. There are no additional peaks in the XRD pattern, indicating the absence of any impurities in the sample, confirming the single phase nature of the synthesized sample.

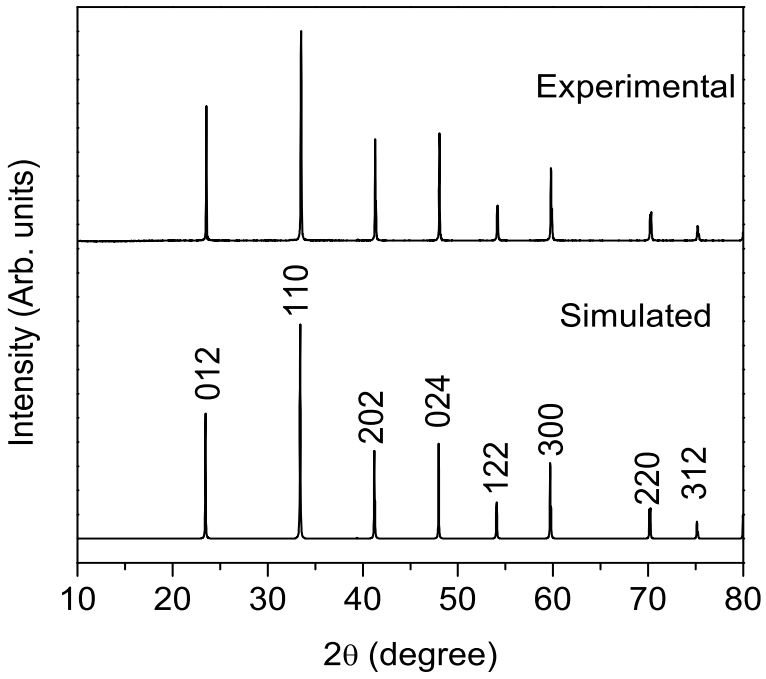


*Figure 4.1: Experimental and simulated XRD patterns of $LaAlO_3$.*

Since three space groups are proposed for $LaAlO_3$, Rietveld refinement studies have been carried out with the space groups $R\bar{3}$, R3c and $R\bar{3}c$. However, refinement of the XRD pattern using the $R\bar{3}$ space group did not give a good fit because of the differences in the relative intensities of the peaks in the experimental and simulated patterns. The experimental as well as the calculated powder XRD patterns, using the space groups R3c and $R\overline{3}c$, are shown in figures 4.2 and 4.3, respectively. Rietveld refinement analysis shows that the experimental XRD pattern fits reasonably well with both R3c and $R\overline{3}c$ structure models. The zoomed view of the (024) peak is shown in figure 4.4. The parameters which indicate the goodness of the fit, $\chi^2$ and the R-factors, and the refined lattice parameters are given in table 4.1. Both the space groups give similar R-factors, because of which it is very difficult to distinguish between the two space groups. However, $\chi^2$ is relatively lower for the R3c space group. All the Al-O bond lengths are equal to 1.899 Å for $R\overline{3}c$. For the structure with space group R3c, there are distorted $AlO_6$ octahedra where distortion involves a polar distribution of oxygen atoms

*Table 4.1: Rietveld refinement parameters of $LaAlO_3$ from XRD patterns recorded at different temperatures.*

| Temperature (K) | Space group | $\chi^2$ | $R_{wp}$ | $R_{F^2}$ | $a$ (Å) | $c$ (Å) |
|---|---|---|---|---|---|---|
| 298 (RT) | R3c | 2.146 | 0.0509 | 0.0218 | 5.3640 | 13.1107 |
| | R$\overline{3}$c | 2.148 | 0.0509 | 0.0219 | 5.3640 | 13.1106 |
| 198 | R3c | 2.190 | 0.0814 | 0.0482 | 5.3574 | 13.0974 |
| | R$\overline{3}$c | 2.436 | 0.0858 | 0.0467 | 5.3567 | 13.0949 |
| 123 | R3c | 2.301 | 0.0830 | 0.0512 | 5.3568 | 13.0917 |
| | R$\overline{3}$c | 2.184 | 0.0808 | 0.0410 | 5.3499 | 13.0749 |

with triangular faces of unequal size. The Al-O bond lengths obtained from the structure for the R3c space group are 1.863 Å for three Al-O bonds and 1.936 Å for the other three Al-O bonds in the $AlO_6$ octahedra. Such a difference in the bond lengths during the rotation of the octahedra can cause a slight displacement of Al or La atoms from the centre of symmetry resulting in the space group R3c instead of R$\overline{3}$c. But if the shift of Al atoms from the centre of inversion is very small, then the non-centrosymmetric structure R3c differs only marginally from the centrosymmetric R$\overline{3}$c structure. This is the probable reason why the X-ray diffraction experiments are not able to detect the lowering of the symmetry.

In order to verify whether the local breakdown in the symmetry is arising from temperature induced phase transitions, the powder XRD patterns were recorded at lower temperatures. The XRD patterns recorded at the temperatures, 298 K (room temperature), 198 K and 123 K are compared in figure 4.5.

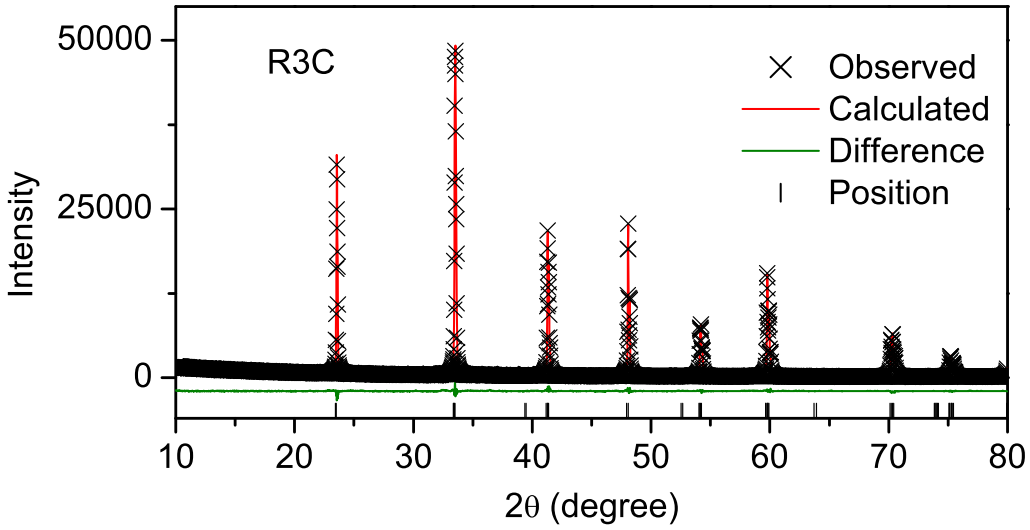


*Figure 4.2: Result of the Rietveld refinement of the XRD pattern of $LaAlO_3$ at room temperature using the space group R3c.*

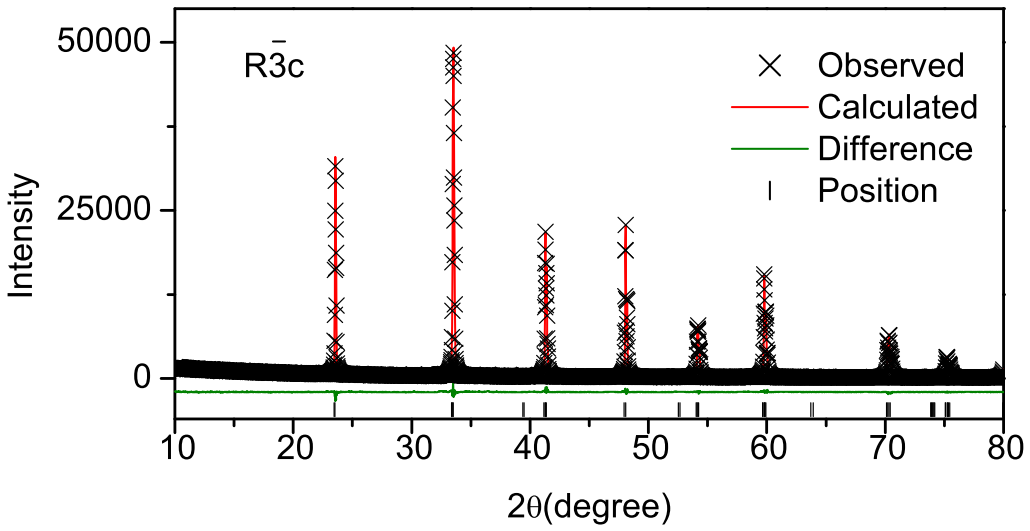


*Figure 4.3: Result of the Rietveld refinement of the XRD pattern of $LaAlO_3$ at room temperature using the space group $R\bar{3}c$.*

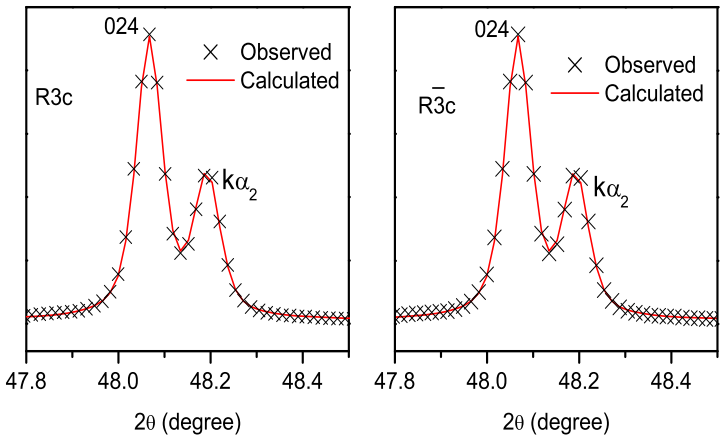


*Figure 4.4: Zoomed view of the (024) peak from the refinement of the XRD pattern of $LaAlO_3$ using the space groups R3c and R$\bar{3}$c. The doublet is due to the $K_{\alpha_1}$ and $K_{\alpha_2}$ components.*

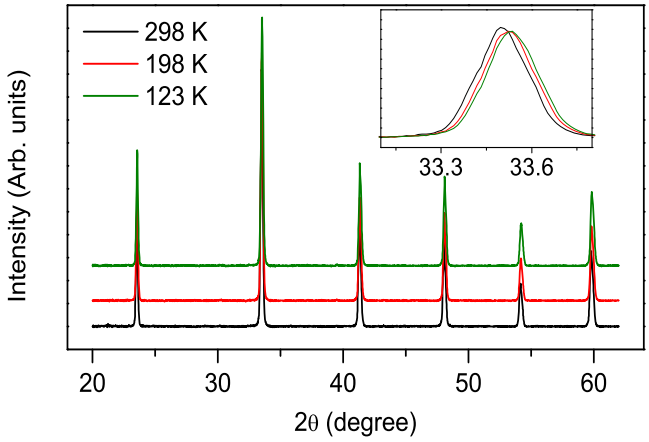


*Figure 4.5: Comparison of the XRD patterns of $LaAlO_3$ recorded at and below room temperature.*

The peaks in the XRD pattern is shifted slightly to higher angles as the temperature is decreased (the major peak at 33.4° is shown in the inset of the figure), which indicates a dependence of the lattice parameters of $LaAlO_3$ on temperature, as observed from the neutron diffraction study by Heyverd et al [27]. The

difference in the lattice parameters could be due to lattice contraction, or due to a change in the space group of lanthanum aluminate as observed from the Raman spectral studies [10]. In order to verify this, Rietveld refinement analysis of the low-temperature XRD patterns was carried out using the space groups R$\bar{3}$c and R3c. The refinement plots for the pattern recorded at 123 K are shown in figures 4.6 and 4.7. The refinement parameters are given in table 4.1.

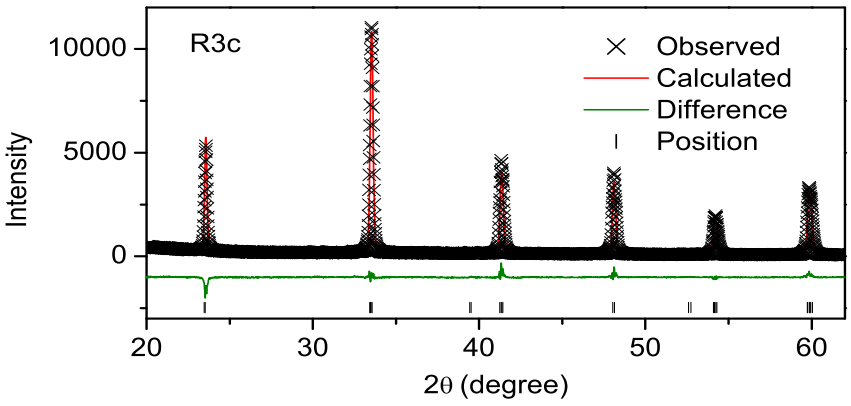


*Figure 4.6: Result of the Rietveld refinement of the XRD pattern of $LaAlO_3$ at 123 K using the space group R3c.*

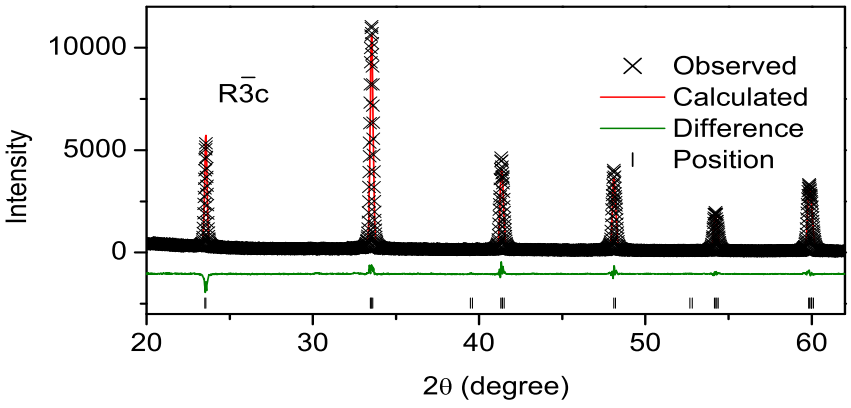


*Figure 4.7: Result of the Rietveld refinement of the XRD pattern of $LaAlO_3$ at 123 K using the space group R$\bar{3}$c.*

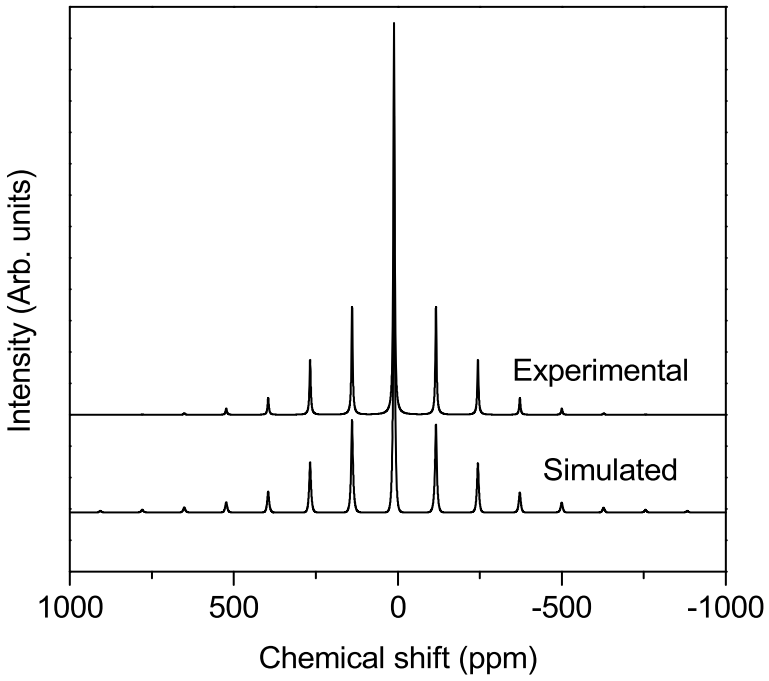


*Figure 4.8: Experimental and simulated $^{27}Al$ MAS NMR spectra of $LaAlO_3$ recorded at 7.05 T.*

Interestingly, at room temperature and at 198 K, using R3c space group gives a lower $\chi^2$ value compared to the R$\bar{3}$c space group. In contrast to this, for the pattern recorded at 123 K, lower values are obtained for the best fit parameters using the space group R$\bar{3}$c, indicating that the correct space group of the material at room temperature may be R3c and that there may be a temperature induced phase transition in the material as suggested from the Raman spectroscopic studies [10].

## 4.5 $^{27}$Al NMR

The $^{27}$Al MAS NMR spectrum of $LaAlO_3$ recorded at the field 7.05 T (300 MHz) at a spinning speed of 10 kHz is shown in figure 4.8. The spectrum shows a single peak at a chemical shift of 11.7 ppm, with the sidebands occurring at multiples of the spinning speed, confirming the presence of an octahedral site, and consistent with the earlier reports [8,13–16].

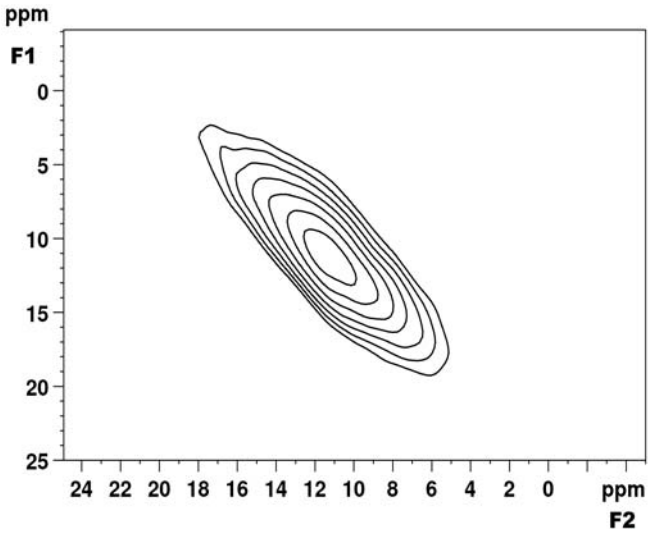


*Figure 4.9: $^{27}Al$ 3QMAS NMR spectra of lanthanum aluminate recorded at 7.05 T.*

The main objective of this NMR study is to characterize the coordination environment of Al so as to provide fresh insights into the correct space group of this material. Since the Raman spectral studies suggested the possibility of two different Al sites in lanthanum aluminate [10], the two dimensional MQMAS experiment was carried out to verify if two Al sites are present. A good MQMAS spectrum is obtained only at the low field of 7.05 T, which showed the presence of a single site with very low $C_q$. The center of gravities of the contour are coinciding at around 11.2 ppm in both the F1 and F2 dimensions in the MQMAS spectra indicating the very low quadrupole coupling constant. If the $C_q$ is more, the center of gravity in the F1 dimension will shift downwards, suggesting a quadrupole induced shift. Previous solid-state NMR studies on $LaAlO_3$ also showed a very low quadrupole coupling constant of 150 kHz [13–16].

In order to obtain the NMR parameters, the experimental MAS NMR spectrum was simulated with the DMFIT program [28]. Since the quadrupole coupling constant of $LaAlO_3$ is very small, only the first order effects of quadrupolar interactions needs to be considered for simulating the SSNMR spectrum which is already incorporated in the DMFIT program [28]. The experimental and simulated NMR spectra showing the full sideband profile recorded at a spinning speed

of 10 kHz are shown in figure 4.8.

From the simulation of the NMR spectrum, the spectral parameters for lanthanum aluminate are obtained as the isotropic chemical shift, $\delta_{iso} = 11.58$ ppm, and the quadrupole coupling constant, $C_q = 150$ kHz, which are in close agreement with the values reported in the literature [8,13–16]. This very low value of $C_q$, compared to the values reported for octahedral Al site in different materials ($> 600$ kHz) [12,17–23] is attributed to the near-cubic symmetry of the Al site [15]. Similar low value for Cq ($\sim 360$ kHz) has been reported for ettringite, the initial hydration product of the calcium aluminates in Portland cements, and is attributed to equivalent, octahedrally coordinated positions in the unit cell [29].

However, to obtain the experimentally obtained NMR spectral lineshape, the simulated spectrum calculated using a $C_q$ of 150 kHz need to be convoluted with a Lorentzian broadening of 380 Hz. This is not expected for the solid-state NMR spectrum of a powder sample. This indicates the possibility of Al ion mobility in $LaAlO_3$. This possibility was also suggested in a study on $LaAlO_3$ by Blanc et al., where it was observed that the asymmetry parameter of the quadrupolar interaction is non-zero despite the presence of $\bar{3}$ operator at the Al site, suggesting the need for considering the dynamical effects in the NMR simulations [15]. In another study where in-situ high temperature Al MAS NMR study on aluminosilicate glasses have shown that the lineshape of the central transition changes from Gaussian to Lorentzian with increasing temperature which is attributed to the onset of rapid isotropic motions of the Al atom [30]. Similar changes in lineshape have been observed for the $^7$Li NMR spectra of an intercalation compound $Li_{0.1}MoS_2[(C_2H_5)_2NH]_{0.2}$ and amorphous $LiNbO_3$ when Li ion is mobile in the sample [31,32]. However, similar motion of Al in the perovskite structure is not expected.

To estimate the order of the motion of the Al ions in $LaAlO_3$, if present, variable temperature MAS NMR experiments from room temperature to 373 K, at a spinning speed of 8 kHz, have been carried out. There are no noticeable changes in the $^{27}$Al MAS NMR spectral lineshape when the temperature is increased, as

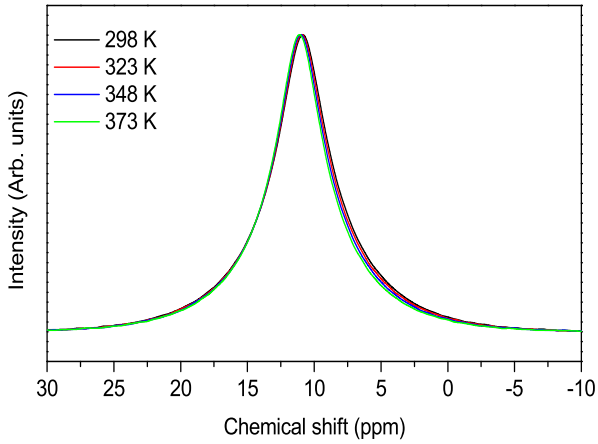


*Figure 4.10: Central transition region of $^{27}Al$ MAS NMR spectra of $LaAlO_3$ at different temperatures recorded at a spinning speed of 8 kHz.*

seen from figure 4.10, where the central transition region of the spectra are shown. This indicate that there is no change in the order of the motion of Al in the lattice, if at all present. However, a small decrease in the quadrupolar coupling constant and increase in the isotropic chemical shift, with increase in the temperature, are observed and the values are given in table 4.2. The $C_q$ decreased from 150 kHz at 298 K to 136 kHz at 373 K. Similarly, the chemical shift increased from 11.58 to 11.90 ppm. These small changes in the parameters are likely to be due to the decrease in the rhombohedral distortion or due to the changes in the lattice parameter of $LaAlO_3$ with increasing temperature, as reported in the literature from high-temperature neutron diffraction experiments [27].

Due to the limitations in the experimental set up, MAS NMR spectra below room temperature could not be carried out. Therefore, static $^{27}$A solid-state NMR experiments have been carried out at room temperature as well as at both low- and high- temperatures. Variable temperature static solid-state NMR experiments are useful for probing the structural changes and the dynamics over a wide range of time scales [33]. The static $^{27}$Al SSNMR spectrum recorded at room temperature is shown in figure 4.11. The spectrum shows five distinct set of transitions which corresponds to the central transition, $1/2 \leftrightarrow -1/2$, and four satellite transitions

*Table 4.2: The isotropic chemical shift and quadrupolar coupling constant used for the simulation of MAS NMR spectra of $LaAlO_3$ recorded at different temperatures.*

| Temperature (K) | $\delta_{iso}$ (ppm) | $C_q$ (kHz) |
|---|---|---|
| 298 | 11.58 | 150 |
| 323 | 11.71 | 147 |
| 348 | 11.79 | 142 |
| 373 | 11.90 | 136 |

corresponding to the $-3/2 \leftrightarrow -5/2$, $-1/2 \leftrightarrow -3/2$, $3/2 \leftrightarrow -1/2$ and $5/2 \leftrightarrow 3/2$ transitions. Detailed analysis of the singularity positions of the different transitions allows the estimation of chemical shift and quadrupolar interactions [17].

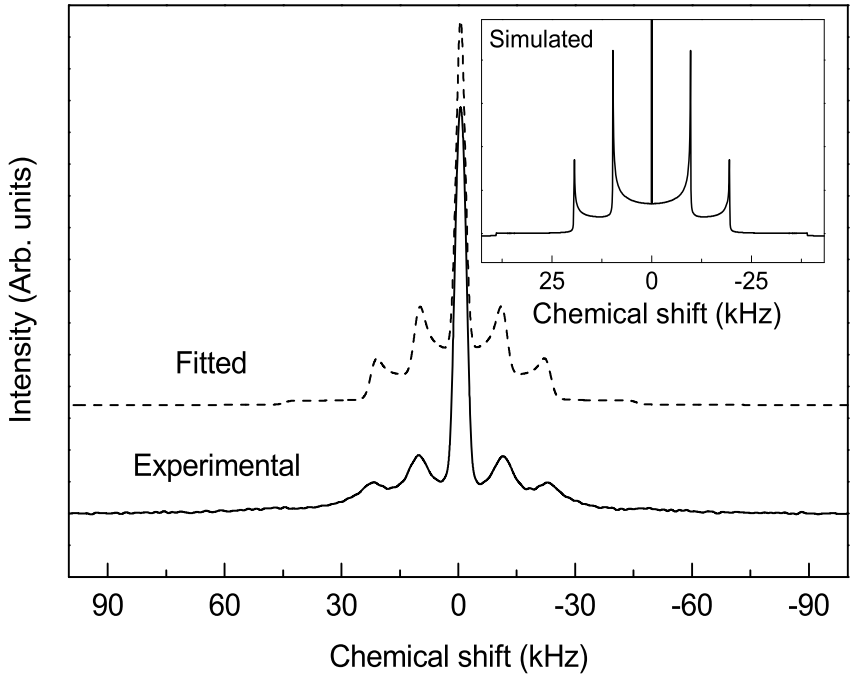


*Figure 4.11: Experimental and the best fit $^{27}Al$ static NMR spectra of $LaAlO_3$ obtained with the Simpson optimization using a Gaussian broadening. Inset shows the Simpson simulated NMR spectrum using $C_q$ of 150 kHz.*

$^{27}$Al static solid-state NMR spectrum, simulated with a $C_q$ of 150 kHz, using the SIMPSON [34] program, is shown in the inset of 4.11. In the simulated spectrum, the central transition is very sharp and narrow since this line is unaffected by the first order quadrupolar interaction. However, in the experimental spectrum, a substantial broadening is observed for all the transitions, probably as a consequence of local disorder in the position of the Al atoms. It is found that when the simulated spectrum is convoluted with a Guassian broadening of 3 kHz, the lineshapes of the central as well as the satellite transitions are similar to that in the experimental spectrum except for the slight differences in the relative intensities of the central and the satellite transitions. Ashbrook et al, from studies on the static Cs (I = 7/2) NMR studies on pollucite ($CsAlSi_2O_6$), which has a low quadrupole coupling constant of 120 kHz, found similar Gaussian lineshape and broadening and this has been attributed to a motion of the order of 1-2 kHz [35]. Therefore, the characteristics of the static $^{27}$Al NMR spectrum of $LaAlO_3$ probably indicates the possibility of Al ion mobility, of the order of 2-3 kHz, in the system.

Variable temperature static solid-state NMR experiments and lineshape analysis of the resulting spectra are useful for probing the structural changes and the dynamics over a wide range of time scales. Therefore, variable temperature $^{27}$Al static NMR experiments were carried out in the temperature range 198–373 K. The spectra recorded at different temperatures are shown in figure 4.12. A closer look at the spectra, shown in figure 4.12, reveals that there is only a minor change in the lineshape with increase in the temperature. However, as the temperature is increased, there is a shift of the satellite transitions towards the central transition, associated with a large decrease in the intensity of the central peak. This is likely to be due to the local averaging of the electric field gradient surrounding the quadrupolar nucleus, resulting in a decrease in the quadrupolar coupling which may occur because of the increasing motion of $Al^{3+}$ ions [36]. This shows that the $C_q$ which is obtained at room temperature from the MAS spectra may be a motionally averaged value of $C_q$.

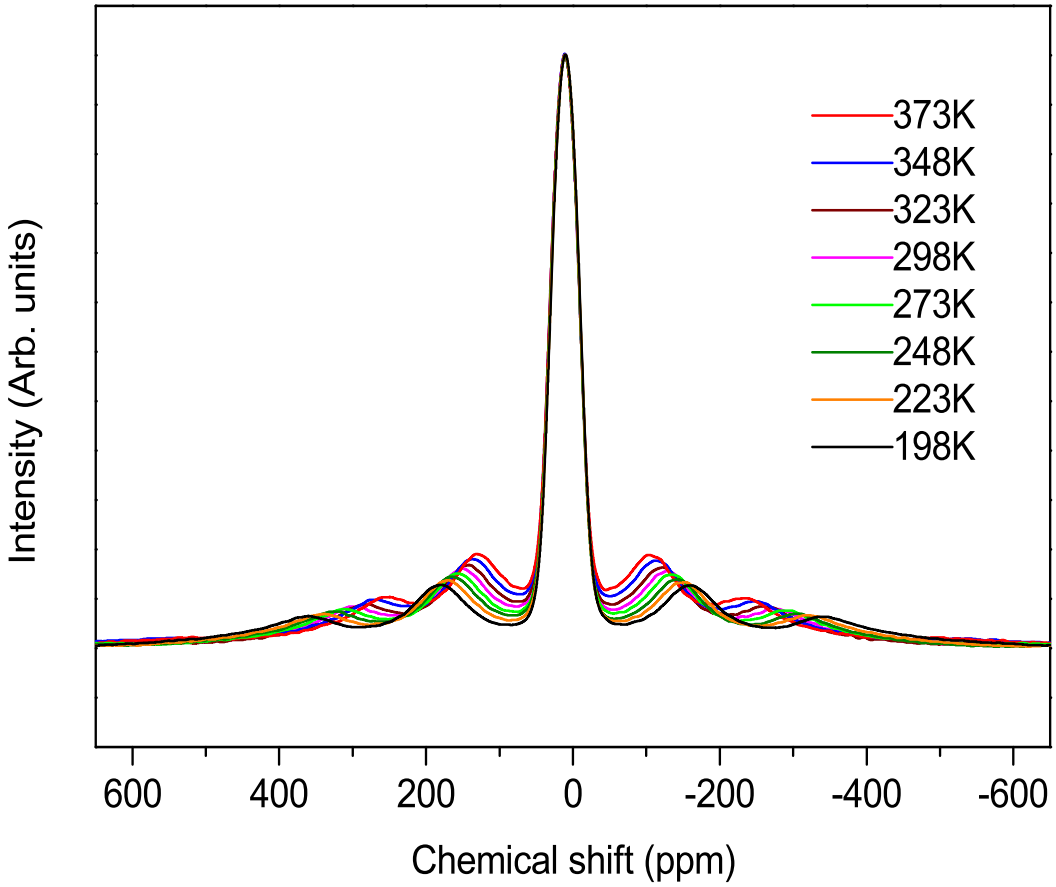


*Figure 4.12: $^{27}Al$ static NMR spectra of $LaAlO_3$ recorded at different temperatures.*

The variation of $C_q$ values calculated from the difference in the singularity positions of the inner and the outer satellite transitions, as a function of temperature are shown in figure 4.13 and the values are given in table 4.3. A linear decrease in the value of $C_q$, with increasing temperature, is observed. The decreasing value of $C_q$ with increasing temperature, as observed in the case of MAS NMR, can be due to the decreasing rhombohedral distortion as well as the change in the lattice parameter. It is clear that motion of Al ions, if at all any, has not been arrested even at the low temperature of 198 K. Because of the experimental limitations, the spectra could not be recorded below 198 K.

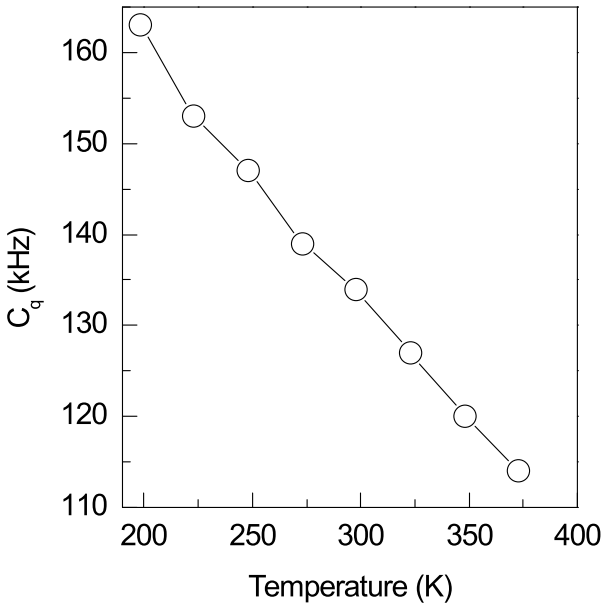


*Figure 4.13: Variation of the $^{27}Al$ $C_q$ obtained from the static NMR spectra as a function of temperature.*

*Table 4.3: $^{27}Al$ quadrupolar coupling constant of $LaAlO_3$ calculated from the static NMR spectra recorded at different temperatures.*

| Temperature (K) | $C_q$ (kHz) |
|---|---|
| 198 | 163 |
| 223 | 153 |
| 248 | 147 |
| 273 | 139 |
| 298 | 134 |
| 323 | 127 |
| 348 | 120 |
| 373 | 114 |

An important observation is that the quadrupolar lineshape of the static powder spectrum remains the same even at low and high temperatures, implying that,

if there is motion of Al ions in the lattice, the order of the motion of the Al ions at these temperatures is still the same and it is clear that if the motions were of the order of 1-2 kHz, there would have been substantial changes in static lineshape at lower temperatures.

Thus, the MAS and static NMR studies suggest that the very low $C_q$ and the Lorentzian lineshape are likely to be originated from the highly symmetric environment in the structure of $LaAlO_3$ and very fast motions. The related layered perovskite $LaSrAlO_4$ ($SrO.LaAlO_3$), in which the perovskite layer is separated by SrO layers shows a very high $C_q > 2$ MHz and a Gaussian distribution [23].

## 4.6 $^{139}$La NMR

If there are two Al environments in the structure of $LaAlO_3$, as proposed by Sathe and Dubey [10] from Raman spectroscopic studies, it should show up in the $^{139}$La NMR spectra, since the different space groups may be due to shift of Al or La from their symmetric positions. Therefore, $^{139}$La MAS NMR experiments have been carried out on the sample on low- (7.05 T) and high- field (16.4 T) NMR spectrometers, at a spinning speed of 12.5 kHz and 60 kHz, respectively. The experimental and the simulated $^{139}$La NMR spectra of lanthanum aluminate recorded at 7.05 T and 16.4 T are shown in figures 4.14 and 4.15, respectively. The spectra are simulated with the DMFIT program, assuming pure quadrupolar lineshape. Both the spectra show evidence for a single lanthanum site, corresponding to only one crystallographic site in the structure, where La is in the symmetric $LaO_{12}$ coordination environment. In the spectrum recorded at 16.4 T, with a high spinning speed of 60 kHz, the peaks arising out of the satellite transitions for the quadrupolar nuclei are observed, in addition to the central transition. The isotropic chemical shift and the quadrupolar coupling constants are obtained as 386.02 ppm and 6.88 MHz from the low-filed spectrum and as 385.35 ppm and 6.796 MHz from the high-field spectrum, respectively, and the values are in accordance with the earlier report [13].

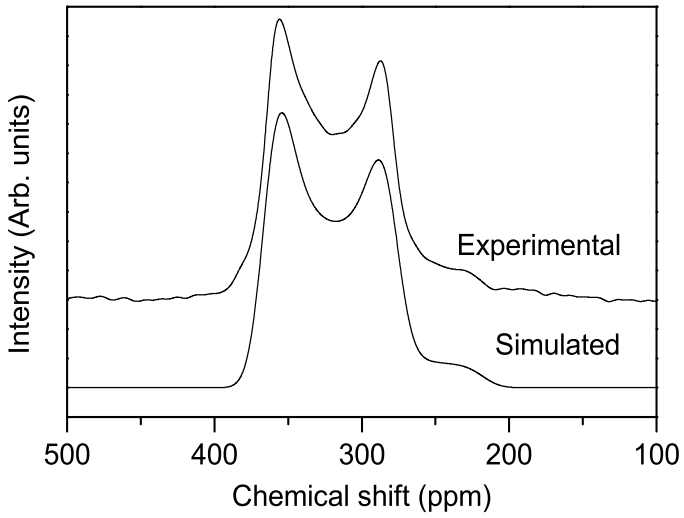


*Figure 4.14: Experimental and simulated $^{139}La$ MAS NMR spectra of $LaAlO_3$ at 7.05 T at a spinning speed of 12.5 kHz.*

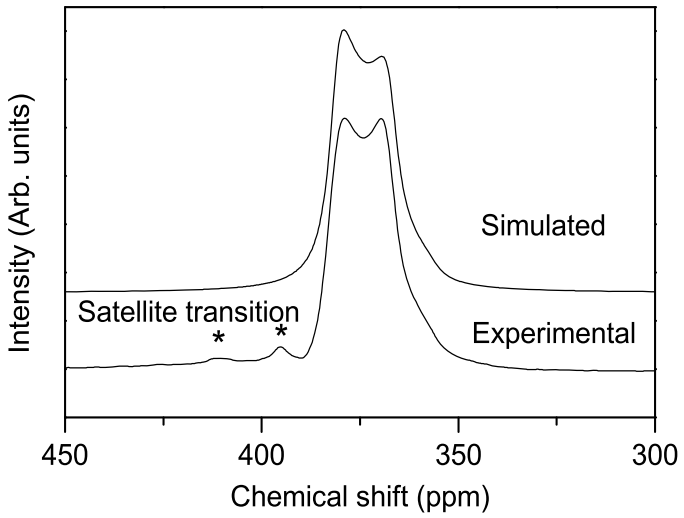


*Figure 4.15: Experimental and simulated $^{139}La$ MAS NMR spectra of $LaAlO_3$ at 16.4 T at a spinning speed of 60 kHz.*

Thus, the La NMR experiment shows the absence of more than one Al center in $LaAlO_3$. If there is mobility of Al ions in lanthanum aluminate, this is likely to

be due to the slight shift of the Al atoms from the center of inversion which is not detectable through the NMR experiments or this could also be due to the oxygen ion mobility.

## 4.7 Second harmonic generation

Second harmonic generation (SHG) is an important optical method to confirm the lack of center of inversion in the crystal structure, since centrosymmetric molecules cannot generate second harmonic signals [38]. Preliminary non-linear optical (NLO) measurements were carried out following the Kurtz-Perry method [37], using a Q-switched Nd:YAG laser of $\lambda$=1064 nm (pulse width of 10 ns and repetition rate of 10 Hz; Spectra Physics, PROLAB 170). The second harmonic generation behavior of $LaAlO_3$ was confirmed from NLO measurements. With an input beam energy of 3.2 mJ/pulse, SHG signal (bright green emission) of 4.3 mV was observed for $LaAlO_3$, compared to 7.6 mV for the reference sample potassium dihydrogen phosphate (KDP). Therefore, $LaAlO_3$ showed roughly half the SHG efficiency of the standard KDP reference. From the result, it can be concluded that the crystal structure of $LaAlO_3$ is non-centrosymmetric, with the space group as R3c, which implies that the $AlO_6$ octahedra are slightly distorted.

## 4.8 Conclusions

Magic angle spinning (MAS) and static $^{27}$Al solid-state NMR studies on $LaAlO_3$ at different temperatures, in combination with Rietveld refinement of the powder XRD patterns, suggested that the possible space group of the compound is non-centrosymmetric R3c instead of the centrosymmetric R$\bar{3}$c. This is supported by the second harmonic generation studies, which indicated the absence of center of inversion in the lanthanum aluminate structure. The $^{27}$Al NMR studies indicated the possibility of Al ion mobility in the sample. Detailed studies are required to understand this, which is beyond the scope of present work.

# Bibliography


[1] S.-Y. Cho, I.-T. Kim and K. S. Hong, *J. Mater. Res* 1999, 14, 114-119.

[2] G. Malandrino, L. M. S. Perdicaro, G. Condorelli, I. L. Fragala, A. Cassinese and M. Barra, *J. Mater. Chem.* 2005, 15, 4718-4722.

[3] S. Jin, T. H. Tiefel, M. McCormack, R. A. Fastnacht, R. Ramesh and L. H. Chen, *Science* 1994, 264, 413-415.

[4] T. Tagawa and H. Imai, *J. Chem. Soc., Faraday Trans.* 1988, 84, 923-929.

[5] Z.-y. Mao, D.-j. Wang, Q.-f. Lu, W.-h. Yu and Z.-h. Yuan, *Chem. Commun.* 2009, 346-348.

[6] J. Zhao, N. L. Ross and R. J. Angel, *J. Phys.: Condens. Matter* 2004, 16, 8763-8773.

[7] S. Geller and V. B. Bala, *Acta Crystallogr.* 1956, 9, 1019-1025.

[8] K. A. Müller, E. Brun, B. Derighetti, J. E. Drumheller and F. Waldner, *Phys. Lett.* 1964, 9, 223-224.

[9] B. Derighetti, J. E. Drumheller, F. Laves, K. A. Muller and F. Waldner, *Acta Crystallogr.* 1965, 18, 557.

[10] V. G. Sathe and A. Dubey, *J. Phys.: Condens. Matter* 2007, 19, 382201.1-7

[11] F. S. Galasso, *Structure, properties and preparation of perovskite-type compounds* (Pergamon, Oxford, 1969).

[12] M. Smith, *Appl. Magn. Reson.*1993, 4, 1-64.

[13] R. Dupree, M. H. Lewis and M. E. Smith, *J. Am. Chem. Soc.* 1989, 111, 5125-5132.

[14] D. Iuga, S. Simon, E. de Boer and A. P. M. Kentgens, *J. Phys. Chem. B* 1999, 103, 7591-7598.

[15] F. Blanc, D. S. Middlemiss, L. Buannic, J. L. Palumbo, I. Farnan and C. P. Grey, *Solid State Nucl. Magn. Reson.* 2012, 42, 87-97.

[16] E. V. Charnaya, C. Tien, N. V. Chejina, M. K. Lee and S. Y. Sun, *Phys. Solid State* 2007, 49, 449-453.

[17] K. J. D. MacKenzie and M. E. Smith, *Multinuclear Solid-State Nuclear Magnetic Resonance of Inorganic Materials* (Pergamon, Oxford, 2002).

[18] L. M. Perander, Z. D. Zujovic, T. Groutso, M. M. Hyland, M. E. Smith, L. A. O' Dell and J. B. Metson, *Can. J. Chem.* 2007, 85, 889-897.

[19] B. Baby, K. K. Dey, T. G. Ajithkumar and P. A. Joy, *J. Am. Ceram. Soc.* 2014, 97, 2990-2995.

[20] V. Sreeja, T. S. Smitha, D. Nand, T. G. Ajithkumar and P. A. Joy, *J. Phys. Chem. C* 2008, 112, 14737-14744.

[21] X. L. Duan, D. R. Yuan and F. P. Yu, *Inorg. Chem.* 2011, 50, 5460-5467.

[22] R. S. Azis, D. Holland, M. E. Smith, A. Howes, M. Hashim, A. Zakaria, J. Hassan, N. M. Saiden and M. K. Ikhwan, *J. Aust. Ceram. Soc.* 2013, 49, 74-80.

[23] C. Tealdi, C. Ferrara, L. Malavasi, P. Mustarelli, C. Ritter, A. Spinella, D. Massiot and P. Florian, *J. Mater. Chem.* 2012, 22, 10488-10495.

[24] W. Li, M. W. Zhuo and J. L. Shi, *Mater. Lett.* 2004, 58, 365-368.

[25] J. H. Christopher, J. K. Brendan and C. C. Bryan, *J. Phys.: Condens. Matter* 2000, 12, 349-365.

[26] W. Kraus and G. Nolze, *PowderCell for Windows (PCW), version 2.4* (The software is freely available from http://www.ccp14.ac.uk.)

[27] S. A. Hayward, F. D. Morrison, S. A. T. Redfern, E. K. H. Salje, J. F. Scott, K. S. Knight, S. Tarantino, A. M. Glazer, V. Shuvaeva, P. Daniel, M. Zhang and M. A. Carpenter, Phys. Rev. B, 2005, 72, 054110.1-17.

[28] D. Massiot, F. Fayon, M. Capron, I. King, S. Le Calv, B. Alonso, J.-O. Durand, B. Bujoli, Z. Gan and G. Hoatson, *Magn. Reson. Chem.* 2002, 40, 70-76.

[29] J. Skibsted, E. Henderson and H. J. Jakobsen, *Inorg. Chem.* 1993, 32, 1013

[30] K. Kanehashi and J. F. Stebbins, *J. Non-Cryst. Solids* 2007, 353, 4001-4010.

[31] A. C. Bloise, J. P. Donoso, C. J. Magon, J. Schneider, H. C. Panepucci, E. Benavente, V. c. Sanchez, M. A. l. Santa Ana and G. Gonzalez, *J. Phys. Chem. B* 2002, 106, 11698-11707.

[32] M. Wilkening, D. Bork, S. Indris and P. Heitjans, *Phys.Chem. Chem. Phys.* 2002, 4, 3246-3251.

[33] S. E. Ashbrook, *Phys. Chem. Chem. Phys.* 2009, 11, 6892.

[34] M. Bak, J. T. Rasmussen and N. C. Nielsen, *J. Magn. Reson.* 2000, 147, 296-330.

[35] S. E. Ashbrook, K. R. Whittle, L. Le Polls and I. Farnan, *J. Amer. Ceram. Soc.* 2005, 88, 1575-1583.

[36] T. L. Spencer, L. A. O'Dell, I. Moudrakovski and G. R. Goward, *J. Phys. Chem. C* 2013, 117, 9558-9565.

[37] S. K. Kurtz and T. T. Perry, *J. Appl. Phys.* 1968, 39, 3798-3813.

[38] R. L. Byer, *Ann. Rev. Mater. Sci.* 1974, 4, 147-190.

# Chapter 5

# Studies on $La_{1-x}Y_xAlO_3$

## 5.1 Introduction

The perovskite $LaMnO_3$ is an antiferromagnetic oxide and ferromagnetism can be induced in the compound when $La^{3+}$ is partially substituted by divalent cations such as $Ca^{2+}$, $Sr^{2+}$, etc [1]. This is due to the conversion of equal amounts of $Mn^{3+}$ to $Mn^{4+}$ as well as the associated structural changes due to the decreased Jahn-Teller distortion of the $MnO_6$ octahedra, changes in the Mn-O-Mn bond angles and Mn-O bond lengths [2]. Large difference in the ferromagnetic Curie temperature as well as the electrical characteristics are reported, depending on the size of the substituted ion, for similar compositions. However, a major observation is the large increase in the magnetization and changes in the electrical properties for $0.1 < x < 0.2$ in $La_{1-x}A_xMnO_3$ (A = Ca, Dr, Ba, Pb), irrespective of the substituted ion. The compounds show ferromagnetic ordering above $x = 0.1$. Similar structural changes and associated changes in the magnetic as well as electrical properties are also observed when La in $LaMnO_3$ is replaced by smaller rare earth ions. Ferromagnetic compositions are shown to become spin glasses by the substitution of smaller rare earth ions such as in $(La_{1-x}Tb_x)_{2/3}Ca_{1/3}MnO_3$ [3] or similar combination of different rare earth ions at the La-site [4–6].

The objective of the work reported in this chapter is to probe the changes in the local coordination environments of the La and Al sites when the La site in the perovskite oxide $LaAlO_3$ is substituted with the smaller rare earth ion $Y^{3+}$, from solid-state NMR studies. $Y^{3+}$ is selected as a representative of the smaller rare-earth ions and also based on the fact that the entire material remains non-magnetic so that line broadening in the NMR spectra due to the presence of magnetic ions can be avoided to get good spectral characteristics. Various properties of the perovskite $LaAlO_3$ are found to change when $La^{3+}$ is replaced by other rare-earth ions and these changes are likely to be due to the changes in the local coordination environment of $LaAlO_3$ due to the replacement of the larger La by the smaller rare-earth ions [7–9]. There are no reports in the literature on the detailed investigation of these changes in the local symmetry and electronic environments.

The crystal structure of $LaAlO_3$ is rhombohedral perovskite with the space group $R\bar{3}c$ [10] and the crystal structure of $YAlO_3$ is orthorhombic with the space group Pbnm [11]. The substitution of Y at the La site can cause two effects in the perovskite structure arising from the quadrupole and size considerations; i) changes in the electronic configuration since $La^{3+}$ has a noble gas configuration of Xe and $Y^{3+}$ has that of Kr, and ii) the size effect which changes the inter-atomic distances and bond angles since ionic radius of $La^{3+}$ is (1.36 Å) is much larger than that of $Y^{3+}$ (1.076 Å) [12].

The structural changes that may occur in $LaAlO_3$ on substitution is due to the local structural distortions when the larger La ion is replaced by the smaller Y ion which has a different electronic distribution and hence is expected to distort the local electronic environment. Such local distortions can be probed by the solid-state NMR which probes the nuclei and hence the local distortions. For example, in the case of $La_{1-x}Eu_xAlO_3$, studied by NMR and molecular dynamics, it has been shown that the Al coordination environment has not changed from the octahedral coordination, since the first neighbor distances are remaining the same as that of pure $LaAlO_3$ even after the Eu substitution, and this is further evidenced from the computational studies [13]. However, in a $^{27}Al$ MAS NMR study on the solid solution of $LaAlO_3$−$La_{0.67}A_{0.33}MnO_3$ (A= Ca, Sr, Ba), additional coordination environments are observed for aluminum, different from the octahedral site as in pure $LaAlO_3$ [14] . In order to understand the local structural variations upon substitution of La by Y, both the $^{27}Al$ and $^{139}La$ NMR spectral studies have been carried out to probe the changes in the local coordination environments in the substituted $LaAlO_3$ compositions.

## 5.2 Synthesis

A series of La-site substituted compositions, $La_{1-x}Y_xAlO_3$ ($x$ = 0.0, 0.03, 0.06, 0.09, 0.11, 0.12, 0.13, 0.14, 0.15, 0.17 0.2, 0.25, 0.33 and 0.38) were prepared using reverse co-precipitation method as reported previously [15]. A mixed water solution of lanthanum nitrate (Aldrich), yttrium nitrate (Aldrich) and aluminium

nitrate (sd fine chemicals) taken in the appropriate molar ratio (1-$x$:$x$:1) was dropped into a dilute ammonia solution of pH $\sim$ 9. For example, for the synthesis of $x = 0.2$ composition, 2.42 g of lanthanum nitrate, 0.54 g of yttrium nitrate and 2.63 g of aluminium nitrate were completely dissolved in distilled water and this solution was dropped into the dilute ammonia solution taken in a beaker with continuous stirring. The precipitate formed was filtered and washed several times with distilled water and finally dried in an oven. The dried powder was then precalcined at 700 °C, 800 °C, 1000 °C, 1200 °C for two hours each and then finally calcined at 1400 °C for 6 hours for the complete phase formation. Composition with $x = 0.4$ and $x = 0.5$ was also synthesized but found to form the garnet phase. Hence, composition up to $x = 0.38$ are studied.

## 5.3 NMR methodology

$^{27}$Al solid-state NMR experiments were carried out at room temperature on a Bruker AV-300 (aluminium resonance frequency, $\nu_{Al}$ = 78.2 MHz) spectrometer, operating at a field of 7.05 T. The experiments were done using a 4 mm BL MAS probe at the magic angle spinning rate of 10 kHz and with a short pulse duration 3 $\mu$s. 200 scans were collected with a recycle delay of 20 s. The 3-quantum magic angle spinning (3QMAS) experiment was carried out using a standard Z-filter pulse sequence on the AV-300 spectrometer. The experiment was optimized at a spinning rate of 10 kHz with the excitation and conversion pulses as 5.8 and 2.2 $\mu$s, respectively at a RF field strength of 90 kHz. The selective 90° Z-filter pulse was set as 25 $\mu$s at a RF field strength of 4 kHz. A recycle delay of 10 s was used for the experiment.

$^{139}$La solid-state NMR experiments were carried out on a Bruker AV-700 ($\nu_{La}$ = 98.1 MHz) operating at a field of 16.4 T. The MAS NMR data on AV-700 was collected using a 2.5 mm MAS probe, with a spinning speed of 60 kHz. The quantitative MAS NMR spectra were recorded using a pulse width of 1 $\mu$s and 8,000 scans were acquired with a recycle delay of 0.25 s.

## 5.4 Characterization

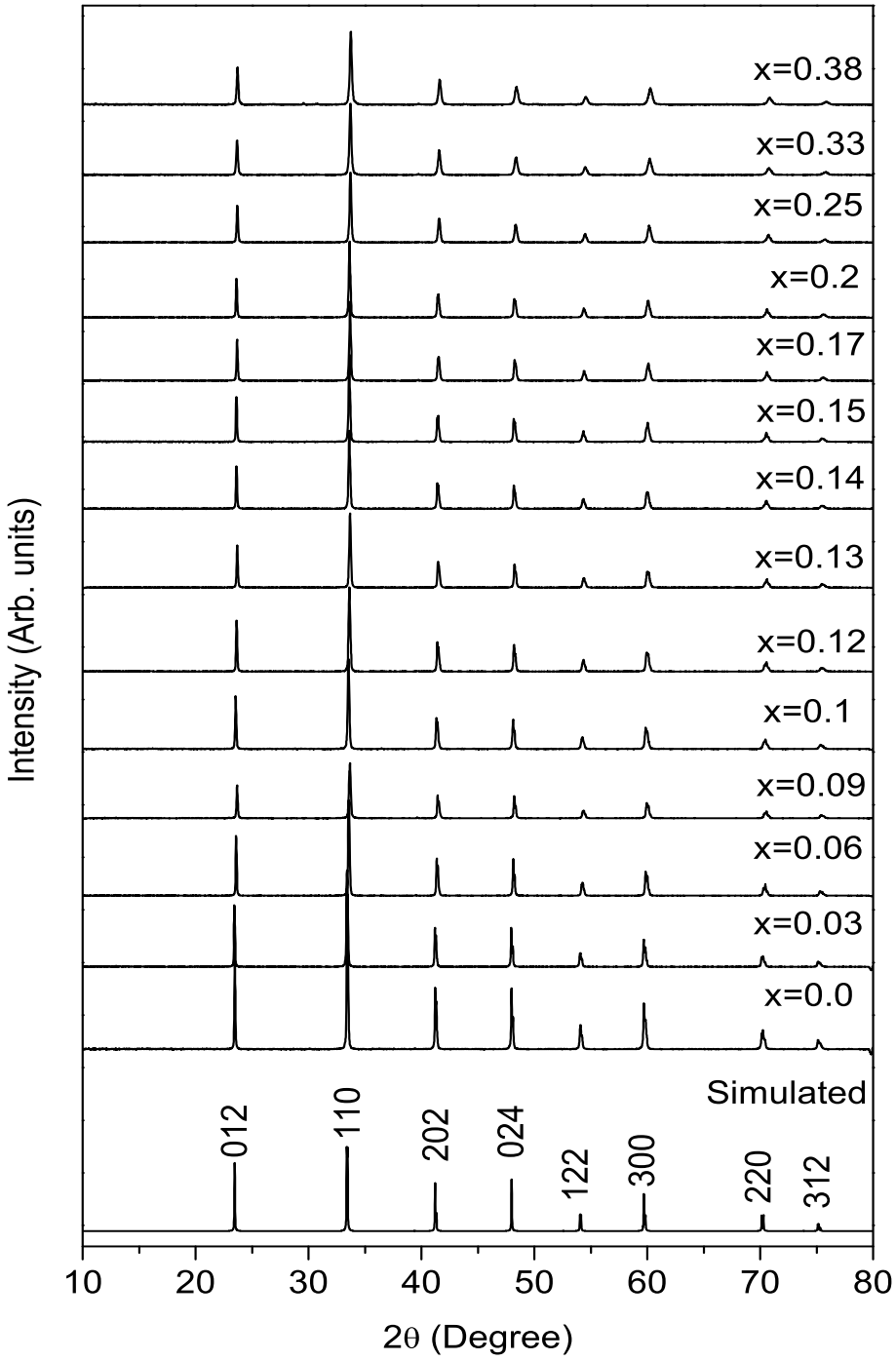


*Figure 5.1: Powder XRD patterns of different compositions in $La_{1-x}Y_xAlO_3$, compared with the simulated pattern of $LaAlO_3$.*

All the $La_{1-x}Y_xAlO_3$ samples are initially characterized by the powder X-ray diffraction method. The XRD patterns of all the Y-substituted samples are shown in figure 5.1. The simulated XRD pattern of $LaAlO_3$ is also shown in the figure for comparison. From a comparison of the experimental and simulated XRD patterns, it is clear that all the samples are crystallized with the perovskite structure and are formed without any impurities. Thus, the perovskite crystalline structure is preserved after the replacement of part of $La^{3+}$ by $Y^{3+}$ which shows the occupancy of $Y^{3+}$ ions in the dodecahedral $La^{3+}$ sites.

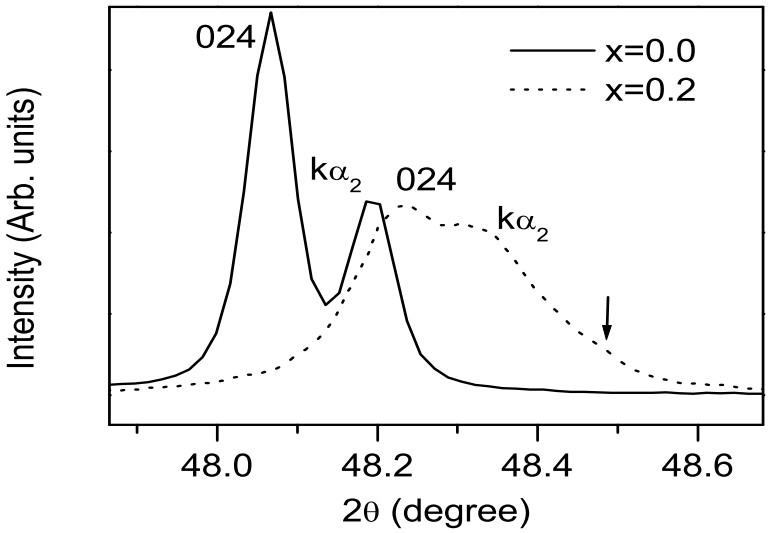


*Figure 5.2: Zoomed XRD patterns showing changes in the relative intensity and diffraction angles of the (024) peak for $x = 0.0$ and 0.2 compositions of $La_{1-x}Y_xAlO_3$. The $K_{\alpha_2}$ components are marked. An additional shoulder observed for $x = 0.2$ is marked by the arrow.*

The zoomed XRD patterns of $x = 0$ and 0.2, showing the (024) peak (observed as a doublet due to the $K_{\alpha_1}$ and $K_{\alpha_2}$ components), are shown in figure 5.2. The peak has shifted to higher diffraction angles indicating a decrease in the lattice parameters. Apart from the shift in the position of the peak, a change in the relative intensities of the first ($K_{\alpha_1}$) and the second ($K_{\alpha_2}$) peaks is also observed for $x = 0.2$, along with a shoulder at higher angles and overall increase in the

width of the peak. The hexagonal lattice parameters '$a$' and '$c$' are calculated by the least squares fitting of the XRD patterns using the PCW software [16] with the space group $R\bar{3}c$ and are given in table 5.1. The variation of the lattice parameters, as a function of $x$ in $La_{1-x}Y_xAlO_3$, is shown in figure 5.3.

*Table 5.1: Lattice parameters for different compositions in $La_{1-x}Y_xAlO_3$.*

| $x$ | $a$ (Å) | $c$ (Å) |
|---|---|---|
| 0.0 | 5.3633 | 13.1091 |
| 0.03 | 5.3629 | 13.0996 |
| 0.06 | 5.3594 | 13.0861 |
| 0.09 | 5.3569 | 13.0789 |
| 0.1 | 5.3539 | 13.0743 |
| 0.12 | 5.3530 | 13.0712 |
| 0.13 | 5.3523 | 13.0683 |
| 0.14 | 5.3485 | 13.0656 |
| 0.15 | 5.3466 | 13.0648 |
| 0.17 | 5.3461 | 13.0624 |
| 0.2 | 5.3404 | 13.0609 |
| 0.25 | 5.3350 | 13.0579 |
| 0.33 | 5.3295 | 13.0482 |
| 0.38 | 5.3249 | 13.0433 |

The lattice parameters are found to decrease with increasing degree of substitution. This is expected because of the smaller ionic size of $Y^{3+}$ compared to that

of $La^{3+}$ (Shannon radii of 1.075 Å for $Y^{3+}$ in 9-fold coordination, 1.36 Å and 1.216 Å for $La^{3+}$ in 12-fold and 9-fold coordinations, respectively [12]). The changes in the lattice parameters are almost linear up to $x = 0.13$, indicating the formation of single phase solid solutions and there is a deviation in the linearity from this region onwards, indicating a structural change in this compositional region.

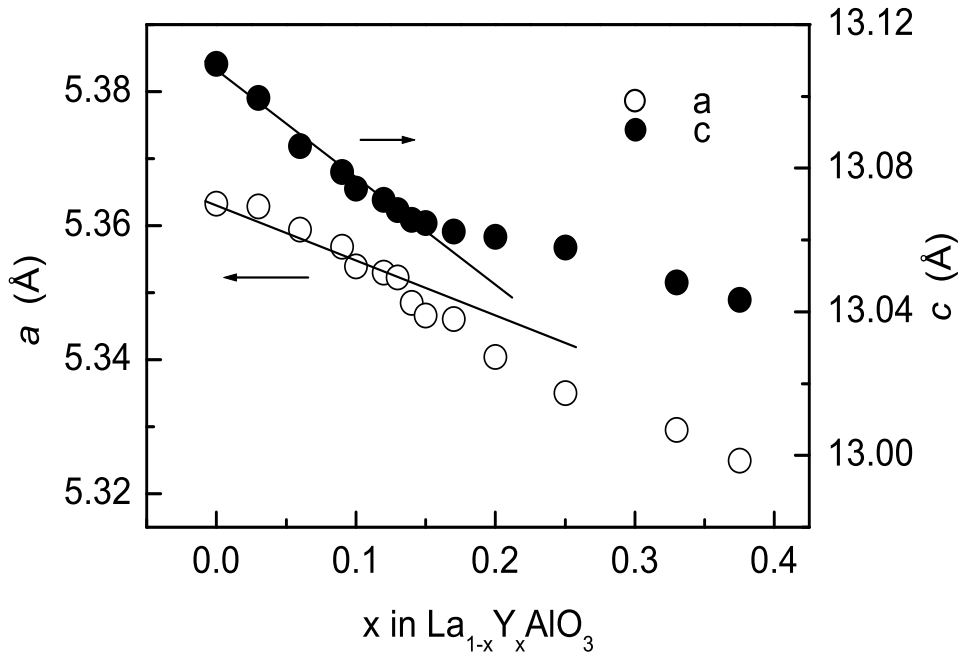


*Figure 5.3: Variation of the hexagonal lattice parameters of $La_{1-x}Y_xAlO_3$ as a function of $x$.*

## 5.5 Rietveld refinement studies

Since there is a non-linear variation in the lattice parameters above $x = 0.13$, Rietveld refinement analysis of the powder XRD patterns is carried out on selected compositions close to $x = 0.13$, to look for any possible structural changes. Since both the space groups R3c and R$\bar{3}$c gave comparable residual factors for $LaAlO_3$ (see section 4.4, chapter 4) and the space group R$\bar{3}$c is the established space group in the literature, the space group, R$\bar{3}$c is used for the present analysis.

The results of the Rietveld analysis are shown in figures 5.4, 5.5, 5.6 and 5.7 for the compositions $x = 0.12$, 0.13, 0.14 and 0.15, respectively. It may be seen that reasonably good fits are obtained for all the compositions. However, the zoomed graphs (insets in figures) showing the fit to the rhombohedral (024) peak (doublet due to the $K_{\alpha_1}$ and $K_{\alpha_2}$ components) show that good fits are obtained for $x = 0.12$ and 0.13 whereas the peak is not fitted well for $x = 0.14$ and $x = 0.15$, the latter showing large difference between the observed and the calculated curves, apart from an additional shoulder at higher angles. Therefore, the Rietveld refinement analysis has been carried out for $x = 0.12$ and 0.13, considering two different phases, a rhombohedral phase similar to that of $LaAlO_3$ with the space group $R\bar{3}c$ and an orthorhombic phase similar to that of $YAlO_3$. However, good fits are not obtained when the space group Pbnm of $YAlO_3$ is used. On the other hand, better fits are obtained with the orthorhombic space group Amm2. The results of the analysis using two different phases co-existing in $x = 0.14$ and 0.15 are shown in figures 5.8 and 5.9, respectively. Better fits are obtained with the two-phase model for both compositions.

These results on the structural studies suggest a mixed phase behavior for the compositions for $x > 0.13$ in $La_{1-x}Y_xAlO_3$. In the substituted compositions, $x \approx 0.13$ corresponds to the compositional region $x = 1/8$, where one La is replaced by Y at the corner of the simple cubic perovskite unit cell, which is shared by eight unit cells. This means that every rhombohedral perovskite unit cell in the lattice contains one Y atom and increasing the amount of Y beyond this limit may lead to a distortion in the rhombohedral structure and thus, a phase separation, due to the very small size of Y compared to that of La in the perovskite structure and the different crystal structures of the end members. It may be recalled that $YAlO_3$ has the orthorhombic perovskite structure. Thus, it may be expected that the structure transforms to orthorhombic for $x > 1/8$ due to the different structures of the end members as observed for other perovskite oxide solid solutions with different structures for the end members [17].

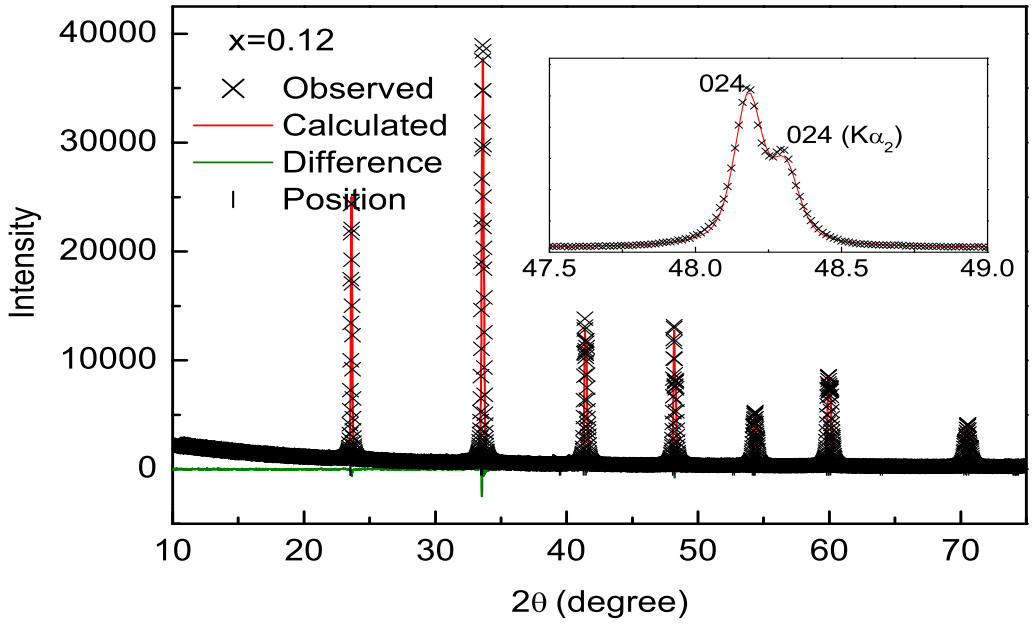


*Figure 5.4: Result of the Rietveld refinement of the XRD pattern of $La_{0.88}Y_{0.12}AlO_3$.*

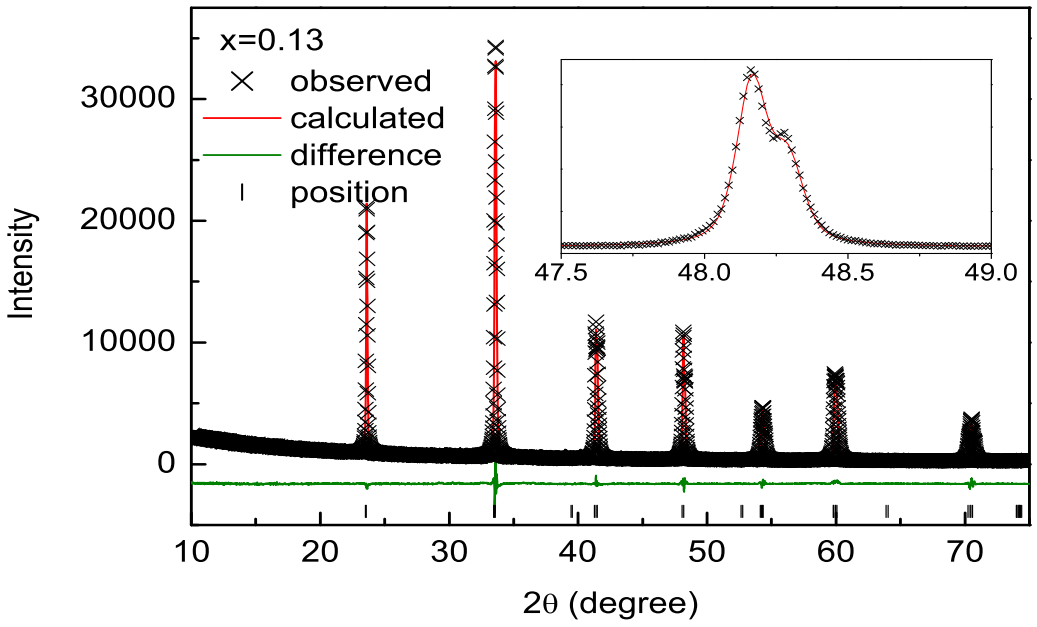


*Figure 5.5: Result of the Rietveld refinement of the XRD pattern of $La_{0.87}Y_{0.13}AlO_3$.*

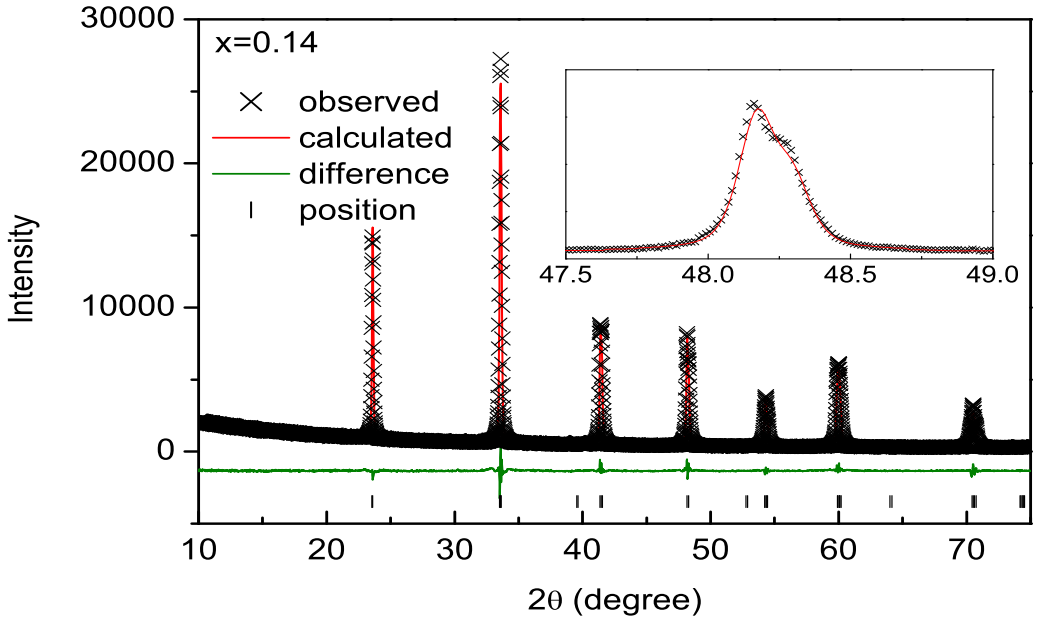


*Figure 5.6: Result of the Rietveld refinement of the XRD pattern of $La_{0.86}Y_{0.14}AlO_3$.*

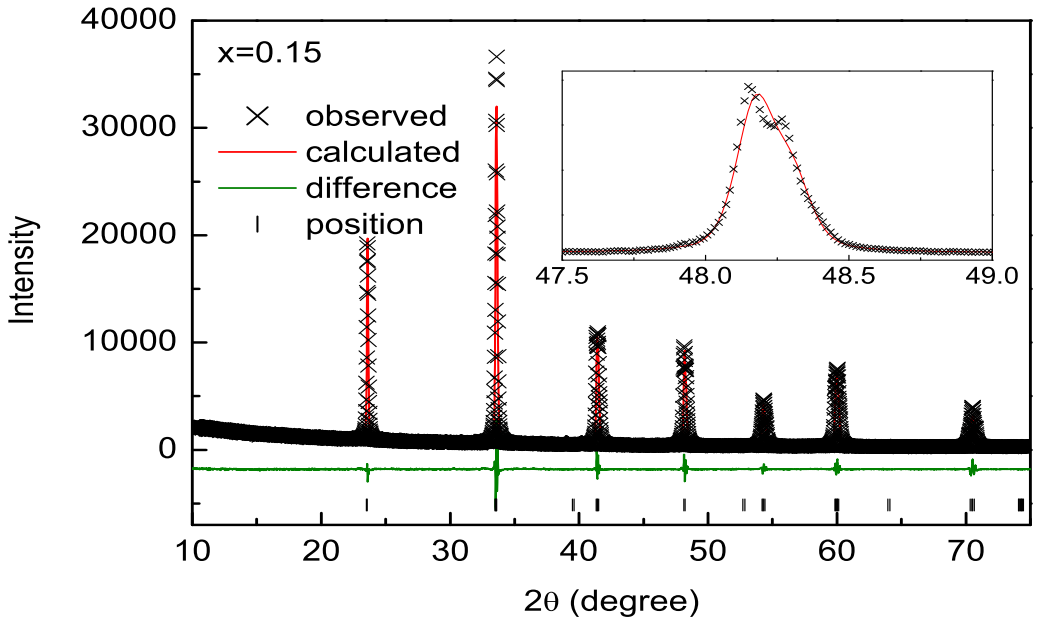


*Figure 5.7: Result of the Rietveld refinement of the XRD pattern of $La_{0.85}Y_{0.15}AlO_3$.*

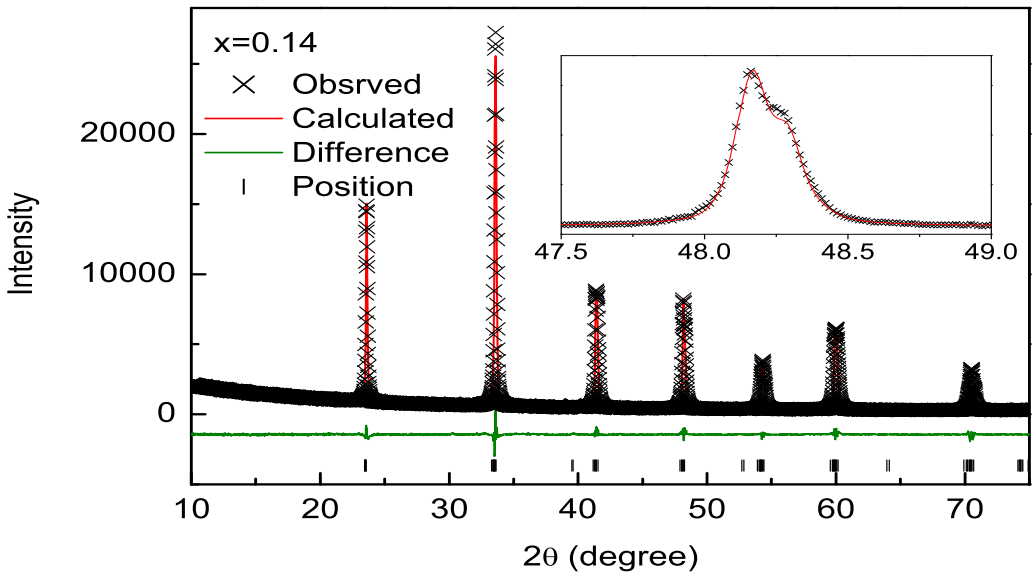


*Figure 5.8: Result of the Rietveld refinement of the XRD pattern of $La_{0.86}Y_{0.14}AlO_3$ using a two phase model consisting of rhombohedral and orthorhombic phases.*

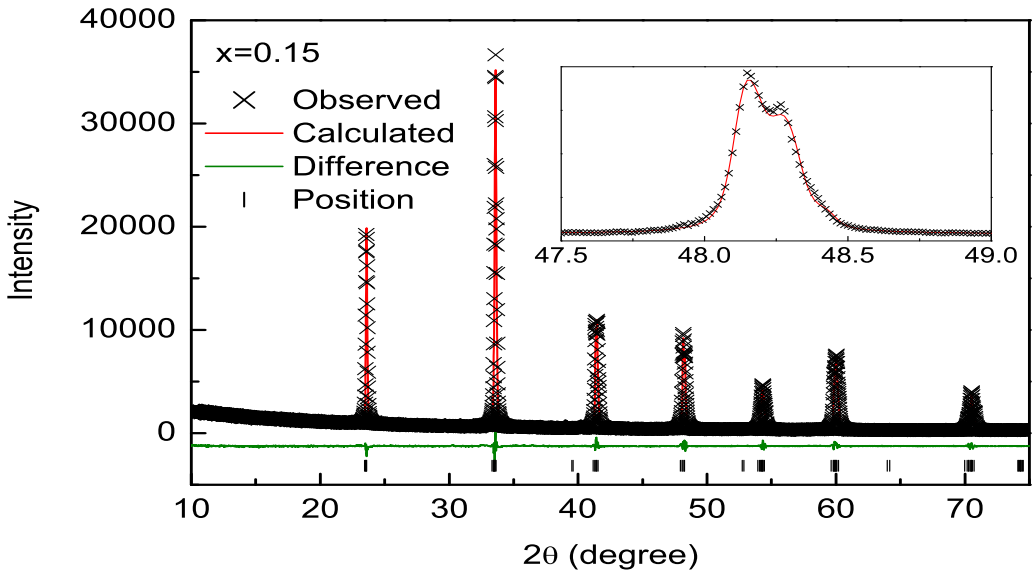


*Figure 5.9: Result of the Rietveld refinement of the XRD pattern of $La_{0.85}Y_{0.15}AlO_3$ using a two phase model consisting of rhombohedral and orthorhombic phases.*

## 5.6 $^{27}$Al NMR

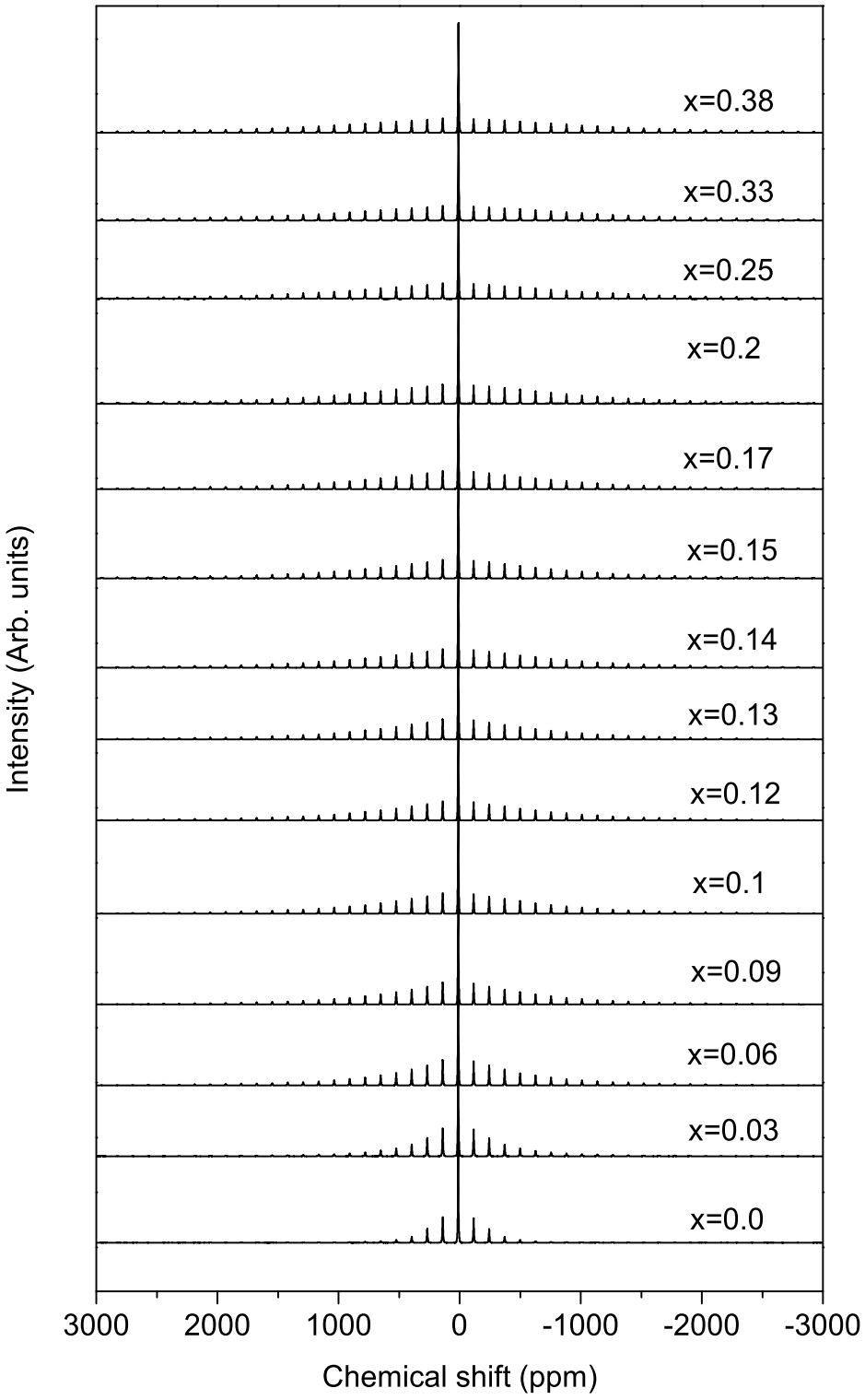


*Figure 5.10: $^{27}$Al MAS NMR spectra of different compositions in $La_{1-x}Y_xAlO_3$ showing the full sideband profile.*

$^{27}$Al NMR spectra for all the compositions with the full spinning side band profile are shown in figure 5.10. As the degree substitution at the La site by Y is increased, the Al coordination environment is affected as seen from the increased intensities of the side bands in the NMR spectra. This is indicating an increase in the quadrupole coupling constant with the degree of substitution.

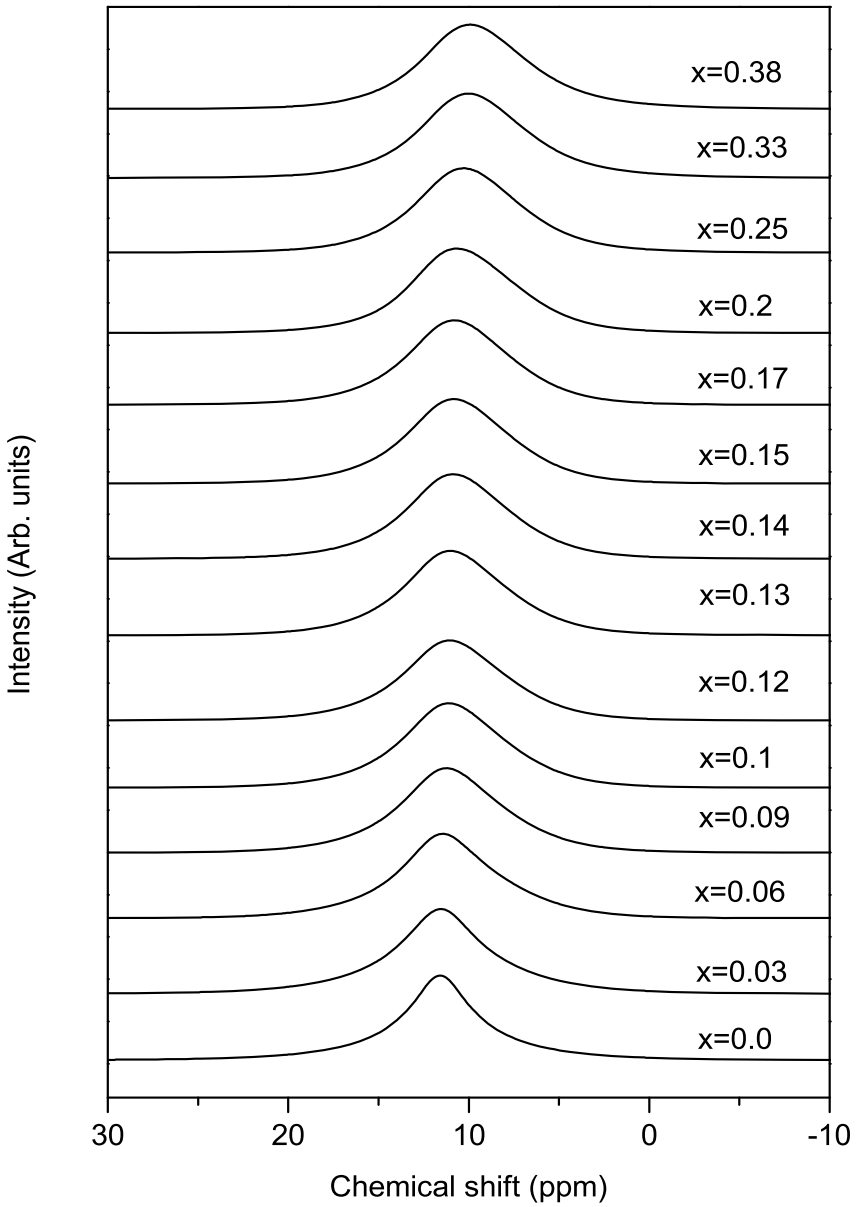


*Figure 5.11: The central transition region in the $^{27}Al$ MAS NMR spectra of different compositions in $La_{1-x}Y_xAlO_3$.*

The central transition in the spectra for all the compositions are compared in figure 5.11. The central transition for all the compositions appears around 11 ppm as reported for the unsubstituted lanthanum aluminate, indicating that Al in all the samples is in the octahedral coordination environment and the coordination environment has not changed by the substitution of Y [14,18–20]. However, there is a clear indication of local distortions in the Al octahedra by the yttrium substitution as evidenced from the slight change in the chemical shift and the broadening of the spectra which is in accordance with the NMR and molecular dynamics simulation results reported for $La_{1-x}Eu_xAlO_3$ [13]. In order to find out whether any additional coordination environments for Al, are arising out of the substitution of Y for La, as reported for the diluted solid solutions $LaAlO_3$−$La_{0.67}A_{0.33}MnO_3$ (A = Ca, Sr, Ba) with the alkali earth ion substitution [14], we have carried out the triple quantum magic angle spinning experiments for the compositions $x = 0.12$ and $x = 0.2$.

The 3QMAS spectra for $x = 0.12$ and 0.2 are shown in figures 5.12 and 5.13, respectively. From the 3QMAS NMR spectra, it is clear that there is only one octahedral environment even in the substituted compositions. However, the center of gravity of the contour in the F1 dimension for the $x = 0.12$ composition is at 12 ppm, and it is slightly shifted downwards to 13 ppm for the $x = 0.2$ composition, indicating the quadrupole induced shift caused by the increase in the quadrupole coupling constant with the substitution.

In order to obtain the NMR parameters, all the $^{27}Al$ MAS NMR spectra were deconvoluted using the DMFIT programme [21]. Since the quadrupole coupling constant of $LaAlO_3$ is around 150 kHz, we have used a simulation model which accounts for the first order quadrupolar interactions. The central transition region of the experimental and simulated spectra of the compositions $x = 0.1$ and $x = 0.2$ is shown in figure 5.14.

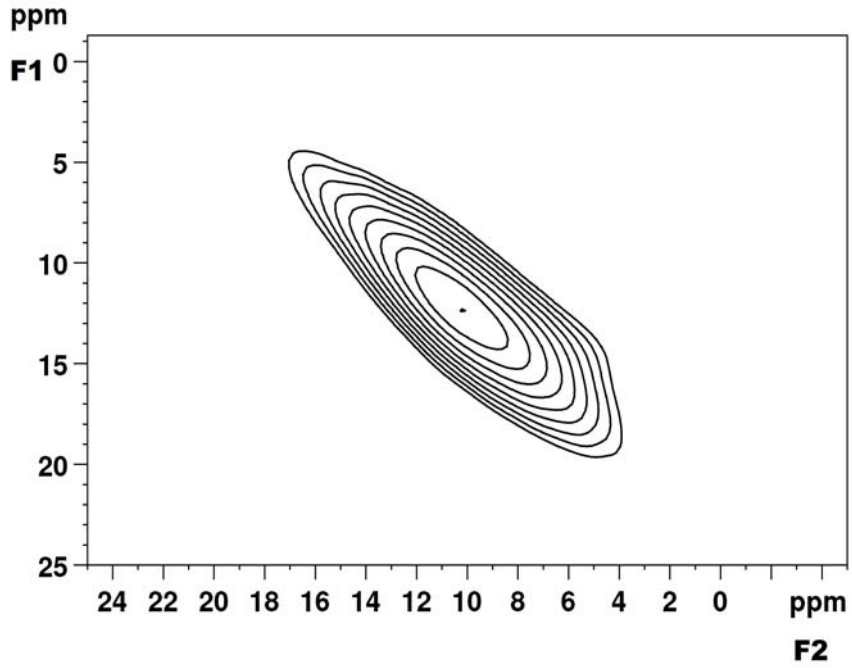


*Figure 5.12: $^{27}Al$ 3QMAS NMR spectrum of $La_{0.88}Y_{0.12}AlO_3$.*

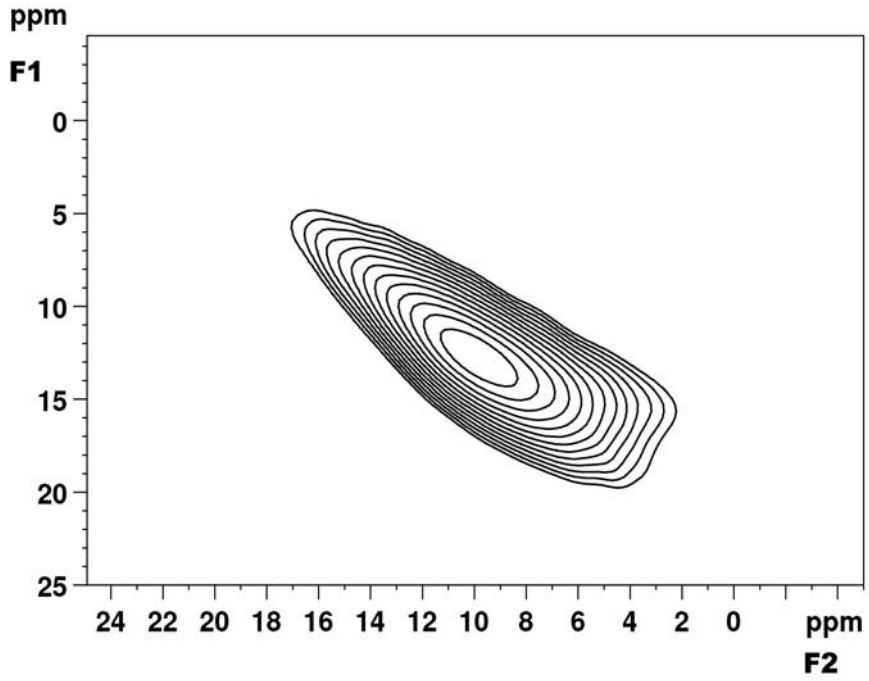


*Figure 5.13: $^{27}Al$ 3QMAS NMR spectrum of $La_{0.8}Y_{0.2}AlO_3$.*

The NMR parameters; isotropic chemical shift ($\delta_{iso}$) and the quadrupole coupling constant ($C_q$), are given in table 5.2. In the substituted samples, the chemical shift decreases marginally from 11.6 ppm for the unsubstituted compound to 9.7 ppm for the substitution $x = 0.38$. The small decrease in the chemical shift is because of the quadrupole induced shift [22], which is not taken into account while simulating the NMR pattern. A quad-first model is used for the simulation, which takes care of only the first order quadrupole interactions. However,quadrupole coupling constant increases from 150 kHz for the unsubstituted compound to 910 kHz for the substitution of $x = 0.38$. From the plot of $C_q$ versus degree of substitution, as shown in figure 5.15, a small jump in the value of quadrupole coupling constant is observed above $x = 0.13$, apart from another jump in the value above $x = 0.03$. The jump close to $x = 0.13$ matches with the structural change as observed from the structural studies. More detailed structural studies are required to explain the jump above $x = 0.03$ which is a very low level of substitution, and is beyond the scope of the present work.

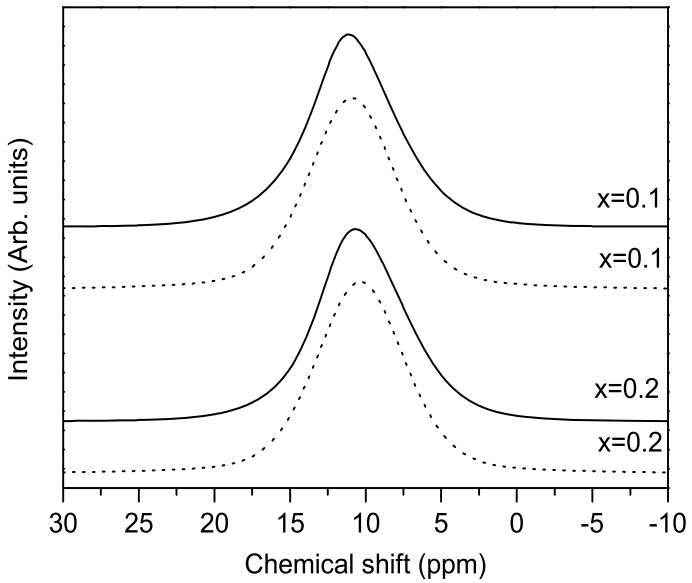


*Figure 5.14: Experimental and simulated $^{27}Al$ MAS NMR spectra of $La_{1-x}Y_xAlO_3$ for $x = 0.1$ and 0.2 (solid and broken lines represent experimental and simulated NMR patterns, respectively).*

*Table 5.2: $^{27}Al$ NMR parameters for different compositions in $La_{1-x}Y_xAlO_3$.*

| $x$ | $\delta_{iso}$ (ppm) | $C_q$ (kHz) |
|---|---|---|
| 0.0 | 11.58 | 150 |
| 0.03 | 11.52 | 192 |
| 0.06 | 11.25 | 452 |
| 0.09 | 11.04 | 527 |
| 0.1 | 10.90 | 566 |
| 0.12 | 10.87 | 579 |
| 0.13 | 10.81 | 584 |
| 0.14 | 10.67 | 681 |
| 0.15 | 10.64 | 688 |
| 0.17 | 10.62 | 703 |
| 0.2 | 10.35 | 740 |
| 0.25 | 10.09 | 832 |
| 0.33 | 9.81 | 893 |
| 0.38 | 9.70 | 910 |

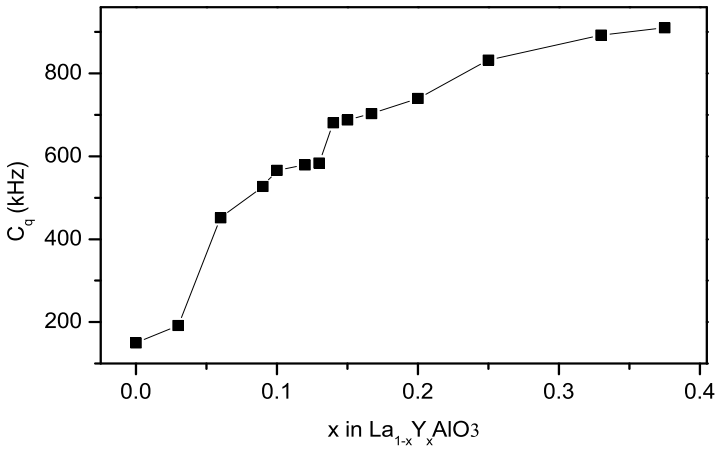


*Figure 5.15: Variation of the $^{27}Al$ quadrupole coupling constant of $La_{1-x}Y_xAlO_3$ as a function of $x$.*

## 5.7 $^{139}$La NMR

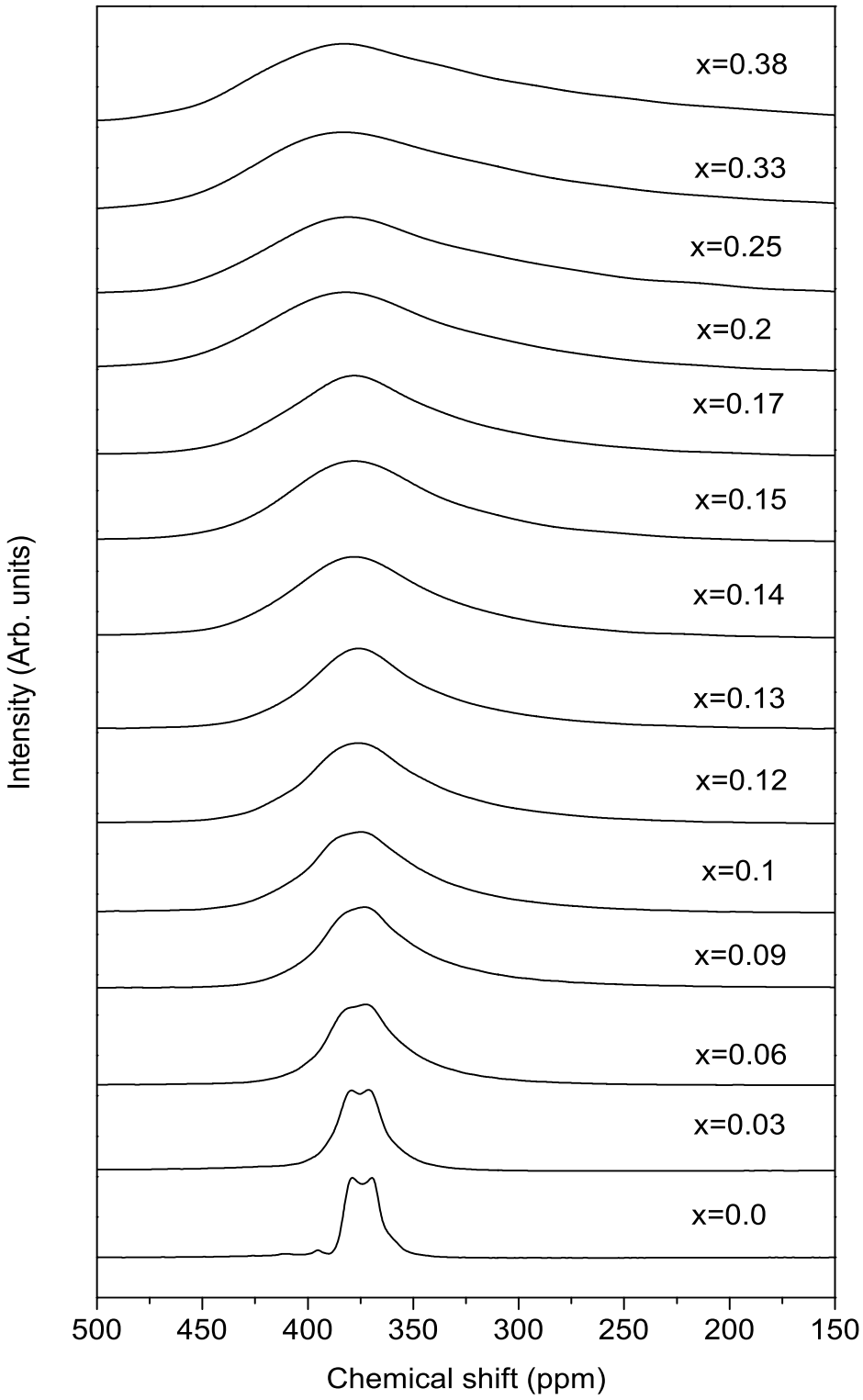


*Figure 5.16: $^{139}La$ MAS NMR spectra of different compositions in $La_{1-x}Y_xAlO_3$.*

The $^{139}$La MAS NMR spectra of all the compositions in $La_{1-x}Y_xAlO_3$, recorded on a 700 MHz spectrometer at the spinning speed of 60 kHz, are shown in figure 5.16. The $^{139}$La MAS NMR spectrum of $LaAlO_3$ has the typical lineshape of a quadrupolar nuclei with two horns and two small peaks at a higher chemical shift side attributed to the satellite transitions. There is a substantial effect on the lineshape of the spectrum of $LaAlO_3$ as the amount of substitution is increased, which is directly observable as a broadening of the spectral lines (for the unsubstituted sample, the spectra spans the range of 400 to 350 ppm whereas for $x = 0.38$, the spectra spans a range of 450 to 200 ppm) and vanishing of the distinct features of lineshape of a quadrupolar nuclei. The changes in the lineshape are arising due to the increase in the quadrupolar coupling constant. In order to estimate the exact chemical shift and the quadrupolar coupling constant, all the spectra were fitted using the DMFIT programme. The experimental and the simulated spectra of the compositions $x = 0.03$, 0.2 and 0.38 are shown in figure 5.17.

The spectra of the unsubstituted compound and that of $x = 0.03$ composition could be simulated using a pure quadrupole lineshape. However, the spectra of the samples with substitution $x \geq 0.06$ could be fitted only using the Czjzek model [23] where there is a distribution of the isotropic chemical shift and quadrupole coupling constant [24], as described in section 2.3.2.6, chapter 2. In the Czjzek model, a distribution in the chemical shift and quadrupole coupling constant are used to fit the spectra. The $^{139}$La NMR spectral parameters: isotropic chemical shift ($\delta_{iso}$), quadrupole coupling constant ($C_q$), Chemical shift distribution ($\Delta_{CS}$) and the asymmetry ($\eta$) parameters are given in table 5.3.

The $^{139}$La NMR parameters are plotted in figure 5.18 and 5.19 as a function of $x$ in $La_{1-x}Y_xAlO_3$. Both the isotropic chemical shift and the quadrupole coupling constant increase with the increasing level of yttrium substitution. The small jump above $x = 0.03$ is due to the difference in the fitting model. However, both the chemical shift and the coupling constant are lower for $x = 0.13$ compared to that for $x = 0.12$, showing a small jump, and a non-linear variation is observed for both parameters for $0.13 \leq x \leq 0.17$. This probably indicates a difference in the

local coordination environment and/or structural changes for substitution above $x > 0.12$. Similar anomalous change in the value of $C_q$ is observed above $x = 0.13$ from the $^{27}Al$ spectra also.

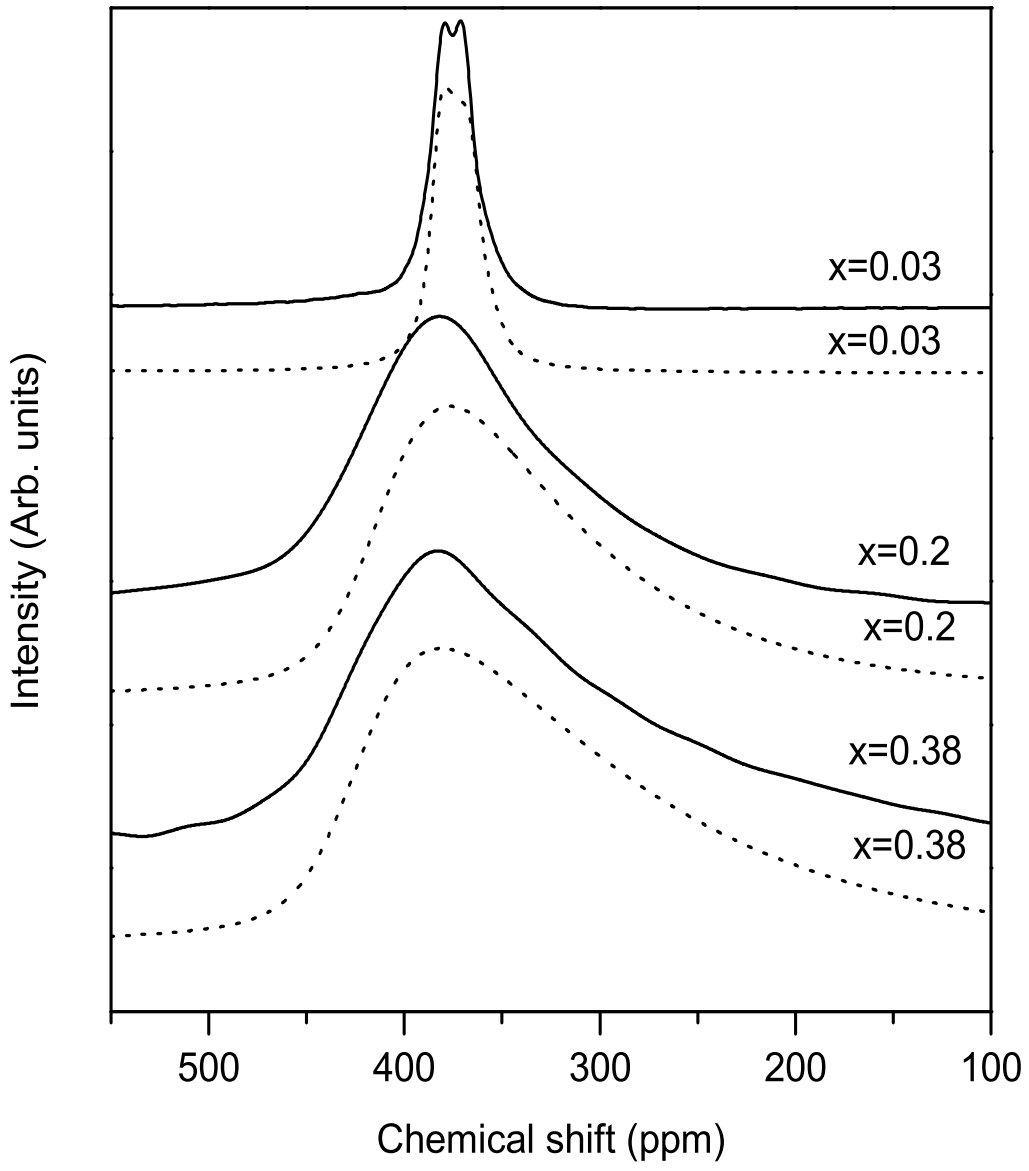


*Figure 5.17: Experimental and simulated $^{139}La$ MAS NMR spectra of $La_{1-x}Y_xAlO_3$ for $x$ = 0.03, 0.2 and 0.38 (solid and broken lines represent experimental and simulated NMR patterns, respectively).*

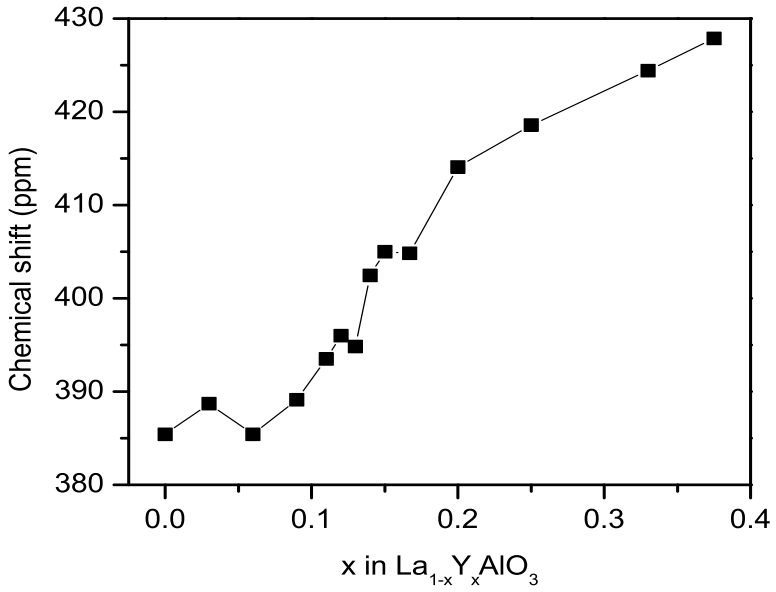


*Figure 5.18: Variation of the $^{139}La$ isotropic chemical shift for $La_{1-x}Y_xAlO_3$ as a function of $x$.*

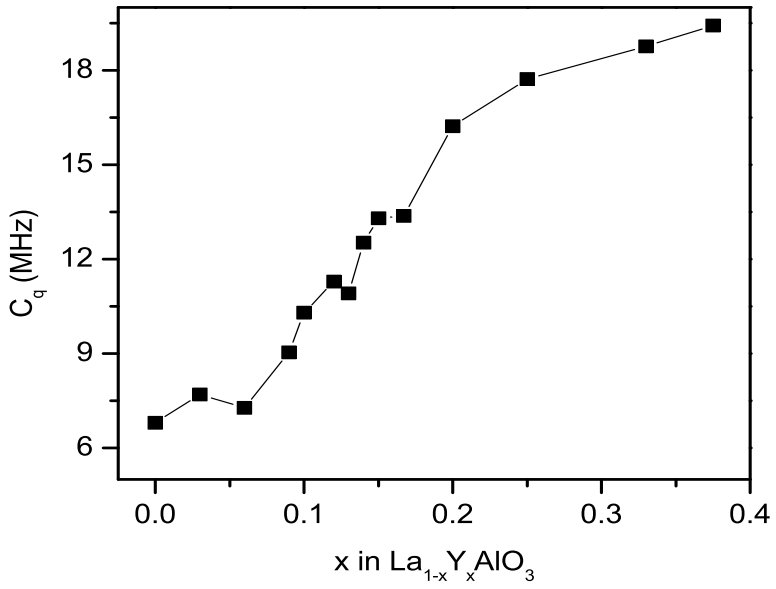


*Figure 5.19: Variation of the $^{139}La$ quadrupole coupling constant for $La_{1-x}Y_xAlO_3$ as a function of $x$.*

*Table 5.3: $^{139}La$ NMR parameters for different compositions in $La_{1-x}Y_xAlO_3$.*

| $x$ | $\delta_{iso}$ (ppm) | $C_q$ (MHz) | $\Delta_{CS}$ | $\eta$ |
|---|---|---|---|---|
| 0.0 | 385.4 | 6.8 | - | 0 |
| 0.03 | 388.7 | 7.7 | - | 0 |
| 0.06 | 385.4 | 7.3 | 21.2 | - |
| 0.09 | 389.1 | 9.0 | 24.1 | - |
| 0.1 | 393.5 | 10.3 | 29.8 | - |
| 0.12 | 396.0 | 11.3 | 30.8 | - |
| 0.13 | 394.8 | 10.9 | 30.4 | - |
| 0.14 | 402.5 | 12.5 | 41.4 | - |
| 0.15 | 405.0 | 13.3 | 43.3 | - |
| 0.17 | 404.8 | 13.4 | 43.5 | - |
| 0.2 | 414.1 | 16.2 | 46.8 | - |
| 0.25 | 418.6 | 17.7 | 42.3 | - |
| 0.33 | 424.4 | 18.8 | 42.4 | - |
| 0.38 | 427.9 | 19.4 | 45.3 | - |

Thus, both the $^{27}Al$ and $^{139}La$ NMR studies indicate that there are some changes in the local coordination environments of $La_{1-x}Y_xAlO_3$ around $x \approx 0.12$-0.13, associated with a structural change as observed from XRD studies. It is noteworthy that the composition at which the anomaly is seen in the variation of the parameters in the $^{139}La$ NMR spectra is at $x = 0.12$ and in the $^{27}Al$ NMR spectra is at $x = 0.13$. This is probably due to the fact that larger La is substituted by smaller Y and the substitution directly affects the La environment. Changes in the local structural environment around La are detected by NMR as soon as they develop in the structure. On the other hand, the effect on Al coordination environment is indirect (due to distortion of $LaO_{12}$ coordination polyhedra, $AlO_6$ octahedra are distorted) and hence small difference in the compositions at which La and Al NMR parameters are deviated.

## 5.8 Conclusions

From the $^{139}La$ and $^{27}Al$ solid-state NMR studies, it is found that the spectral parameters; quadrupolar coupling constant and isotropic chemical shift, show a drastic change around $x = 0.13$ in the $La_{1-x}Y_xAlO_3$ solid solution series, indicating a possible structural change above this composition. Detailed analysis of the powder X-ray diffraction patterns by the Rietveld refinement method indicated multiphase behaviour for compositions $x > 0.13$. The presence of a rhombohedral phase similar to that of $LaAlO_3$ and an orthorhombic phase similar to that of the other end member $YAlO_3$ is verified from the XRD analysis. The structural change takes place in the compositional region corresponding to the substitution of $1/8^{th}$ of La by Y in the pseudo-cubic perovskite unit cell such that each Y is shared by eight unit cells. For $x > 0.125$, more than one La per unit cell will be replaced by Y and due to the large difference in the ionic sizes of these ions, phase separation takes place leading to formation of more than one crystallographic phase to accommodate the Y-rich compositions. The results show that solid-state NMR studies can predict possible structural changes in the solid solution series, and the results may be extendable to other similar systems also.

# Bibliography


[1] G. H. Jonker and J. H. van Santen, *Physica* 1950, 16, 337-349.

[2] Y. Tokura, *Colossal Magnetoresistive Oxides* (Gordon and Breach science publishers, Singapore, 2000).

[3] C. Raj Sankar, S. Vijayanand, P. A. Joy, emphSolid State Sci. 2009, 11, 714718.

[4] H. Y. Hwang, S. W. Cheong, P. G. Radaelli, M. Marezio and B. Batlogg, emphPhys. Rev. Lett. 1995, 75, 914-917.

[5] H. Y. Hwang, T. T. M. Palstra, S. W. Cheong and B. Batlogg, emphPhys. Rev. B 1995, 52, 15046-15049.

[6] B. Raveau, A. Maignan, C. Martin, and M. Hervieu, emphChem. Mater. 1998, 10, 2641-2652

[7] Z. Q. Liu, W. K. Chim, S. Y. Chiam, J. S. Pan and C. M. Ng, *Thin Solid Films* 2013, 534, 177-182.

[8] P. J. Deren and R. Mahiou, Opt. Mater. 2007, 29, 766-772

[9] X. Dong, X. Cui, Z. Fu, S. Zhou, S. Zhang and Z. Dai, *Mater. Res. Bull.* 2012, 47, 212-216.

[10] J. Zhao, N. L. Ross and R. J. Angel, *J. Phys. Condens. Matter* 2004, 16, 8763-8773.

[11] R. Diehl and G. Brandt, *Mater. Res. Bull.* 1975, 10, 85-90.

[12] R. D. Shannon, *Acta Cryst. A* 1976, 32, 751-767.

[13] E. Lima, M. E. Villafuerte-Castrejn, J. Saniger, V. Lara, J. E. Snchez-Snchez and L. Javier lvarez, *Adv. Mater. Science and Engg.* 2012, 2012, 238075.1-7.

[14] E. V. Charnaya, C. Tien, N. V. Chejina, M. K. Lee and S. Y. Sun, *Phys. Solid State* 2007, 49, 449-453.

[15] W. Li, M. W. Zhuo and J. L. Shi, *Mater. Lett.* 2004, 58, 365-368.

[16] W. Kraus and G. Nolze, *PowderCell for Windows (PCW), version 2.4* (The software is freely available from http://www.ccp14.ac.uk.)

[17] B. Jaffe, W. R. Cook and H. Jaffe, *Piezoelectric Ceramics.* Academic Press, London, 1971

[18] R. Dupree, M. H. Lewis and M. E. Smith, *J. Am. Chem. Soc.* 1989, 111, 5125-5132.

[19] D. Iuga, S. Simon, E. de Boer and A. P. M. Kentgens, *J. Phys. Chem. B* 1999, 103, 7591-7598.

[20] F. Blanc, D. S. Middlemiss, L. Buannic, J. L. Palumbo, I. Farnan and C. P. Grey, *Solid State Nucl. Magn. Reson.* 2012, 42, 87-97.

[21] D. Massiot, F. Fayon, M. Capron, I. King, S. Le Calv, B. Alonso, J.-O. Durand, B. Bujoli, Z. Gan and G. Hoatson, *Magn. Reson. Chem.* 2002, 40, 70-76.

[22] E. Gaudin, F. Taulelle, R. Stoyanova, E. Zhecheva, R. Alcántara, P. Lavela and J. L. Tirado, *J. Phys. Chem. B* 2001, 105, 8081-8087.

[23] G. Czjzek, J. Fink, F. Gätz, H. Schmidt, J. M. D. Coey, J. P. Rebouillat and A. Lionard, *Phys. Rev. B* 1981, 23, 2513-2530.

[24] D. R. Neuville, L. Cormier, and D. Massiot, *Geochim. Cosmochim. Acta* 2004, 68, 5071-5079.

[25] F. S. Galasso, *Structure, properties and preparation of perovskite-type compounds* (Pergamon, Oxford, 1969).

# Chapter 6

# Studies on $LaAl_{1-x}M_xO_3$ (M = Co, Ga)

## 6.1 Introduction

Lanthanum manganate, $LaMnO_3$, is an antiferromagnetic material. However, it is known that ferromagnetism can be induced in $LaMnO_3$ by the substitution of Mn-site by other transition metal ions as in $LaMn_{1-x}M_xO_3$ (M = Cr, Co, Ni, Ru, etc) [1–5]. A large increase in the magnetization and changes in the electrical conductivity as well as the Seebeck coefficient are observed between $x = 0.1$ and 0.2 in these substituted compositions. From the detailed magnetic studies on different compositions in $LaMn_{1-x}Co_xO_3$, it has been shown that true ferromagnetic character is observed for compositions $x > 0.125$ [6]. These results indicate the possibility of local structural changes associated with the distribution of the substituted ions in the crystal lattice, apart from the size and nature of the substituted ions, in deciding the physical properties of the substituted compositions.

The objective of the work reported in this chapter is to study the local structural changes in $LaAlO_3$, arising from the substitution of cations at the Al-site, using solid-state NMR. It is expected that the results may be relevant to explain some of the changes in the properties observed in the related magnetic materials. In order to study the effect of substitution as well as the size of the substituted ion, on the octahedral distortion and the local structural changes, the $Al^{3+}$ ion is substituted by two different ions, $Co^{3+}$ and $Ga^{3+}$. $Co^{3+}$ is selected because of its comparable ionic size with that of $Al^{3+}$ since the ionic radius of $Al^{3+}$ is 0.535 Å and that of low-spin $Co^{3+}$ is 0.545 Å in the octahedral coordination environment [7]. Also, $Co^{3+}$ is expected to exist in the low-spin state as reported for Al-substituted $LaCoO_3$, so that the entire material remains non-magnetic and the NMR line broadening due to the presence of magnetic ions can be avoided to get good spectral characteristics [8,9]. $Ga^{3+}$ with ionic radius of 0.625 Å is selected as a representative ion with larger ionic radius compared to that of $Al^{3+}$. Due to the differences in the electron distribution between the two elements Co and Ga, the electric field gradient around the Al atom is also expected to change which would result in different quadrupole behaviors around the Al atom, which can be probed through solid-state NMR.

## 6.2 NMR methodology

$^{27}$Al solid-state NMR experiments were carried out at room temperature on a Bruker AV-300 (aluminium resonance frequency, $\nu_{Al}$ = 78.2 MHz) spectrometer, operating at a field of 7.05 T. The MAS NMR experiments were done using a 4 mm BL MAS probe at the magic angle spinning rate of 10 kHz and a short pulse duration 3 $\mu$s was used. 200 scans were collected with a recycle delay of 20 s.

$^{139}$La solid-state NMR experiments were carried out on a Bruker AV-700 ($\nu_{La}$ = 98.1 MHz) spectrometer, operating at a field of 16.4 T. The MAS NMR data on AV-700 were collected using a 2.5 mm MAS probe, at a spinning speed of 60 kHz. The quantitative MAS NMR spectra were recorded using a pulse width of 1 $\mu$s and 8,000 scans were acquired with a recycle delay of 0.25 s.

## 6.3 Studies on $LaAl_{1-x}Co_xO_3$

The crystal structure of $LaAlO_3$ as well as $LaCoO_3$ is rhombohedral. A Rietveld refinement study on $LaAlO_3$ and $LaCoO_3$ has shown that both materials crystallize with the space group $R\bar{3}c$ and the lattice parameters of $LaCoO_3$ are slightly larger when compared to that of $LaAlO_3$ [10]. This is because of the small size difference between the Al and the Co ions.

Unlike $LaAlO_3$ which is non-magnetic, $LaCoO_3$ exhibits magnetic properties also, because the $Co^{3+}$ ions ($d^6$ configuration) can exist in high-spin (S = 2, $t_2g^4e_g^2$), intermediate-spin (S = 1, $t_2g^5e_g^1$) or low-spin (S = 0, $t_2g^6e_g^0$) states [11–14]. $Co^{3+}$ in $LaCoO_3$ is shown to exist in the low-spin or intermediate-spin state at room temperature with very low magnetic susceptibility [15,16]. It has been reported that $Co^{3+}$ exists in the low-spin state (S = 0) in $LaCoO_3$ when Co is substituted by Al or Ga [8]. Therefore, different compositions in $LaAl_{1-x}Co_xO_3$ are expected to be non-magnetic due to the lack of any unpaired electrons in $Co^{3+}$.

### 6.3.1 Synthesis

A series of Co-substituted lanthanum aluminate compositions, $LaAl_{1-x}Co_xO_3$ ($x$ = 0.0, 0.06, 0.09, 0.10, 0.12, 0.13, 0.14, 0.17 and 0.2) were prepared using the sol-gel method. Ethylene glycol (Ranbaxy), citric acid (Sd fine), aluminium nitrate (Sd fine), cobalt nitrate (sd fine) and lanthanum nitrate (Aldrich) were used as-received without any further purification. Aluminium nitrate was added to a mixture of citric acid and ethylene glycol. After complete dissolution, the solution was heated at 80 °C and stoichiometric quantities of lanthanum nitrate and cobalt nitrate were added. The molar ratio of 1:1 was maintained for citric acid to total metal cations concentration and 1:4 ratio was maintained between citric acid and ethylene glycol. For example, for the synthesis of $x = 0.2$ composition, 2.86 g of citric acid and 2.04 g of aluminium nitrate were completely dissolved in 4 ml of ethylene glycol. The solution was then heated to 80 °C and to this solution, 2.94 g of lanthanum nitrate and 0.40 g of cobalt nitrate were added. After the complete evaporation of superfluous water, the resulting viscous mass was heated at 140 °C for 2 hours which produced a solid amorphous resin, which was transferred to a pre-heated oven at 250 °C for charring for 2 hrs. The resulting powder was calcined at 700, 800, 1000, 1100 °C and 1200 °C for 2 hrs each with intermediate grindings. The calcined powders were finally heated at 1400 °C for 6 hours, so as to get $LaAl_{1-x}Co_xO_3$ in single phase forms without any impurities.

### 6.3.2 Characterization

All the $LaAl_{1-x}Co_xO_3$ samples are initially characterized by the powder X-ray diffraction method. The XRD patterns of all the Co substituted samples are shown in figure 6.1. The simulated pattern of $LaAlO_3$ is also shown in the figure for comparison. From the patterns, it is clear that single phase compositions are formed without any impurities.

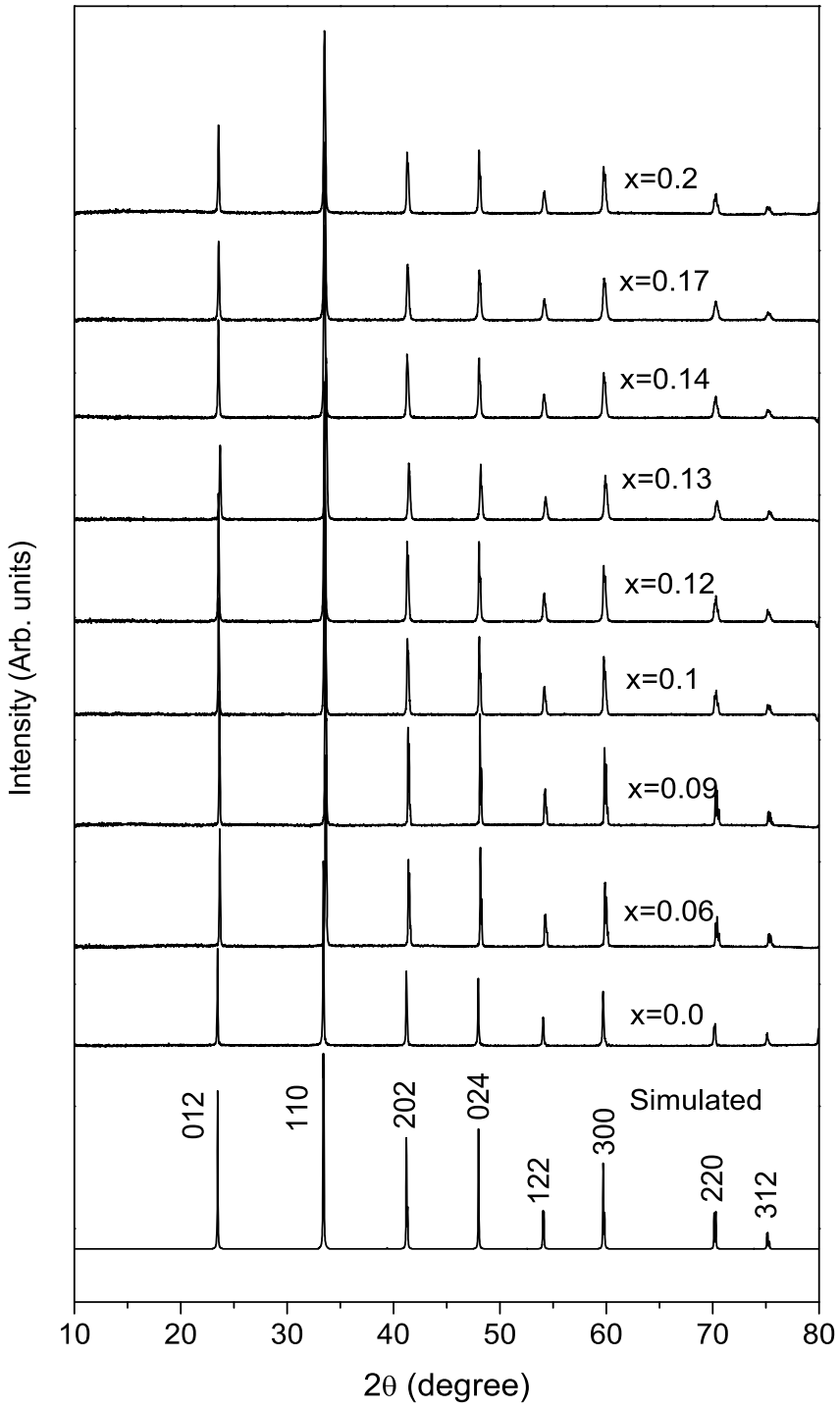


*Figure 6.1: Powder XRD patterns of different compositions in $LaAl_{1-x}Co_xO_3$, along with the simulated pattern of $LaAlO_3$.*

The zoomed view of (024) peak of the compositions for $x = 0$ and 0.2, are shown in figure 6.2. From the figure, it is clear that the compositions are still in the rhombohedral phase even after the substitution of Co up to $x = 0.2$ in $LaAl_{1-x}Co_xO_3$. However, there is a small shift of the peak to lower angles indicating a small increase in the lattice parameter for the Co substituted samples, which is expected due to the slightly larger size of the $Co^{3+}$ ions.

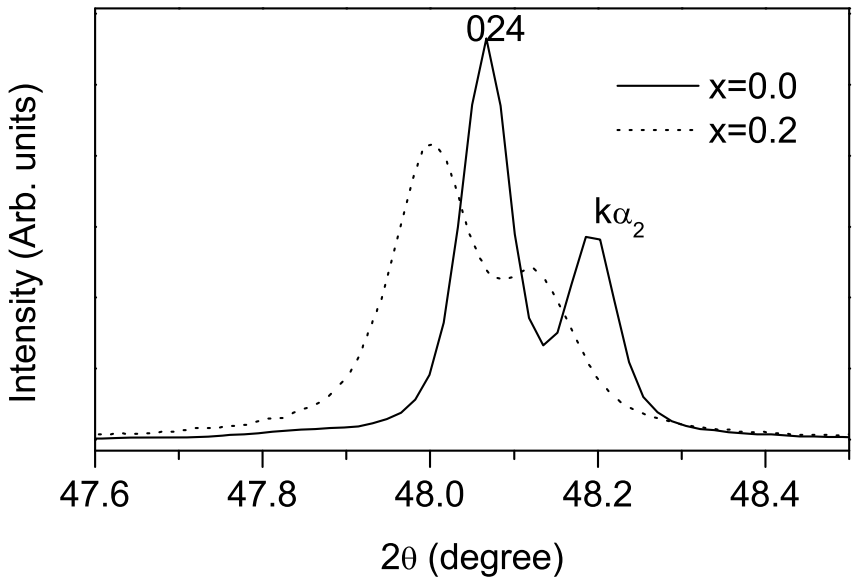


*Figure 6.2: Zoomed XRD pattern showing the rhombohedral (024) peak of $LaAl_{1-x}Co_xO_3$ for $x = 0.0$ and 0.2.*

The lattice parameters of the different compositions of $LaAl_{1-x}Co_xO_3$ are calculated by a least squares fitting of the XRD patterns and the calculated values are given in table 6.1. The variation of the lattice parameters with $x$ in $LaAl_{1-x}Co_xO_3$ is shown in figure 6.3. From the figure, it is clear that there is a small but systematic increase in the lattice parameter '$a$' with increasing degree of substitution. For both '$a$' and '$c$', the difference in the lattice parameters for $x = 0$ and 0.2 is very small, around 0.003 Å. This confirms that the $Co^{3+}$ ions are in their low-spin state where the size of $Co^{3+}$ is comparable to that of $Al^{3+}$ (the size of high-spin $Co^{3+}$ is 0.61 Å which is much larger than that of $Al^{3+}$ and hence, a large increase

in the lattice parameters is expected). However, a small anomaly in the variation of the lattice parameters is observed around $x \approx 0.12$. A small jump is observed for '$c$' at this value of $x$ and a change in the slope is observed for '$a$'. This could be due to a minor distortion of the structure around $x = 1/8$.

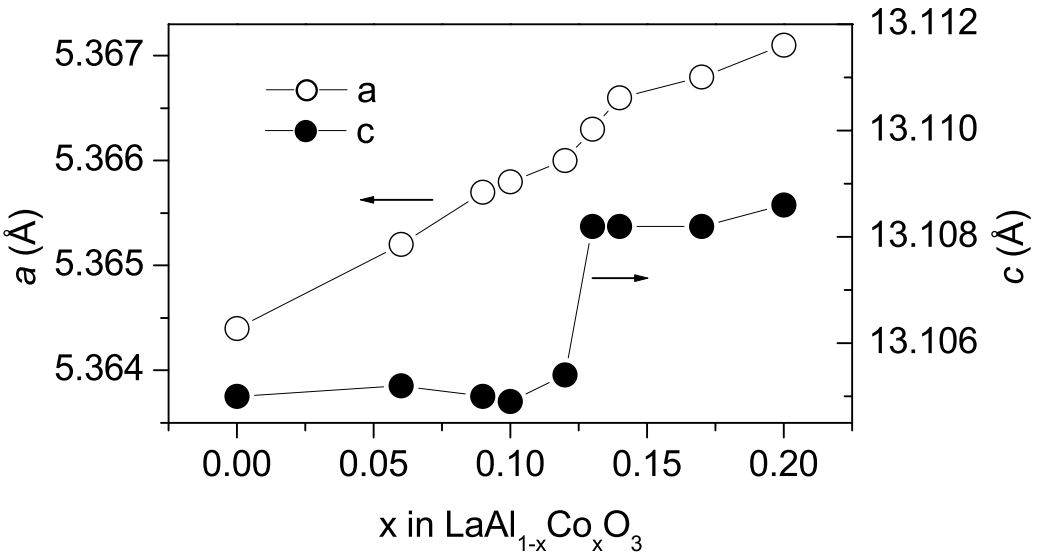


*Figure 6.3: Variation of the hexagonal lattice parameters of $LaAl_{1-x}Co_xO_3$ as a function of $x$.*

Rietveld refinement analysis of the XRD pattern of the composition $x = 0.2$ has been carried out, using the two different space groups R3c and R$\overline{3}$c, to verify whether there is any change over of the space group on substitution of Al by Co. For LaAlO3, both space groups gave identical best fit parameters, as described in chapter 4 (see section 4.4). The refinement plots for $LaAl_{0.8}Co_{0.2}O_3$ are shown in figures 6.4 and 6.5. The best fit parameters are compared in table 6.2. From the Rietveld refinement of the unsubstituted sample, it was not possible to distinguish between these two space groups because of the comparable $\chi^2$ and residual factors for both the space groups. However, for the Co-substituted sample, even though good fits are obtained using both the space groups, the $\chi^2$ and $R_{wp}$ values are lower for the R3c space group compared to the R$\overline{3}$c space group. This suggests

that the possible space group of the unsubstituted compound also can be R3c. Thus, the structural studies indicate that the substituted compositions are still having the rhombohedral symmetry and suggest a stabilization of the R3c space group after Co substitution. The results also indicate minor structural changes around $x = 1/8$, probably due to the uniform distribution of Co in the $LaAlO_3$ lattice around this value of $x$.

*Table 6.1: Lattice parameters for different compositions in $LaAl_{1-x}Co_xO_3$.*

| $x$ | $a$ (Å) | $c$ (Å) |
|---|---|---|
| 0.0 | 5.3644 | 13.1050 |
| 0.06 | 5.3652 | 13.1052 |
| 0.09 | 5.3657 | 13.1050 |
| 0.1 | 5.3658 | 13.1049 |
| 0.12 | 5.3660 | 13.1054 |
| 0.13 | 5.3663 | 13.1082 |
| 0.14 | 5.3666 | 13.1082 |
| 0.17 | 5.3668 | 13.1082 |
| 0.2 | 5.3671 | 13.1086 |

*Table 6.2: Rietveld refinement parameters for $LaAl_{0.8}Co_{0.2}O_3$.*

| space group | $\chi^2$ | $R_{wp}$ | $R_{F^2}$ |
|---|---|---|---|
| R3c | 3.646 | 0.0641 | 0.0351 |
| $R\bar{3}c$ | 3.838 | 0.0658 | 0.0351 |

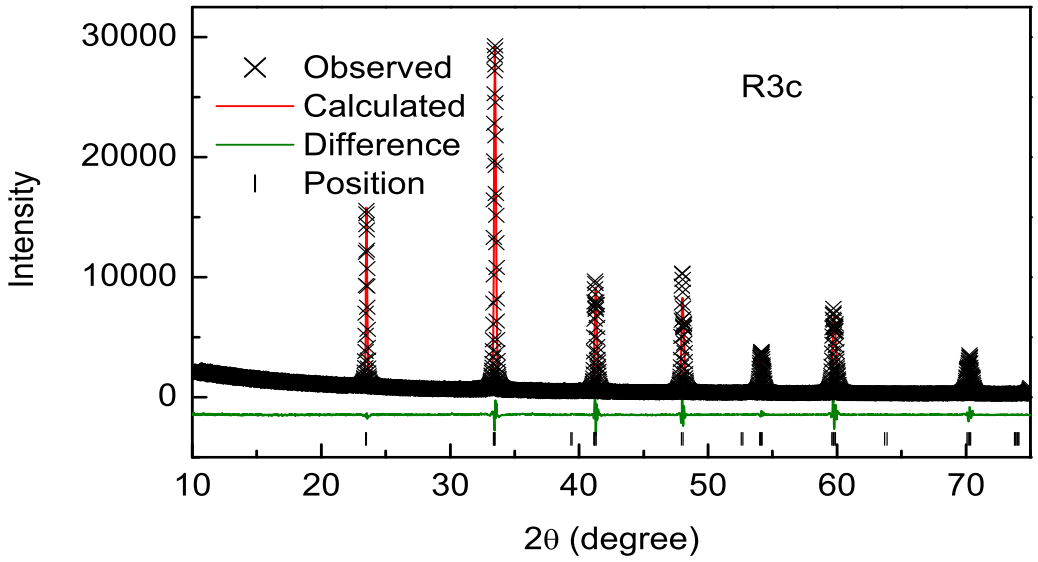


*Figure 6.4: Result of the Rietveld refinement of the XRD pattern of $LaAl_{0.8}Co_{0.2}O_3$ using the space group R3c.*

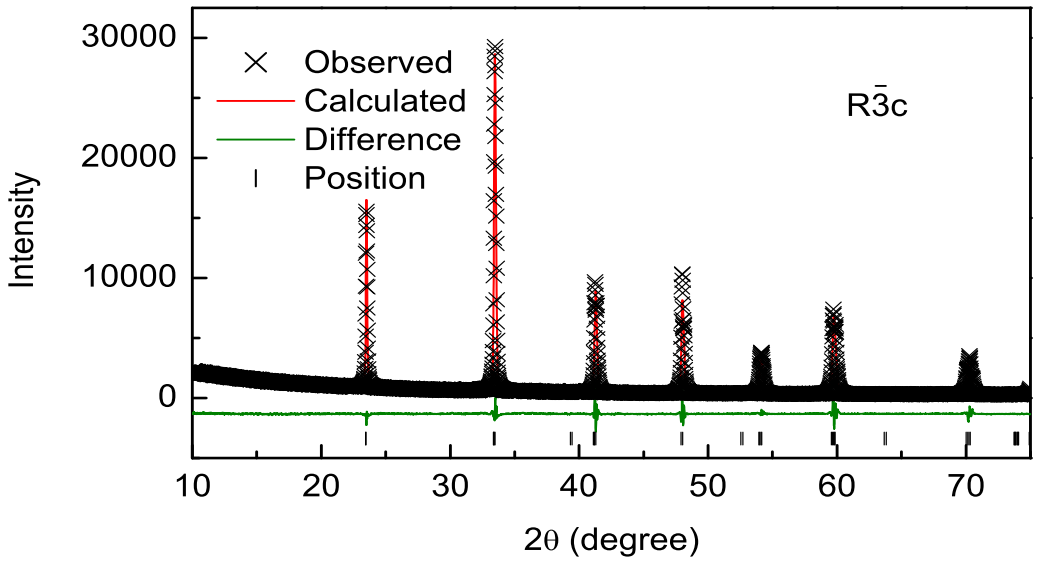


*Figure 6.5: Result of the Rietveld refinement of the XRD pattern of $LaAl_{0.8}Co_{0.2}O_3$ using the space group $R\bar{3}c$.*

### 6.3.3 $^{27}$Al NMR

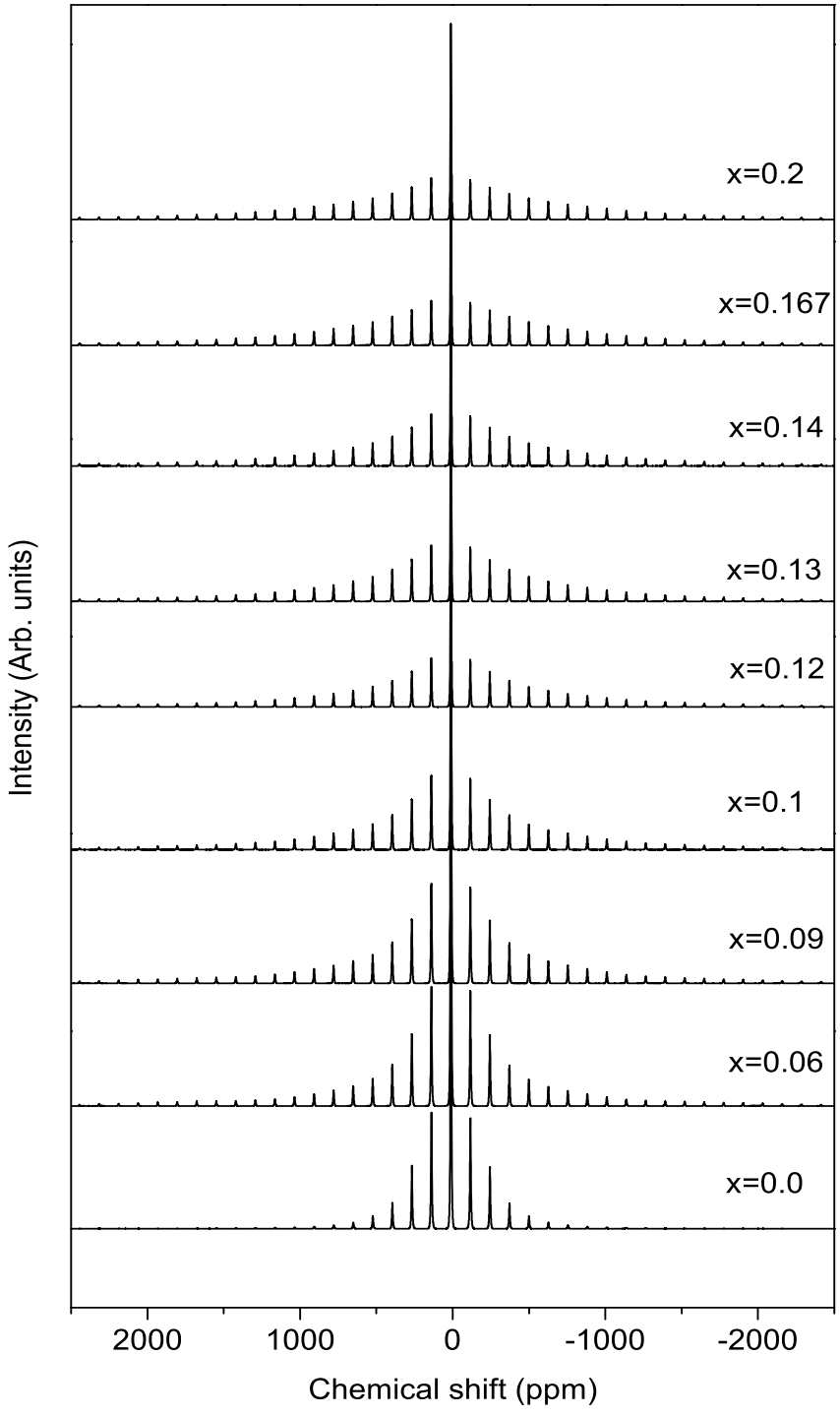


*Figure 6.6: $^{27}Al$ MAS NMR spectra of different compositions in $LaAl_{1-x}Co_xO_3$.*

$^{27}$Al MAS NMR spectra of the $LaAl_{1-x}Co_xO_3$ samples were recorded on a 300 MHz spectrometer. The spectra of different compositions, recorded at a spinning speed of 10 kHz, with full spinning sidebands, are shown in figure 6.6. The intensities of the spinning sidebands increase with the amount of Co substitution at the Al-site, indicating an increase in the quadrupole coupling constant with the degree of substitution.

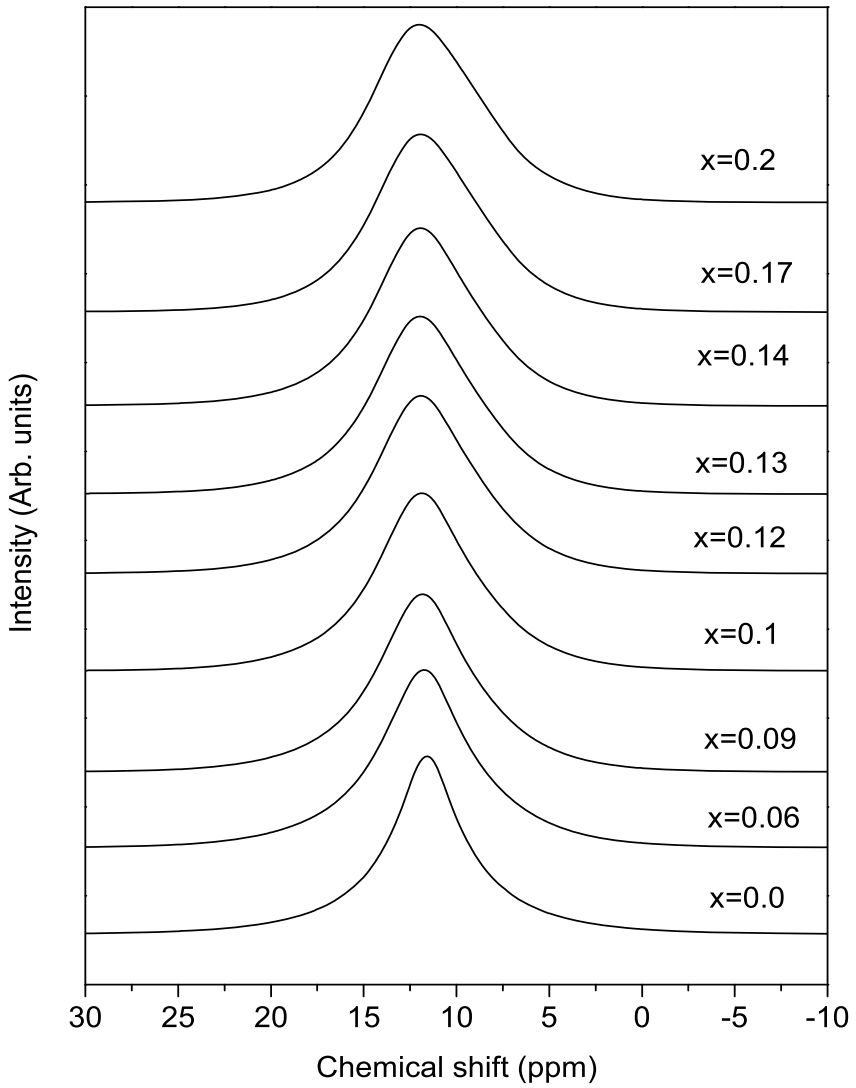


*Figure 6.7: The central transition region of the $^{27}Al$ MAS NMR spectra of $LaAl_{1-x}Co_xO_3$.*

A close view of the central transition region of the $^{27}$Al NMR spectra in figure 6.7 shows that the peak for different compositions are centered around ∼11 ppm and there is not much change in the chemical shift for the substituted samples, indicating the presence of a single octahedral site. However, there is a small increase in the broadening of the spectral lines, with increasing Co content, arising due to the slight increase in the quadrupole coupling constant. This effect is very much obvious for $x = 0.06$, and this is because of the sudden changes in the electron distribution around the Al nucleus caused by the substitution of Al by Co. Since the ionic radii of Al and Co are comparable, there is no drastic effect seen in the spectra.

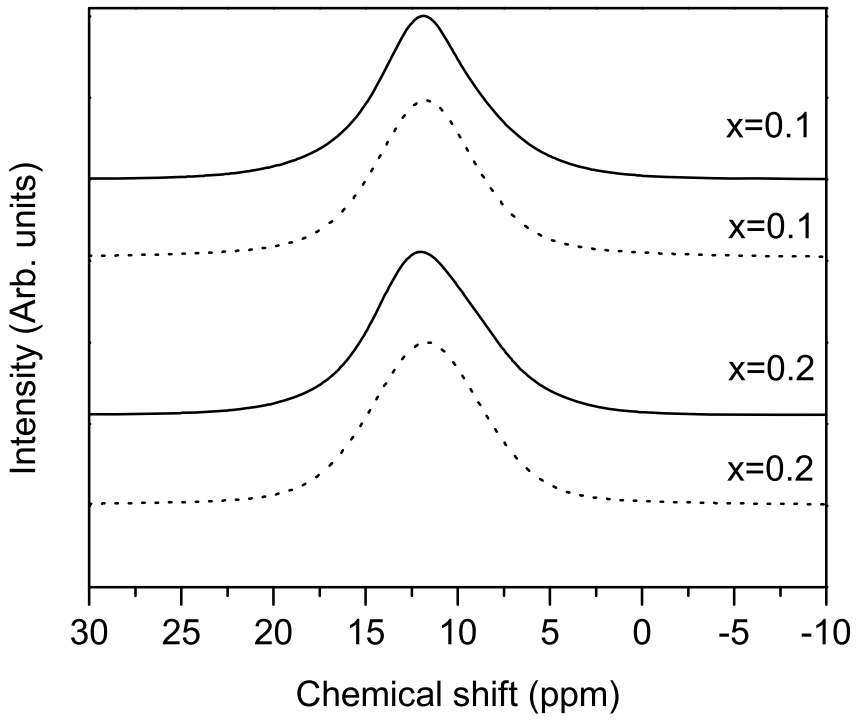


*Figure 6.8: Experimental and simulated $^{27}$Al MAS NMR spectra of $LaAl_{1-x}Co_xO_3$ for $x = 0.1$ and 0.2 in the central transition region (solid and broken lines represent experimental and simulated NMR patterns, respectively).*

*Table 6.3: $^{27}Al$ NMR parameters for $LaAl_{1-x}Co_xO_3$.*

| $x$ | $\delta_{iso}$ (ppm) | $C_q$ (kHz) |
|---|---|---|
| 0.0 | 11.58 | 150.0 |
| 0.06 | 11.74 | 269.7 |
| 0.09 | 11.77 | 299.1 |
| 0.1 | 11.75 | 308.0 |
| 0.12 | 11.74 | 333.0 |
| 0.13 | 11.76 | 403.0 |
| 0.14 | 11.74 | 409.0 |
| 0.17 | 11.65 | 524.0 |
| 0.2 | 11.69 | 545.0 |

The NMR parameters are obtained for the different compositions by the simulation of the NMR lineshapes using the DMFIT program. The $^{27}$Al NMR parameters obtained are given in table 6.3. The experimental and the simulated NMR patterns for the $x = 0.1$ and $x = 0.2$ compositions are given in figure 6.8. From the table, it is clear that the $^{27}$Al NMR parameters are not much affected by the Co substitution at the Al-site compared to the $^{27}$Al NMR parameter variations observed in the case of substitution of Y at the La-site, $La_{1-x}Y_xAlO_3$ (see section 5.6, chapter 5) despite the fact that in the present case the substituted site is directly probed. In the Co-substituted samples, the chemical shift shows an unsystematic variation between 11.58 and 11.77 ppm, which is within the error limit of the analysis. However, the quadrupole coupling constant increases from 150 kHz for the unsubstituted sample to 545 kHz for $x = 0.2$, indicating some distortion of the $AlO_6$ octahedra which is arising from the difference in the electron distribution in Al and Co. From the plot of $C_q$ as a function of the amount of substitution, as shown in figure 6.9, it may be seen that $C_q$ increases almost linearly up to $x = 0.12$ and a small jump in the value of the quadrupole coupling constant is observed above $x = 0.12$. It may be recalled that the structural studies

also indicated a small jump in the lattice parameter above this value of $x \approx 1/8$ (see figure 6.3), suggesting that the small jump in the value of $C_q$ is associated with some minor local structural changes.

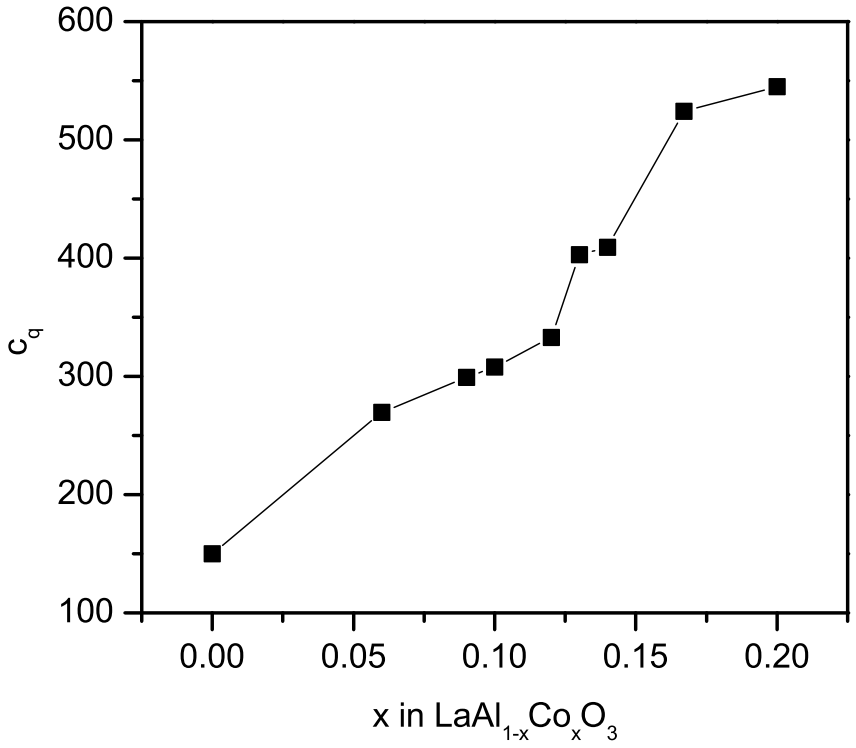


*Figure 6.9: Variation of the $^{27}Al$ quadrupole coupling constant of $LaAl_{1-x}Co_xO_3$ as a function of $x$.*

### 6.3.4 $^{139}$La NMR

Although the Al-site is substituted in $LaAlO_3$ by Co, slight changes in the La environment are also expected because of the difference in the coordination behaviors arising from the difference in the electron distribution around the nucleus with increasing amount of substitution. $^{139}$La MAS NMR spectra of the substituted samples recorded on a 700 MHz spectrometer, at a spinning speed of 60 kHz, are shown in figure 6.10.

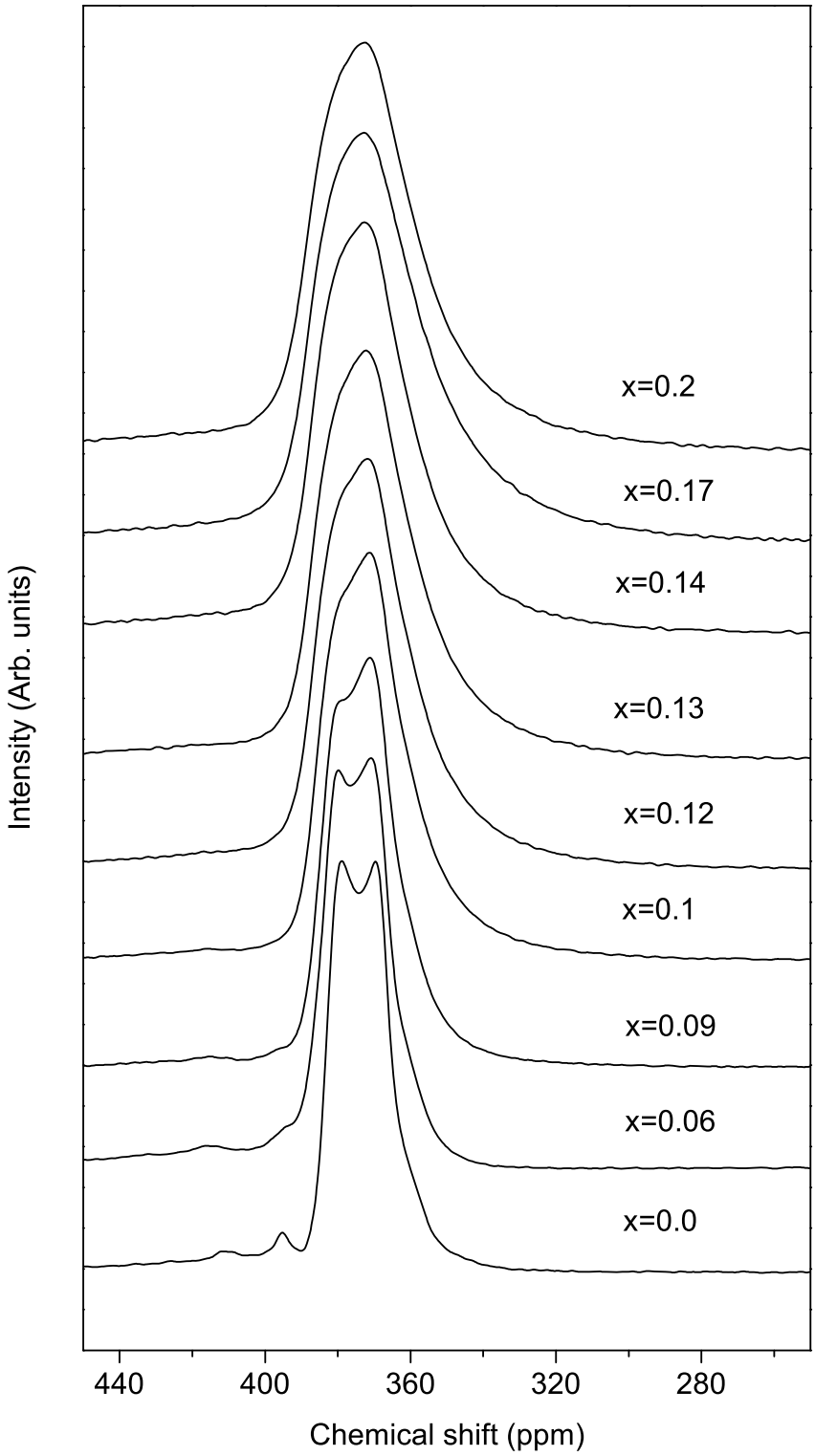


*Figure 6.10: $^{139}La$ MAS NMR spectra of different compositions in $LaAl_{1-x}Co_xO_3$.*

*Table 6.4: $^{139}La$ NMR parameters for $LaAl_{1-x}Co_xO_3$.*

| $x$ | $\delta_{iso}$ (ppm) | $C_q$ (MHz) | $\eta$ |
|---|---|---|---|
| 0.0 | 385.4 | 6.8 | 0.00 |
| 0.06 | 387.0 | 6.9 | 0.25 |
| 0.09 | 387.8 | 7.2 | 0.44 |
| 0.1 | 388.3 | 7.5 | 0.47 |
| 0.12 | 389.1 | 7.8 | 0.44 |
| 0.13 | 389.6 | 7.9 | 0.46 |
| 0.14 | 389.8 | 8.0 | 0.40 |
| 0.17 | 390.3 | 8.4 | 0.34 |
| 0.2 | 391.1 | 8.5 | 0.40 |

From the figure, it is clear that the La environment is slightly affected by the Co substitution at the Al-site. The quadrupole lineshape remains almost unaffected by the Co substitution up to $x = 0.1$. However, the lineshape continuously changes above $x = 0.1$ onwards, which may be due to a change in the asymmetry parameter or from a distribution of the NMR parameters. For $x = 0.2$, the chemical shift appears to be the same as that for $x = 0$. However, there is a slight broadening of the spectra at higher values of $x$. The spectra for $x = 0.2$ covers the range from 400 ppm to 325 ppm compared to the spectra of $x = 0$, which covers a range from 380 to 350 ppm.

In order to get the actual NMR parameters, all the spectra are fitted using a quadrupolar model incorporated in the DMFIT program. The experimental and simulated $^{139}$La MAS NMR spectra of $x = 0.1$ and 0.2 are shown in figure 6.11 and the NMR parameters obtained from the deconvolution of the spectra are given in table 6.4. From table 6.4, it may be seen that the chemical shift of the substituted samples is found to vary from 385 ppm to 391 ppm and the quadrupole coupling constant is varied from 6.8 MHz to 8.5 MHz. The variations of the NMR parameters are shown in figure 6.12 and 6.13. There is no drastic change in the

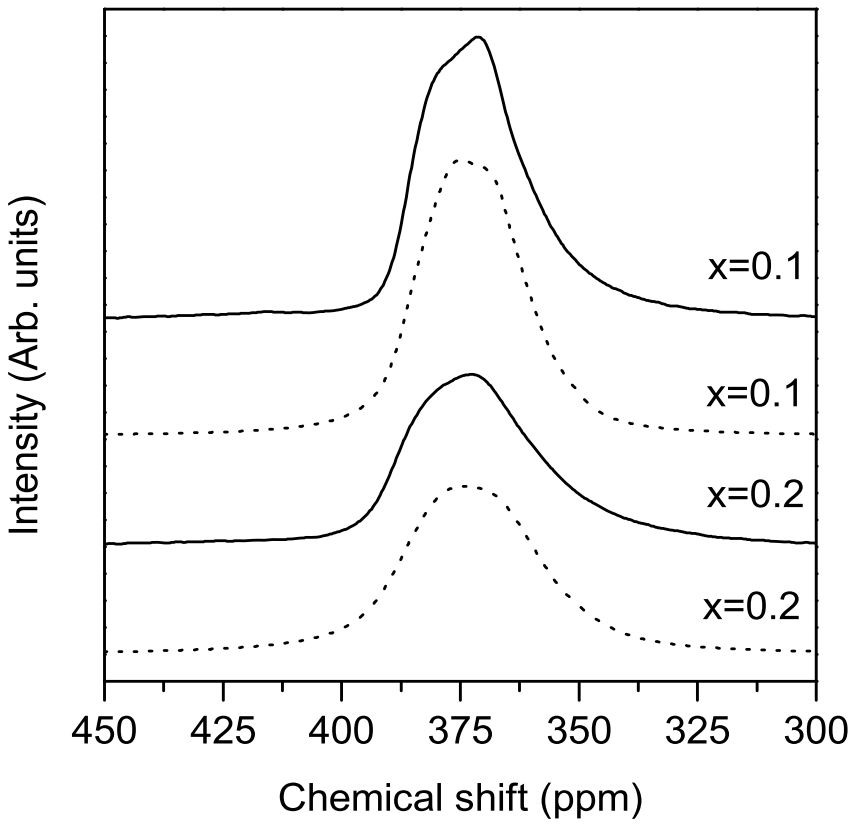


*Figure 6.11: Experimental and simulated $^{139}La$ MAS NMR spectra of $LaAl_{1-x}Co_xO_3$ for $x = 0.1$ and 0.2 (solid and broken lines represent experimental and simulated NMR patterns, respectively).*

chemical shift or the quadrupole coupling constant for $LaAl_{1-x}Co_xO_3$ compared to that observed for the Y substituted $La_{1-x}Y_xAlO_3$ compositions (see figure 5.17, section 5.7, chapter 5). This is because, in case of $La_{1-x}Y_xAlO_3$, the nucleus at the site of substitution is probed and moreover, the ionic sizes of $La^{3+}$ and $Y^{3+}$ are different which caused greater changes in the spectra. In the case of $LaAl_{1-x}Co_xO_3$, the nuclei which is far from the substituted site is probed and also the size difference between the $Al^{3+}$ and $Co^{3+}$ ions are very small so that there are no drastic changes due to the size. However, it may be noted that a slope change is observed above $x = 0.12$ in the linear variation of the chemical shift. Similar changes are also observed in the variation of $C_q$.

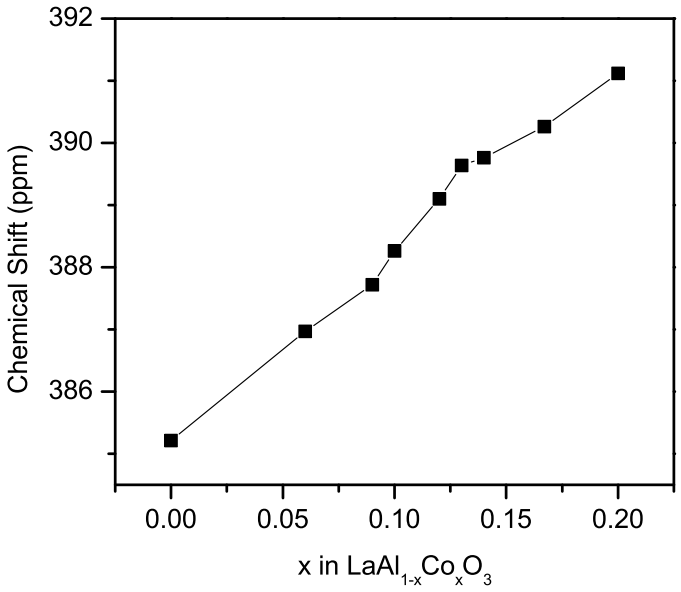


*Figure 6.12: Variation of the $^{139}La$ isotropic chemical shift of $LaAl_{1-x}Co_xO_3$ as a function of $x$.*

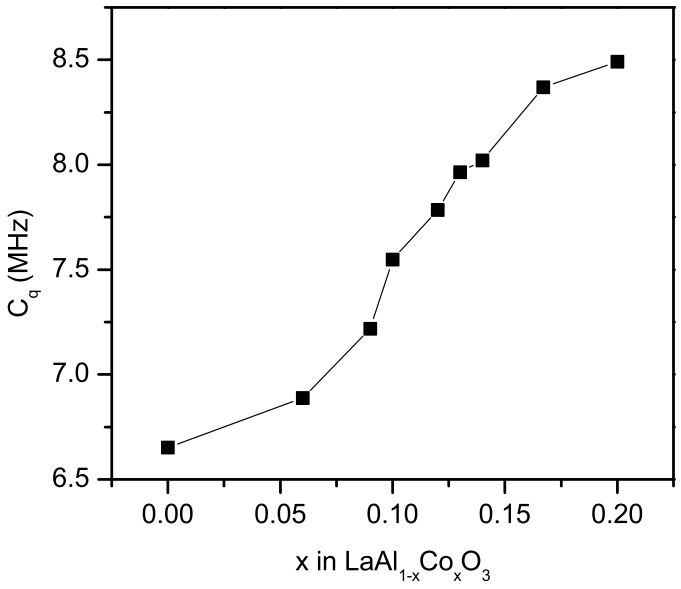


*Figure 6.13: Variation of the $^{139}La$ quadrupole coupling constant of $LaAl_{1-x}Co_xO_3$ as a function of $x$.*

### 6.3.5 Summary

The structural studies on different compositions in $LaAl_{1-x}Co_xO_3$ showed that all the samples are formed in the rhombohedral crystal structure. A linear variation in the lattice parameters is observed up to $x = 0.12$ and a small jump is observed above this composition. Rietveld refinement analysis showed that $LaAl_{0.8}Co_{0.2}O_3$ crystallizes with the space group R3c, indicating that the possible space group of the unsubstituted compound is also the same even though both space groups R3c and $R\overline{3}c$ gave identical residual parameters. Both $^{139}La$ and $^{27}Al$ NMR spectral parameters are found to vary only slightly suggesting a slight distortion of the Al octahedra on Co substitution. The substitution also affects the La environment as seen from the variation of the La NMR spectral parameters. The NMR spectral parameters also showed a deviation above $x = 0.12$, indicating a possible structural rearrangement above $x = 1/8$.

## 6.4 Studies on $LaAl_{1-x}Ga_xO_3$

The ionic radius of $Ga^{3+}$ is 0.62 Å, which is larger than that of $Al^{3+}$ (0.535 Å), in octahedral coordination. Therefore, substitution of $Al^{3+}$ by $Ga^{3+}$ in $LaAlO_3$ offers a way to understand the size effect on the local structural aspects by the substitution at the B-site of the perovskite lattice.

### 6.4.1 Synthesis

A series of Ga substituted compositions, $LaAl_{1-x}Ga_xO_3$ ($x$ = 0.0, 0.06, 0.09, 0.10, 0.12, 0.13, 0.14, 0.17, 0.2, 0.25, 0.33, 0.38, 0.5), were prepared by the sol-gel method, followed by calcination, as reported previously [17]. Ethylene glycol (Ranbaxy), citric acid (Sd fine), aluminium nitrate (Sd fine), gallium nitrate (Aldrich) and lanthanum nitrate (Aldrich) were used as-received without any further purification. Aluminium nitrate was added to a mixture of citric acid and ethylene glycol. After complete dissolution, the solution was heated at 80 °C and stoichiometric quantities of lanthanum nitrate and gallium nitrate were added. The molar

ratio of 1:1 was maintained for citric acid to total metal cations concentration and 1:4 ratio was maintained between citric acid and ethylene glycol. For example, for the synthesis of $x = 0.2$ composition, 2.01 g of aluminium nitrate and 0.28 g of citric acid were dissolved completely in 4 ml of ethylene glycol. The solution was then heated at 80 °C and 2.90 g of lanthanum nitrate and 0.56 g of gallium nitrate were added to this solution. After the complete evaporation of superfluous water, the resulting viscous mass was heated at 140 °C for 2 hours which produced a solid amorphous resin, which was transferred to a pre-heated oven at 250 °C for charring for 2 hrs. The resulting powder was calcined at 700, 800, 1000, 1100 °C and 1200 °C for 2 hrs each with intermediate grindings. The calcined powders were finally heated at 1400 °C for 6 hours, so as to get $LaAl_{1-x}Ga_xO_3$ in single phase forms without any impurities.

### 6.4.2 Characterization

The powder XRD patterns of all the Ga substituted compositions in $LaAl_{1-x}Ga_xO_3$ are shown in figure 6.14. Although the end composition $LaGaO_3$ has the orthorhombic crystal structure, it is clear from the XRD patterns that all the samples are formed in single phase with the rhombohedral perovskite structure of $LaAlO_3$. A close view of the (024) peaks of the compositions $x = 0$ and 0.5 are shown in figure 6.15. A shift in the position of the peak to lower angles is observed indicating an increase in the lattice parameters. The lattice parameters are obtained by least squares fitting of the whole patterns and the values are given in table 6.5. The lattice parameters of the substituted samples are found to be increasing considerably as shown in figure 6.16. This is expected because of the substitution of $Al^{3+}$ which has ionic radius 0.535 Å by $Ga^{3+}$ whose ionic radius is 0.62 Å. The lattice parameter '$a$' increases almost linearly with increasing $x$. However, a non-linear behaviour is observed between $x = 0.1$ and 0.15. Similarly, the value of '$c$' varies only a little for $x > 0.3$.

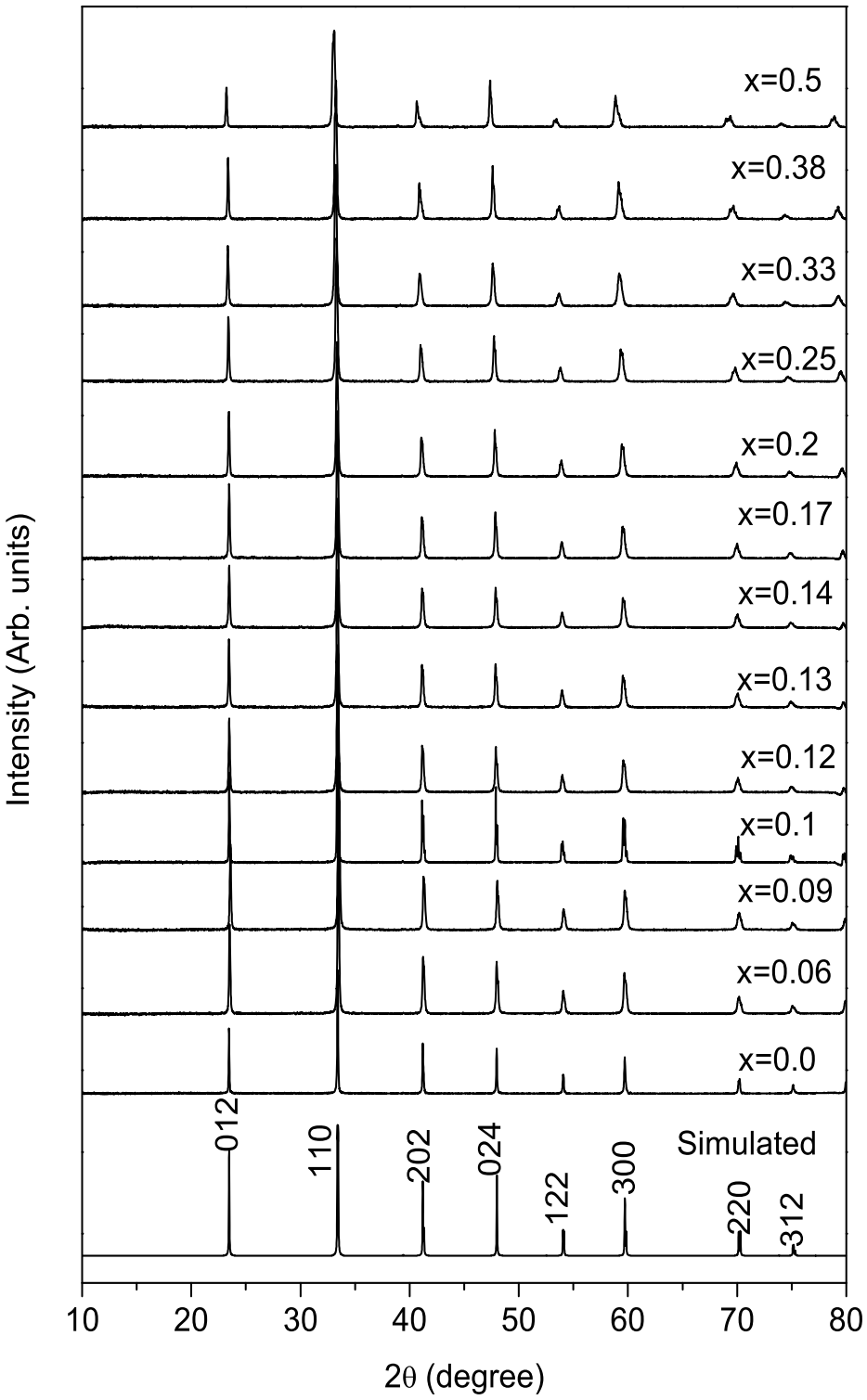


*Figure 6.14: Powder XRD patterns of different compositions in $LaAl_{1-x}Ga_xO_3$. The simulated pattern of $LaAlO_3$ is shown for comparison.*

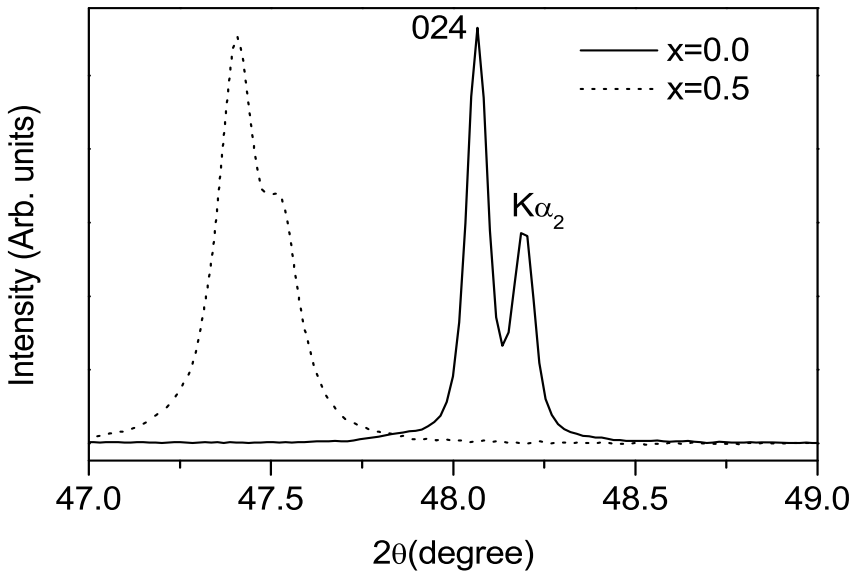


*Figure 6.15: XRD patterns showing the zoomed rhombohedral (024) peak of $LaAl_{1-x}Ga_xO_3$ for $x = 0.0$ and 0.5.*

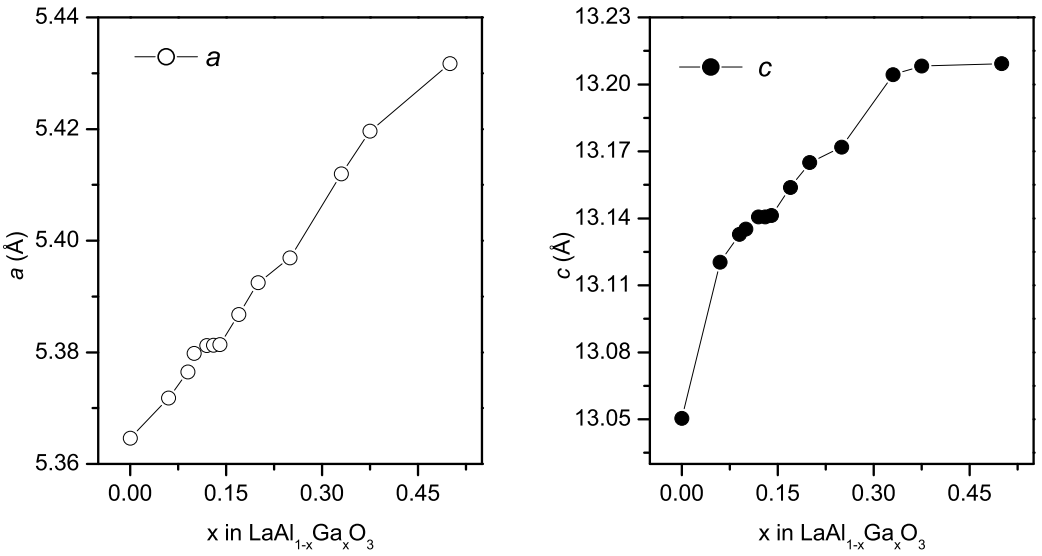


*Figure 6.16: Variation of the hexagonal lattice parameters of $LaAl_{1-x}Ga_xO_3$ as a function of $x$.*

*Table 6.5: Hexagonal lattice parameters of $LaAl_{1-x}Ga_xO_3$.*

| $x$ | $a$ (Å) | $c$ (Å) |
|---|---|---|
| 0.0 | 5.3646 | 13.0504 |
| 0.06 | 5.3718 | 13.1203 |
| 0.09 | 5.3765 | 13.1328 |
| 0.1 | 5.3798 | 13.1352 |
| 0.12 | 5.3812 | 13.1407 |
| 0.13 | 5.3813 | 13.1406 |
| 0.14 | 5.3814 | 13.1413 |
| 0.17 | 5.3868 | 13.1539 |
| 0.2 | 5.3925 | 13.1649 |
| 0.25 | 5.3969 | 13.1719 |
| 0.33 | 5.4120 | 13.2043 |
| 0.38 | 5.4196 | 13.2082 |
| 0.5 | 5.4317 | 13.2092 |

Rietveld refinement analysis has been carried out for the compositions with $x$ = 0.2, 0.38 and 0.5, using the two different space groups R3c and R$\bar{3}$c. Results of the XRD refinement analysis are shown in figures 6.17 to 6.22 and the best fit parameters are given in table 6.6. The best fit parameters for $x = 0$ ($LaAlO_3$) are also shown in the table for comparison (see section 4.4, chapter 4, for details). The best fit parameters are smaller for the R3c space group for $x = 0.2$, relatively smaller for the R$\overline{3}$c space group for $x = 0.375$ and much smaller for $x = 0.5$ for the same space group. Thus, it intimated that the space group of Ga substituted sample may be changing from R3c to R$\overline{3}$c around $x = 0.38$ as seen from the lower $\chi^2$ and R-values for this composition, $x = 0.38$ corresponding to the ratio 3/8, that is, replacing 3 out of 8 Al in a cubic perovskite unit cells by Ga leads to distortions of all the $AlO_6$ octahedra.

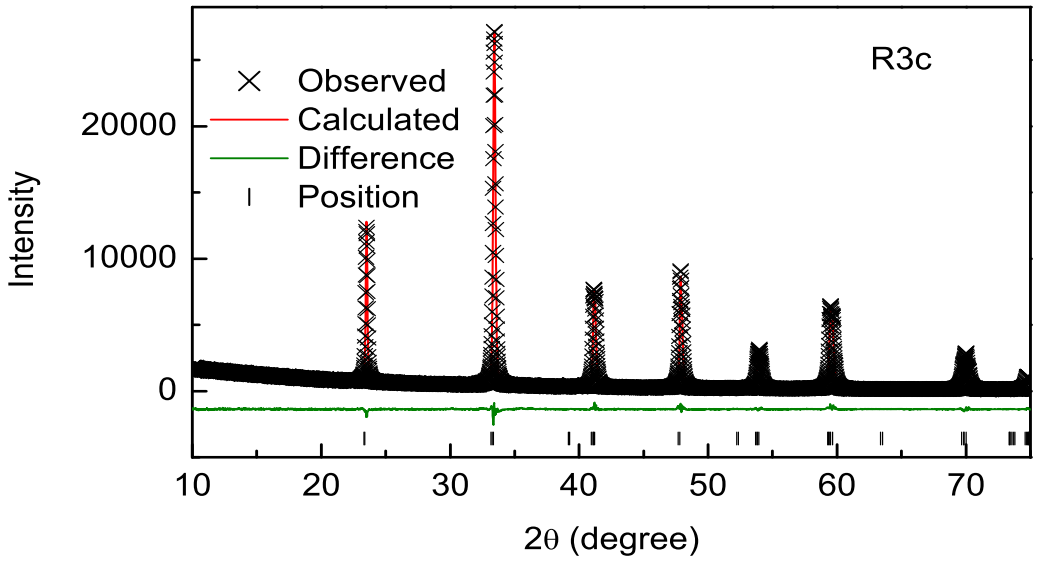


*Figure 6.17: Result of the Rietveld refinement of the XRD pattern of $LaAl_{0.8}Ga_{0.2}O_3$ using the space group R3c.*

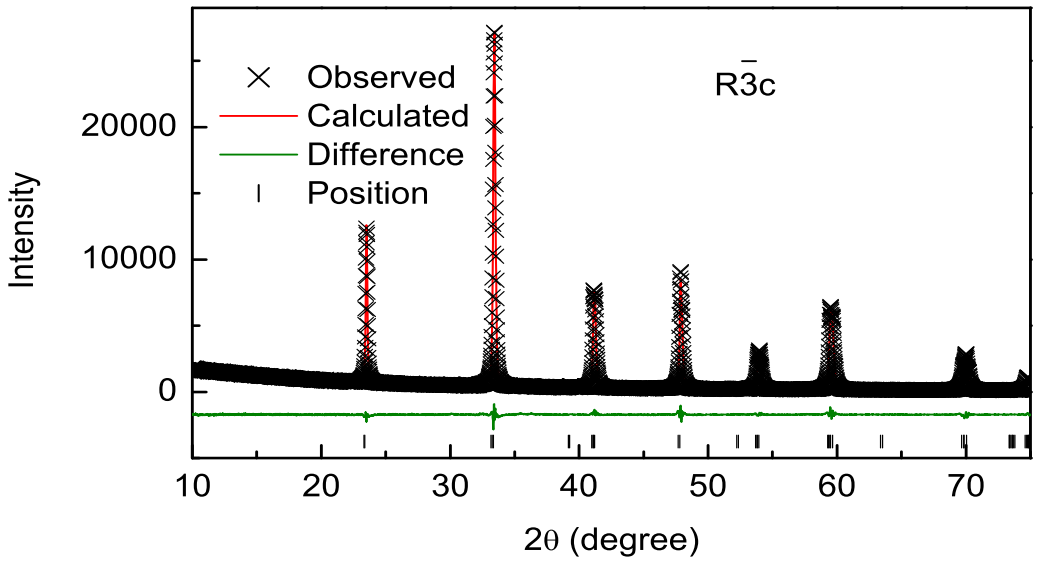


*Figure 6.18: Result of the Rietveld refinement of the XRD pattern of $LaAl_{0.8}Ga_{0.2}O_3$ using the space group $R\bar{3}c$.*

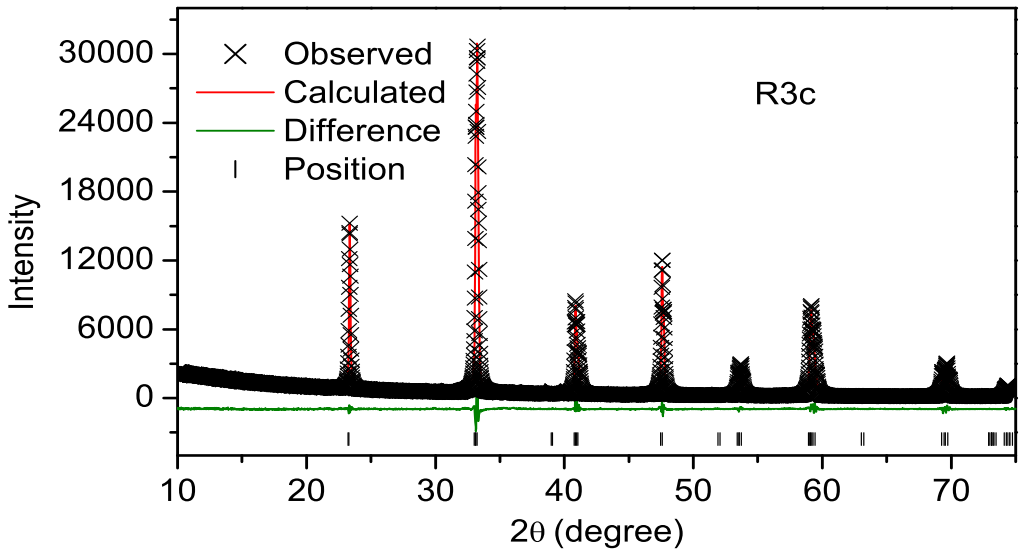


*Figure 6.19: Result of the Rietveld refinement of the XRD pattern of $LaAl_{0.62}Ga_{0.38}O_3$ using the space group R3c.*

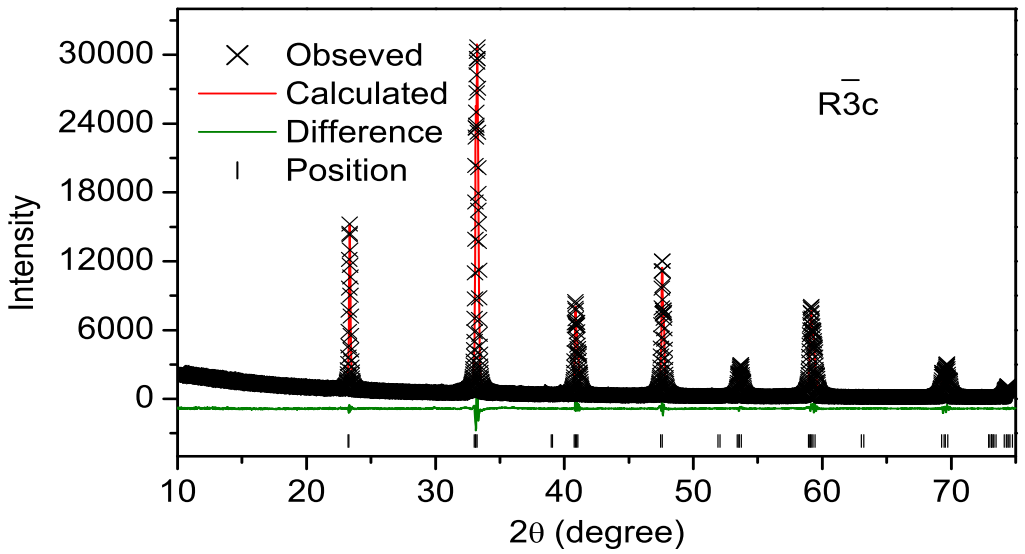


*Figure 6.20: Result of the Rietveld refinement of the XRD pattern of $LaAl_{0.62}Ga_{0.38}O_3$ using the space group $R\bar{3}c$.*

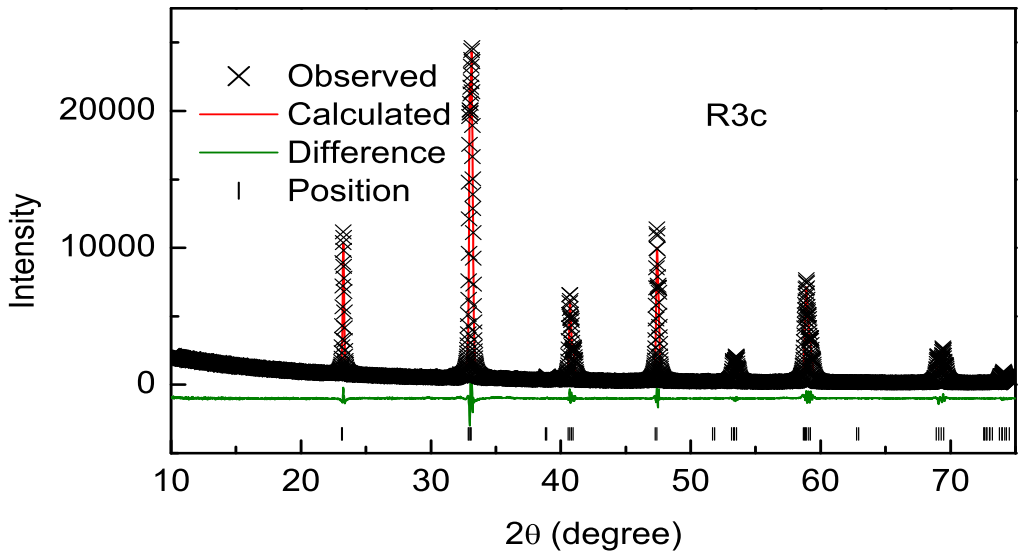


*Figure 6.21: Result of the Rietveld refinement of the XRD pattern of $LaAl_{0.5}Ga_{0.5}O_3$ using the space group R3c.*

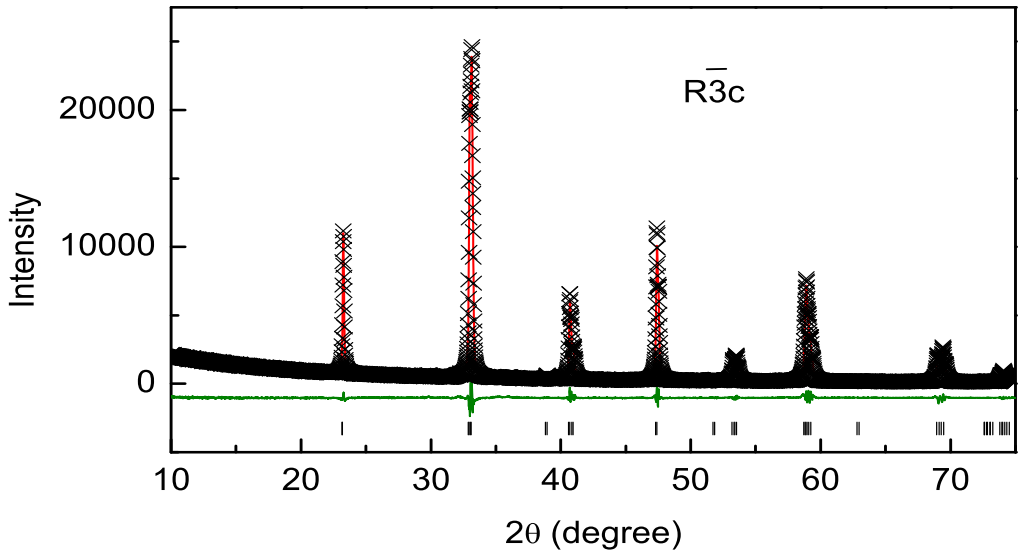


*Figure 6.22: Result of the Rietveld refinement of the XRD pattern of $LaAl_{0.5}Ga_{0.5}O_3$ using the space group $R\bar{3}c$.*

*Table 6.6: Rietveld refinement best fit parameters for $LaAl_{1-x}Ga_xO_3$.*

| $x$ | space group | $\chi^2$ | $R_{wp}$ | $R_{F^2}$ |
|---|---|---|---|---|
| 0.0 | R3c | 2.146 | 0.0509 | 0.0218 |
| 0.0 | R$\overline{3}$c | 2.148 | 0.0509 | 0.0219 |
| 0.2 | R3c | 1.759 | 0.0476 | 0.0256 |
| 0.2 | R$\overline{3}$c | 1.913 | 0.0515 | 0.0216 |
| 0.38 | R3c | 2.253 | 0.0511 | 0.0191 |
| 0.38 | R$\overline{3}$c | 2.249 | 0.0510 | 0.0189 |
| 0.5 | R3c | 2.749 | 0.0588 | 0.0297 |
| 0.5 | R$\overline{3}$c | 2.607 | 0.0572 | 0.0261 |

### 6.4.3 $^{27}$Al NMR

$^{27}$Al NMR spectra of the Ga-substituted samples, with full spinning sidebands, recorded at the spinning speed of 10 kHz on a 300 MHz spectrometer are shown in figure 6.23. The spread of the spinning sidebands as the level of substitution increases indicate the increase in the quadrupole coupling constant, as observed in the spectra of the Co-substituted $LaAl_{1-x}Co_xO_3$ (see figure 6.6) and also in the spectra of Y-substituted $La_{1-x}Y_xAlO_3$ (see figure 5.10, section 5.1, chapter 5). A close view of the central transition region of the spectra of $LaAl_{1-x}Ga_xO_3$, shown in figure 6.24, tells that there is only one octahedral coordination environment present in all the substituted samples with a slight change in the NMR parameters; chemical shift and the quadrupole coupling constant, on substitution.

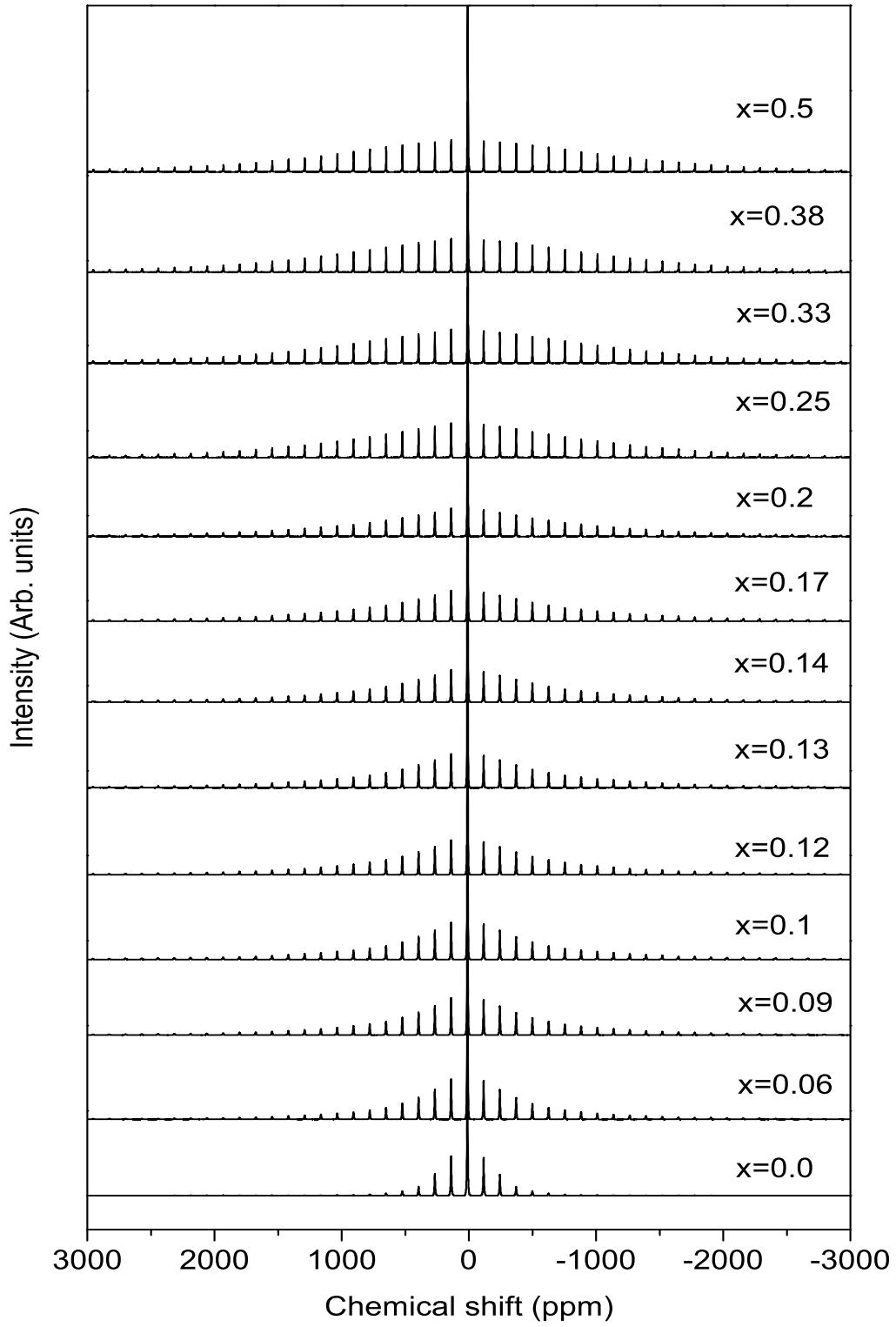


*Figure 6.23: $^{27}Al$ MAS NMR spectra of different compositions in $LaAl_{1-x}Ga_xO_3$.*

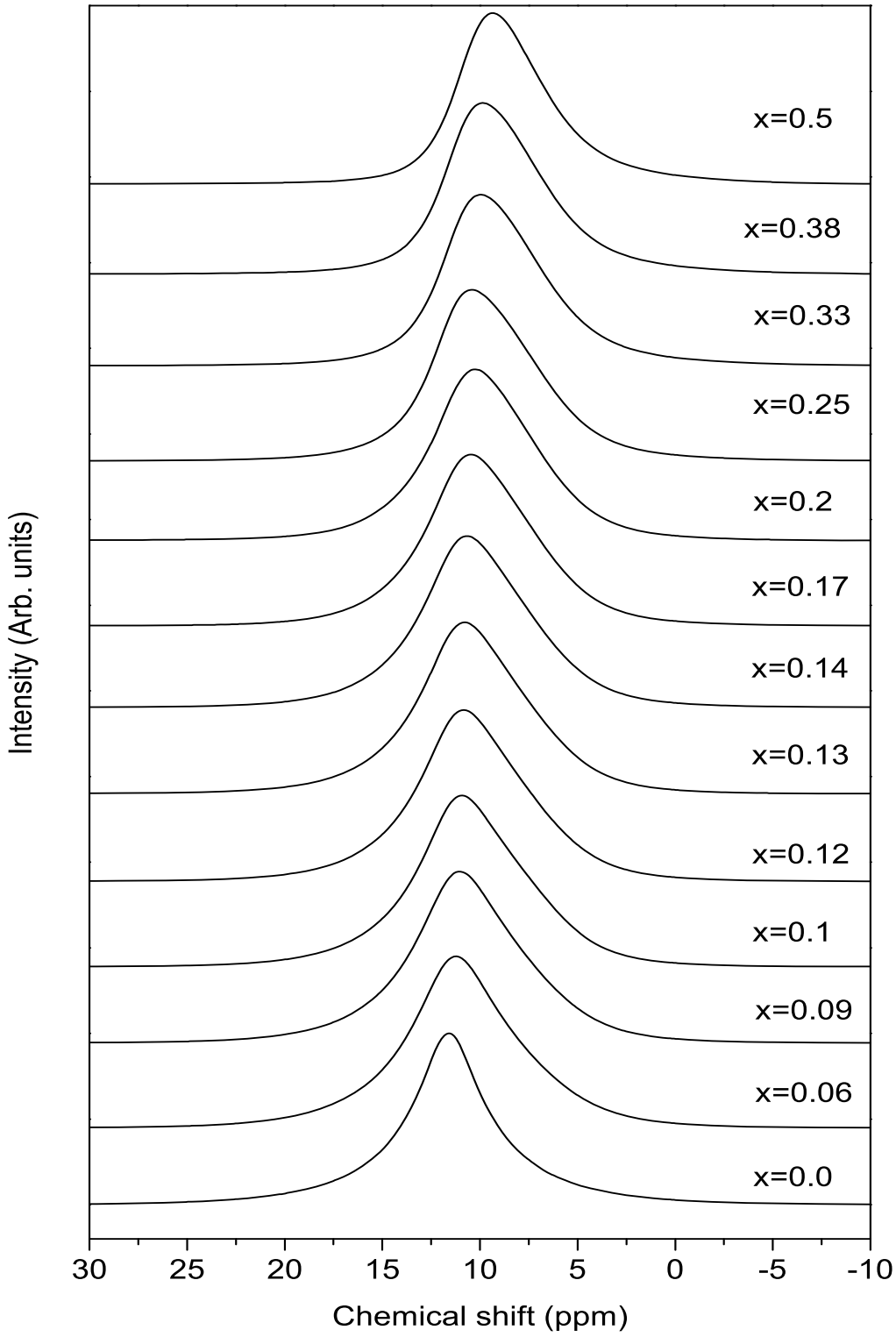


*Figure 6.24: The central transition in the $^{27}Al$ MAS NMR spectra of different compositions in $LaAl_{1-x}Ga_xO_3$.*

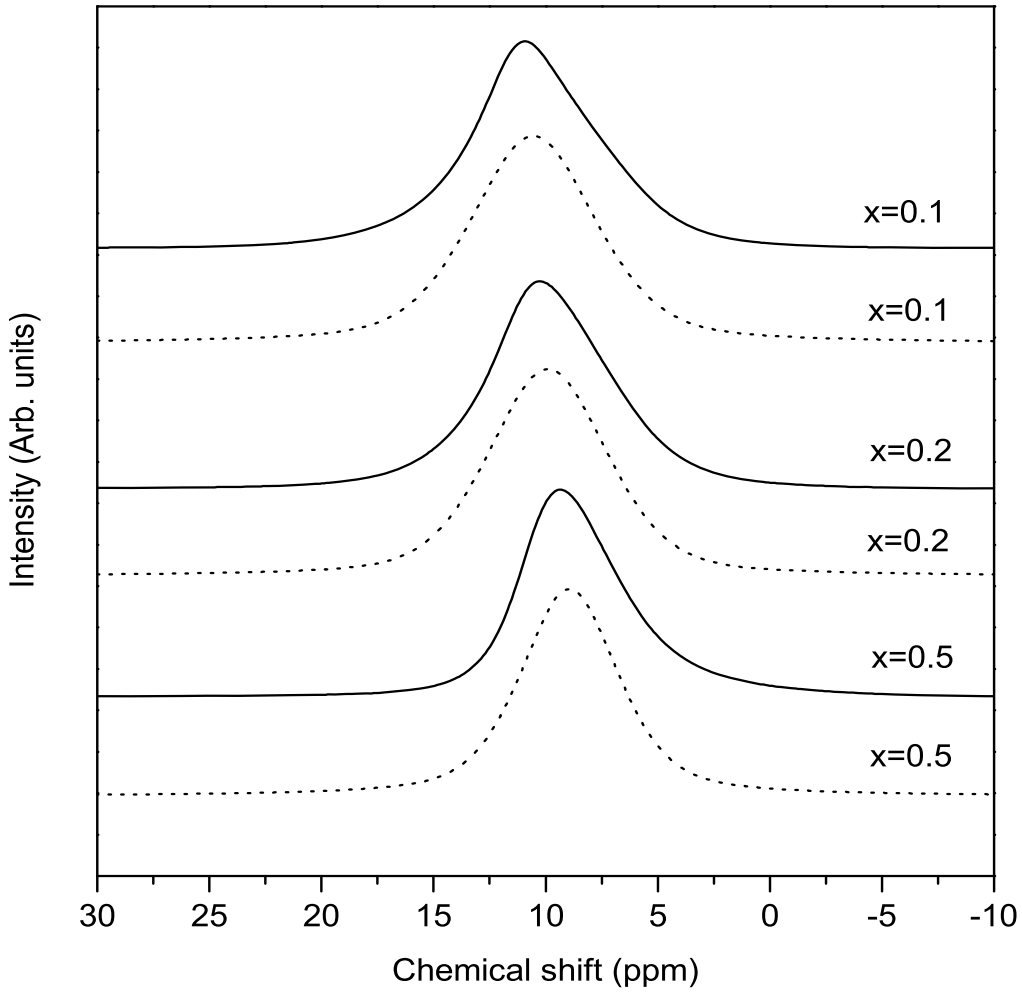


*Figure 6.25: Experimental and simulated $^{27}Al$ MAS NMR spectra of $LaAl_{1-x}Ga_xO_3$ in the central transition region for $x$ = 0.1, 0.2, and 0.5 (solid and broken lines represent experimental and simulated NMR patterns respectively).*

The $^{27}$Al MAS NMR parameters of the different compositions are obtained by fitting the entire spectra. The experimental and the simulated spectra for $x$ = 0.1, 0.2 and 0.5 are shown in figure 6.25 and the NMR parameters obtained are given in the table 6.7. From the variation of the isotropic chemical shift shown in figure 6.26, it is clear that the chemical shift decreases continuously. This is mainly because only the first order quadrupolar interactions are considered which neglects the contributions from the quadrupole induced shifts. The quadrupole induced

*Table 6.7: $^{27}Al$ NMR spectral parameters for $LaAl_{1-x}Ga_xO_3$.*

| $x$ | $\delta_{iso}$ (ppm) | $C_q$ (kHz) |
|---|---|---|
| 0.0 | 11.58 | 150.0 |
| 0.06 | 11.00 | 360.0 |
| 0.09 | 10.74 | 453.0 |
| 0.1 | 10.56 | 476.0 |
| 0.12 | 10.49 | 528.0 |
| 0.13 | 10.44 | 569.0 |
| 0.14 | 10.30 | 609.0 |
| 0.17 | 10.09 | 654.0 |
| 0.2 | 9.90 | 730.0 |
| 0.25 | 9.84 | 748.0 |
| 0.33 | 9.34 | 793.0 |
| 0.38 | 9.24 | 808.0 |
| 0.5 | 8.94 | 831.6 |

shifts adds to the isotropic chemical shifts and decreases with increasing field strength [18] which is seen here. It is also possible that the octahedral distortion decreases when the smaller ion $Al^{3+}$ is replaced by the larger ion $Ga^{3+}$. The small increase in the quadrupole coupling constant in the Ga substituted samples, as shown in figure 6.27, compared to that of the Co-substituted samples (see figure 6.9) is due to the difference in the sizes of $Ga^{3+}$ and $Co^{3+}$. A small deviation from linearity is observed in the variation of the chemical shift as well as $C_q$, around $x \approx 0.12$, suggesting a possible structural disorder as evidenced from the XRD studies.

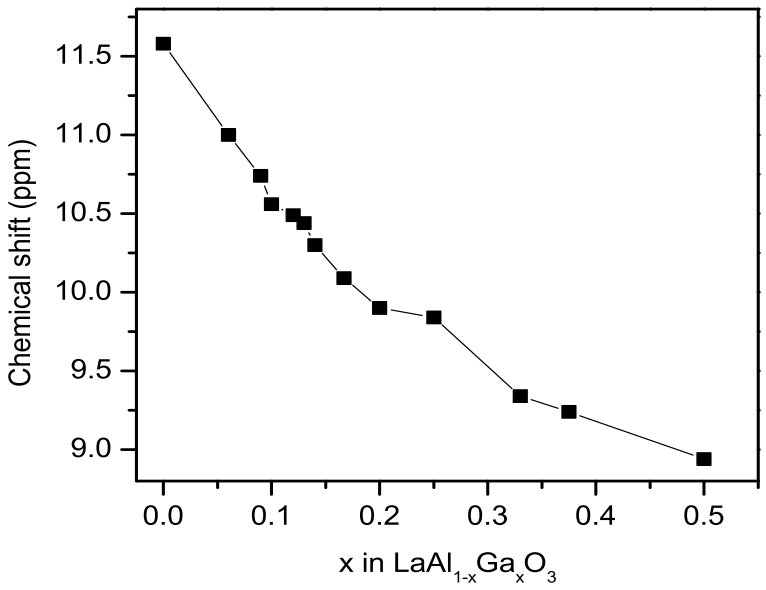


*Figure 6.26: Variation of the $^{27}Al$ NMR isotropic chemical shift of $LaAl_{1-x}Ga_xO_3$ as a function of $x$.*

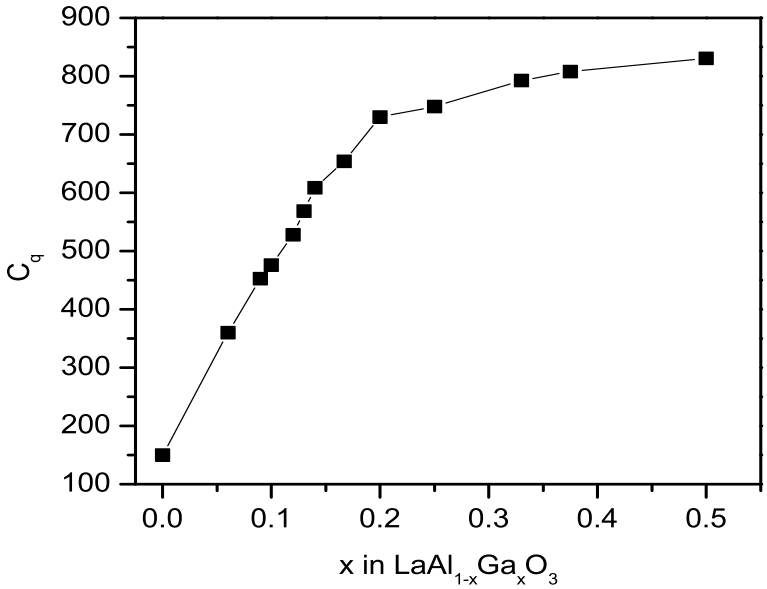


*Figure 6.27: Variation of the $^{27}Al$ NMR quadrupole coupling constant of $LaAl_{1-x}Ga_xO_3$ as a function of $x$.*

### 6.4.4 $^{139}$La NMR

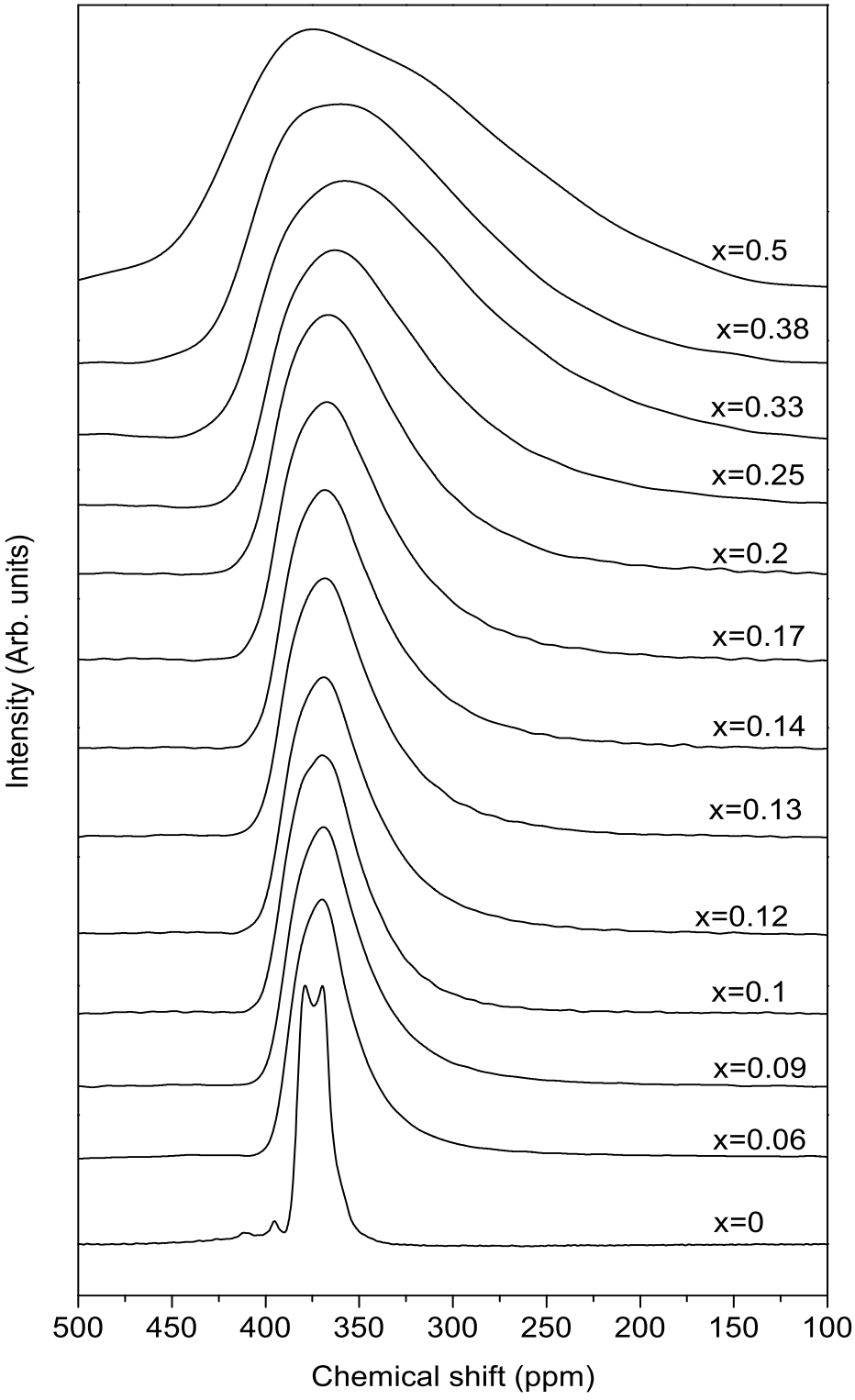


*Figure 6.28: $^{139}La$ MAS NMR spectra of different compositions in $LaAl_{1-x}Ga_xO_3$.*

$^{139}$La MAS NMR spectra of all the Ga-substituted samples are shown in figure 6.28. From the figure it is clear that the La spectra is highly affected by the substitution of Ga at the Al site. When the $^{139}$La MAS NMR spectra of the $x$ = 0.2 composition, for both the Co- and Ga-substituted samples is compared, it is seen that the spectral width over which the spectra is spanning for the Ga sample is (425 ppm to 250 ppm) more than that for the Co-substituted sample, indicating a large increase in the quadrupole coupling constant due to the Ga-substitution, and also because of the larger size of $Ga^{3+}$ compared to that of $Al^{3+}$. This increase is due to the large difference in the electric field gradients around the nucleus caused by the electronic environment difference from the Ga-substitution. The effect is almost similar to that observed for the Y substituted samples (see section 5.7, Chapter 5).

In order to find out the actual NMR parameters which causes the distortion of the spectra, all the spectra are fitted using the DMFIT program. The experimental and the simulated spectra for the compositions $x$ = 0.1, 0.2 and 0.5 are given in figure 6.29. The $^{139}$La NMR parameters obtained after deconvolution of the spectra are given in table 6.8 and the variations of the parameters, as a function of $x$, are shown in figures 6.30 and 6.31. Unlike in the case of $LaAl_{1-x}Co_xO_3$, where the La spectra is largely affected above $x > 0.1$, the spectra in the case of $LaAl_{1-x}Ga_xO_3$ are affected even at a small level of substitution of Ga.

The isotropic chemical shift is found to be continuously increasing from 385 to 418 ppm and there is slope change around $x$ = 0.12 and $x$ = 0.38. Similarly, the quadrupole coupling constant increases continuously from 6.8 MHz to 17.8 MHz for the substitution up to $x$ = 0.5, indicating continuous distortions of the $AlO_6$ octahedra caused by the Ga substitution. The $C_q$ values are very large for the Ga-substituted compositions when compared with the $C_q$ values of Co-substituted compositions (see figure 6.13). This indicate that the octahedral distortions are greater when Al is substituted with an ion of larger ionic radius than when it is substituted with an ion of comparable ionic radius. There is a change in the slope around $x$ = 0.12 and a discontinuity in the quadrupole coupling constant at $x$ =

0.38 composition. The latter is likely to be due to the phase transition (change of space group) as seen from the structural studies.

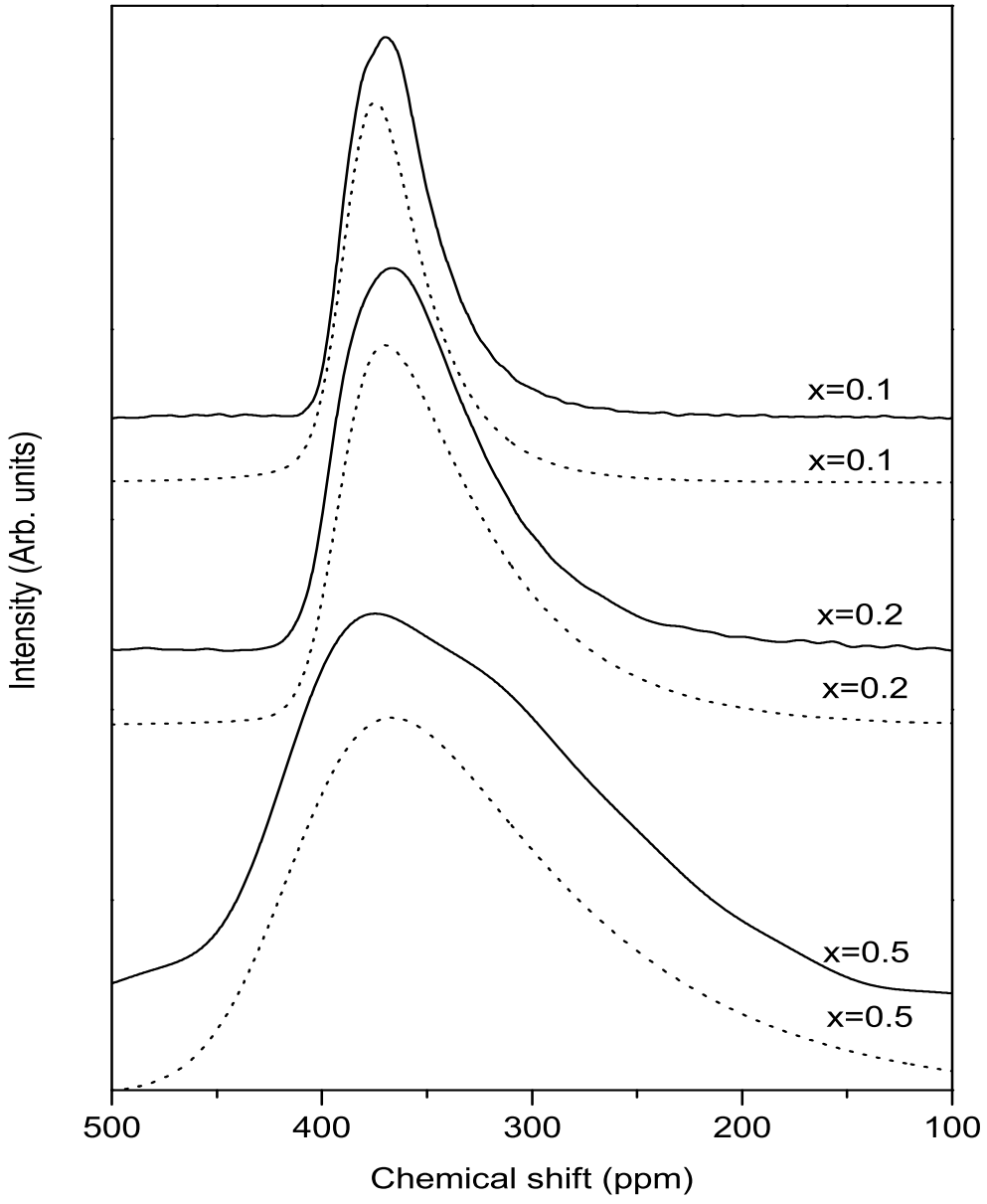


*Figure 6.29: Experimental and simulated $^{139}La$ NMR spectra of $LaAl_{1-x}Ga_xO_3$ for x = 0.1, 0.2 and 0.5 (solid and broken lines represent experimental and simulated NMR patterns, respectively).*

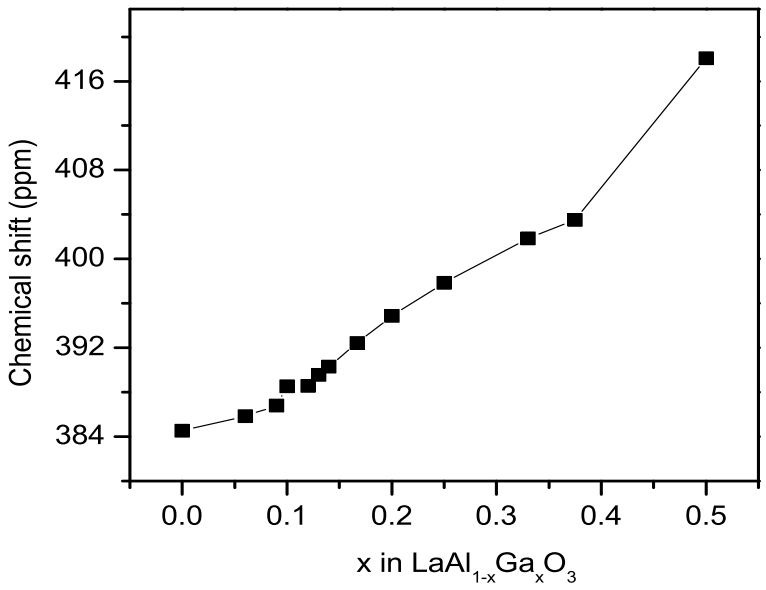


*Figure 6.30: Variation of the $^{139}La$ NMR chemical shift of $LaAl_{1-x}Ga_xO_3$ as a function of $x$.*

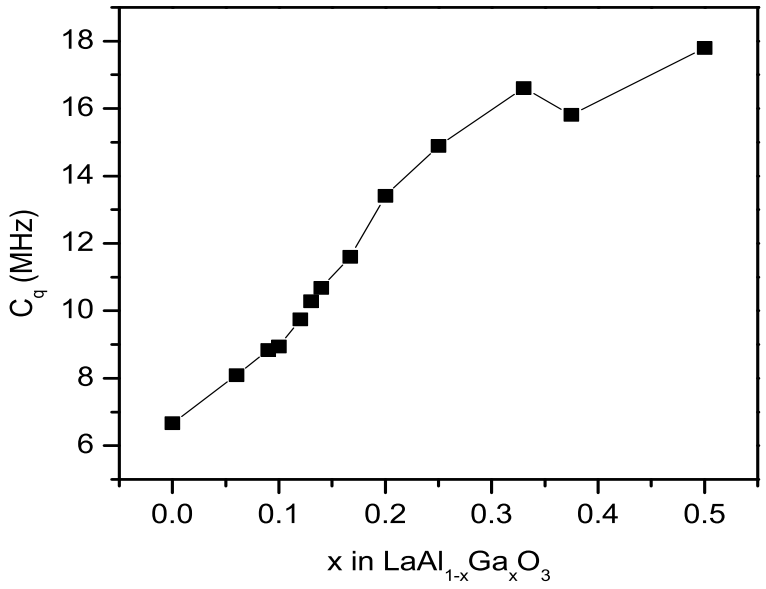


*Figure 6.31: Variation of the $^{139}La$ NMR quadrupole coupling constant of $LaAl_{1-x}Ga_xO_3$ as a function of $x$.*

*Table 6.8: $^{139}La$ NMR spectral parameters for $LaAl_{1-x}Ga_xO_3$.*

| $x$ | $\delta_{iso}$ (ppm) | $C_q$ (MHz) | $\eta$ | $\Delta_{CS}$ |
|---|---|---|---|---|
| 0.0 | 385.4 | 6.8 | 0.00 | - |
| 0.06 | 385.8 | 8.1 | - | 19.6 |
| 0.09 | 386.8 | 8.8 | - | 21.4 |
| 0.1 | 388.5 | 8.9 | - | 23.1 |
| 0.12 | 388.6 | 9.8 | - | 22.6 |
| 0.13 | 389.6 | 10.3 | - | 22.5 |
| 0.14 | 390.3 | 10.7 | - | 23.7 |
| 0.17 | 392.4 | 11.6 | - | 25.1 |
| 0.2 | 394.9 | 13.4 | - | 27.3 |
| 0.25 | 397.9 | 14.9 | - | 30.2 |
| 0.33 | 401.9 | 16.6 | - | 48.0 |
| 0.38 | 403.5 | 15.8 | - | 57.3 |
| 0.5 | 418.1 | 17.8 | - | 70.9 |

### 6.4.5 Summary

The structural studies on the $LaAl_{1-x}Ga_xO_3$ samples shows that all the samples are formed in single phase form with the rhombohedral crystal structure. However, the Rietveld refinement studies on the $x = 0.2$, 0.38 and 0.5 samples showed that the space group has changed from R3c to R$\bar{3}$c at or above $x = 0.38$. $^{27}$Al and $^{139}$La NMR parameters for the $LaAl_{1-x}Ga_xO_3$ varied continuously indicating the continuous distortions of the $AlO_6$ octahedra when Ga is substituted at the Al sites. There is a discontinuity in the quadrupole coupling constant at $x = 0.38$ due to the minor structural change.

## 6.5 Conclusions

Structural as well as $^{27}Al$ and $^{139}La$ solid-state NMR studies on different compositions of $LaAl_{1-x}Co_xO_3$ and $LaAl_{1-x}Ga_xO_3$ have been carried out to understand the structural changes when $Al^{3+}$ in $LaAlO_3$ is partially substituted by ions of comparable ($Co^{3+}$) and larger ($Ga^{3+}$) sizes, respectively. Structural studies using powder XRD indicated a possible structural distortion above $x \approx 0.12$. Similar observations are made from both Al and NMR studies also. The local and structural distortions are found to be very small when Al is substituted with an ion of comparable ionic size whereas there is a continuous and large distortion of the $AlO_6$ octahedra arising out of the substitution of the larger ion. The present results for $LaAl_{1-x}Co_xO_3$ and $LaAl_{1-x}Ga_xO_3$ may be extended to explain the changes in the electrical and magnetic properties of similar compositions in transition metal ion substituted $LaMnO_3$, where drastic changes in the magnetization and electrical conductivity are observed above $x > 0.1$.

# Bibliography


[1] U. H. Bents, *Phys. Rev.* 1957, 106, 225-230.

[2] J. B. Goodenough, A. Wold, R. J. Arnott and N. Menyuk, *Phys. Rev.* 1961, 124, 373-384.

[3] G. H. Jonker, *J. Appl. Phys.* 1966, 37, 1424-1430.

[4] V. Narasimhan, H. V. Keer and D. K. Chakrabarty, *phys. stat. sol. (a)* 1985, 89, 65-71.

[5] L. W. Zhang, G. Feng, H. Liang, B. S. Cao, Z. Meihong and Y. G. Zhao, *J. Magn. Magn. Mater.* 2000, 219, 236-240.

[6] J.V.L. Joseph *Synthesis, Characterization and Magnetic Properties of Substituted Perovskite - Type Manganates and Related Oxides*(Ph.D. Thesis submitted to National Chemical Laboratory, Pune, 2004)

[7] R. D. Shannon, *Acta Cryst. A* 1976, 32, 751-767.

[8] T. R. Kyâmen, Y. Asaka and M. Itoh, *Phys. Rev. B* 2003, 67, 144424.1-6.

[9] K. Tomiyasu, Y. Kubota, S. Shimomura, M. Onodera, S. I. Koyama, T. Nojima, S. Ishihara, H. Nakao and Y. Murakami, *Phys. Rev. B* 2013, 87, 224409.1-8.

[10] J. Prado-Gonjal, A. M. Arevalo-Lopez and E. Moran, *Mater. Res. Bull.* 2011, 46, 222-230.

[11] Z. Zhu, J. Gua, Y. Jia and X. Hu, *physica status solidi (b)* 2010, 247,308-312.

[12] C. Y. Chang, B. N. Lin, H. C. Ku and Y. Y. Hsu *Chin. J. Phys.*2003, 41, 662-670.

[13] I. A. Nekrasov, S. V. Streltsov, M. A. Korotin and V. I. Anisimov, *Phys. Rev. B* 2003, 68, 235113.1-7.

[14] N. S.-O. Marta, R. G. Fernando, R. g. Jesus and D. Gerard*J. Phys.: Condens. Matt.* 2011, 23, 415501.1-6

[15] J. B. Goodenough, *J. Phys. Chem. Solids* 1958, 6, 287-297

[16] P. M. Raccah and J. B. Goodenough, *Phys. Rev. B* 1967, 155, 932-943

[17] A. Matraszek, M. Miller, L. Singheiser and K. Hilpert, *J. Am. Ceram. Soc.* 2003, 86, 1911-1917.

[18] E. Gaudin, F. Taulelle, R. Stoyanova, E. Zhecheva, R. Alcántara, P. Lavela and J. L. Tirado, *J. Phys. Chem. B* 2001, 105, 8081-8087.

# Chapter 7

# Conclusions and Future Perspectives

## 7.1 Introduction

This thesis deals with the structural and NMR characterization of compounds belonging to two families of oxides, the magnetoplumbite and the perovskite structures. The objective behind this study is to correlate the structural characteristics for the substituted non-magnetic compositions in these two systems with the magnetic properties of the corresponding magnetic compositions.

In the magnetoplumbite structure, strontium aluminate $SrAl_{12}O_{19}$ is studied instead of the magnetic $SrFe_{12}O_{19}$ which is used as a permanent magnetic material for various applications. In the case of $SrFe_{12}O_{19}$, it is found that the magnetic properties are enhanced upon simultaneous substitution of Sr by La and Fe by Co, as in $Sr_{1-x}La_xFe_{12-x}Co_xO_{19}$. The properties are found to be maximum, especially for the La-Co substituted compositions, for $x \approx 0.2$ and 0.3. There are many studies reported on these substituted systems, in order to identify the sites of substitution of Co in these compounds, among the five different sites available for Fe in the magnetoplumbite crystal structure. Most of the studies indicated that the 2a and $4f_2$ octahedral sites in the structure are occupied by Co ions upon substitution and some studies indicated the occupation of other sites. That is, there is no agreement between the various studies. Additionally, the magnetoplumbite crystal structure is explained by two structural models; the 'central atom model' and the 'split atom model', based on the coordinative nature of the trigonal bipyramid ions. The evidences for both the structural models have been obtained from solid-state NMR studies on $SrAl_{12}O_{19}$.

In the perovskite structure, we have selected $LaAlO_3$ in order to understand the corresponding magnetic system $LaMnO_3$. $LaMnO_3$ is an antiferromagnetic compound and changes to ferromagnetic upon substitution at the La-site or the Mn-site and shows interesting properties such as colossal magnetoresistance. Both the La-site as well as the Mn-site substituted $LaMnO_3$, such as $La_{1-x}Ca_xMnO_3$ and $LaMn_{1-x}Co_xO_3$ are known to exhibit a large change in the properties near $x$ = 0.12. Moreover, the space group of $LaAlO_3$ is under dispute from the earlier studies. Therefore, we have attempted to get a clear idea of space group of $LaAlO_3$

from the structural and the NMR studies. Detailed structural and NMR studies have been carried out on La-site and Al-site substituted $LaAlO_3$ to obtain the structural information and the octahedral distortions in these compositions.

## 7.2 Studies on unsubstituted and La-Zn substituted $SrAl_{12}O_{19}$

Previous NMR studies on $SrAl_{12}O_{19}$ showed either a pentacoordinated trigonal bipyramidal site (central atom model) or a distorted tetrahedral site (split atom model) for one of the Al sites, out of five different sites, in the magnetoplumbite structure. However, the present $^{27}Al$ solid-state NMR studies on $SrAl_{12}O_{19}$, at different field strengths, have clearly shown evidence for six different crystallographic sites in the magnetoplumbite structure, where both the five coordinated and the distorted tetrahedral sites are partially occupied. Moreover, XRD refinement studies on $SrAl_{12}O_{19}$ have shown that both the central atom model and split atom model are equally possible and the most possible structure model for $SrAl_{12}O_{19}$ is a physical mixture of the two phases in the material, where both the phases with central atom and split atom models co-exist simultaneously.

The sites of substitution in La-Zn substituted compositions, $Sr_{1-x}La_xFe_{12-x}Co_xO_{19}$, are identified as the 2a and $4f_2$ octahedral sites, supporting the conclusions derived from Mössbauer spectroscopic studies on the La-Co substituted strontium ferrite. However, the present studies gave additional information on the relative change in the distribution of Al in the penta coordinated and distorted tetra coordinated sites. Based on the present NMR studies, it is proposed that increase in the magnetic performance of La-Co substituted $SrFe_{12}O_{19}$ around $x = 0.2$ is due to the combined effect of the changes in the coordination environment of Al at the 2a and $4f_2$ octahedral sites as well as the stabilization of the trigonal bipyramidal site.

## 7.3 Studies on $LaAlO_3$

From XRD studies on $LaAlO_3$, it is found that both the rhombohedral space groups R3c and R$\bar{3}$c give similar results. SSNMR studies revealed the presence of a single Al-coordination environment. However, a Lorentzian lineshape for the $^{27}$Al NMR spectrum is observed, which is normally not expected, indicating the possible mobility of Al ions in $LaAlO_3$. However, it was impossible to obtain the range of motions in the perovskite structure from the present studies and for this, more in-depth studies and analysis are required.

## 7.4 Comparative studies on La-site and Al-site substituted $LaAlO_3$

In the chapters 5 and 6, we have studied the variations in the NMR parameters; isotropic chemical shift, $\delta_{iso}$, and quadrupole coupling constant, $C_q$, for both $^{27}$Al and $^{139}$La spectra, when the La and Al-sites are substituted with different ions i.e. $La_{1-x}Y_xAlO_3$, $LaAl_{1-x}Co_xO_3$ and $LaAl_{1-x}Ga_xO_3$. Although we expect distortions in the coordination polyhedra of the substituted sites, we have observed distortions of both La dodecahdra and Al octahedra in the structure, irrespective of the site of substitution. Hence, we have attempted to compare the variations in the NMR parameters, when La-site and Al-site are substituted with different ions.

In the case of $La_{1-x}Y_xAlO_3$, where the larger La-ions are replaced partially with the smaller Y-ions, the La-coordination environments are found to be highly distorted as seen from the broadening of the spectra along with large changes in the chemical shift and the quadrupole coupling constants arising from the differences in the surrounding electric field gradients. However, it is also noted that there are associated changes in the Al-coordination environments also as seen from the increase in the quadrupole coupling constant and decrease in the chemical shift despite the fact that the substitution is at the La-site. Similar effect was observed in the Al-site substituted spectra, where there are associated changes in the La-coordination environments as seen from the broadening of the spectra with a

corresponding increase in the quadrupole coupling constant. Thus, the changes occurring in A-site or B-site of the perovskite structure are almost correlated for the reason that the O atoms are shared by the A and B-site ions and because of the difference in the electric field gradient around the different nuclei. The difference in the electron distribution around the nucleus causes the difference in electric field gradient, which in turn drives the distortions of the $AlO_6$ octahedra and the $LaO_{12}$ dodecahedra, irrespective of the site of substitution and the substituting atoms.

### 7.4.1 Comparison of $^{27}$Al NMR spectra

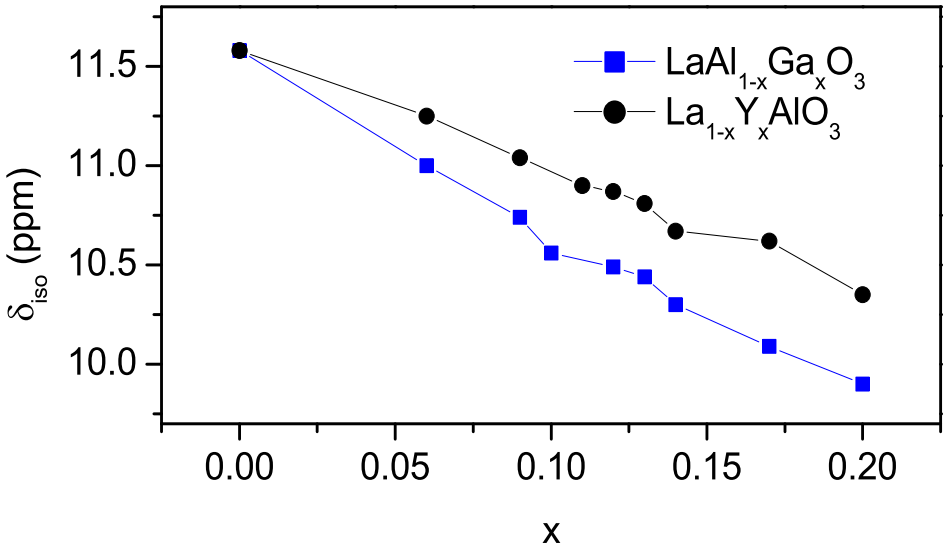


*Figure 7.1: Variation in the $^{27}$Al isotropic chemical shift as function of $x$*

The variations of Al NMR parameters, the isotropic chemical shift and quadrupole coupling constant, up to $x = 0.2$ in the Co, Ga and Y substituted compositions are shown and compared in figures 7.1 and 7.2. The chemical shifts for the Co-substituted $LaAl_{1-x}Co_xO_3$ is not shown, since there is only a small random variation of the chemical shifts arising due to the comparable sizes of $Co^{3+}$ and $Al^{3+}$ ions. The small decrease in the chemical shift upon substitution of the larger ion

$Ga^{3+}$ for $Al^{3+}$ and the smaller ion $Y^{3+}$ for $La^{3+}$ is due to the quadrupole induced shift. Similar to the $^{27}Al$ isotropic chemical shift changes, larger changes in the quadrupole coupling constant are observed for Ga and Y substituted compositions compared to the Co substituted composition. What is interesting is the deviation from the linearity for the chemical shift as well as the quadrupole coupling constant around $x \approx 0.12$–13 for both the La-site and Al-site substitutions.

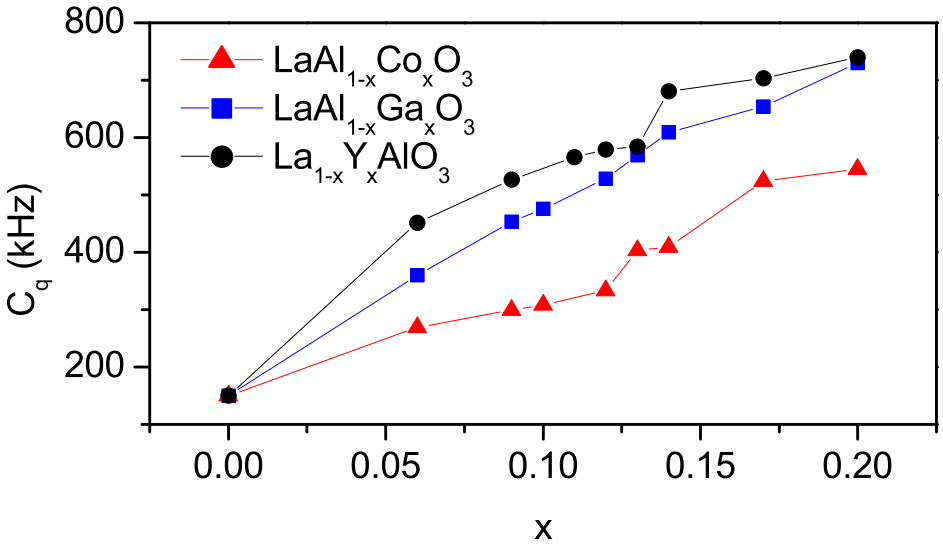


*Figure 7.2: Variation in the $^{27}Al$ quadrupole coupling constant as function of $x$*

### 7.4.2 Comparison of $^{139}$La NMR spectra

The $^{139}$La NMR parameters, isotropic chemical shift and quadrupole coupling constant up to $x = 0.2$ are shown in figures 7.3 and 7.4 respectively. The changes in the NMR parameters between $x$ =0.1 and 0.15 are similar to that observed for the $^{27}$Al NMR spectral parameters. Thus, variations in both the $^{27}$Al and $^{139}$La NMR parameters indicate the importance of compositions around $x = 0.125$, where, $1/8^{th}$ of the corresponding atoms are replaced from a simple cubic perovskite unit cell.

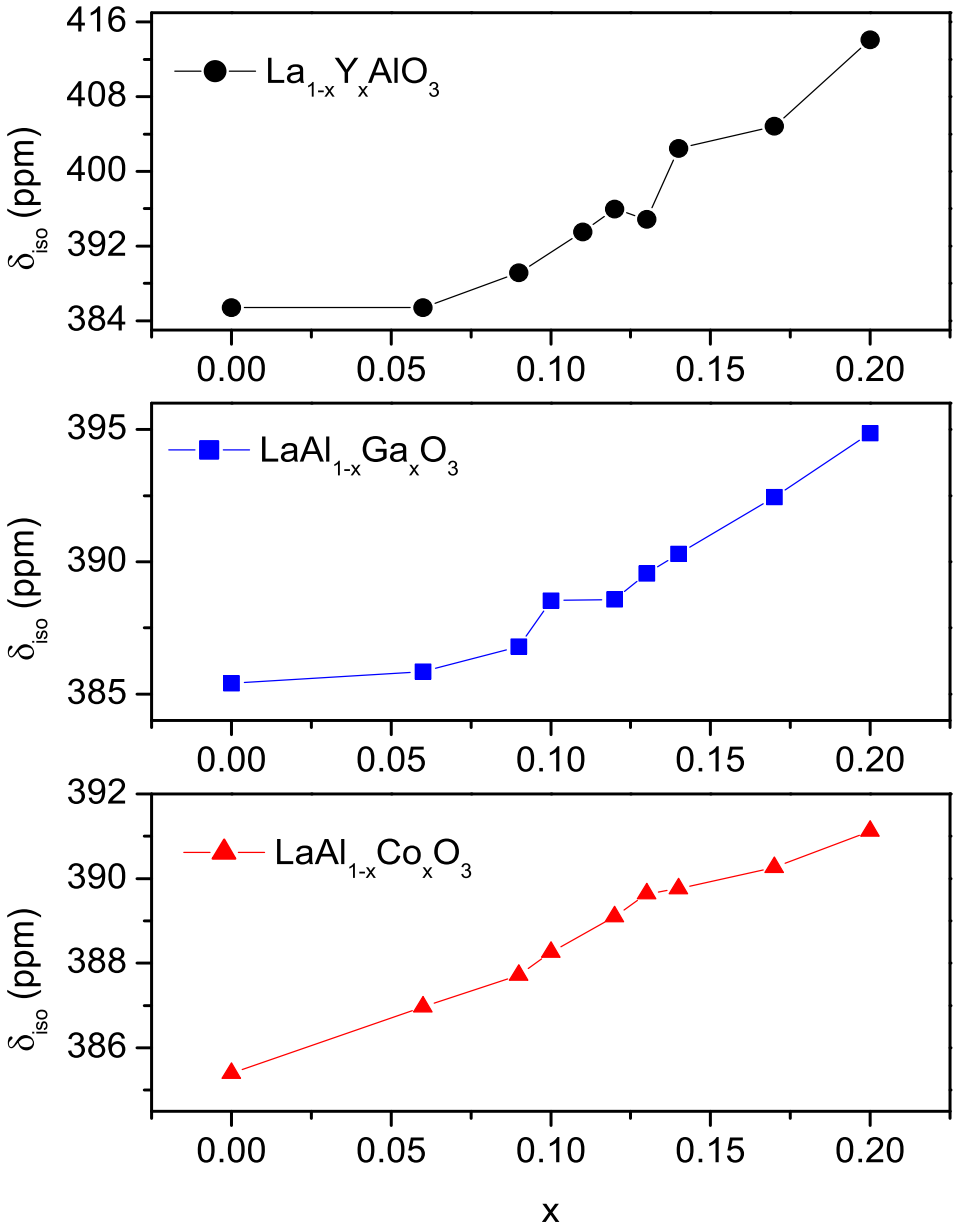


*Figure 7.3: Variation in the $^{139}La$ isotropic chemical shift as function of $x$.*

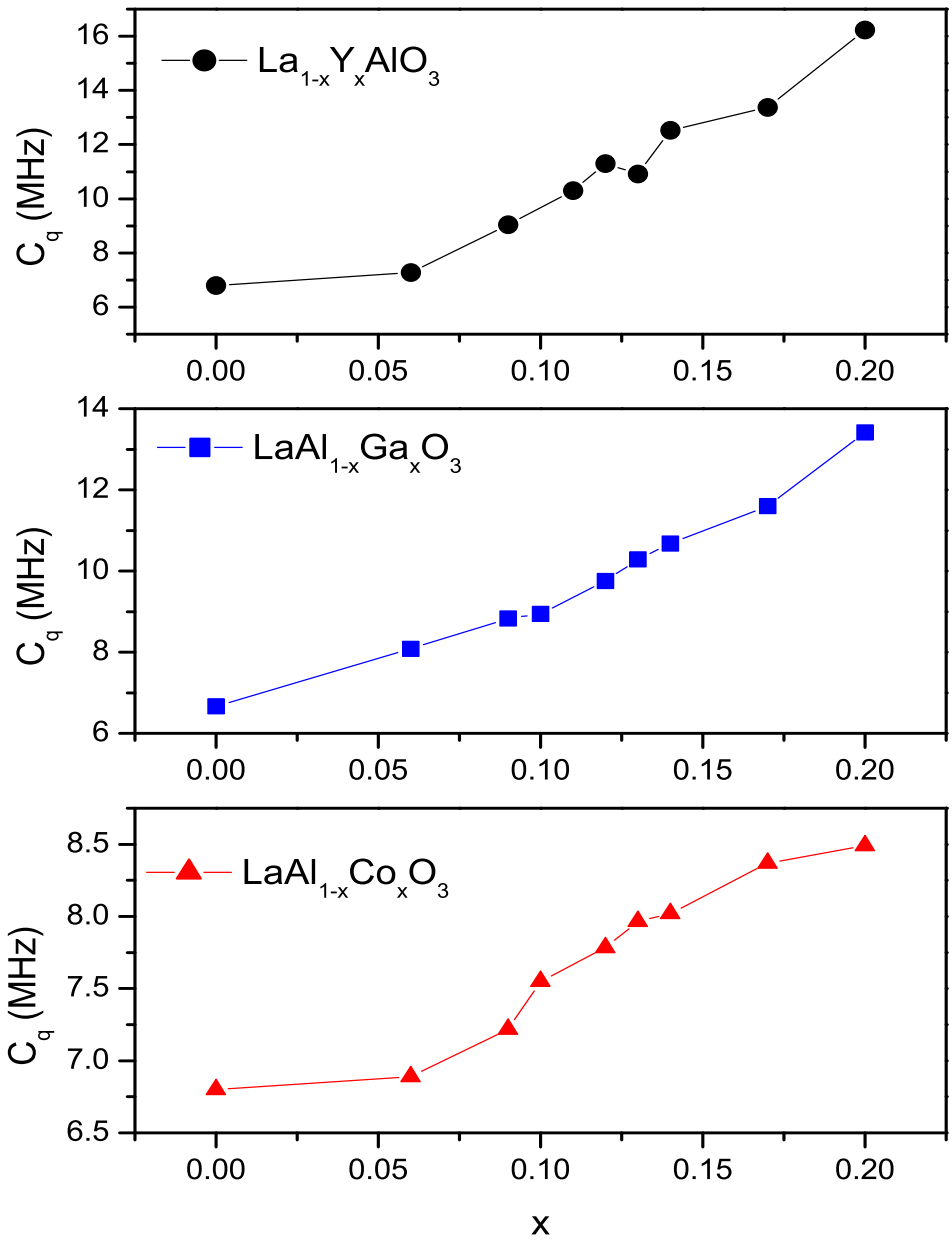


*Figure 7.4: Variation in the $^{139}$La quadrupole coupling constant as function of x*

The $ABO_3$ cubic perovskite structure can be represented in two different ways. In the A-type cubic perovskite structure, the larger A-ions are at the center of the unit cell, the smaller B-cations are at the corners of the cube, and the O ions are at the center of the edges of the unit cell. In the B-type perovskite structure, the B-cations are at the center of the unit cell, A cations are at the corners and the O

ions are at the centers of the faces of the unit cell. Both the A-type and B-type perovskite structure of $LaAlO_3$, consisting of eight cubic unit cells, are shown in figures, 7.5 and 7.6. The rhombohedral unit cell is also shown in the figures for comparison.

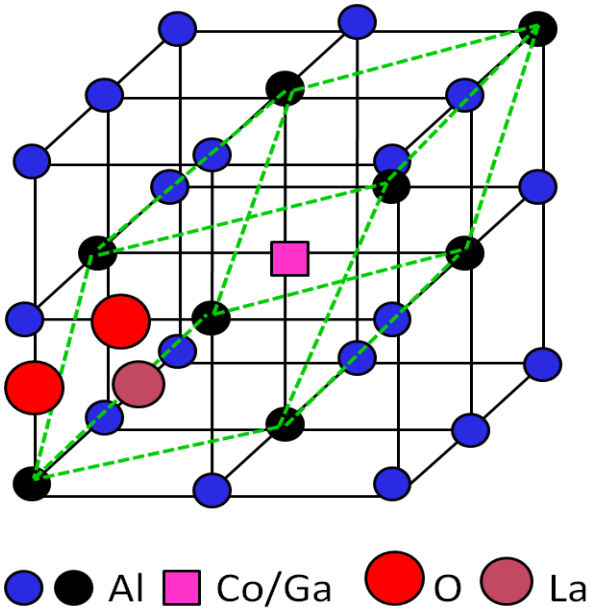


*Figure 7.5: A-type unit cell of $LaAlO_3$*

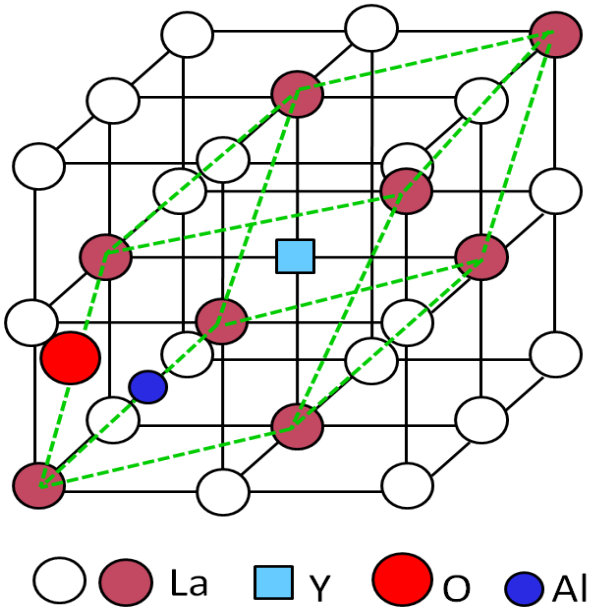


*Figure 7.6: B-type unit cell of $LaAlO_3$*

As shown in the figures, when one atom from the corners of a cubic unit cell is replaced by a different atom, it is shared by 8 unit cells in both the A-type and B-type unit cells. This corresponds to the replacement of one atom in the rhombohedral unit cell. That is when $x = 1/8$, this results in a uniform replacement of the atom from every rhombohedral unit cell of the perovskite structure leading to a homogeneous distribution of the substituted atom in the lattice. This is the probable reason for the drastic changes in physical properties of the La-site and Mn-site substituted $LaMnO_3$ between 10 to 15% substitution, at the corresponding sites, as reported in the literature.

### 7.4.3 Conclusions

$^{27}$Al and $^{139}$La solid-state NMR studies on different compositions in $LaAl_{1-x}Co_xO_3$ and $LaAl_{1-x}Ga_xO_3$ showed that there is continuous distortion of the $AlO_6$ octahedra in the perovskite structure, with increasing amount of substitution. However, the distortions are very small when Al is substituted with an ion of comparable ionic size and larger distortions occur when substituted with an ion of larger ionic size. This indicates that the internal chemical pressure plays an important role in determining the structure of the material and thereby varies its properties. Both the $^{27}$Al and $^{139}$La NMR spectral studies indicated signatures for distortion of the corresponding polyhedra around the region $x = 0.13$, where $1/8^{th}$ of all the corresponding atoms are replaced from the unit cell and this indeed affect the magnetic properties as reported for the corresponding magnetic system $LaMnO_3$.

## 7.5 Future perspectives

In $SrAl_{12}O_{19}$, it is possible that there exists a dynamic disorder between the penta coordinated and the distorted tetrahedral sites. It may be that the system undergoes dynamic disorder between between these two sites at higher temperatures and freezes in with some Al stuck in the distorted tetrahedral and some in the bipyramidal configuration. Thermal quenching studies may be able to give an

insight about the distribution of Al and nature of these sites.

Although we have observed the occupancy of Zn ions in the octahedral sites of $SrAl_{12}O_{19}$, Zn ions have a preferential occupancy at the tetrahedral sites. Therefore, in order to precisely find out the substitutional sites in $SrAl_{12}O_{19}$, the Al-site can be substituted with larger divalent ions which occupies only at the octahedral sites. Similarly, it would be interesting to study the effect of size of the substituted ion at the Sr-site, such as $Y^{3+}$, and substitution of other divalent ions such as $Ca^{2+}$, $Pb^{2+}$ at the Sr-site so that trivalent ions of different ions can be substituted at the Al sites like larger ions $In^{3+}$, $Sc^{3+}$, etc. These studies are expected to give more structural related information, in combination with structural studies using X-ray diffraction, on the effect of substitution and distribution in the different sites in the magnetoplumbite structure.

In $LaAlO_3$, since the $^{27}$Al quadrupole coupling constant $C_q$ is very low, measurements at the lowest possible fields, for example using a 60 MHz spectrometer, may give more insights into the structure of the system, especially on the motion of the Al ions in the structure. The static NMR experiments at very low temperatures may give an idea about the range of motions. $^{27}$Al relaxation studies also can give some insight into the range of motions inside the molecule. Molecular dynamics studies are also essential to get an understanding of the dynamics. Similarly, SSNMR studies using very close compositions, such as a difference of $\Delta x = 0.1$ or less in the A-site or B-site substituted perovskite compositions $A_{1-x}A'_xBO_3$ and $AB_{1-x}B'_xO_3$, may shed more light into the changes in the physical properties of different substituted functional perovskites such as ferroelectric and ferromagnetic compositions, associated with the changes in the structure of those materials.

## List of Publications

1. **Bindhu Baby**, K.K. Dey, T.G. Ajithkumar and P. A. Joy, "Identification of the Zn Substitution Sites in La-Zn Substituted $SrAl_{12}O_{19}$ from $^{27}Al$ Solid-State NMR Studies." *J. Am. Ceram. Soc.* 2014, 97, (9), 2990-2995.

2. **Bindhu Baby**, T.G. Ajithkumar and P. A. Joy, "Structural studies of $LaAlO_3$ using $^{27}Al$ and $^{139}La$ Solid-State NMR Spectroscopy." Manuscript submitted.

3. **Bindhu Baby**, T.G. Ajithkumar and P. A. Joy,"Structural Phase Transition in $La_{1-x}Y_xAlO_3$ Studied by $^{139}La$ and $^{27}Al$ Solid-State NMR Spectroscopy." Manuscript under preparation.

4. **Bindhu Baby**, T.G. Ajithkumar and P. A. Joy, " Solid-State NMR Study of $LaAl_{1-x}M_xO_3$ Perovskites." Manuscript under preparation.

## Awards:

"**Best Poster Award**" in the Annual Divisional Symposium held on December 13, 2011 at Physical and Materials Chemistry Division, National Chemical Laboratory, Pune, India.